



AFRL-RQ-WP-TM-2013-0222

MULTIDISCIPLINARY COMPUTATIONAL AERODYNAMICS

Miguel R. Visbal

**Aerodynamic Technology Branch
Aerospace Vehicles Division**

**OCTOBER 2013
Interim Report**

Approved for public release; distribution unlimited.

See additional restrictions described on inside pages

STINFO COPY

**AIR FORCE RESEARCH LABORATORY
AEROSPACE SYSTEMS DIRECTORATE
WRIGHT-PATTERSON AIR FORCE BASE, OH 45433-7542
AIR FORCE MATERIEL COMMAND
UNITED STATES AIR FORCE**

NOTICE AND SIGNATURE PAGE

Using Government drawings, specifications, or other data included in this document for any purpose other than Government procurement does not in any way obligate the U.S. Government. The fact that the Government formulated or supplied the drawings, specifications, or other data does not license the holder or any other person or corporation; or convey any rights or permission to manufacture, use, or sell any patented invention that may relate to them.

This report was cleared for public release by the USAF 88th Air Base Wing (88 ABW) Public Affairs Office (PAO) and is available to the general public, including foreign nationals.

Copies may be obtained from the Defense Technical Information Center (DTIC) (<http://www.dtic.mil>).

AFRL-RQ-WP-TM-2013-0222 HAS BEEN REVIEWED AND IS APPROVED FOR PUBLICATION IN ACCORDANCE WITH ASSIGNED DISTRIBUTION STATEMENT.

*/Signature//

MIGUEL R. VISBAL, Team Lead
Aerodynamic Technology Branch
Aerospace Vehicles Division

//Signature//

CHRISTOPHER P. GREEK, Branch Chief
Aerodynamic Technology Branch
Aerospace Vehicles Division

//Signature//

FRANK C. WITZEMAN JR
Division Chief
Aerospace Vehicles Division

This report is published in the interest of scientific and technical information exchange, and its publication does not constitute the Government's approval or disapproval of its ideas or findings.

*Disseminated copies will show “//Signature//” stamped or typed above the signature blocks.

REPORT DOCUMENTATION PAGE				Form Approved OMB No. 0704-0188	
<p>The public reporting burden for this collection of information is estimated to average 1 hour per response, including the time for reviewing instructions, searching existing data sources, gathering and maintaining the data needed, and completing and reviewing the collection of information. Send comments regarding this burden estimate or any other aspect of this collection of information, including suggestions for reducing this burden, to Department of Defense, Washington Headquarters Services, Directorate for Information Operations and Reports (0704-0188), 1215 Jefferson Davis Highway, Suite 1204, Arlington, VA 22202-4302. Respondents should be aware that notwithstanding any other provision of law, no person shall be subject to any penalty for failing to comply with a collection of information if it does not display a currently valid OMB control number. PLEASE DO NOT RETURN YOUR FORM TO THE ABOVE ADDRESS.</p>					
1. REPORT DATE (DD-MM-YY) October 2013		2. REPORT TYPE Interim	3. DATES COVERED (From - To) 01 October 2011 – 30 September 2013		
4. TITLE AND SUBTITLE MULTIDISCIPLINARY COMPUTATIONAL AERODYNAMICS			5a. CONTRACT NUMBER In-house		
			5b. GRANT NUMBER		
			5c. PROGRAM ELEMENT NUMBER 61102F		
6. AUTHOR(S) Miguel R. Visbal			5d. PROJECT NUMBER 2307		
			5e. TASK NUMBER		
			5f. WORK UNIT NUMBER Q05N		
7. PERFORMING ORGANIZATION NAME(S) AND ADDRESS(ES) Aerodynamic Technology Branch, Aerospace Vehicles Division Air Force Research Laboratory, Aerospace Systems Directorate Wright-Patterson Air Force Base, OH 45433-7542 Air Force Materiel Command, United States Air Force			8. PERFORMING ORGANIZATION REPORT NUMBER AFRL-RQ-WP-TM-2013-0222		
9. SPONSORING/MONITORING AGENCY NAME(S) AND ADDRESS(ES) Air Force Research Laboratory Aerospace Systems Directorate Wright-Patterson Air Force Base, OH 45433-7542 Air Force Materiel Command United States Air Force			10. SPONSORING/MONITORING AGENCY ACRONYM(S) AFRL/RQVA		
			11. SPONSORING/MONITORING AGENCY REPORT NUMBER(S) AFRL-RQ-WP-TM-2013-0222		
12. DISTRIBUTION/AVAILABILITY STATEMENT Approved for public release; distribution unlimited.					
13. SUPPLEMENTARY NOTES This report contains color. Public Affairs (PA) Office clearance case numbers appear with the respective publications in 14. ABSTRACT .					
14. ABSTRACT <p>Progress has been achieved in a number of multidisciplinary research areas pertinent to the present task. Significant accomplishments include: discovery of the separated flow topology on maneuvering low-aspect-ratio wings for small unmanned air systems, prediction of excrescence-induced boundary-layer transition critical for energy efficiency, elucidation of the dynamics of hovering wings for micro-air-vehicles, explanation of the improved performance of dragonfly biomimetic corrugated wings at low Reynolds numbers, large-eddy simulations of membrane low-aspect ratio wings for small-unmanned systems, detailed simulations of dynamic stall of a pitching wing at realistic Reynolds numbers, simulation of aero-optical aberration in a shock turbulent boundary layer interaction required for laser integration in future air dominance (FAD), discovery of new self-excited oscillations in flexible panels subject to impinging shocks critical for FAD and hypersonic vehicles in hot descent. Given the space limitations, only selected research highlights pertaining to some of the above topics are presented. The following titles published in professional journals and conference proceedings, and unpublished preprints, are provided in the appendices:</p> <ul style="list-style-type: none"> “Flow Structure and Unsteady Loading Over a Pitching and Perching Low-Aspect-Ratio Wing” (88ABW-2012-3243) “Aeroelastic Simulations of an Aspect Ratio Two Flexible Membrane Wing” (88ABW-2011-2447) “Numerical Exploration of the Origin of Aerodynamic Enhancements in [low-Reynolds number] Corrugated Airfoils” (88ABW-2013-0368) “Investigation of aspect ratio and dynamic effects due to rotation for a revolving wing using high-fidelity simulation” (88ABW-2013-2666) “Numerical Simulation of Excrescence Generated Transition” (88ABW-2013-2608) “Shock/Boundary Layer Interaction Over a Flexible Panel” (88ABW-2011-6531) “Computational investigation of the influence of unsteady shock motion on aberrating structures in supersonic boundary layers” (88ABW-2013-2843) 					
15. SUBJECT TERMS					
16. SECURITY CLASSIFICATION OF:			17. LIMITATION OF ABSTRACT: SAR		
a. REPORT Unclassified	b. ABSTRACT Unclassified	c. THIS PAGE Unclassified	18. NUMBER OF PAGES 210	19a. NAME OF RESPONSIBLE PERSON (Monitor) Miguel R. Visbal 19b. TELEPHONE NUMBER (Include Area Code) N/A	

Table of Contents

<u>Section</u>	<u>Page</u>
List of Figures	ii
List of Tables	ii
Research Objectives.....	1
Technical Summary	2
ELEMENT I: Flow Structure and Loading Over Pitching and Perching Low-Aspect-Ratio Wings	3
ELEMENT II: Effect of Surface Compliance on the Flow Structure and Loads of a Stationary Low-Aspect-Ratio Wing.....	8
ELEMENT III: Exploration of the Origin of Aerodynamic Enhancements in Low-Reynolds-Number Corrugated Airfoils.....	11
ELEMENT IV: Dynamics of Revolving Wings	14
ELEMENT V: Plasma-Based Control of Excrescence-Induced Transition	17
ELEMENT VI: Interaction of an Oblique Shock with a Flexible Panel	19
ELEMENT VII: Aero-Optical Aberration in Supersonic Flows	22
Publications:.....	24
Published in Peer Reviewed Journals, Books, etc:.....	24
Published in Conference Proceedings:	25
Invited Lectures, Presentations, Talks, etc:.....	27
Professional Activities:	27
Honors Received:	29
Collaborations / Interactions	29
Transitions	30
APPENDIX A “Flow Structure and Unsteady Loading Over a Pitching and Perching Low-Aspect-Ratio Wing”	31
APPENDIX B “Aeroelastic Simulations of an Aspect Ratio Two Flexible Membrane Wing”	61
APPENDIX C “Numerical Exploration of the Origin of Aerodynamic Enhancements in [low-Reynolds number] Corrugated Airfoils”	78
APPENDIX D “Investigation of aspect ratio and dynamic effects due to rotation for a revolving wing using high-fidelity simulation”	116
APPENDIX E “Numerical Simulation of Excrescence Generated Transition”	139
APPENDIX F “Shock/Boundary Layer Interaction Over a Flexible Panel”	159
APPENDIX G “Computational investigation of the influence of unsteady shock motion on aberrating structures in supersonic boundary layers”	183

List of Figures

Figure	Page
Figure 1. Computed instantaneous three-dimensional flow structure for pitching wing.....	4
Figure 2. Comparison of computed and experimental three-dimensional flow structure over pitching wing.....	5
Figure 3. Effect of pitch rate on wing aerodynamic loading	6
Figure 4. Flow structure and aerodynamic loading for a perching wing.....	7
Figure 5. Time-averaged flow structure for (a) rigid, (b) rigid cambered and (c) fully flexible wing. Figure displays contours of surface pressure and limiting streamlines.....	9
Figure 6. Total surface deflection z/c (upper) and difference from the mean deflection $(z-z_{\text{mean}})/c$ (lower): a) $\tau=0.0$, b) $\tau=0.25$, c) $\tau=0.5$, d) $\tau=0.75$ e) $\tau=1.0$	9
Figure 7. Iso-surfaces of Q-criterion colored by pressure coefficient for the flexible-membrane wing: a) $\tau=0.0$, b) $\tau=0.25$, c) $\tau=0.5$, d) $\tau=0.75$ e) $\tau=1.0$	10
Figure 8. Summary of results for several airfoil sections at $\alpha = 10^\circ$ and $\text{Rec} = 3.4 \times 10^4$. From top to bottom: leading-edge geometry, time-averaged streamwise velocity and streamlines, instantaneous spanwise vorticity and mean pressure contours.	12
Figure 9. (a) Revolving wing configuration and (b) lift, drag, and pitching moment coefficients for wings of various aspect ratio.	15
Figure 10. Three-dimensional flow structure for revolving wings depicted using an iso-surface of relative total pressure	16
Figure 11. Evolution of the surface pressure distribution on the suction side of the wing with overlaid iso-surface of relative total pressure highlighting the vortex core along the leading edge. (1) Denotes the expansion of the vortex core due to breakdown. (2) Indicates the undulation of the vortex core for higher aspect ratios.....	16
Figure 12. Direct simulation of excrescence-induced transition.....	18
Figure 13. Control of excrescence-induced transition using a surface-mounted plasma actuator	18
Figure 14. Interaction of a shock with a flexible panel.....	20
Figure 15. Oblique shock impingement on a flexible panel for inviscid Mach 2.0 flow: maximum deflection amplitude at 3/4-chord panel location as a function of pressure ratio and dynamic pressure (left) and instantaneous pressure contours 	20
Figure 16. Laminar shock boundary layer interaction over a flexible panel: instantaneous density contours (left), mean and instantaneous surface pressure (center) and time- averaged velocity (right).	21
Figure 17. Aero-optical aberration in shock turbulent boundary layer interactions	23

List of Tables

Table	Page
Table 1. Time-averaged aerodynamic coefficients for rigid and flexible wings	10
Table 2. Summary of time-averaged aerodynamic forces for several airfoil sections at $\alpha = 10^\circ$ and $\text{Rec} = 3.4 \times 10^4$	13

Research Objectives

To develop and demonstrate advanced multidisciplinary numerical simulation capabilities for aerospace vehicles with emphasis on highly accurate, massively parallel computational methods for a broad range of applications, including Direct and Large-Eddy simulation of transition and turbulence, traditional and plasma-based active flow control, aero-optics, unsteady aerodynamics and nonlinear fluid/structure interactions. These technical objectives directly support AFRL & the Aerospace Systems Directorate's requirements on persistent ISR, Future Air Dominance and Energy Efficiency. This in-house task, designated as a Star Team by AFOSR, is a key core task within the Computational Sciences Center of Excellence.

Technical Summary

During this reporting period, significant progress has been achieved in a number of multidisciplinary research areas pertinent to the present task. A partial list of significant accomplishments include:

- Discovery of the separated flow topology on maneuvering low-aspect-ratio wings for small unmanned air systems
- Prediction of excrescence-induced boundary-layer transition critical for energy efficiency
- Elucidation of the dynamics of hovering wings for micro-air-vehicles
- Explanation of the improved performance of dragonfly biomimetic corrugated wings at low Reynolds numbers
- First large-eddy simulations of membrane low-aspect ratio wings for small-unmanned systems
- Most detailed simulations of dynamic stall of a pitching wing at realistic Reynolds numbers: a model for unsteady separation in vertical gusts
- First simulation of aero-optical aberration in a shock turbulent boundary layer interaction required for laser integration in Future Air Dominance (FAD)
- Discovery of new self-excited oscillations in flexible panels subject to impinging shocks: critical for FAD and hypersonic vehicles in hot descent
- Exploration of plasma-based control strategies for transitional flows critical for drag reduction and energy efficiency.

Given space limitations, only highlights of selected research elements are provided. Details of these and other topics can be found in the extensive list of citations provided at the end of this report (some of which are provided as appendices to this report).

ELEMENT I: Flow Structure and Loading Over Pitching and Perching Low-Aspect Ratio Wings

The process of unsteady separation and stall generated by large transient excursions in angle of attack, referred to in general as dynamic stall, represents a long-standing issue in maneuvering aircraft and rotorcraft applications. In recent years, interest in dynamic stall at moderate Reynolds numbers has re-emerged driven by its importance to small unmanned air vehicle system operation, as well as to the understanding of the remarkable performance found in natural flight. Detailed characterization of the dynamic stall process is also critical for the prediction of vehicle gust response and to suggest possible gust rejection strategies.

Under this task, we have addressed the flow structure and unsteady loading arising over a rectangular wing of aspect ratio two subjected to high-amplitude transient pitching and perching maneuvers. Canonical pitching motions for a non-translating wing in the presence of a constant freestream were first investigated in order to elucidate the three-dimensional dynamic stall process and the effects of pitch rate and Reynolds number on flow structure and aerodynamic loads. A simple perching maneuver involving simultaneous rotation and deceleration to rest was also considered in order to explore the effects of variable horizontal velocity on the flow evolution and loading relative to the constant-freestream case. The flow fields were computed employing the extensively validated high-fidelity implicit large-eddy simulation (ILES) approach originally developed under previous AFOSR sponsorship. This ILES methodology relies on a 6th-order compact scheme for the spatial derivatives and on up to 10th-order Pade-type low-pass filters which do not dissipate the spatially resolved content of the solution. The most interesting results are summarized in this section whilst a more complete account of this research can be found in Appendix A at the end of this report.

The three-dimensional instantaneous flow structure for non-dimensional pitch rate $\Omega = 0.2$ is shown in Fig. 1 at several points during the maneuver employing an iso-surface of constant total pressure, the corresponding wing surface pressure and contours of vorticity magnitude on the symmetry plane. As the wing is pitched and the angle of attack increases, one can observe a nascent leading-edge vortex which is pinned at the wing front corners and which appears initially to be fairly uniform across a significant portion of the span. By the time the wing has reached an angle of attack $\alpha = 15^\circ$, the flow has become highly three dimensional, and large transverse velocities directed towards the centerline exist within the leading-edge vortex core. Examination of the vortical structure on the symmetry plane indicates that the LEV is initially laminar and similar to that found in 2D dynamic stall. By $\alpha = 30^\circ$ the emergence of fine-scale structures is apparent due to the onset of transitional effects. The process of transition or breakdown of the LEV is enhanced by the strong axial currents within the vortex core, which eventually reach the wing centerplane. As the angle of attack increases further, the leading-edge vortex system evolves into a Λ -shaped structure as the vortex lifts away from the plate near the symmetry plane while remaining pinned at the wing front corners. Eventually the LEV detaches from the edges forming an arch-type vortex with legs normal to the wing surface. This arch vortex resides over the wing and establishes a well-defined large-scale swirling pattern on the wing surface.

Due to the presence of the LEV system, the wing surface pressure displays a region of strong suction that extends from the wing corner to the centerline. The pressure is lowest near the corner where the vortex is in closest proximity to the wing surface. As the arch-vortex forms, a concentric region of low pressure emerges and a large-scale circulatory pattern is established over the wing. Animations of the flow field revealed that this region of low pressure (corresponding to the legs of the arch-vortex) propagates towards the wing leading edge before finally moving downstream and outboard. This interesting behavior may be attributable, based on inviscid arguments, to the self-induced velocity of the arch-vortex and interaction with its own image on the plate.

A distinct property of the arch-vortex and its accompanying circulatory motion is the very long residence time over the wing. The last frames in Fig. 1 correspond to an elapsed time of 4.5 convective times after reaching the maximum angle of attack. Even at this stage, a weakened arch vortex is still observed over the wing and a region of circulation and low pressure persists on the wing upper surface. This represents an interesting new finding associated with the three-dimensional unsteady separation process for a low-aspect-ratio wing that is quite different from the 2D counterpart where the dynamic stall vortex is readily shed following its detachment from the leading edge. Another distinct element in the pitching wing 3D flow structure is the tip vortex seen in the iso-surface plots of Fig. 1. This vortex strengthens with increasing angle of attack inducing a narrow region of low pressure near the tips on the wing surface. At very high angles of attack, the tip vortex experiences vortex breakdown and ultimate collapse.

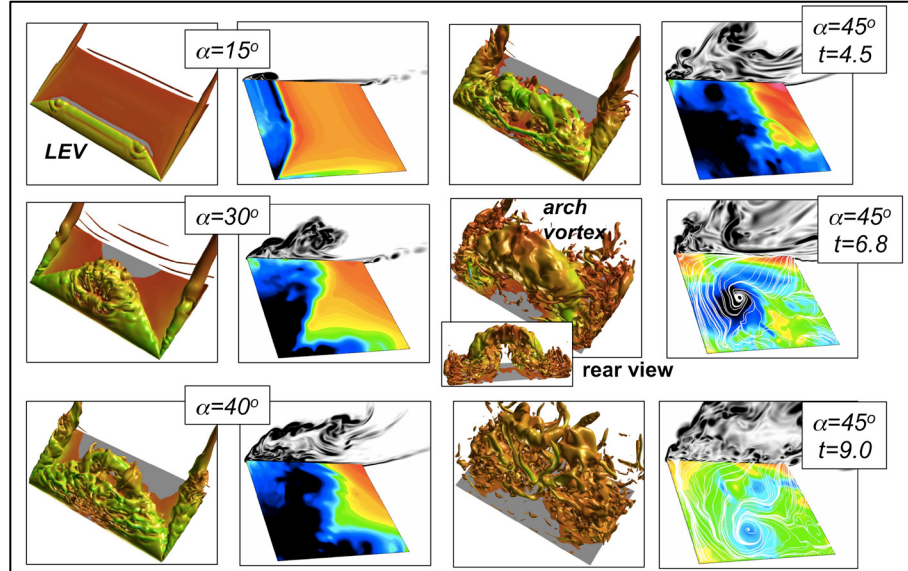


Figure 1. Computed instantaneous three-dimensional flow structure for pitching wing

New volumetric PIV measurements for the same pitching wing configuration were performed at Lehigh University under AFOSR sponsorship. The experimental and computed flow structures are compared in Fig. 2 at two points during the pitching maneuver. The experimental frames display an iso-surface of the Q-criterion ($Q = 5$) for the phased-averaged flow. These figures clearly show the Λ -type vortical structure and the subsequent formation of the arch-type vortex previously described. The computational iso-surfaces exhibit fine-scale features not seen in the experiments. This is attributed primarily to the much finer spatial resolution

provided by the computational mesh relative to the spacing between sampling planes used for the experimental volume reconstruction. In order to provide a more direct comparison between experiment and computation, the computed flow field was filtered down to a spatial resolution comparable to that of the experimental measurements using the procedure developed under our task. The iso-surfaces derived from the filtered computational results (with similar spatial resolution as the experiments) display good agreement with the volumetric measurements.

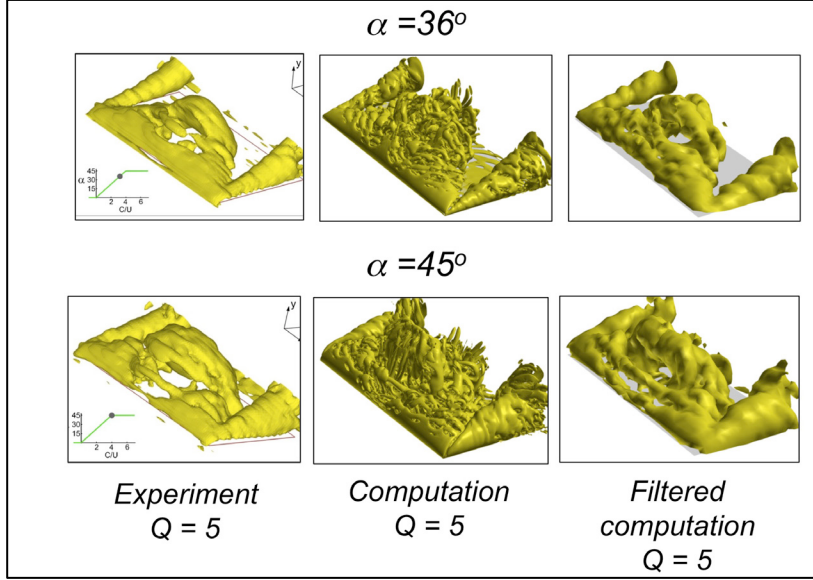


Figure 2. Comparison of computed and experimental three-dimensional flow structure over pitching wing.

The effect of pitch rate on the wing aerodynamic loading is presented in Fig. 3. Several trends are apparent in the lift and pitching moment coefficient histories as a function of pitch rate. In all cases, there is a non-circulatory spike in the lift and pitching moment induced by the angular acceleration. The peak in lift ΔC_{L1} displays a linear variation as a function of pitch rate. Following this initial surge, the lift distribution becomes fairly linear with a slope close to the static value of π (in radians) but shifted by an offset ΔC_{L2} . Figure 3 also displays the quantity denoted as ΔC_M corresponding to the magnitude of the approximately constant negative value of pitching moment established after the end of angular acceleration. Both ΔC_{L2} and ΔC_M exhibit an effective linear dependence on pitch rate. The offsets in lift and moment coefficients observed after reaching a constant angular rate are consistent with a rotation-induced apparent camber. The overall history of the lift coefficient indicates that both the maximum value of C_L and its corresponding angular position increase with pitch rate. Even for the smallest pitch rate, there is a significant increase in maximum lift, which is almost twice the maximum static value. It is interesting to note that the occurrence of maximum lift follows the emergence of the arch-vortex at least for lower values of pitch rate.

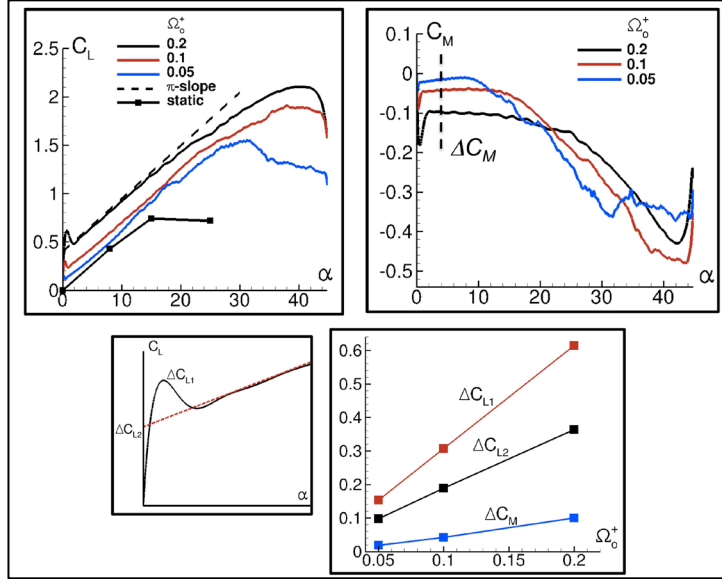


Figure 3. Effect of pitch rate on wing aerodynamic loading

The effect of variable freestream velocity on the dynamic stall process of a pitching low-aspect-ratio wing was considered. This effect is of interest since in a typical perching maneuver, pitching is also accompanied by deceleration to an effectively zero velocity. Another potential application is the case of pitching in the presence of variable freestream velocity such as in a horizontal gust encounter. In this exploratory study, a simplified perching-type maneuver is prescribed such that the wing accelerates from rest and at zero angle of attack to a constant velocity in quiescent flow. This constant speed is maintained for a sufficiently long time in order to effectively eliminate transients. The wing then pitches from zero incidence to a maximum angle attack of 45° while it simultaneously decelerates and comes to a full stop. Since the freestream velocity is zero, the Reynolds number and pitch rate are defined in terms of the maximum translating speed.

The flow structure for the perching wing corresponding to $\Omega = 0.2$ is presented in Fig. 4. Comparison of Figs. 1 and 4 shows that the flow structure for the perching case is similar to the constant freestream situation for small angles of attack. However, as the wing translating velocity is appreciably reduced, significant differences arise between the perching and pitching cases. For the perching case, the LEV vortex does not evolve into the arch-type structure seen in the pure-pitch situation. Instead, the growth of the LEV is halted and it remains closer to the leading edge. Eventually, as the wing approaches its final horizontal position, the LEV actually moves forward of the plate. The formation underneath the plate of a stopping trailing-edge vortex with the same sense of rotation as the LEV system is also observed.

Rescaling the loads using the local translational speed shows agreement between the perching and standard cases only up to a limited angle of attack. Beyond this point, there are significant differences not only quantitatively but also in the trends, which can be different depending on pitch rate itself. Values of lift derived from experiments in a constant freestream facility can either under predict or over predict the lift force when rescaled to the perching maneuver. The present results suggest that simplified generalizations cannot be made regarding the behavior of

the loads for a perching maneuver in relation to its constant-freestream counterpart. Further computations/experiments exploring the flow evolution and loads as a function of the phase relationship between the rotational and translational motions are required.

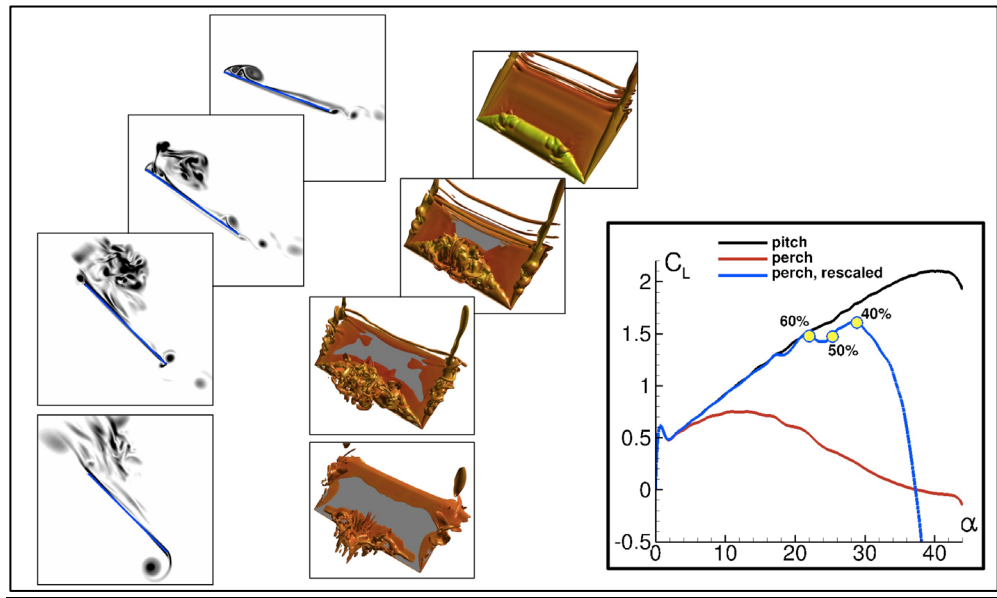


Figure 4. Flow structure and aerodynamic loading for a perching wing.

ELEMENT II: Effect of Surface Compliance on the Flow Structure and Loads of a Stationary Low-Aspect-Ratio Wing.

The dynamics of flexible wings is critical to the performance of small-unmanned air vehicles and to their ability to withstand gusts. The membrane wing considered in this study is based on the experimental model developed at Bath University (UK) under AFOSR/EOARD sponsorship. The wing of aspect ratio AR=2 consists of a rigid stainless steel rectangular frame with an airfoil shaped cross-section which is covered by an attached latex membrane. The latex sheet had a thickness of $t=0.2\text{mm}$, Young's modulus of 2.2MPa , and a density, $\rho_m = 1\text{gr / cm}^3$. The experiments were performed over an angle-of- attack range from $\alpha=0$ to 25 degrees, and Reynolds number based on chord length $Re=24,300$. Computations for an angle-of-attack $\alpha=16^\circ$ were carried out in the present work. The most prominent results are summarized in this section whilst a more complete account of this research can be found in Appendix B at the end of this report.

Fully rigid and flexible membrane configurations were considered. In order to distinguish the influence of deformation-induced mean camber from the actual membrane dynamic fluctuations, computations for a rigid cambered wing (with the shape of the mean deflection) were also performed. In order to demonstrate the effect of structural compliance, Fig. 5 shows the pressure coefficient and limiting streamline pattern on the upper-surface of the membrane wing. For the rigid wing, separated flow covers the majority of the surface with the attachment line reaching the trailing edge over the mid-section of the wing. Two stable foci are observed in the separated flow region. Low-pressure associated with the separated flow covers a significant portion of the wing, with lower pressures located under the two distinct stable foci. Two narrow suction regions observed along the tips of the wing are due to the imprint of the tip vortices.

Introducing the static mean cambering effect of the flexible-membrane wing results in a decrease in the size of the main separated flow region, with primary flow attachment occurring upstream from the trailing edge. The two foci observed for the baseline rigid wing have moved upstream and outboard, and are now located near the upstream corners of the wing. Lower values of the pressure coefficient are observed in the separated flow region. Lastly, results for the fully flexible wing display further reduction in the size and extent of the separated region, with flow attachment located near the wing mid-chord. Additional reduction in surface pressure is observed in the separation region particularly in the vicinity of the front corners.

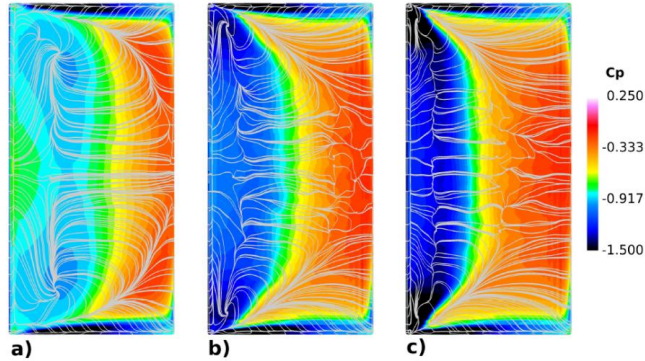


Figure 5. Time-averaged flow structure for (a) rigid, (b) rigid cambered and (c) fully flexible wing. Figure displays contours of surface pressure and limiting streamlines.

Figure 6 displays the dynamic response of the membrane over approximately one-cycle of the structural motion. The upper-half of the figure shows the total membrane deflection suggesting a predominantly first-mode global structural response. The region of maximum deflection moves downstream and subsequently back upstream over one-cycle of the membrane motion. If the mean first-mode deflection is subtracted from the total surface deflection, a second streamwise structural mode is more clearly discerned in the lower half of Fig. 6. These observations concerning the membrane dynamics are consistent with the behavior found in the experiments.

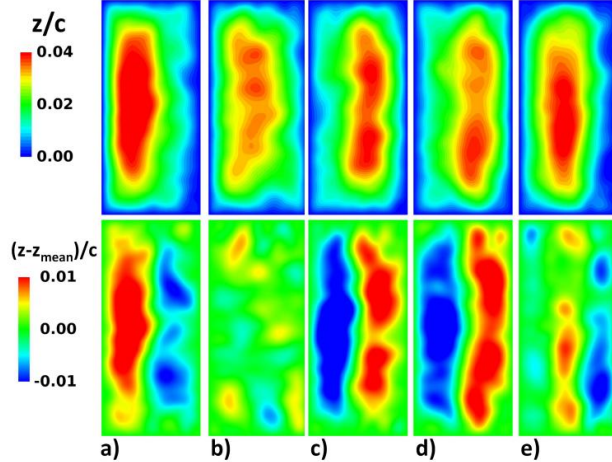


Figure 6. Total surface deflection z/c (upper) and difference from the mean deflection $(z-z_{\text{mean}})/c$ (lower): a) $\tau=0.0$, b) $\tau=0.25$, c) $\tau=0.5$, d) $\tau=0.75$ e) $\tau=1.0$

The three-dimensional instantaneous flow structure over the flexible wing is visualized in Fig. 7 using an iso-surface of the Q-criterion colored by pressure coefficient. The flow detaches from the leading edge and the separated shear-layer rolls up into a series of discrete vortical sub-structures. A complex amalgamation of these sub-structures is formed and is subsequently shed and convected downstream. These structures are subject to spanwise instabilities and ultimate breakdown giving rise to fine-scale flow features. Such a distinct shedding process is not clearly discerned in the rigid wing case, and results from the influence of the membrane motion on the separated shear-layer dynamics.

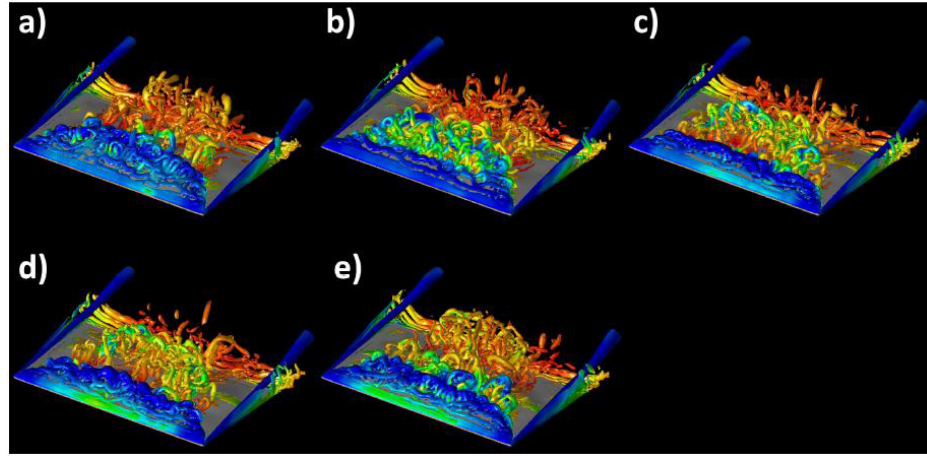


Figure 7. Iso-surfaces of Q-criterion colored by pressure coefficient for the flexible-membrane wing: a) $\tau=0.0$, b) $\tau=0.25$, c) $\tau=0.5$, d) $\tau=0.75$ e) $\tau=1.0$

The modification of the flow structure, due to the flexibility of the membrane wing, impacts its aerodynamic performance. Table 1 lists the aerodynamic coefficients for each of the cases computed. The rigid cambered wing demonstrates a slight improvement in the total lift coefficient, albeit at the cost of increased drag and reduced L/D. The flexible case performs better than the mean cambered airfoil, indicating a favorable effect due to the dynamic motion of the membrane. The pitching moment exhibits a continual reduction of the nose-down pitching moment when going from the rigid, flat-membrane wing to the flexible-membrane wing.

	CL	CD	L/D	<i>Cm_y</i>
Rigid Flat Wing	0.965	0.235	4.112	-0.160
Rigid Cambered Wing	1.020	0.269	3.794	-0.140
Flexible Wing	1.026	0.263	3.903	-0.123

Table 1. Time-averaged aerodynamic coefficients for rigid and flexible wings

ELEMENT III: Exploration of the Origin of Aerodynamic Enhancements in Low-Reynolds-Number Corrugated Airfoils.

In recent years, the development of small-unmanned air systems (UASs) has become an area of great interest for researchers in both civilian and military applications. Design of these small aircrafts must overcome a number of challenges including low Reynolds numbers, low weight requirements, and more challenging aerodynamics. Good aerodynamic performance is difficult to maintain under low-speed conditions since the flow fields contain significant regions of laminar flow which are prone to separation even at moderate angles of attack. Many successful examples of small-scale flight may be found in nature. Dragonflies are of particular interest due to their broad range of flight capabilities including hovering and gliding. While gliding is an uncommon flight mode for insects, it is commonly observed in dragonflies as an energy saving technique and may be useful in small UAS design. Dragonfly wings were found to have among the highest lift coefficients of all insects studied in gliding flight while drag coefficients are similar to those of a flat plate. These wings exhibit large aspect ratio and a highly corrugated structure.

Several wind tunnel studies have shown possible advantages of surface corrugations in dragonfly wings. In addition to the aerodynamic benefits, corrugations have been shown to improve structural rigidity necessary for the high aspect-ratio wings configurations. A number of two-dimensional, low-order numerical studies have also been presented in the literature with emphasis on very low Reynolds numbers ($Re_c < 5,000$). Improvements in aerodynamic performance were attributed to the circulatory regions formed in the valleys of the corrugated surface.

We have conducted a high-fidelity numerical study of a bio-inspired corrugated airfoil using implicit large-eddy simulations. The effects of angle of attack and Reynolds number were studied over the ranges of $\alpha = 5^\circ$ to 10° and $Re_c = 5 \times 10^3$ to 5.8×10^4 respectively. This work is the first three-dimensional computational study of bio-inspired corrugated wing sections and considers Reynolds numbers bridging the low values considered in previous numerical laminar investigations with higher values of interest where transitional flow features emerge. The most interesting results are summarized in this section whilst a more complete account of this research can be found in Appendix C at the end of this report.

Selected flow fields for $\alpha = 10^\circ$ and $Re_c = 3.4 \times 10^4$ are displayed in Fig. 8. Three different geometries were considered including a standard flat plate, a baseline corrugated section used in previous experiments, as well as a modified corrugated configuration. The latter was obtained by increasing slightly the height of the first corrugation peak.

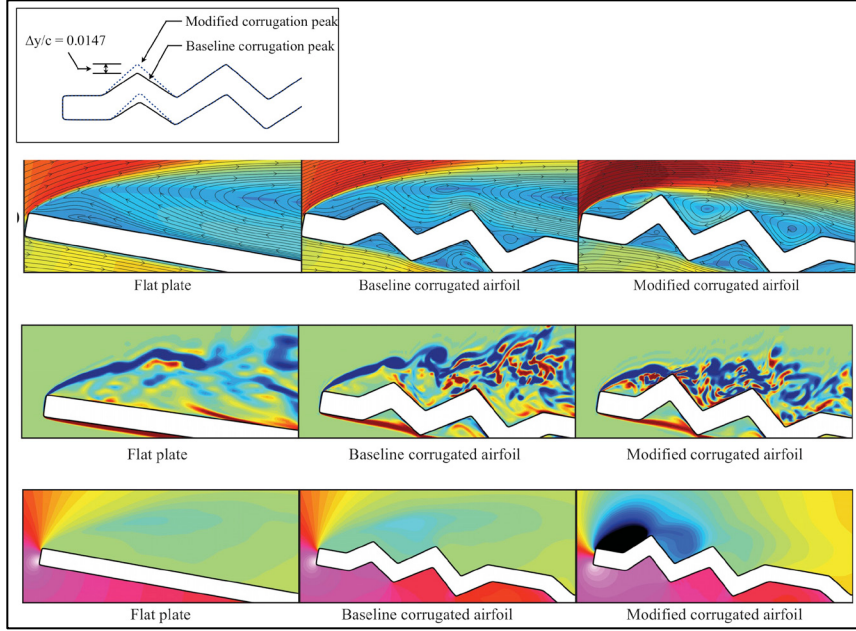


Figure 8. Summary of results for several airfoil sections at $\alpha = 10^\circ$ and $Re = 3.4 \times 10^4$. From top to bottom: leading-edge geometry, time-averaged streamwise velocity and streamlines, instantaneous spanwise vorticity and mean pressure contours.

Two significant findings emerged from this work. First, interaction between the shear layer and the leading-edge corrugations plays an important role in promoting early transition to turbulence. The presence of corrugations induces recirculation near the first peak promoting instabilities in the vortex sheet emanating from the leading edge. Either removing the corrugations or increasing the angle of attack reduces shear layer-corrugation interaction and the onset of transition eventually leading to stall. By contrast, this interaction can be enhanced and exploited by raising the first corrugation peak to capture the shear layer at higher angles of attack further delaying stall. This benefit is clearly evident in Fig. 8 for the modified corrugated geometry.

Secondly, a new drag-reducing mechanism was demonstrated as a consequence of the unique corrugated geometry. The separation region between the leading edge and the first corrugation promotes rapid turning of fluid around the leading edge. A strong suction region forms as a result along the forward-facing surface of the first corrugation, as seen in the time-averaged pressure contours in Fig. 8. Due to the forward inclination of the corrugation surface, the local pressure forces not only enhance lift but also reduce drag. A summary of the time-averaged aerodynamic performance coefficients is given in Table 2. Relative to the corrugated baseline section, the modified configuration displays an improvement in L/D of more than a 100%.

The present work demonstrates that flow behavior for bio-inspired wing sections can be highly sensitive to the leading-edge configuration due to transitional effects. Such a simple modification as slightly increasing the first corrugation peak results in further stall delay and greatly enhanced gliding ratios compared to a flat plate. The leading-edge corrugations are of particular importance and could be optimized to properly manipulate flow at higher angles of

attack and improve gliding ratios. These could be further exploited for changing flow conditions in flight through a morphing wing configuration.

Geometry	α	\bar{C}_L	\bar{C}_D	\bar{C}_{D_p}	\bar{C}_{D_s}	\bar{L}/\bar{D}
Flat Plate	10°	0.7053	0.1726	0.1645	0.0080	4.089
Baseline corrugated	10°	0.7290	0.1802	0.1776	0.0027	4.046
Modified corrugated	10°	0.9705	0.1154	0.1141	0.0013	8.410

Table 2. Summary of time-averaged aerodynamic forces for several airfoil sections at $\alpha = 10^\circ$ and $Re_c = 3.4 \times 10^4$.

ELEMENT IV: Dynamics of Revolving Wings

A number of unresolved issues still remain in the understanding of hovering flight. This regime is of interest not only for natural fliers but also for very small unmanned air vehicles. The genesis and persistence of lift at the very high angles of attack encountered in hover are mainly attributable to the presence of a stable leading-edge vortex (LEV). Aspects of the problem contributing to the formation, strength and stability of this LEV need further elucidation. Under the present task, we have conducted and extensive study to examine the vortex structure and aerodynamic loading on revolving wings using high-fidelity, implicit large-eddy simulation. The most interesting results are summarized in this section whilst a more complete account of this research can be found in Appendix D at the end of this report.

Several aspect ratios (AR = 1, 2, and 4) were considered at a root-based Reynolds number of 1,000. A schematic of the problem is shown in Fig. 9a. A coherent and attached vortex was achieved over each wing shortly after the onset of the motion (Fig. 10). The proximity of the vortex to the surface of the wing promotes a strong region of suction along the leading edge that persists to the mid-span, regardless of aspect ratio (Fig.11). Past mid-span, the vortex lifts off the surface into an arch-type structure as it reorients itself along the tip. The highest aspect-ratio-wing promotes the development of substructures in the feeding sheet of the leading edge vortex. The origins of these features have been traced back to the eruption of near-wall vorticity underneath the vortex that disrupts the feeding sheet, causing it to roll-up into discrete substructures. The substructures did not have an effect on overall force production, but lead to larger unsteady fluctuations around the mean loading. For a fixed root-based Reynolds number of 1,000, the lower aspect ratio wings do not have sufficient spans for these transitional elements to manifest.

While the substructure of the LEV feeding sheet shows a correlation with the local, span-based Reynolds number, vortex breakdown shows a stronger dependence on the established pressure gradient between the root and tip of the wing since breakdown was observed around mid-span regardless of aspect ratio. The mechanisms behind the shear-layer development and vortex breakdown very closely resemble those observed for the flow structure about swept delta wings. These similarities between rotating wings and swept delta wings can be extremely important for further understanding of revolving wing dynamics.

Since the leading edge vortex grows almost proportionally to the distance from the wing root, the chordwise extent of the vortex eventually becomes constrained by the trailing edge with increased aspect ratio, leading to a saturation of the aerodynamic loads (Fig. 9b). This geometric constraint indicates that there is no advantage of increasing aspect ratio once the extent of the LEV occupies the entire chord of the wing, which happens to be around an aspect ratio of AR = 2 for this study. With AR = 1, the edge of the vortex never reaches the trailing edge, which allows the vortex to continue to grow slightly during rotation resulting in a small increase of the lift and drag coefficients throughout the motion.

The size and shear-layer development of the leading edge vortex was shown to be sensitive to the distance from the root of the wing, indicating that a Reynolds number based on spanwise position may be appropriate for comparisons of wings of differing aspect ratio. Matching of the

root-based Reynolds numbers between different wing platforms ensures that the variation of Reynolds number along the span is kept consistent. This is much like the scaling used for swept delta wings.

The centrifugal, Coriolis, and pressure gradient forces were analyzed for each of the different aspect-ratio-wings. The normal and spanwise components of the pressure gradient force at the 25%-span location were shown to dominate the other two forces by an order of magnitude in the core of the LEV regardless of aspect ratio. However, the centrifugal force was found to be equally important outside the vortex core, and the two forces, together, are responsible for the large regions of outboard flow above the wing. The normal component of the Coriolis force was observed to be directed away from the wing surface at the base and in the core of the leading edge vortex. This finding clearly demonstrates that contrary to previous assertions it does not promote attachment of the vortex system, but rather, the opposite regardless of aspect ratio. The established outboard spanwise flow induced by the centrifugal and pressure gradient forces is believed to act like the convecting velocity over a swept-delta wing. This outboard flow prevents the separation at the tip from propagating inboard, which allows for the continual attachment of the leading edge vortex.

As a means of isolating dynamic effects due to rotation, the aspect-ratio-two wing was simulated with the addition of a source term in the governing equations to oppose and eliminate the centrifugal force near the wing surface. The initial formation and development of the leading edge vortex was unhindered by the absence of this force; however, later in the motion, the separation of the LEV near the tip was able to propagate inboard. Without the opposing outboard centrifugal force to keep the separation past mid-span, the vortex eventually separated and moved away from the surface much like that of a translating wing undergoing stall.

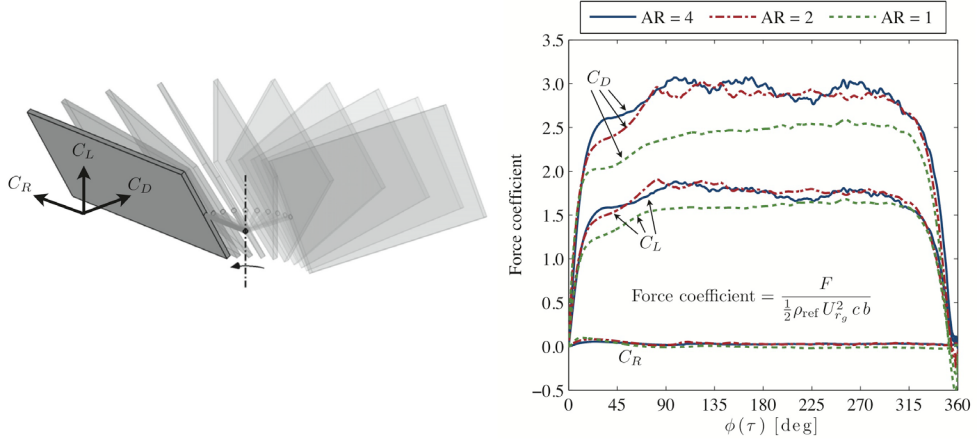


Figure 9. (a) Revolving wing configuration and (b) lift, drag, and pitching moment coefficients for wings of various aspect ratio.

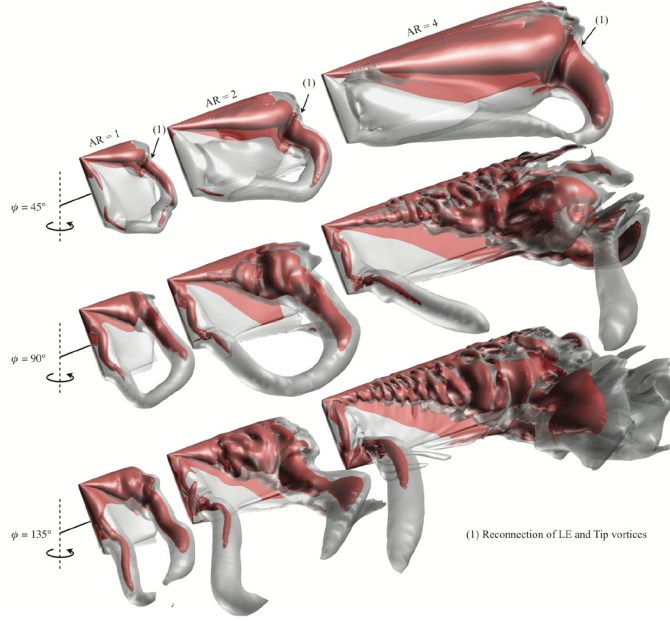


Figure 10. Three-dimensional flow structure for revolving wings depicted using an iso-surface of relative total pressure

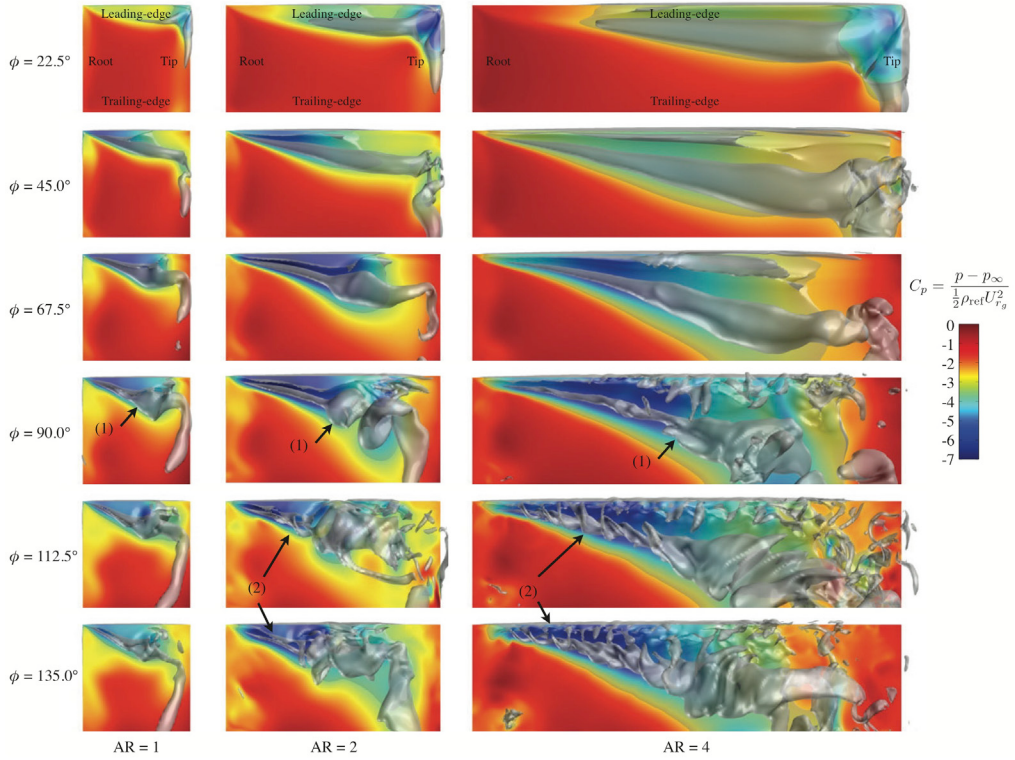


Figure 11. Evolution of the surface pressure distribution on the suction side of the wing with overlaid iso-surface of relative total pressure highlighting the vortex core along the leading edge. (1) Denotes the expansion of the vortex core due to breakdown. (2) Indicates the undulation of the vortex core for higher aspect ratios.

ELEMENT V: Plasma-Based Control of Excrescence-Induced Transition

One of the principal considerations in the design and construction of aircraft is that of configuration drag. This is especially true for unmanned air systems (UAS) and high altitude long endurance (HALE) vehicles, which are primarily used for intelligence, surveillance, and reconnaissance missions requiring extensive loiter times at altitude. An approach for reducing drag in such applications is the use of wings devised to maintain laminar flow. Through a judicious design process, wings may be constructed so that the boundary layer can have a transition location which is significantly downstream of that in a conventional situation. This results in a smaller fraction of the vehicle wetted surface being exposed to turbulent flow and a reduction in drag, leading directly to lower fuel consumption, energy efficiency, longer range, larger payloads, or increased flight times.

The exploitation of laminar flow on air vehicles requires stringent manufacturing tolerances in the production of aerodynamic surfaces. Specifically, the heights of steps, the width of gaps, and the undulations of surfaces must be minimized. In order to define allowable variations in these properties, they must first be quantified with regard to their ability to generate transition. It is the purpose of this investigation to assist in characterizing allowable sizes of surface imperfections on laminar-flow wings to preclude premature transition to turbulence. This will aid in development of criteria for manufacturing tolerances during the design and fabrication of long-endurance air vehicles.

Large-eddy simulations were performed in order to simulate the flow past a flat-plate configuration with forward-facing and rearward-facing steps downstream of the leading edge. The steps were representative of excrescences generated during fabrication of aerodynamic surfaces, which disrupt laminar flow, leading to a premature transition to turbulence. The configuration and roughness-based Reynolds number for the steps were similar to that of an experimental investigation. Solutions were obtained using a high-fidelity numerical scheme and implicit LES approach, in order to replicate the observed transition. When the computations were conducted without use of numerical perturbations, transition did not occur in a consistent manner. This situation was overcome by applying small amplitude numerical forcing of the normal surface velocity, in the step region. The forcing frequency was selected as a value within the unstable range based upon the stability diagram for the boundary layer, whose properties were modified by the step. Use of forcing regularized the transition process, making the transition location rather insensitive to spatial resolution.

A grid sensitivity study was carried out, and indicated that solutions obtained on the finest computational meshes were reasonably well resolved. Results of the simulations elucidated some aspects of the flow evolution to turbulence. As predicted by theory, the process initially consists of very small coherent two-dimensional structures, which are amplified by the geometric disturbances, and convect downstream of the step. Eventually, these structures lose their coherence, breakdown into more complex forms, and evolve to a chaotic state. Skin friction distributions and transition locations resulting from the simulations were found to agree well with measurements from the experiment. In the most downstream region of the computational domain, it was found that the solution had not yet evolved to the high-Reynolds number asymptotic form.

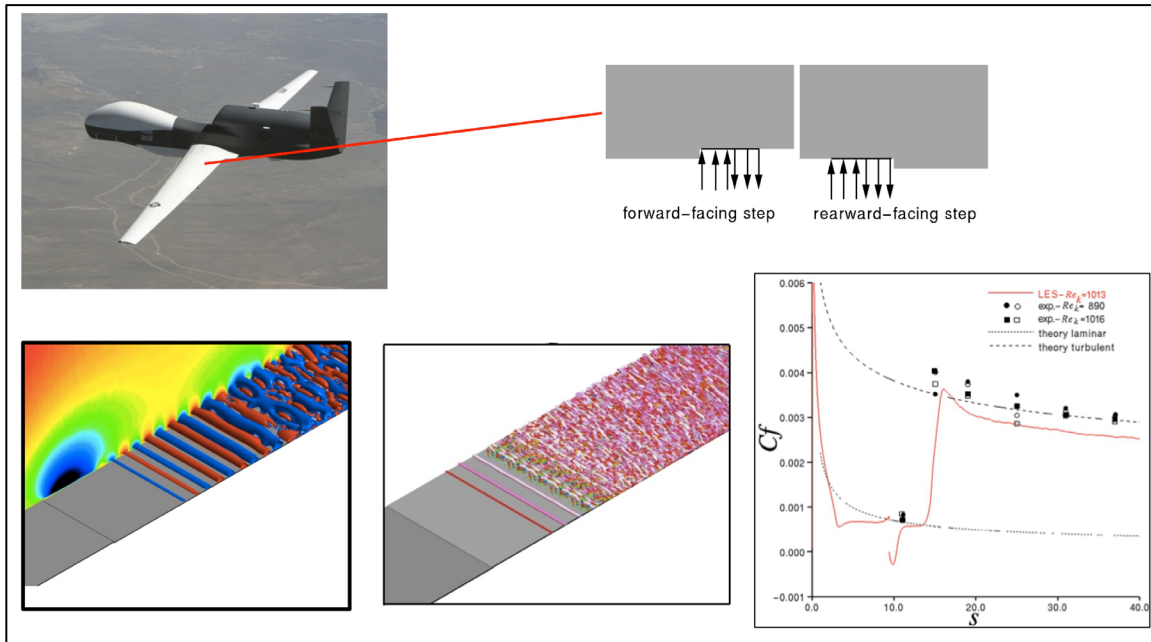


Figure 12. Direct simulation of excrescence-induced transition

Current research is focused on the delay of the onset of transition by means of surface-conforming dielectric-barrier-discharge (DBD) plasma actuators. Figure 13 shows the downstream displacement of transition (from left to right) following the onset of actuation at a location downstream of the step. The results indicated a significant reduction in integrated drag despite the local increase in skin friction in the immediate vicinity of the actuator generated by the time-averaged near-wall induced jet. Benefits in drag reduction were achieved with either continuous or pulsed actuation, the latter mode being associated with reduced power requirements. The impact of other additional factors such as incoming disturbances, three-dimensionality (i.e., corners) and streamwise pressure gradients are being assessed. Comparison with design-oriented transition prediction criteria will be provided. Additional details on the present simulations can be found in Appendix E at the end of this report.

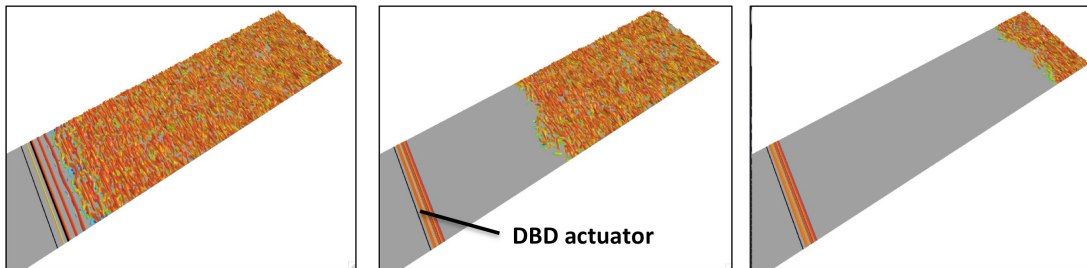


Figure 13. Control of excrescence-induced transition using a surface-mounted plasma actuator

ELEMENT VI: Interaction of an Oblique Shock with a Flexible Panel

Complex fluid-structural interactions may arise in both subsonic and supersonic flow over flexible panels in aerospace vehicles. The aeroelastic response of a compliant panel can have a significant impact on structural integrity, fatigue and acoustic radiation. This situation is exacerbated by design trends seeking to improve range and energy efficiency which translate in turn into lighter weight structures. Flexible panel interactions are of critical importance both for supersonic Future Air Dominance concepts, as well as for hypersonic vehicles during hot descent. Previous research has dealt primarily with the panel elastic response in an incoming uniform flow in the absence of additional superimposed complex flow features. For the case of impinging shocks, for instance, limited understanding is available regarding potentially detrimental regimes engendered by the aeroelastic response of flexible panels.

We have studied numerically for the first time the case of supersonic flow over a flexible panel in the presence of an impinging (and reflecting) oblique shock, as depicted in the schematic of Fig.14. Oblique shock reflection is a common feature encountered both in external and internal supersonic flow applications. Attention is given first to the inviscid situation. This is done in order to demonstrate that beyond just buffeting due to unsteady separation, a true aeroelastic (inviscid) instability can arise from the coupling of the oblique shock reflection system with the elastic deflections of the panel. For a two-dimensional inviscid shock reflection, both static deformation and limit-cycle oscillation regimes have been found depending on the shock strength and dynamic pressure (Fig. 15). For a weak shock, the stiffening effects induced by the deformation eliminate the standard panel flutter which may be present in the absence of a shock. For higher shock strengths, limit-cycle oscillations emerge from either subcritical or supercritical bifurcation points. In addition to the incident and reflected main shocks, the unsteady flow is characterized by a leading-edge shock and by a strong recompression/expansion near the plate trailing edge. For fixed dynamic pressure, the LCO amplitude and frequency are observed to increase with shock strength. The critical dynamic pressure also diminishes with increasing shock strength and can be much lower than that corresponding to standard panel flutter in the absence of a shock. This observation suggests that a new aeroelastic instability (distinct from regular panel flutter) is at play and arises from the complex interaction of the incident and reflected wave system with the panel flexural modes even in the absence of viscous separated flow effects. The panel exhibits a complex dynamics as the shock impingement point is displaced from the mid-point towards the plate leading edge. As the shock location moves upstream, the oscillations cease. They subsequently re-emerge, albeit at much higher modes, for an impingement point close to the panel leading edge.

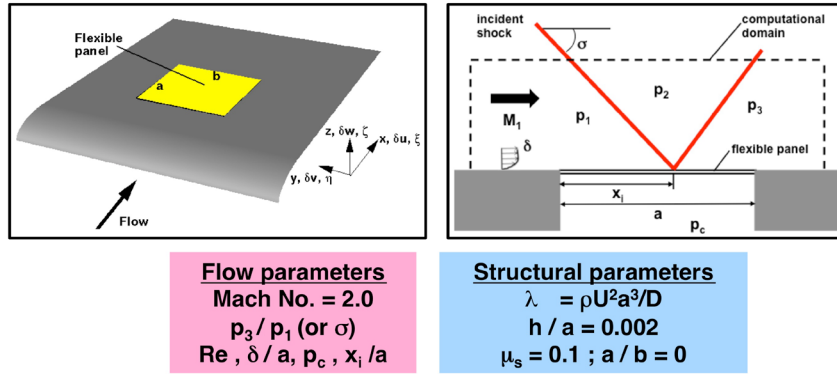


Figure 14. Interaction of a shock with a flexible panel

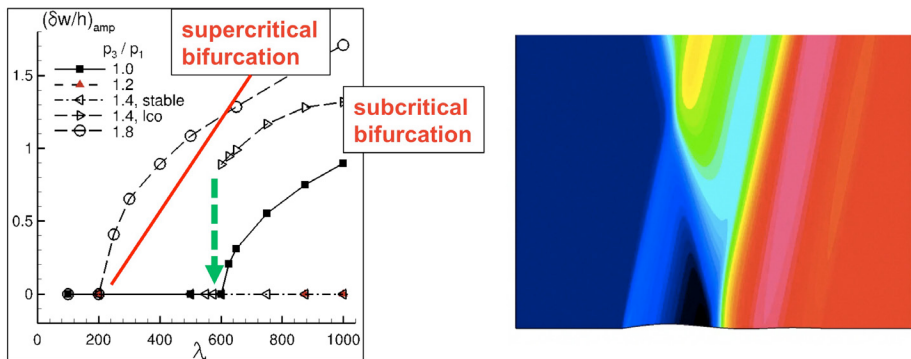


Figure 15. Oblique shock impingement on a flexible panel for inviscid Mach 2.0 flow: maximum deflection amplitude at 3/4-chord panel location as a function of pressure ratio and dynamic pressure (left) and instantaneous pressure contours ($p_3/p_1=1.4$, $\lambda=875$).

A separated shock laminar boundary layer interaction has also been studied in detail (Fig.16). When the panel is allowed to deflect, aperiodic self-sustaining oscillations emerge which result in a much more complex flow field relative to the rigid-panel case. An unexpected benefit of the fluttering panel is the observed significant reduction in the extent of the time-averaged separation region. This finding suggests the potential use of an aeroelastically-tailored flexible panel as a means of passive flow control. Forced panel oscillations, induced by a specified variable cavity pressure underneath the panel, were also found to be effective in reducing separation. The significant unsteadiness generated by the fluttering panel propagates along the complex reflected expansion/recompression wave system with potential structural implications not only for the panel but also for opposing surfaces in internal flow applications. Current research is focused on more practical turbulent interactions employing either Reynolds-averaged or large-eddy simulation approaches. Additional details of this study can be found in Appendix F.

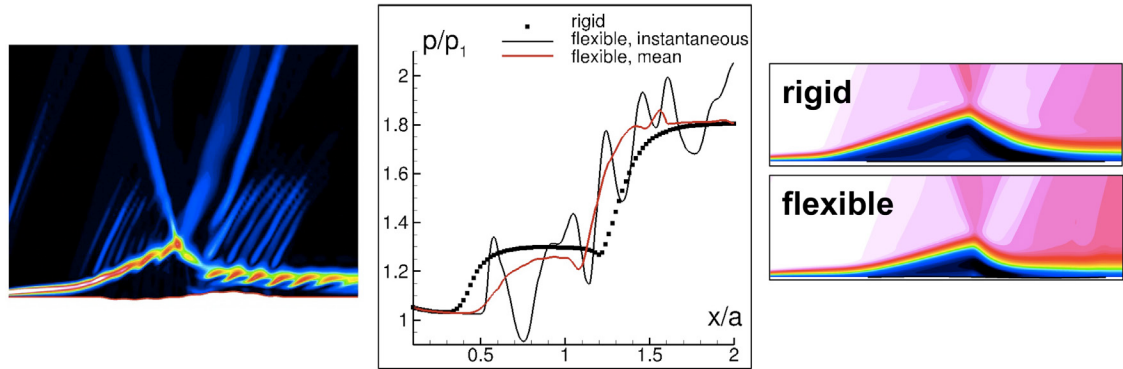


Figure 16. Laminar shock boundary layer interaction over a flexible panel: instantaneous density contours (left), mean and instantaneous surface pressure (center) and time-averaged velocity (right).

ELEMENT VII: Aero-Optical Aberration in Supersonic Flows

The aberration of an airborne laser beam propagating through a compressible turbulent flow is of critical importance in a number of applications including optical communications, targeting and laser weapon system integration. Study of the one-way interaction of the beam with the variable index-of-refraction field surrounding the aperture is termed aero-optics. Renewed emphasis in the field has been spurred by advances in flow control techniques, wave sensors, and by the many potential tactical and strategic advantages envisioned with high-energy laser weapon systems. Critical to further progress is the need for a more complete understanding of the role of the turbulent flow structure on wavefront distortion. New insights into the primary aberration mechanisms will aid in the development of improved prediction models and in combined flow control/adaptive optics techniques for increased lethality. Our previous research efforts were focused on the development of high-fidelity numerical simulation tools for the analysis of aero-optical aberration in the near-field encountered in tactical laser weapon applications, improved understanding of the role of coherent multi-scale unsteady flow features on the overall optical distortion pattern, and investigation of flow control strategies to either regularize (low-frequency forcing) or break-up (high-frequency forcing) large-scale coherent structures. We developed and validated a high-order paraxial beam solver and explored the aero-optics of shear layers, boundary layers and turrets in subsonic flow.

Our current research efforts are focused on wavefront aberration encountered in canonical low supersonic flows ($M < 2.0$). This is motivated by the Air Force's potential use of laser systems in Future Air Dominance (FAD) concepts for laser communication, targeting and self-protection. Limited information is available on the aero-optics of supersonic flows with shocks, and insights into the problem would be extremely valuable for weapon integration trade studies. To this end, we have conducted extensive investigation of aberration in supersonic turbulent boundary layers including effects of heating and cooling. During the past year, large-eddy simulations of a shock turbulent boundary layer interaction over a 20 deg. compression ramp at Mach 2.0 have been initiated (Fig. 17). This canonical configuration is intended to model the interaction of a beam for a submerged turret in the look-forward situation. Supersonic flight poses numerous challenges to the study of aero-optics. Alongside the formidable issues of beam quality due to the presence of turbulent density fluctuations in the boundary layer, an additional difficulty arises with the onset of unsteady shocks and other compression/expansion waves driven by boundary layer separation. Even not accounting for these compressible features, the more active boundary layer downstream of separation results in increased optical distortion. The tip/tilt corrected optical path difference (OPD) was found to be three times larger in the perturbed flow downstream of separation relative to the incoming equilibrium turbulent boundary layer. Another important finding of this study so far deals with the numerical spatial resolution required for accurate aero-optical aberration prediction. It was determined that grids, which might be acceptable for many SBLI simulations, are not adequate for the problem of aero-optics. It was found that a combination of grid stretching and misalignment of the shock and grid system led to spurious aberrations in the shock and in the inviscid region between the shock and the edge of the boundary layer. The use a finer (> 280 million points) overset mesh system more closely aligned with the shock had a significant impact on the predicted OPD (Fig. 17). Future efforts will concentrate on characterization of

the shock-motion induced aberration, as well as on the comparison of the present high-fidelity LES with standard hybrid RANS/LES approaches used in industry in support of USAF projects. Additional details of this study can be found in Appendix G.

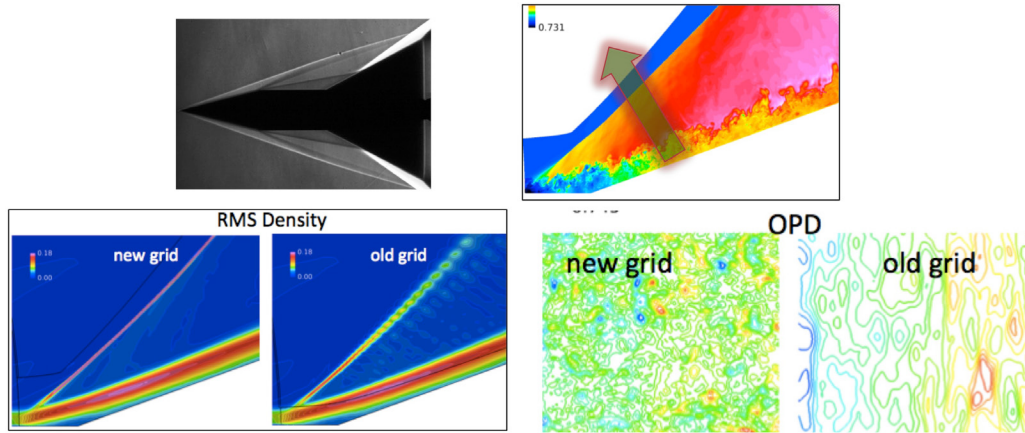


Figure 17. Aero-optical aberration in shock turbulent boundary layer interactions

Publications:

Published in Peer Reviewed Journals, Books, etc:

1. Garmann, D., Visbal, M. and Orkwis, P., "Three-dimensional flow structure and aerodynamic loading on a revolving wing", *Physics of Fluids*, Vol. 25, 2013.
2. Visbal, M., Yilmaz, T. and Rockwell, D., "Three-dimensional vortex formation on a heaving low-aspect-ratio wing: computations and experiments", *Journal of Fluids and Structures*, Vol. 38, 2013.
3. Garmann, D., "Compact finite-differencing and filtering procedure applied to the incompressible Navier-Stokes equations", *AIAA Journal*, Vol. 51, 2013.
4. Visbal, M., "On the interaction of an oblique shock with a flexible panel," *Journal of Fluids and Structures*, Vol. 30, 2012
5. Garmann, D., Visbal, M. and Orkwis, P., "Comparative study of implicit and subgrid-scale LES techniques for low-Reynolds number airfoil applications", *International Journal for Numerical Methods in Fluids*, Vol. 71, No. 12, 2013.
6. Rizzetta, D. P., and Visbal, M. R., "Exploration of Plasma-Based Control for Low-Reynolds Number Airfoil/Gust Interaction," *International Journal of Computational Fluid Dynamics*, Vol. 25, No. 10, 2011.
7. Rizzetta, D. P., and Visbal, M. R., "Effect of Plasma-Based Control on Low-Reynolds Number Flapping Airfoil Performance," *AIAA Journal*, Vol. 50, No. 1, 2012.
8. Rizzetta, D. P., and Visbal, M. R., "Plasma Flow Control Simulations of a Low-Reynolds Number Low-Aspect-Ratio Wing," *Computers and Fluids*, Vol. 70, Nov. 2012.
9. Rizzetta, D. P., and Visbal, M. R., "Plasma Control for a Maneuvering Low-Aspect-Ratio Wing at Low Reynolds Number," *ASME Journal of Fluids Engineering*, Vol. 134, 2012.
10. Bisek, N. J., Rizzetta, D. P., and Poggie, J., "Plasma Control of a Turbulent Shock Boundary-Layer Interaction," *AIAA Journal*, Vol. 51, No. 8, Aug. 2013.
11. Rizzetta, D. P., and Visbal, M. R., "Numerical Simulation of Excrescence Generated Transition," in press, *AIAA Journal*, 2013.
12. Rizzetta, D. P., and Visbal, M. R., "The Effect of Two-Dimensional Geometric Disturbances on Boundary-Layer Stability", submitted, *Journal of Theoretical and Computational Fluid Mechanics*, 2013
13. Jaworski, J. and Gordnier, R. E., "High-order simulations of low Reynolds number membrane airfoils under prescribed motion," *Journal of Fluids and Structures*, Vol. 31, May, 2012.
14. Gordnier, R. E., Visbal, M. R. and Barnes, C. J., "Highly Accurate Simulations of Low Reynolds Number Micro Air Vehicle Aerodynamics," *The International Test and Evaluation Journal*, Vol. 34, number 1, March 2013.
15. Gordnier, R. E., Chimakurthi, S. K., Cesnik, C. E. and Attar, P. A., "High-fidelity aeroelastic computations of a flapping wing with spanwise flexibility," *Journal of Fluids and Structures*, Vol. 40, 2013.
16. Gordnier, R. E. and Attar, P. A., "Impact of Flexibility on an Aspect Ratio Two Membrane Wing," *Journal of Fluids and Structures*, to appear.
17. Visbal, M., "Numerical investigation of deep dynamic stall of a plunging airfoil," *AIAA Journal*, Vol. 49, No. 10, 2011.
18. Cleaver, D., Wang, Z., Gursul, I. and Visbal, M., "Lift enhancement by means of small-

amplitude airfoil oscillations at low Reynolds numbers, *AIAA J.*, Vol. 49, No.9, 2011.

19. Morgan, P., and Visbal, M., "Hybrid RANS/LES Simulation Investigating Control of Flow Over a Turret," *Journal of Aircraft*, Vol. 49, No. 6, 2012.
20. White, M., Morgan, P. and Visbal, M., "Simulation of Aero-Optics over Conformal and Flat Window Turrets," *Journal of Directed Energy*, Vol. 5, No. 1, 2013.
21. Barnes, C. J. and Visbal, M. R., "Numerical exploration of the origin of aerodynamic enhancements in low-Reynolds number corrugated airfoils," *submitted, Physics of Fluids*, 2013.
22. Jelic, R., Sherer, S.E., Greendyke, R., "Simulation of Various Turrets at Subsonic and Transonic Flight Conditions Using OVERFLOW", *Journal of Aircraft*, Vol. 50, No.2, 2013.
23. Golubev, V. and Visbal, M., "Modeling MAV Response in Gusty Urban Environment, *International Journal of Micro Air Vehicles*, Vol. 4, No. 1, March 2012.
24. Luo, H., Segawa, H. and Visbal, M., "An Implicit Discontinuous Galerkin Method for the Unsteady Compressible Navier-Stokes Equations," *Computers & Fluids*, Vol. 53, 2012.
25. Visbal, M. "Viscous and Inviscid Interactions of an Oblique Shock with a Flexible Panel," accepted for publication, *Journal of Fluids and Structures*, 2013.
26. Calderon, D., Wang, Z., Gursul, I. and Visbal, M., "Volumetric measurements and simulations of the vortex structures generated by low-aspect-ratio plunging wings," *Physics of Fluids*, Vol. 25, 2013.
27. Olson, D., Naguib, A., Koochesfahani, M., Rizzetta, D. and Visbal, M., "On the Challenges in Experimental Characterization of Flow Separation over Airfoils at Low Reynolds Numbers," *Experiments in Fluids*, Vol. 54, 2013.
28. Mullenix, N., Gaitonde, D. and Visbal, M., "Spatially Developing Supersonic Turbulent Boundary Layer with a Body-Force-Based Method, *AIAA Journal*, Vol. 51, Aug. 2013.

Published in Conference Proceedings:

1. Rizzetta, D. P., and Visbal, M. R., "The Effect of Two-Dimensional Geometric Disturbances on Boundary-Layer Stability", AIAA Paper 2013-3108, Jun. 2013.
2. Rizzetta, D. P., and Visbal, M. R., "Numerical Simulation of Excrescence Generated Transition," AIAA Paper 2013-0079, Jan. 2013.
3. Rizzetta, D. P., and Visbal, M. R., "Plasma Flow Control Simulations of a Low-Reynolds Number Low-Aspect-Ratio Wing," AIAA Paper 2012-1138, Jan. 2012
4. Rizzetta, D. P., and Visbal, M. R., "Plasma Control for a Maneuvering Low-Aspect-Ratio Wing at Low Reynolds Number," AIAA Paper 2012-2956, Jun. 2012.
5. Bisek, N. J., Rizzetta, D. P., and Poggie, J., "Exploration of Plasma Control for Supersonic Turbulent Flow over a Compression Ramp," AIAA Paper 2012-2760, Jun. 2012.
6. Gordnier, R. E. and Demasi, L., "Implicit LES Simulations of a Flapping Wing in Forward Flight," FEDSM2013-16540, ASME 2013 Fluids Engineering Summer Conference, July 2013.
7. Demasi, L., Gordnier, R. Santarpia, E. and Dipace, A., "High-Fidelity Simulations of a Flexible Flapping Wing in Forward Flight," AIAA Paper 2013-1648, April 2013.
8. Gordnier, R. E. and Attar, P. A., "Aeroelastic Simulations of an Aspect Ratio Two Flexible Membrane Wing," AIAA Paper 2012-0711, Jan. 2012.
9. Jaworski, J. and Gordnier, R. E., "Thrust Augmentation of Flapping Airfoils in Low Reynolds Number Flow Using a Flexible Membrane," AIAA Paper 2012-1640, April 2012.

10. Gordnier, R. E. and Attar, P. A., "Impact of flexibility on the aerodynamics of an aspect ratio two membrane wing," FEDSM2012-72296, July 2012.
11. Garmann, D. and Visbal, M., "A numerical study of hovering wings undergoing revolving or translating motions," AIAA 2013-3052, June 2013
12. Garmann, D., Visbal, M. and Orkwis, P., "Investigation of aspect ratio and dynamic effects due to rotation for a revolving wing using high-fidelity simulation," AIAA Paper 2013-0086, Jan. 2013.
13. Garmann, D., Visbal, M. and Orkwis, P., "Numerical Investigation of the Three-Dimensional Flow Structure about a Revolving Wing," ASME FEDSM2012-72388, July 2012.
14. Visbal, M. and Garmann, D., "Flow Structure Above Stationary and Oscillating Low-Aspect-Ratio Wings," ASME FEDSM2012-72405, July 2012.
15. Garmann, D., Visbal, M. and Orkwis, P., "Three-Dimensional Flow Structure and Aerodynamic Loading on a Low-Aspect Ratio, Revolving Wing," AIAA Paper 2012-3277, Jun 2012.
16. Morgan, P. and Visbal, M., "Numerical Simulations Exploring Dielectric Barrier Discharge-Induced Steady and Pulsed Suction," AIAA Paper 2013-2744, June 2013.
17. Morgan, P. and Visbal, M., "Effectiveness of Flow Control for a Submerged Hemispherical Flat-Window Turret," AIAA Paper 2013-1015, January 2013.
18. Morgan, P., White, M. and Visbal, M., "Application of Overset Grids for Aero-Optical Simulations of Turrets," 11th Symposium on Overset Composite Grids & Solution Technology, Dayton, OH, October 2012.
19. Morgan, P. and Visbal, M., "Numerical Simulation of Flow Over a Submerged Flat-Window Turret," AIAA Paper 2012-3042, June 2012.
20. White, M. D. and Visbal, M., "Computational investigation of the influence of unsteady shock motion on aberrating structures in supersonic boundary layers," AIAA Paper 2013-3134, Jun 2013.
21. White, M. D. and Visbal, M., "Computational Investigation of Wall Cooling and Suction on the Aberrating Structures in a Transonic Boundary Layer," AIAA Paper 2013-0720, Jan 2013.
22. White, M. D. and Visbal, M., "Aero-optics of Compressible Boundary Layers in the Transonic Regime," AIAA Paper 2012-2984, June 2012.
23. White, M., Morgan, P. and Visbal, M., "Simulation of Aero-Optics over Conformal and Flat Window Turrets," 14th Annual Directed Energy Symposium, Nov. 2011.
24. Barnes, C. J. and Visbal, M. R. "High-Fidelity Simulations of a Flexible, Heaving Finite-Aspect-Ratio Wing," AIAA Paper 2013-3179, June 2013.
25. Barnes, C. J. and Visbal, M. R., "High-Fidelity Simulations of a Hovering Wing," AIAA Paper 2012-2699, June 2012.
26. Barnes, C. J. and Visbal, M. R. "High-Fidelity Simulations of a Corrugated Airfoil," AIAA Paper 2012-0753, Jan. 2012
27. Sherer, S.E. and Graves, R., "Application-Oriented Processes for Implementation of Overset Grid Methodologies", AIAA Paper 2013-0384, Jan 2013.
28. Visbal, M., "Shock/Boundary Layer Interaction Over a Flexible Panel, AIAA Paper 2012-1092, Jan 2012.

29. Calderon, D., Wang, Z., Gursul, I. and Visbal, M., "Volumetric measurements and simulations of the vortex structures generated by low-aspect-ratio plunging wings," AIAA Paper 2012-0914, Jan 2012.
30. Visbal, M., "Flow Structure and Unsteady Loading Over a Pitching and Perching Low-Aspect-Ratio Wing," AIAA Paper 2012-3279, June 2012.
31. Apte, S., Liburdy, J., and Visbal, M., "Low Reynolds Number Flow Dynamics of a Thin Airfoil with Elastically Mounted Trailing Edge, AIAA Paper 2012-2841, June 2012.
32. Mullenix, N., Gaitonde, D. and Visbal, M., "Generation of an Equilibrium Turbulent Boundary Layer for Upstream Boundary Condition Specification," AIAA Paper 2012-0439, Jan 2012.
33. Zimmerman, B., Wang, Z. and Visbal, M., "High-Order Spectral Difference: Verification and Acceleration Using GPU Computing," AIAA Paper 2013-2941, June 2013.
34. Nguyen, L., Golubev, V., Dudley, J. and Visbal, M., "High-Fidelity Simulations of Transitional Airfoil Interacting with Canonical Upstream Flow Disturbances," AIAA Paper 2012-2696, June 2012.
35. Golubev, V., Mankbadi, R., Roger, M. and Visbal, M., "Acoustic Feedback-Loop Interactions in Transitional Airfoils," AIAA Paper 2013-2111, May 2013.

Invited Lectures, Presentations, Talks, etc.:

Visbal:

Plenary Speaker, 7th International Conference in Computational Fluid Dynamics, July 2012
 Invited Speaker, International Workshop on the Future of CFD, Japan, 2012
 Invited speaker, ARO Workshop on Simulation of Dynamic Stall, Texas A&M U., Aug. 2012.
 Invited seminar, NASA Glenn Research Center, Aug. 2012.
 Invited speaker, Jameson-Van Leer- Roe CFD Symposium, June 2013
 Invited seminar, Aerospace & Mech. Engineering Dept., Univ. of Notre Dame, Sept. 2012
 Invited presentation, DARPA/ARL workshop on plasma flow control for rotorcraft, Oct 2011
 Invited Seminar, Lehigh Univ., Sept 2011
 Lecturer, ASME Course "Advances in Turbines Aero-thermo-mechanical Design and Analysis", IGT Institute, Vancouver, June 2011

Rizzetta:

Invited Seminar, University of Louisville, October 2011

Gordnier:

Invited Seminar, University of Louisville, 2012

White:

Invited seminar Naval Academy Physics Department, 2012

Professional Activities:

Visbal:

Associate Editor, AIAA Journal
 Member, AIAA Aero-acoustics Technical Committee
 Member, ASME Fluids Engineering Division Awards Committee
 Member, ASME CFD Technical Committee
 Member, AFRL HPC Task Force
 Lead organizer, ASME International Symposium on Large-Eddy Simulation

Member, Organizing Committee for 2nd AIAA/AFOSR/DLR International Workshop on High-Order CFD methods, May 2013, Cologne, Germany

Member, Scientific Committee for International Conference on Computational Fluid Dynamics (ICCFD)

Co-organizer of international bi-annual Working Group on benchmark experiments & computations for LES validation and airframe noise-prediction

Session Chair, multiple AIAA and ASME conferences

Reviewer, AIAA J., Computers and Fluids, Int. J. of CFD, Physics of Fluids

PhD Thesis Committees: Univ. of Cincinnati, Wright State Univ., Michigan State Univ. and Univ. of Florida.

Proposal evaluator for ARO

Gordnier:

Associate Editor, AIAA Journal

Chair, ASME CFD Technical Committee

Member, AIAA Structural Dynamics Technical Committee/Chair Awards sub-committee

Chair, AIAA 2013 Ashley Award for Aeroelasticity

Lead Organizer, ASME Symposium on Fluid-Structure Interaction and Flow Induced Noise

Session Chair, multiple AIAA and ASME conferences

Reviewer, AIAA J. and F. of Fluids and Structures

Rizzetta:

Member, AIAA Fluid Dynamics Technical Committee

Chair AIAA TC LES Working Group

Session Chair, multiple AIAA conferences

Reviewer, AIAA J. Spacecraft and Rockets, J. of Renewable Energy

Proposal evaluator for ONR

Morgan:

Member, AIAA Applied Aerodynamics Technical Committee

Chair, AIAA Validation of Numerical Models Discussion Group

Member, AIAA Large Eddy Simulation Technical Working Group

Session organizer, session chair and reviewer for AIAA conferences

Reviewer for AIAA J., J. of Fluids Engineering

Garmann:

Participant, AIAA Low-Re Unsteady Aerodynamics Discussion Group

Contributor, RTO AVT-202

Session chair, AIAA and ASME conferences

Reviewer, AIAA J. and Physics of Fluids

White:

Member of the AIAA Plasmadynamics & Lasers Technical Committee

Co-organizer for upcoming 45th AIAA Plasmadynamics & Lasers Conference

Ph.D. dissertation committee, University of Dayton.

WPAFB Educational Outreach to teach aerodynamics at DoD Sponsored "Starbase" (2011-2013).

Sherer:

Chairperson, 11th Symposium on Overset Composite Grids and Solution Technology, 2012

Member, Overset Grid Symposium Scientific Committee, 2010-Present.

Reviewer for the Journal of the Acoustical Society of America, International Journal of

Numerical Methods in Fluids, International Journal of CFD, Journal of Computational Physics and Computers and Fluids.

Honors Received:

Visbal:

AIAA Fellow (2012)
AFRL Fellow (1995)
Plenary Speaker, 7th International Conference in Comp. Fluid Dynamics (2012)
Air Force Basic Research Award (2004)
Outstanding Scientist of Dayton, Affiliate Societies Council of Dayton (2002)
Air Vehicles Directorate Foulois Award for In-House research (1990, 1999, and 2006)
AIAA Best Paper Awards (1992, 2006, 2008, 2010 and 2013)
Member, Advisory Board, Embry-Riddle Aeronautical University

Rizzetta:

Distinguished Alumni, Western Michigan University College of Engineering and Applied Sciences, 2011
Outstanding Technical Contribution-Science Award, AIAA Dayton-Cincinnati Section, 2011
Air Vehicles Directorate Foulois Award for In-House research (2001)

Gordnier:

AFRL Fellow (2003)
Outstanding Technical Contribution-Science Award, AIAA Dayton-Cincinnati Section, 2012
Outstanding Scientist of Dayton, Affiliate Societies Council of Dayton, 2012

Garmann:

AIAA Best Paper Award in Fluid Dynamics, 2013
Best Technical Presentation in Fluid Dynamics, AIAA DCASS 2013
Art-in-Science Award, AIAA DCASS 2012

Barnes:

Best Technical Presentation in CFD Applications, AIAA DCASS, 2012
Co-op of the year, AFRL/RB 2012
Civilian of the Quarter Award, Aeronautical Sciences Division, 2011
Excellence in Teaching Award for Teaching Assistants, Wright State Univ., 2011

Collaborations / Interactions

As part of a strategy for a more efficient execution of this research, we have pursued targeted and mutually beneficial collaborations with a number of research teams in AFRL, DoD and academia. We also leverage manpower and resources within the Collaborative Center for Computational Sciences construct funded by AFRL/RQV. These collaborative efforts involve cross-validation of computations with high-resolution experiments and sharing of computational tools for enhanced multi-disciplinary simulation and analysis. Fruitful collaborations and extended interactions included:

D. Rockwell, Lehigh Univ.; comparison with 3D PIV measurements of vortex flows
Gursul, Bath Univ., UK; vortical flows, flexible wings
C. Cesnik, Univ. of Michigan; fluid-structure interaction modeling
P. Attar, Univ. of Oklahoma; fluid-structure interaction, harmonic balance
GE Global Research, NY; aero-acoustics, massively parallel high-order solver
V. Golubev, Embry-Riddle Univ.; gust-airfoil interactions
S. Lele, Stanford Univ.; high-order overset methods, shock-capturing
B. Saric & H. Reed, Texas A& M, distributed-roughness transition

S. Roy, Univ. of Florida, plasma flow control
M. Koochesfahani/A. Naguib, Michigan State Univ., unsteady aerodynamics
E. Jumper/S. Gordeyev, Univ. of Notre dame, aero-optics
D. Gaitonde, Ohio State Univ.; plasma flow control, LES
NATO RTO AVT-202, Unsteady Aerodynamics
NATO RTO AVT-190, Plasma flow control
B. Glaz, Army Research Laboratory, dynamic stall
I. Mezic, UC Santa Barbara, Koopman mode analysis of unsteady flows
P. Mikulski, US Naval Academy high-order parabolic beam equations solver
L. Demasi, San Diego State University, structural models for flexible wings
W. Liou, Western Michigan University, simulation of planetary flows
M. Ringuette, University of Buffalo, revolving wing aerodynamics
A. Jones, University of Maryland, revolving wing aerodynamics
M. Roger, Ecole Central de Lyon (France), airfoil acoustic resonance
M. Rumpfkeil, Univ. of Dayton, airfoil acoustics
M. Aftosmis, NASA Ames Research Center, urban gust characterization
A. Sescu, Mississippi State Univ., inflow conditions for transitional flows

Transitions

The unique high-fidelity computational tools (*FDL3DI*) developed under this task have been transferred to many users in the aerospace community, including GE Global Research and Aviation Divisions, Argonne National Laboratory, NASA Ames Research Center, Stanford University, University of Cincinnati, University of Florida, Michigan State Univ., Ohio State Univ., and Texas A&M University among others. The method is empowering researchers to perform massively-parallel high-fidelity simulations for a broad range of challenging USAF-relevant problems including cross-flow instability, shock/boundary layer interactions, jet and airfoil trailing-edge noise predictions, film cooling, control of low pressure turbines for high-altitude aircraft, distributed-roughness transition, flapping wing aerodynamics and laser turrets.

APPENDIX A

Flow Structure and Unsteady Loading Over a Pitching and Perching Low-Aspect-Ratio Wing

Miguel R. Visbal *

Air Force Research Laboratory, Wright-Patterson AFB, OH 45433

This study addresses the flow structure and unsteady loading arising over a low-aspect-ratio rectangular wing subjected to high-amplitude pitching and perching maneuvers under low-Reynolds-number conditions of interest in small unmanned aerial vehicle operation and gust interactions. Simulations are performed employing an extensively-validated high-fidelity computational approach capable of accurately capturing the complex unsteady transitional flows. Canonical pitching motions for a non-translating wing in the presence of a constant freestream are first investigated in order to elucidate the effects of pitch rate and Reynolds number on the flow structure and aerodynamic loading. The wing is pitched about its quarter-chord axis to a maximum incidence of 45° with nominal non-dimensional angular rates $0.05 \leq \Omega^+ \leq 0.2$. The Reynolds number based on the wing chord varied from 10^3 to 4×10^4 . For the highest pitch rate, good agreement between the computed three-dimensional flow structure and recent experimental measurements is demonstrated. The 3D dynamic stall process is characterized by the formation of an initial spanwise-oriented leading-edge vortex which evolves into an arch-type structure with legs anchored on the wing surface. This dominant flow element of low-aspect-ratio wings exhibits a long residence time and establishes a well-defined low-pressure region and swirling pattern on the wing surface. Increasing pitch rate promotes an angular delay in the flow evolution and corresponding aerodynamic loads. Even for the lowest pitch rate, a significant increase in maximum lift is achieved relative to the static situation. The low-aspect-ratio of the wing also promotes further delay of dynamic stall and a much smoother behavior of the aerodynamic coefficients when compared to a pitching 2D wing section. The formation of the arch vortex and swirling pattern are found to be qualitatively similar over the range of Reynolds number studied. At fixed pitch rate, higher Reynolds number promotes a more compact arch vortex, a stronger suction on the wing and further stall delay. Canonical perching maneuvers involving simultaneous rotation and deceleration to rest are considered at two values of pitch rate. The reduction in translating velocity halts the development of the leading-edge vortex system which eventually moves upstream in front of the wing. Attempts to correlate the perching loads with the constant-freestream pitching cases indicate that agreement can only be achieved for the initial portion of the maneuver. Discrepancies arise at high angles of attack which depend on the value of pitch rate itself.

Nomenclature

c	= wing chord
C_L, C_D, C_M	= lift, drag and quarter-chord pitching moment coefficients
C_{Lo}, C_{Do}, C_{Mo}	= non-dimensional lift, drag and pitching moment for perching wing
C_{Lw}, C_{Dw}, C_{Mw}	= lift, drag and pitching moment for perching wing rescaled with translational velocity
C_p	= pressure coefficient
E	= total specific energy
$\hat{F}, \hat{G}, \hat{H},$	= inviscid vector fluxes
$\hat{F}_v, \hat{G}_v, \hat{H}_v$	= viscous vector fluxes
J	= Jacobian of the coordinate transformation
LEV	= leading-edge vortex
M	= Mach number
p	= static pressure
\vec{Q}	= vector of dependent variables
Re_c	= Reynolds number based on chord, $\rho_\infty U_\infty c / \mu_\infty$

*Technical Area Leader, Computational Sciences Center. AIAA Fellow

S	= wing semi-span
t	= time
U_∞	= freestream velocity
U_w	= wing translational velocity
u, v, w	= streamwise, vertical and spanwise velocity components
$\hat{U}, \hat{V}, \hat{W}$	= contravariant velocity components
x, y, z	= Cartesian coordinates
X_{CL}	= chordwise location of center of lift
α	= angle of attack
γ	= specific heat ratio, 1.4 for air
Δt	= time step size
μ	= molecular viscosity coefficient
ξ, η, ζ	= body-fitted computational coordinates
ρ	= fluid density
Ω^+	= non-dimensional pitch rate, $\Omega^+ = \dot{\alpha}c/U_\infty$
Ω_o^+	= nominal non-dimensional pitch rate
$\omega_x, \omega_y, \omega_z$	= vorticity components

I. INTRODUCTION

The process of unsteady separation and stall generated by large transient excursions in angle of attack, referred to in general as dynamic stall, represents a long-standing issue in maneuvering aircraft and rotorcraft applications.¹⁻³ In recent years, interest in dynamic stall at moderate Reynolds numbers has re-emerged driven by its importance to small unmanned air vehicle system operation, as well as to the understanding of the remarkable performance found in natural flight.^{4,5}

Dynamic stall has been studied extensively⁶⁻¹³ for effectively two-dimensional wing geometries represented by means of spanwise-periodic computations or wall-to-wall experimental configurations. These studies have provided a great deal of insight on the formation and transition of these dynamic stall vortices and on the highly unsteady loads elicited by their convection along the aerodynamic surface. In practical applications, wings have a finite span and therefore the induced three-dimensional nature of the unsteady separation process requires further elucidation. Although the literature on unsteady separation over three-dimensional configurations is not as numerous as its two-dimensional counterpart, several studies have provided valuable information on various aspects of the problem.

The non-linear lift characteristics for several stationary low-aspect-ratio planforms at low Reynolds numbers have been measured by Torres and Mueller.¹⁴ Excellent wind-tunnel smoke visualizations describing the structure of the combined leading-edge and tip vortex system over finite-aspect-ratio wings undergoing different transient maneuvers have been presented by Freymuth et al.¹⁵⁻¹⁷ Experimental investigations addressing the near-wake structure of flapping or pitching low-aspect-ratio wings have been conducted by Von Ellenrieder et al.¹⁸ and Buchholz and Smits.¹⁹ Yilmaz and Rockwell²⁰ provided flow visualizations and PIV measurements above a plunging low-aspect-ratio rectangular wing under low-Reynolds-number conditions. Their investigation illustrated the existence of pronounced axial flows within the core of the developing leading-edge vortex followed by the formation of large-scale patterns of streamwise-oriented vorticity near the wing centerline. In a subsequent investigation,²¹ flow visualizations acquired in two different experimental facilities were shown to exhibit similar features for a broad range of maneuvers. Calderon et al.²² studied the effect of small-amplitude plunging oscillations for low-aspect-ratio wings at post-stall angles of attack, and determined optimal planform-dependent forcing frequencies for maximum lift production. Yilmaz and Rockwell²³ examined in detail by means of volumetric particle image velocimetry techniques, the flow structure generated over rectangular and elliptical wing planforms subjected to a rapid pitch-up maneuver. They found that despite differences in the initial separation process, both geometries exhibit a similar final flow state characterized by the presence of a large-scale swirl pattern on the wing. Granlund et al.²⁴ provided flow visualizations and force measurements for low-aspect-ratio wings undergoing either pitch-up or pitch-hold-and-return high-rate motions and for multiple pitch-axis locations. Calderon et al.²⁵ provided volumetric three-component velocimetry measurements for low-aspect-ratio rectangular and elliptical wings subjected to small amplitude plunging oscillations. The effects of forcing frequency and aspect ratio on the 3D flow structure was described including the unusual formation of a tip vortex ring.

Computations by Blondeaux et al.²⁶ examined the wake topology and vortex dynamics behind relatively thick flapping airfoils at low Reynolds numbers ($Re_c \leq 10^3$). Dong et al.²⁷ considered the wake structure generated by

elliptic planforms in hovering at Reynolds numbers below 1000. Taira and Colonius²⁸ presented a detailed computational study of impulsively translating low-aspect-ratio wings at high incidence and for Reynolds numbers of 300 and 500. They also investigated the effect of simulated actuation in the post-stall regime.²⁹ Trizila et al.³⁰ considered the case of an aspect ratio 4 plate in hovering motion for a Reynolds number of 100 and investigated the impact of wing kinematics on lift production. Visbal³¹ performed high-fidelity computations for a heaving low-aspect-ratio wing and Reynolds numbers in the range $10^3 \leq Re_c \leq 2 \times 10^4$. The results were found to be in good agreement with flow visualizations and PIV measurements of Yilmaz and Rockwell.²⁰ In Ref. 31, a model of three-dimensional dynamic stall for a low-aspect-ratio wing was developed which is characterized by the evolution of the leading-edge vortex into an arch vortex with legs normal to the wing surface. This vortex is eventually shed as a ring-like structure following reconnection at the symmetry plane.

The present study addresses the flow structure and unsteady loading arising over a rectangular wing of aspect ratio two (Fig. 1) subjected to high-amplitude transient pitching and perching maneuvers. Canonical pitching motions for a non-translating wing in the presence of a constant freestream are first investigated in order to elucidate the three-dimensional dynamic stall process and the effects of pitch rate and Reynolds number on flow structure and aerodynamic loads. The wing is pitched about its quarter-chord axis to a maximum incidence of 45° with nominal non-dimensional angular rates $0.05 \leq \Omega^+ \leq 0.2$. The Reynolds number based on the wing chord is varied from 10^3 to 4×10^4 . A simple perching maneuver involving simultaneous rotation and deceleration to rest is also considered to explore the effects of variable horizontal velocity on the flow evolution and loading relative to the constant-freestream case.

The flow fields are computed employing an extensively validated high-fidelity implicit large-eddy simulation (ILES) approach.^{32,33} This ILES methodology relies one a 6th-order compact scheme for the spatial derivatives and on up to 10th-order Pade-type low-pass filters which do not dissipate the spatially-resolved content of the solution. The high-order scheme aids in accurately capturing the laminar separation and transition processes, whereas the discriminating low-pass filter operator provides regularization in turbulent flow regions in lieu of standard sub-grid-scale models. This method is particularly effective for the present moderate Reynolds number flows exhibiting mixed laminar, transitional and turbulent regions.

II. GOVERNING EQUATIONS

For these maneuvering wing simulations, the governing equations are the unfiltered full compressible Navier-Stokes equations cast in strong conservative form after introducing a general time-dependent curvilinear coordinate transformation $(x, y, z, t) \rightarrow (\xi, \eta, \zeta, \tau)$ ^{34,35} from physical to computational space. In terms of non-dimensional variables, these equations can be written in vector notation as:

$$\frac{\partial}{\partial \tau} \left(\frac{\vec{U}}{J} \right) + \frac{\partial \hat{F}}{\partial \xi} + \frac{\partial \hat{G}}{\partial \eta} + \frac{\partial \hat{H}}{\partial \zeta} = \frac{1}{Re} \left[\frac{\partial \hat{F}_v}{\partial \xi} + \frac{\partial \hat{G}_v}{\partial \eta} + \frac{\partial \hat{H}_v}{\partial \zeta} \right] \quad (1)$$

where $\vec{U} = \{\rho, \rho u, \rho v, \rho w, \rho E\}$ denotes the solution vector, $J = \partial(\xi, \eta, \zeta, \tau) / \partial(x, y, z, t)$ is the transformation Jacobian, and \hat{F} , \hat{G} and \hat{H} are the inviscid fluxes given by:

$$\hat{F} = \begin{bmatrix} \rho \hat{U} \\ \rho u \hat{U} + \hat{\xi}_x p \\ \rho v \hat{U} + \hat{\xi}_y p \\ \rho w \hat{U} + \hat{\xi}_z p \\ (\rho E + p) \hat{U} - \hat{\xi}_t p \end{bmatrix} \quad (2)$$

$$\hat{G} = \begin{bmatrix} \rho \hat{V} \\ \rho u \hat{V} + \hat{\eta}_x p \\ \rho v \hat{V} + \hat{\eta}_y p \\ \rho w \hat{V} + \hat{\eta}_z p \\ (\rho E + p) \hat{V} - \hat{\eta}_t p \end{bmatrix} \quad (3)$$

$$\hat{H} = \begin{bmatrix} \rho \hat{W} \\ \rho u \hat{W} + \hat{\zeta}_x p \\ \rho v \hat{W} + \hat{\zeta}_y p \\ \rho w \hat{W} + \hat{\zeta}_z p \\ (\rho E + p) \hat{W} - \hat{\zeta}_t p \end{bmatrix} \quad (4)$$

where

$$\hat{U} = \hat{\xi}_t + \hat{\zeta}_x u + \hat{\zeta}_y v + \hat{\zeta}_z w \quad (5)$$

$$\hat{V} = \hat{\eta}_t + \hat{\zeta}_x u + \hat{\zeta}_y v + \hat{\zeta}_z w \quad (6)$$

$$\hat{W} = \hat{\zeta}_t + \hat{\zeta}_x u + \hat{\zeta}_y v + \hat{\zeta}_z w \quad (7)$$

$$E = \frac{T}{\gamma(\gamma-1)M_\infty^2} + \frac{1}{2}(u^2 + v^2 + w^2). \quad (8)$$

Here, $\hat{\xi}_x = J^{-1} \partial \xi / \partial x$ with similar definitions for the other metric quantities. The viscous fluxes, \hat{F}_v , \hat{G}_v and \hat{H}_v can be found, for instance, in Ref. 36. In the expressions above, u, v, w are the Cartesian velocity components, ρ the density, p the pressure, and T the temperature. The perfect gas relationship $p = \rho T / \gamma M_\infty^2$ is also assumed. For the case of a constant freestream, all flow variables have been normalized by their respective reference freestream values except for pressure which has been non-dimensionalized by $\rho_\infty u_\infty^2$. For the perching maneuver in a quiescent fluid, a similar normalization based on the maximum translational velocity is applied.

It should be noted that the above governing equations correspond to the original *unfiltered* Navier-Stokes equations, and are used without change in laminar, transitional or fully turbulent regions of the flow. Unlike the standard LES approach, no additional sub-grid stress (SGS) and heat flux terms are appended. Instead, a high-order low-pass filter operator (to be described later) is applied to the conserved dependent variables during the solution of the standard Navier-Stokes equations. This highly-discriminating filter selectively damps only the evolving poorly resolved high-frequency content of the solution.^{32,33} This filtering regularization procedure provides an effective alternative to the use of standard sub-grid-scale (SGS) models, and has been validated extensively for several canonical turbulent flows. A re-interpretation of this implicit LES (ILES) approach in the context of an Approximate Deconvolution Model³⁷ has been presented by Mathew *et al.*³⁸ As the grid resolution increases or Reynolds number decreases, this ILES becomes an effective direct numerical simulation.

III. NUMERICAL PROCEDURE

All simulations are performed with the extensively validated high-order Navier-Stokes solver *FDL3DI*.^{39,40} In this code, a finite-difference approach is employed to discretize the governing equations, and all spatial derivatives are obtained with high-order compact-differencing schemes.⁴¹ For any scalar quantity, ϕ , such as a metric, flux component or flow variable, the spatial derivative ϕ' is obtained along a coordinate line in the transformed plane by solving the tridiagonal system:

$$\alpha \phi'_{i-1} + \phi'_i + \alpha \phi'_{i+1} = \beta \frac{\phi_{i+2} - \phi_{i-2}}{4} + \gamma \frac{\phi_{i+1} - \phi_{i-1}}{2} \quad (9)$$

where α, γ and β determine the spatial properties of the algorithm. For the airfoil computations reported in this paper, a sixth-order scheme is used corresponding to $\alpha = \frac{1}{3}$, $\gamma = \frac{14}{9}$ and $\beta = \frac{1}{9}$. At boundary points, higher-order one-sided formulas are utilized which retain the tridiagonal form of the scheme.^{39,40} Typically, Neumann boundary conditions are implemented with third-order one-sided expressions.

The derivatives of the inviscid fluxes are obtained by forming the fluxes at the nodes and differentiating each component with the above formula. Viscous terms are obtained by first computing the derivatives of the primitive variables. The components of the viscous flux are then constructed at each node and differentiated by a second application of the same scheme.

For the case of a maneuvering wing, the grid is moved in a rigid fashion using the prescribed airfoil motion. To ensure that the Geometric Conservation Law (GCL) is satisfied, the time metric terms are evaluated employing the procedures described in detail in Ref. 42.

In order to eliminate spurious components, a high-order low-pass spatial filtering technique^{39,43} is incorporated. If a typical component of the solution vector is denoted by ϕ , filtered values $\hat{\phi}$ at interior points in transformed space satisfy,

$$\alpha_f \hat{\phi}_{i-1} + \hat{\phi}_i + \alpha_f \hat{\phi}_{i+1} = \Sigma_{n=0}^N \frac{a_n}{2} (\phi_{i+n} + \phi_{i-n}) \quad (10)$$

Equation (10) is based on templates proposed in Refs. 41 and 44 and with proper choice of coefficients, provides a $2N$ th-order formula on a $2N + 1$ point stencil. The $N + 1$ coefficients, a_0, a_1, \dots, a_N , are derived in terms of α_f using Taylor- and Fourier-series analysis. These coefficients, along with representative filter transfer functions, can be found in Refs. 40 and 45. The filter is applied to the conserved variables along each transformed coordinate direction once after each time step or sub-iteration. In the present simulations, an interior 8th-order filter with $\alpha_f = 0.4$ was prescribed. For the near-boundary points, the filtering strategies described in Refs. 39 and 45 are used. For transitional and turbulent flows, the previous high-fidelity spatial algorithmic components provide an effective implicit LES approach in lieu of traditional SGS models, as demonstrated in Refs. 32 and 33. Finally, time-marching is accomplished by incorporating an iterative, implicit approximately-factored procedure.^{32,33}

IV. RESULTS

A. Details of Computations

Computations were carried out for the low-aspect-ratio plate wing shown in Fig. 1. The wing has an aspect ratio $2S/c = 2$, a uniform thickness $t/c = 0.016$ and all edges are squared-off. The Reynolds number varied over the range $10^3 \leq Re_c \leq 4 \times 10^4$.

Computations were performed on a stretched Cartesian mesh containing approximately 30 million grid points (Fig. 1). The grid consisted of five zones and had overall dimensions of $440 \times 469 \times 146$ in the streamwise, normal and spanwise directions respectively. Clustering was provided near the plate in order to capture the near-field complex vortical structure generated by the pitching motion.

Simulations were performed using the parallel high-order *FDL3DI* Navier-Stokes solver.^{46,47} The mesh was decomposed into a set of 256 overlapped sub-domains or blocks which were assigned to individual processors. A five-point inter-block overlap was employed in order to retain high-order numerical accuracy. Due to the simple topological structure of the mesh, all overlapping planes were coincident and high-order interpolation was not required.

The boundary conditions were prescribed as follows. Along the entire wing surface, a no-slip adiabatic condition was employed in conjunction with a zero normal pressure gradient. The surface velocity components (u_s, v_s, w_s) were determined from the imposed pitching or perching motions described below. In order to improve spatial resolution with available computational resources, the flow was assumed to be symmetric about the wing centerline. This simplification was considered based on examination of the experiments of Yilmaz and Rockwell²³ which displayed a fairly symmetric overall flow structure. On the far field boundaries, located approximately 100 chords away from the wing, freestream conditions were specified. It should be noted that prior to reaching this boundary, the grid is stretched rapidly. This stretching in conjunction with the low-pass spatial filter provides a buffer-type treatment found previously⁴⁸ to be quite effective in reducing spurious reflections.

Two different types of maneuvers were considered and referred to in the following as pitching and perching. For the more standard pitching maneuver, the wing is stationary (i.e., $U_w = 0.0$, Fig. 1) and there is a uniform incoming freestream U_∞ . The wing is pitched about its quarter-chord axis from zero incidence to a maximum angle of attack $\alpha_{max} = 45^\circ$ and then held fixed. In order to avoid discontinuities in the angular acceleration, the angle of attack is prescribed employing a modified version of the ramping function of Eldredge et al.⁴⁹ The angle of attack, α , is given by

$$\alpha(t) = \frac{\Omega_0^+}{2a} \ln \left[\frac{\cosh(a(t - t_1))}{\cosh(a(t - t_2))} \right] + \frac{1}{2} \alpha_{max} \quad (11)$$

In this equation, a controls the smoothing of the angular acceleration and deceleration, $\Omega_0^+ = \alpha_{max}/(t_2 - t_1)$ is the nominal non-dimensional pitch rate, and t_1 and t_2 define the nominal pitching time interval. In all of the cases to be presented, $t_1 = 0.5$ and $a = 11$. The instantaneous angular rate can be obtained by straight forward differentiation of Eq. (11). The variations of angle of attack and angular rate are shown in Fig. 3 for all pitch rates considered.

For the perching maneuvers, the wing is initially at rest in a quiescent fluid (i.e., $U_\infty = 0$). It then accelerates at zero incidence during a time interval $tU_o/c = 0.5$ until reaching a constant speed U_o (Fig. 4). The wing maintains this constant speed and zero incidence for an additional time interval $tU_o/c = 5.5$ in order to achieve a quasi-steady condition. Subsequently, the wing is pitched up about its quarter-chord axis while simultaneously decelerating to rest (Fig. 4). The angle of attack variations are prescribed by the same function used for the pitching cases (Eq. 11). The translational velocity U_w is described in terms of a 4th-degree polynomial ensuring continuous velocity and acceleration. At the end of the maneuver, the wing remains at rest and at the maximum angle of attack of 45° . For the perching cases, the Reynolds number and nominal pitch rate are defined in terms of the maximum wing translational

velocity U_o .

Pitching and perching simulations were started from the corresponding computed static solutions at zero-degree angle of attack or from fully quiescent conditions respectively. A very small computational non-dimensional time step $\Delta t U_\infty / c = 6.25 \times 10^{-5}$ was prescribed in order to provide sufficient temporal resolution of the transitional fine-scale flow evolution. This value of Δt corresponded to 64,000 time steps during the pitching interval $\tau_2 - \tau_1$ for the highest pitch rate considered. Finally, all computations were performed employing a low freestream Mach number $M_\infty = 0.1$ with the present compressible Navier-Stokes solver.

B. Stationary Wing

In order to provide a reference for comparison and to highlight lag effects for the pitching maneuvers, the flow structure over the stationary wing is briefly considered first. Further details for the stationary wing can be found in Refs. 31 and 50. Figure 5 shows the instantaneous flows for $\alpha = 8^\circ, 15^\circ$ and 25° at the baseline Reynolds number $Re_c = 10^4$. The overall three-dimensional flow structure, depicted in terms of an iso-surface of total pressure, is characterized by a detached shear layer separating from the leading edge which rolls up and breakdowns into fine-scale structures. For $\alpha = 8^\circ$, the convergence toward the symmetry plane of the edges of the vortex sheet emanating from the leading edge is quite apparent (Fig. 5a). As described in Ref. 31, there is a strong transverse flow towards the centerplane and the flow is inherently three-dimensional even at this modest incidence. The instantaneous limiting streamlines display a recirculation pattern encompassing a region of low-pressure which provides the main contribution to the aerodynamic lift. Separation from the wing tip results in the formation of a coherent tip vortex and in a corresponding very narrow region of low pressure on the wing surface. As the angle of attack increases to $\alpha = 15^\circ$, the tip vortices become more prominent and the separated shear layer extends over a larger portion of the wing. There is also a larger region of low pressure on the wing. For $\alpha = 25^\circ$ the edge of the shear layer exhibits less convergence toward the plane of symmetry and the direct contribution of the tip vortex to the surface pressure is not discernable. At this higher angle, the extent of separated flow normal to the wing increases significantly, as seen in the contours of vorticity magnitude on the centerplane (Fig. 5f). In addition, as shown in Ref. 50, attachment to the wing upper surface is no longer observed in the time-averaged flow pattern.

C. Pitching Maneuver

1. Effect of Pitch Rate

In this section we study the evolution of the flow structure over the pitching wing as a function of pitch rate. Three values of Ω_o^+ are considered, $\Omega_o^+ = 0.05, 0.1$ and 0.2 with nominal pitch time intervals of 16, 8 and 4 convective times respectively. The highest pitch rate corresponds to the recent experiments of Yilmaz and Rockwell.²³

The three-dimensional instantaneous flow structure for $\Omega_o^+ = 0.2$ is shown in Fig. 6 at several points during the maneuver employing an iso-surface of constant total pressure. The corresponding wing surface pressure and contours of vorticity magnitude on the symmetry plane are shown in Fig. 7. As the wing is pitched and the angle of attack increases, one can observe a nascent leading-edge vortex which is pinned at the wing front corners and which appears initially to be fairly uniform across a significant portion of the span (Fig. 6a). By the time the wing has reached $\alpha = 15^\circ$, the flow has become highly three dimensional, and large transverse velocities directed towards the centerline exist within the leading-edge vortex core. This feature is common to the structure found in previous experimental²⁰ and computational³¹ studies for a heaving wing. Examination of the vortical structure on the symmetry plane (Fig. 7a-c) indicates that the LEV is initially laminar and similar to that found in 2D dynamic stall.^{9,11} By $\alpha = 25^\circ$ the emergence of fine-scale structures is apparent due to the onset of transitional effects. The process of transition or breakdown of the LEV is enhanced by the strong axial currents within the vortex core which eventually reach the wing centerplane. As the angle of attack increases from $\alpha = 25^\circ$ to 35° (Figs. 6d-f), the leading-edge vortex system evolves into a Λ -shaped structure as the vortex lifts away from the plate near the symmetry plane while remaining pinned at the wing front corners. Eventually the LEV detaches from the edges forming an arch-type vortex with legs normal to the wing surface (Figs. 6h,i). This structure is similar to that first described by Visbal³¹ for a plunging wing albeit it is in the present case less compact and with legs that are located further outboard. In addition, since the wing remains at high angle of attack, the arch vortex resides over the wing and is capable of establishing a well-defined large-scale swirling pattern on the wing surface.

Due to the presence of the LEV system, the wing surface pressure displays a region of strong suction which extends from the wing corner to the centerline (Fig. 7c). The pressure is lowest near the corner where the vortex is in closest proximity to the wing surface. As the arch-vortex forms, a concentric region of low pressure emerges and a large-scale

circulatory pattern is established over the wing (Fig. 7i). Animations of the flow field revealed that this region of low pressure (corresponding to the legs of the arch-vortex) propagates towards the wing leading edge before finally moving downstream and outboard. This interesting behavior may be attributable, based on inviscid arguments, to the self-induced velocity of the arch-vortex and interaction with its own image on the plate. This upstream propagation effect is more readily apparent at the intermediate pitch rate $\Omega_o^+ = 0.1$ discussed later.

A distinct property of the arch-vortex and its accompanying circulatory motion on the wing is the very long residence time over the wing. The last frames in Figs. 6 and 7 correspond to an elapsed time of 4.5 convective times after reaching the maximum angle of attack. Even at this stage, a weakened arch vortex is still observed over the wing and a region of circulation and low pressure persists on the wing upper surface. This represents an interesting new finding associated with the three-dimensional unsteady separation process for a low-aspect-ratio wing which is quite different from the 2D counterpart where the dynamic stall vortex is readily shed following its detachment from the leading edge.^{7,9,11} Further discussion of the comparison between 2D and 3D dynamic stall is provided below.

Another distinct element in the pitching wing 3D flow structure is the tip vortex clearly seen in the iso-surface plots of Fig. 6. This vortex strengthens with increasing angle of attack inducing a narrow region of low pressure near the tips on the wing surface. At very high angles of attack, the tip vortex experiences vortex breakdown and ultimate collapse.

As noted earlier, the highest pitch rate ($\Omega_o^+ = 0.2$) was selected to allow comparison with recent experiments by Yilmaz and Rockwell.²³ The experimental and computed flow structures are compared in Fig. 8 at two points during the pitching maneuver. The experimental frames (Figs. 8a,e) show an iso-surface of the Q-criterion⁵¹ ($Q = 5$) for the phased-averaged flow. These figures clearly show the A-type vortical structure and the subsequent formation of the arch-type vortex previously described. The corresponding instantaneous iso-Q representations for the computed flow field are shown in Figs. 8b,f. The computational iso-surfaces exhibit fine-scale features not seen in the experiments. This is attributed primarily to the much finer spatial resolution provided by the computational mesh relative to the spacing between sampling planes used for the experimental volume reconstruction.²³ Differences may also arise in part from the phased-averaging employed in the experiments. Unfortunately, a meaningful phase-averaged representation is not possible in the transient computations unless small perturbations (occurring naturally in the experiment) are added for different realizations, a process which becomes prohibitive in terms of computational resources. In order to provide a more direct comparison between experiment and computation, the computed flow field was filtered down to a spatial resolution comparable to that of the experimental measurements using the procedure developed by Garman et al.⁵² The Q iso-surfaces derived from the filtered computational results are shown in Figs. 8c,g. On similar spatial resolutions, the good agreement between the computed and experimental three-dimensional flow structures is now apparent. Both computation and experimental measurements display the same key flow elements. The last row in Fig. 8 displays the computed flow structure in terms of an iso-surface of stagnation pressure. One can observe that this variable (used in previous and most subsequent figures) filters out fine-scale features and provides a clearer depiction of the dominant flow elements. The previous as well as additional comparison between computation and experiment²³ indicate that in both cases the unsteady separation process culminates with the formation of an arch vortex which induces a large-scale swirl pattern on the wing surface.

Results for the lower pitch rates $\Omega_o^+ = 0.1$ and 0.05 are shown in Figs. 9 - 12. Comparison of all pitch rates indicates that the unsteady 3D separation process is characterized by the same basic sequence of events starting with the leading-edge vortex formation and culminating with its evolution into an arch-type vortical structure. With increasing pitch rate several trends can be observed: (i) there is an angular delay in the emergence of the flow features similar to that found in 2D dynamic stall, (ii) the initial LEV vortex is more compact and forms closer to the wing leading edge, (iii) lower values of pressure are present on the wing surface under the LEV, arch-vortex and tip vortices, and (iv) the arch-vortex becomes more compact.

The case of $\Omega_o^+ = 0.1$ serves to more clearly illustrate the dynamics of the arch-vortex with its accompanying low-pressure region and circulatory pattern on the wing. As the arch-vortex fully emerges between $\alpha = 30^\circ$ and 40° (Fig. 9e-g), the surface pressure (Fig. 10e-g) evolves into a more coherent concentric distribution with progressively lower values of minimum pressure. This process is due to the establishment of a fully three-dimensional circulatory pattern on the wing surface associated with the normal vorticity of the legs of the arch vortex. One can also observe the movement of the approximate center of this low pressure region. As noted earlier, this center propagates upstream and gets closer to the wing leading edge at the instant shown in Fig. 10h before moving toward the trailing edge (Fig. 10i). This upstream movement of the arch-vortex against the prevailing flow is postulated to be the result of the self-induced velocity of the vortex/image system. The long residence time of the arch-vortex and swirling motion above the wing is also observed for $\Omega_o^+ = 0.1$. The last frames in Figs. 9 and 10 show that both features are still well-defined even after a time interval of 3.5 convective time scales has elapsed following cessation of the pitch-up motion.

Although the detailed dynamics of the tip vortex is not described in detail, it is interesting to point out the onset of vortex breakdown seen in the insets of Figs. 9d and 11c. The tip vortex is depicted using a lower value of total pressure in order to highlight the vortex core structure. For both values of pitch rate, the onset of vortex breakdown is clearly seen and its structure is characterized by a bubble-like bursting followed by a spiral tail which winds in a sense opposite to that of the prevailing swirling flow. This structure is similar to that found by Visbal⁵³ during onset of vortex breakdown in the leading-edge vortex over a pitching delta wing.

Aerodynamic Loading

The effect of pitch rate on the wing aerodynamic loading is considered next. The history of the aerodynamic coefficients is presented in Fig. 13. Several trends are apparent in the lift and pitching moment coefficient histories as a function of pitch rate. In all cases, there is a non-circulatory spike in the lift and pitching moment induced by the angular acceleration (Figs. 13a,c). The peak in lift ΔC_{L1} displays a linear variations as a function of pitch rate, as shown in Figure 13d. Following this initial surge, the lift distribution becomes fairly linear with a slope close to the static value of π (in radians) but shifted by an offset ΔC_{L2} (as defined in the inset of Fig. 13d). Figure 13d also displays the quantity denoted as ΔC_M which corresponds to the magnitude of the approximately constant negative value of pitching moment established after the end of angular acceleration. For convenience, this value is selected at $\alpha = 4^\circ$ at which point a constant angular velocity prevails even for the highest Ω_o^+ considered. Both ΔC_{L2} and ΔC_M exhibit an effective linear dependence on pitch rate. The offsets in lift and moment coefficients observed after reaching a constant angular rate are consistent with a rotation-induced chordwise camber.⁵⁴⁻⁵⁶

The overall history of the lift coefficient (Fig. 13a) indicates that both the maximum value of C_L and its corresponding angular position ($\alpha_{C_{Lmax}}$) increase with pitch rate. The values of C_{Lmax} and $\alpha_{C_{Lmax}}$ for $\Omega_o^+ = 0.05, 0.1$ and 0.2 are approximately $(1.5, 31.3^\circ)$, $(1.89, 38.4^\circ)$ and $(2.1, 40.6^\circ)$ respectively. Even for the smallest pitch rate, there is a significant increase in maximum lift which is almost twice the maximum static value (Fig. 13a). It is interesting to note that the occurrence of maximum lift follows the emergence of the arch-vortex at least for the two lower values of pitch rate. The moment coefficient histories (Fig. 13c) show that following a fairly flat initial distribution a rapid drop in C_M takes place beginning at an angle which increases with Ω_o^+ .

Figure 13e displays the chordwise position of the center of lift X_{CL} as a function of angle of attack. This parameter was computed for only a few available flow fields after the computations had been performed and therefore the distributions are rather coarse. Nonetheless, a few trends can be observed. For the static case, X_{CL} moves downstream with increasing incidence as found to be the case experimentally.¹⁴ For the lowest pitch rate, the center of lift is upstream of the static situation ($8^\circ \leq \alpha \leq 25^\circ$) as it would be expected from lag effects in the separation process. This is not the case for at low angle of attack for the higher pitch rates for which X_{CL} increases with Ω_o^+ . This effect is due to the higher pressures on the wing lower surface induced by rotation. At higher angles of attack ($\alpha \geq 25^\circ$), as the separated flow and its low pressure region have evolved further, the center of lift is found to be positioned consistently further upstream with increasing pitch rate in accordance with lag effects. An interesting feature for all pitching cases is the local dip in X_{CL} observed in the distributions (for instance, at $\alpha = 40^\circ$ for $\Omega_o^+ = 0.1$ and $\alpha = 30^\circ$ for $\Omega_o^+ = 0.05$). This feature correlates with the previously noted temporary movement toward the wing leading edge of the arch vortex and its corresponding swirling region of low pressure, as seen in Figs. 10g-i and Figs. 12e-g.

The spanwise distribution of the sectional lift coefficient for the static and pitching wing is considered next. For the stationary wing (Fig. 14a), the distributions indicate that most of the lift arises from the leading-edge separated region and that there is only a limited direct contribution from the tip vortices. A large increase in the levels of sectional lift is observed over the mid-section of the wing as angle of attack increases from 8° to 15° . However, the overall levels remain similar when going to $\alpha = 25^\circ$, consistent with the plateau in the total lift distribution (Fig. 13a). A local peak associated with the tip vortex is seen to become more prominent as angle of attack increases from 8° to 15° but it is absent at $\alpha = 25^\circ$. The sectional lift distributions for the intermediate pitch rate $\Omega_o^+ = 0.1$ are shown in Fig. 14b. The distributions for the other two pitch rates were found to be qualitatively similar and are not included. The sectional lift distributions denoted by dashed lines in Fig. 14b ($\alpha = 8^\circ, 15^\circ, 25^\circ$) correspond to a portion of the maneuver prior to the emergence of the arch-vortex. At this stage, the sectional lift is somewhat uniform across a significant portion of the span. At $\alpha = 25^\circ$, several undulations begin to emerge near mid-span and well-defined peaks (with the highest value of $C_L(z)$) are induced by the tip vortices. There is a transformation in the character of the sectional lift following the appearance of the arch vortex ($\alpha = 40^\circ$). The sectional lift distribution exhibits a strong peak on each side of the wing associated with the legs of the arch vortex and the induced swirling pattern over to the wing. No signature of the tip vortex is apparent at this stage of the flow. The distribution at $\alpha = 45^\circ$ shows the outboard movement of the center of the circulatory pattern noted earlier.

2. Comparison of 2D and 3D Dynamic Stall Process for a Pitching Wing

In order to contrast the fundamental differences between the dynamic stall process for a 2-D and a low-aspect-ratio wing, computations were also performed for an effectively infinite aspect ratio plate, emulated by means of spanwise periodic conditions on a prescribed spanwidth ($s/c = 0.4$). The sectional geometry and computational grid were the same as in the previously described 3D cases. Only the intermediate value of pitch rate $\Omega^+ = 0.1$ was considered for the 2D pitching configuration and the corresponding flow field evolution is presented in Fig. 15. The process of 2D dynamic stall is characterized by the formation of an initially laminar leading-edge vortex system which subsequently undergoes transition (even at this modest value of Reynolds number $Re_c = 10^4$) due to the onset of spanwise instabilities effects. The turbulent LEV convects along the wing, and as it nears the trailing edge, a trailing-edge vortex of opposite rotation emerges. Eventually both vortices are shed into the wake as the plate reaches its maximum angle of attack. The surface pressure contours clearly show that these vortices induce regions of low pressure which extend, with only small secondary variations, across the entire span. This flow evolution is similar to that found during the downward stroke for a periodically heaving 2D wing described in detail in Ref. 11.

A comparison of the lift and pitching moment coefficient histories for the 2D and finite-aspect-ratio plates is shown in Fig. 16. The lift and pitching moment for the 2D wing display similar offsets as found previously for the finite plate and are due to the rotation-induced apparent camber effect. In addition to that effect, the 2D wing displays a distinct depression in the lift slope relative to the theoretical value of 2π (in radians) plotted for comparison in Fig. 16a. This effect previously noted in 2D dynamic stall experiments and computations^{54,56} is associated with the lag in the establishment of circulation around the airfoil (i.e. Wagner-type effect) at a given angle of attack. Comparison of the overall C_L histories indicates that the finite aspect ratio promotes further delay of stall from $\alpha_{CLmax} \approx 28^\circ$ to $\alpha_{CLmax} \approx 38.5^\circ$. A much smoother lift distribution is also observed for the 3D wing. Regarding the C_M history, there is also a delay in moment stall with the finite aspect ratio wing, and the elimination of the dual peak seen in the 2D case. This latter feature, as explained for a 2D plunging wing in Ref. 11, is due to the strong trailing-edge vortex which is absent in the 3D wing.

The previous comparison of the flow structure and aerodynamic loading for the finite and 2D plates clearly highlights the inherent three-dimensional nature of dynamic stall for a low-aspect-ratio wing. The latter being characterized by the formation of an arch-type vortex and a strong swirl pattern over the wing which persists for longer times. In the 2D case, the spanwise-oriented leading- and trailing-edge vortices are shed much more readily inducing an earlier stall.

3. Effect of Reynolds Number

The effect of Reynolds number on the flow structure and loading generated by the pitching wing was investigated for the lowest pitch rate ($\Omega_o^+ = 0.05$) by considering three values of Re_c (10^3 , 10^4 and 4×10^4). The instantaneous flow structure for $Re_c = 4 \times 10^4$ is shown in Figs. 17 and 18. As seen previously for $Re_c = 10^4$, the flow evolution is again characterized by the transformation of the LEV into an arch-type structure with its accompanying swirling pattern over the wing surface. The arch vortex appears to be more compact, as can be observed by comparison of Figs. 11h and 17h. In addition, the higher Reynolds number case exhibits earlier transition of the leading-edge vortex and finer scale features. Lower pressures are also observed on the wing surface with increased Re_c (e.g. Fig. 12g and 18g).

The case of $Re_c = 10^3$ is displayed in Figs. 19 and 20. At this very low value of Reynolds number, one can observe throughout the entire pitch-up, the lack of fine-scale flow features associated with transition. At the earlier stages of the flow evolution ($\alpha = 20^\circ, 25^\circ$, Figs. 19c,d), the structure is characterized by a large-scale leading edge vortex and by the formation of hairpin-like vortices near the wing trailing edge. These features display a broad similarity with the investigation of Taira and Colonius²⁸ for an impulsively translating wing at $Re_c = 300$ and $\alpha = 30^\circ$. From $\alpha = 30^\circ$ onwards (Figs. 193-h), the emergence of the arch-type vortex is apparent. The surface pressure contours and limiting streamlines in Fig. 20 show again the induced circulatory motion with weaker suction relative to the higher Reynolds number cases.

The history of the aerodynamic loads, shown in Fig. 21, exhibit significant quantitative effects of Reynolds number on maximum lift and its corresponding angular position. There appears to be a consistent delay in lift stall as the Reynolds number increases. The C_L distribution for $Re_c = 10^3$ has a lower slope and subsequently displays a much smoother character. The pitching moment coefficient also exhibits a more pronounced drop with increasing Re_c .

D. Perching Maneuver

In this section, the effect of variable freestream velocity on the dynamic stall process of a pitching low-aspect-ratio wing is considered. This effect is of interest since in a typical perching maneuver, pitching is also accompanied by deceleration to an effectively zero velocity. Another potential application is the case of pitching in the presence of variable freestream velocity such as in a horizontal gust encounter. In this exploratory study, a simplified perching-type maneuver is prescribed which does not attempt to include all complex flight dynamic effects present in a real perching scenario. The imposed wing kinematics, discussed in Section IV-A, is shown in Fig. 4. The wing accelerates from rest and at zero angle of attack to a constant velocity in quiescent flow. This constant speed is maintained for a sufficiently long time in order to effectively eliminate transients. The wing then pitches from zero incidence to a maximum angle attack of 45° while it simultaneously decelerates and comes to a full stop. Since the freestream velocity is zero, the Reynolds number and pitch rate are now defined in terms of the maximum translating speed U_o (i.e., $Re_c = \rho_\infty U_o c / \mu_\infty$, $\Omega_o^+ = \dot{\alpha} c / U_o$). A Reynolds number of $Re_c = 10^4$ and pitch rates $\Omega_o^+ = 0.05$ and 0.2 are selected in order to match the previous pure-pitching results.

The flow structure for $\Omega_o^+ = 0.2$ is presented in Figs. 22 - 23. It should be noted that an iso-surface of vorticity magnitude is employed (instead of total pressure) in Fig. 22 given the large variation in effective dynamic pressure ρU_w^2 . Comparison of Figs. 6 and 22 shows that the flow structure for the perching case is similar to the constant freestream situation for $\alpha \leq 20^\circ$. As the wing translating velocity is appreciably reduced, significant differences arise between the perching and pitching cases. For the perching case, the LEV vortex does not evolve into the arch-type structure seen in the pure-pitching situation. Instead, the growth of the LEV is halted and it remains closer to the leading edge. Eventually, as the wing approaches its final horizontal position, the LEV actually moves forward of the plate. The arrested development and final upstream movement of the leading-edge vortex can also be seen in Fig. 23 which displays contours of instantaneous vorticity magnitude on the symmetry plane. Figure 23i also shows the formation underneath the plate of a stopping trailing-edge vortex with the same sense of rotation as the LEV system.

The histories of the unsteady loads for $\Omega_o^+ = 0.2$ are plotted in Fig. 24 and compared to the constant freestream pitching case. This figure contains for the perching case the loads normalized by the *maximum* dynamic pressure ρU_o^2 , as well as the loads normalized by the *instantaneous* or effective dynamic pressure ρU_w^2 which varies with translating velocity. The former are the actual non-dimensional forces and moment experienced by the plate whereas the latter permit a comparison with the pure pitching case. Definition of the aerodynamic coefficients using ρU_w^2 is of course only valid prior to the velocity reaching a vanishing value at which point these coefficients become unbounded. The aerodynamic loads are plotted in Fig. 24 both as a function of time (top row) and angle of attack. For the case of the perching wing, time has been shifted relative to the onset of rotation in order to facilitate comparison with the pitching case. The non-dimensional lift force on the perching wing increases initially following the onset of rotation, reaches a peak value near $\alpha \approx 12.3^\circ$ and then drops fairly smoothly becoming negative at high angles of attack. The latter behavior would be expected from the translational deceleration. The drag force displays similar characteristics as found for the lift. The nondimensional moment drops at the onset of rotation due to angular acceleration and rotation-induced apparent camber effects previously discussed for the pure-pitch case. It then rises and becomes positive (i.e. pitch up) at high angles of attack. If one assumes that most of the force and moment characteristics are dominated by the effective dynamic pressure, then renormalization of these quantities using the instantaneous velocity conditions should bring the results closer to the constant freestream pitching situation. Indeed, this is found to be the case for the first part of the maneuver. As seen for instance in Fig. 24d, the rescaled lift coefficient is in close agreement with the standard pitching case up to $\alpha \approx 21.4^\circ$, even after the translating velocity has dropped to 60% of its maximum value. This agreement is clearly lost for higher angles of attack.

Results for the perching maneuver at lower pitch rate ($\Omega_o^+ = 0.05$) are displayed in Figs. 22 - 24. Since the rotation-induced angular lag in the flow development diminishes with lower pitch rate, the effects of decreased translational velocity ensue at a stage when the flow has already evolved further. Therefore at this lower Ω_o^+ , the leading-edge vortex system still displays the incipient formation of the arch vortex and its accompanying swirling motion (Fig. 25e). This contrasts with the perching case for $\Omega_o^+ = 0.2$ where no evidence of the arch-vortex formation is observed (Fig. 22). As the wing decelerates further (Figs. 25f-h), the incipient arch vortex collapses and its remnant moves ahead of the plate leading edge. The presence of the weak swirling pattern is clearly seen in Fig. 25f and this feature tends to eject the vorticity in front of the wing to further outboard stations along the span. The trailing-edge vortex underneath the plate is also found to be less-organized for the lower pitch rate (see Figs. 26g and 23i).

Histories of the loads for the lower pitch rate perching case are shown in Fig. 27. The evolution of the non-dimensional forces and moments displays the same general trend as described previously. It is interesting to note that the maximum non-dimensional lift force occurs at a higher angle of attack ($\alpha \approx 14.1^\circ$) relative to the higher pitch rate ($\alpha \approx 12.3^\circ$). This reverses the behavior for a constant freestream where maximum lift takes place at progressively

higher incidence as Ω_o^+ increases. The lift force renormalized with instantaneous velocity closely matches the constant freestream pitching case up to $\alpha \approx 26^\circ$ at which point the plate velocity has dropped to roughly 40% of its maximum value. The trends observed in the comparison of the rescaled lift for the perching maneuver with the standard pitching case are entirely the opposite for the two values of Ω_o^+ . For $\Omega_o^+ = 0.2$ (Fig. 24d), the maximum (rescaled) lift and its angular position are lower for the perching case relative to constant freestream. The reversed is seen for $\Omega_o^+ = 0.05$ (Fig. 27d) where the lift and its position is higher in the perching maneuver. This implies that values of lift derived from experiments in a constant freestream can either underpredict or overpredict the lift force when rescaled to the perching maneuver. The present results suggest that simplified generalizations cannot be made regarding the behavior of the loads for a perching maneuver in relation to its constant-freestream counterpart. As demonstrated above for different pitch rates, the trends can be reversed and additional interesting effects might be expected depending upon the phase relationship between the rotating and translating motions.

V. SUMMARY AND CONCLUSIONS

This study addresses the flow structure and unsteady loading arising over a rectangular wing of aspect ratio two subjected to high-amplitude pitching and perching maneuvers under low-Reynolds-number conditions of interest in small unmanned aerial vehicle operation and gust interactions. The flow fields are simulated employing an extensively-validated high-fidelity computational approach capable of accurately capturing the complex unsteady transitional flows generated under such extreme maneuvers.

Canonical pitching motions for a non-translating wing in the presence of a constant freestream are first investigated in order to elucidate the effects of pitch rate and Reynolds number on the flow structure and aerodynamic loading. The wing is pitched about its quarter-chord axis to a maximum incidence of 45° over nominal time intervals ranging from four to sixteen convective time scales yielding maximum non-dimensional angular rates $0.05 \leq \Omega_o^+ \leq 0.2$. The Reynolds number based on the wing chord varied from 10^3 to 4×10^4 . The flow field evolution is found to start with the formation of a spanwise-oriented leading-edge vortex which is initially pinned at the front edges of the plate. This vortex evolves at later times into the arch-type structure previously found for a heaving wing.³¹ The arch vortex is here less compact and since the wing remains at high angle of attack, it has the time to establish a well-defined swirling pattern over the wing surface. This inherently three-dimensional circulatory motion extends over most of the wing semi-span and encompasses a region of low pressure. This vortical structure exhibits a long residence time over the wing and it persists for several convective time scales after cessation of the pitch-up motion. At some stages following its formation, the arch vortex even propagates upstream towards the leading edge of the wing prior to finally moving outboard and downstream. This interesting upstream propagation against the prevailing flow is postulated to be the result of the self-induced velocity of the vortex/image system. In addition to the previous leading-edge separation and vortex formation, the flow is characterized by the emergence of tip vortices arising from separation at the wing tips. These tip vortices increase in intensity with angle of attack and exhibit the onset of vortex breakdown in a manner similar to that found in the leading-edge vortex development over a pitching delta wing.⁵³

Despite quantitative differences, the morphology of 3D dynamic stall previously described is found to be universal over the range of pitch rates and Reynolds numbers investigated. Several trends are apparent with increasing Reynolds number or pitch rate. These include (i) a more compact arch vortex system, (ii) a stronger circulatory pattern and lower pressures above the wing surface, (iii) increased maximum lift, and (iv) delay of stall. Even for the lowest pitch rate considered, a significant increase in maximum lift is achieved relative to the static situation. Transitional effects are observed to emerge in all cases with the exception of the lowest Reynolds number flow which lacks fine-scale features.

For $\Omega_o^+ = 0.2$, good agreement is found between the computed three-dimensional flow structure and the recent experimental measurements of Yilmaz and Rockwell²³ provided that the higher-resolution computational results are filtered down to the coarser resolution used in the experimental reconstruction. The experiments and computations also exhibit broad similarities in terms of the final arch-vortex formation and induced swirl pattern. The present pitching wing simulations in conjunction with previous heaving-wing computations,³¹ as well as the available experimental observations^{20,21,23} provide a consistent picture of the main flow elements engendered by dynamic stall of a low-aspect-ratio wing.

Computations are also performed for a 2D wing section (i.e. effectively infinite aspect ratio simulated by spanwise periodic conditions) in order to highlight the fundamentally different flow evolution induced by the finite span of the wing. It is found that although the 2D wing exhibits higher maximum lift, the low-aspect-ratio promotes further delay of stall and a much smoother behavior of the aerodynamic coefficients. This due to the longer residence time of the 3D arch vortex over the wing and contrasts with the spanwise-oriented vortices which are readily shed in 2D dynamic stall.

Canonical perching maneuvers involving simultaneous pitching and deceleration to rest are considered and the aerodynamic loads and flow structure are compared to the constant freestream situation. For the perching case with $\Omega_o^+ = 0.2$, the LEV vortex does not evolve into the arch-type structure since its development is halted as the wing translational speed diminishes. Instead the vortex remains closer to the leading edge and actually moves forward of the wing as the horizontal velocity goes to zero. For $\Omega_o^+ = 0.05$, an incipient arch vortex is formed but weakens and moves forward as the plate decelerates. Rescaling the loads using the local translational speed shows agreement between the perching and standard cases only up to a limited angle of attack. Beyond this point, there are significant differences not only quantitatively but also in the trends which can be reserved for different values of pitch rate. For instance, for $\Omega_o^+ = 0.2$ the maximum (rescaled) lift and its angular position are lower for the perching case relative to constant freestream. The reversed is seen for $\Omega_o^+ = 0.05$. This implies that values of lift derived from experiments in a constant freestream facility can either underpredict or overpredict the lift force when rescaled to the perching maneuver depending on pitch rate itself. Further computations exploring the flow evolution and loads as a function of the phase relationship between the rotational and translational motions are required.

ACKNOWLEDGMENT

This work was supported in part by AFOSR under a task monitored by Dr. D. Smith, and by a grant of HPC time from the DoD HPC Shared Resource Center at AFRL. The author is grateful to D. Garmann for his assistance with the data reduction used for comparison with the experimental data.

References

- ¹W. J.. McCroskey. Unsteady Airfoils. *Annual Rev. Fluid Mech.*, 14:285–311, 1982.
- ²L. Carr. Progress in Analysis and Prediction of Dynamic Stall. *Journal of Aircraft*, 25(1):6–17, 1988.
- ³M. R. Visbal. On Some Physical Aspects of Airfoil Dynamic Stall. *Proceedings of the International Symposium on Non-Unsteady Fluid Dynamics*, (Edited by J. Miller and D. Telionis, Vol. 92, ASME), 1990.
- ⁴T.J. Mueller. Low Reynolds Number Vehicles. *AGARDograph No. 288*, 1985.
- ⁵W. Shyy. *Aerodynamics of Low Reynolds Number Flyers*. Cambridge University Press, 2008.
- ⁶J. Ekaterinaris and M. Platzer. Computational Prediction of Airfoil Dynamic Stall. *Progress in Aerospace Sciences*, 33:759–846, 1997.
- ⁷M.R. Visbal and J.S. Shang. Investigation of the Flow Structure Around a Rapidly Pitching Airfoil. *AIAA Journal*, 27(8):1044–1051, 1989.
- ⁸M.R. Visbal. On the Formation and Control of the Dynamic Stall Vortex on a Pitching Airfoil. *AIAA Paper 1991-0006*, January 1991.
- ⁹P.G. Choudhuri, D.D. Knight, and M.R. Visbal. Two-Dimensional Unsteady Leading-Edge Separation on a Pitching Airfoil. *AIAA Journal*, 32(4):673–681, 1994.
- ¹⁰M.R. Visbal. High-Fidelity Simulation of Transitional Flows past a Plunging Airfoil. *AIAA Journal*, 47(11):2685–2697, 2009.
- ¹¹M.R. Visbal. Numerical Investigation of Deep Dynamic Stall of a Plunging Airfoil. *AIAA Journal*, 49(10):2152–2170, 2011.
- ¹²D. J. Garmann and M. R. Visbal. Numerical Investigation of Transitional Flow Over a Rapidly Pitching Plate. *Physics of Fluids*, 23, 2011.
- ¹³M. V. Ol, L.P. Bernal, C-K Kang, and W. Shyy. Shallow and Deep Dynamic Stall for Flapping Low Reynolds Number Airfoils. *Experiments in Fluids*, 46:883–901, 2009.
- ¹⁴G. E. Torres and T. J. Mueller. Low-Aspect-Ratio Wing Aerodynamics at Low Reynolds Numbers. *AIAA Journal*, 42(5):865–873, 2004.
- ¹⁵P. Freymuth, F. Finaish, and W. Bank. Visualization of Wing Tip Vortices in Accelerating and Steady Flow. *Journal of Aircraft*, 23(9):730–733, 1986.
- ¹⁶P. Freymuth, F. Finaish, and W. Bank. The Wing Tip Vortex System in a Starting Flow. *ZFW*, 10(2):116–118, 1986.
- ¹⁷P. Freymuth. Visualizing the Connectivity of Vortex Systems for Pitching Wings. *Journal of Fluids Engineering*, 111(217), 1989.
- ¹⁸K. Von Ellenrieder, K. Parker, and J. Soria. Flow Structures Behind a Heaving and Pitching Finite-Span Wing. *Journal of Fluid Mechanics*, 490:129–138, 2003.
- ¹⁹Buchholz, J. and Smits, A. On the evolution of the wake structure produced by a low-aspect-ratio pitching panel. *Journal of Fluid Mechanics*, 546:433–443, 2006.
- ²⁰T.O. Yilmaz and D. Rockwell. Three-Dimensional Flow Structure on a Maneuvering Wing. *Experiments in Fluids*, 2009.
- ²¹T. Yilmaz, M. Ol, and D. Rockwell. Scaling of flow separation on a pitching low aspect ratio plate. *Journal of Fluids and Structures*, 26:1034–1041, 2010.
- ²²D. E. Calderon, Z. J. Wang, and I. Gursul. Effect of wing geometry on the lift of a plunging finite wing. *AIAA Paper 2010-4459*, June 2010.
- ²³T.O. Yilmaz and D. Rockwell. Flow Structure on Finite-Span Wings due to Pitch-up Motion. *Journal of Fluid Mechanics*, 691:518–545, 2011.
- ²⁴K. Granlund, M. V. Ol, and L.P. Bernal. Experiments on Pitching Plates: Force and Flowfield Measurements at low Reynolds Numbers. *AIAA Paper 2011-872*, January 2011.
- ²⁵D. E. Calderon, Z. J. Wang, I. Gursul, and M. R. Visbal. Volumetric measurements and simulations of the vortex structures generated by low aspect ratio plunging wings. *AIAA Paper 2012-0914*, January 2012.
- ²⁶P. Blondeaux, F. Fornarelli, L. Guglielmini, M. Triantafyllou, and R. Verzicco. Numerical Experiments on flapping foils mimicking fish-like locomotion. *Physics of Fluids*, 17(11), 2005.
- ²⁷H. Dong, R. Mittal, and F. Najjar. Wake Topology and Hydrodynamic Performance of Low-Aspect-ratio Flapping Foils. *Journal of Fluid Mechanics*, 566:309–343, 2006.

²⁸K. Taira and T. Colonius. Three-dimensional flows around low-aspect-ratio flat-plate wings at low reynolds numbers. *Journal of Fluid Mechanics*, 623:187–207, 2009.

²⁹K. Taira and T. Colonius. On the effect of tip vortices in low-reynolds-number post-stall flow control. *AIAA Paper 2009-376*, January 2009.

³⁰P. Trizila, C.-K. Kang, H. Aono, W. Shyy, and M. Visbal. Low-reynolds-number aerodynamics of a flapping rigid flat plate. *AIAA Journal*, 49(4):806–823, April 2011.

³¹M.R. Visbal. Three-Dimensional Flow Structure on a Heaving Low-Aspect-Ratio Wing. *AIAA Paper 2011-219*, January 2011.

³²M.R. Visbal and D.P. Rizzetta. Large-Eddy Simulation on Curvilinear Grids Using Compact Differencing and Filtering Schemes. *Journal of Fluids Engineering*, 124:836–847, 2002.

³³M.R. Visbal, P.E. Morgan, and D.P. Rizzetta. An Implicit LES Approach Based on High-Order Compact Differencing and Filtering Schemes. *AIAA Paper 2003-4098*, June 2003.

³⁴M. Vinokur. Conservation Equations of Gasdynamics in Curvilinear Coordinate Systems. *Journal of Computational Physics*, 14:105–125, 1974.

³⁵J.L. Steger. Implicit Finite-Difference Simulation of Flow about Arbitrary Two-Dimensional Geometries. *AIAA Journal*, 16(7):679–686, 1978.

³⁶D.A. Anderson, J.C. Tannehill, and R.H. Pletcher. *Computational Fluid Mechanics and Heat Transfer*. McGraw-Hill Book Company, 1984.

³⁷S. Stolz and N. Adams. An Approximate Deconvolution Procedure for Large-Eddy Simulation. *Physics of Fluids*, 11(7):1699–1701, 1999.

³⁸J. Mathew, R. Lechner, H. Foysi, J. Sesterhenn, and R. Friedrich. An explicit filtering method for LES of compressible flows. *Phys. Fluids*, 15(8):2279–2289, 2003.

³⁹M.R. Visbal and D.V. Gaitonde. High-Order Accurate Methods for Complex Unsteady Subsonic Flows. *AIAA Journal*, 37(10):1231–1239, 1999.

⁴⁰D.V. Gaitonde and M.R. Visbal. High-Order Schemes for Navier-Stokes Equations: Algorithm and Implementation into FDL3DI. Technical Report AFRL-VA-WP-TR-1998-3060, Air Force Research Laboratory, Wright-Patterson AFB, 1998.

⁴¹S.K. Lele. Compact Finite Difference Schemes with Spectral-like Resolution. *Journal of Computational Physics*, 103:16–42, 1992.

⁴²M.R. Visbal and D.V. Gaitonde. On the Use of High-Order Finite-Difference Schemes on Curvilinear and Deforming Meshes. *Journal of Computational Physics*, 181:155–185, 2002.

⁴³D.V. Gaitonde, J.S. Shang, and J.L. Young. Practical Aspects of Higher-Order Numerical Schemes for Wave Propagation Phenomena. *Int. Jnl. for Num. Methods in Eng.*, 45:1849–1869, 1999.

⁴⁴P. Alpert. Implicit Filtering in Conjunction with Explicit Filtering. *J. Comp. Phys.*, 44:212–219, 1981.

⁴⁵D.V. Gaitonde and M.R. Visbal. Further Development of a Navier-Stokes Solution Procedure Based on Higher-Order Formulas. *AIAA Paper 99-0557*, January 1999.

⁴⁶P.E. Morgan, M.R. Visbal, and D.P. Rizzetta. A Parallel High-Order Flow Solver for Large-Eddy and Direct Numerical Simulation. *AIAA Paper 2002-3123*, June 2002.

⁴⁷S. Sherer and M. Visbal. Implicit Large Eddy Simulations Using a High-Order Overset Grid Solver. *AIAA Paper 2004-2530*, June 2004.

⁴⁸M. Visbal and D. Gaitonde. Very High-Order Spatially Implicit Schemes for Computational Acoustics on Curvilinear Meshes. *J. Comp. Acoustics*, 9(4):1259–1286, 2001.

⁴⁹J. Eldredge, C. Wang, and M. Ol. A computational study of a canonical pitch-up, pitch-down maneuver. *AIAA Paper 2009-3687*, June 2009.

⁵⁰M. R. Visbal and D. J. Garmann. Flow structure above stationary and oscillating low-aspect-ratio wing. *Proceedings of the ASME 2012 Fluids Engineering Division Summer Meeting*, FEDSM2012-72405, July 2012.

⁵¹J. Jeong and F. Hussain. On the identification of a vortex. *J. Fluid Mech.*, 285:69–94, 1995.

⁵²D. J. Garmann, M. R. Visbal, and P. D. Orkwis. Numerical investigation of the three-dimensional flow structure about a revolving wing. *Proceedings of the ASME 2012 Fluids Engineering Division Summer Meeting*, FEDSM2012-72388, July 2012.

⁵³M.R. Visbal. Onset of Vortex Breakdown Above a Pitching Delta Wing. *AIAA J.*, 32(8), 1994.

⁵⁴M.R. Visbal. Dynamic Stall of a Constant-Rate Pitching Airfoil. *Journal of Aircraft*, 27(5):400–407, 1990.

⁵⁵M.R. Visbal and R.E. Gordnier. Pitch Rate and Pitch-Axis Location Effects on Vortex Breakdown Onset. *J. of Aircraft*, 32(5):929–935, Sep.-Oct. 1995.

⁵⁶E. J. Jumper, S. J. Shreck, and R. L. Dimmick. Lift-Curve Characteristics of an Airfoil Pitching at Constant Rate. *J. of Aircraft*, 24(10):680–687, Sep.-Oct. 1987.

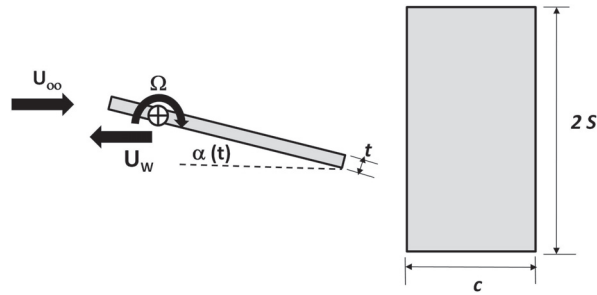


Figure 1. Pitching wing configuration

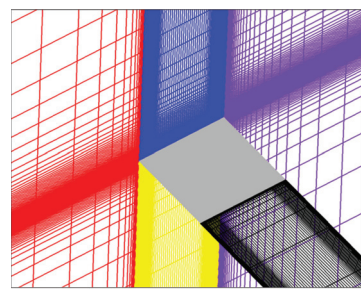


Figure 2. Overset mesh system

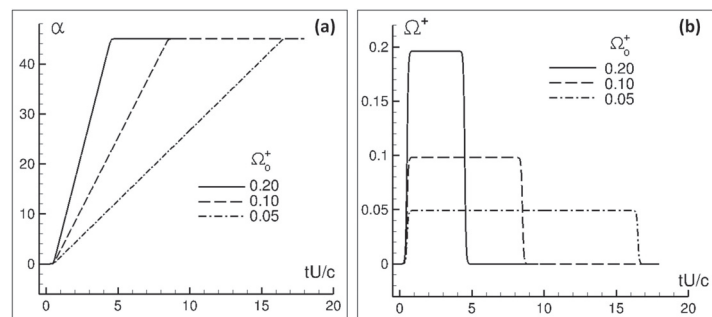


Figure 3. Pitching maneuver: (a) angle of attack and (b) pitch rate

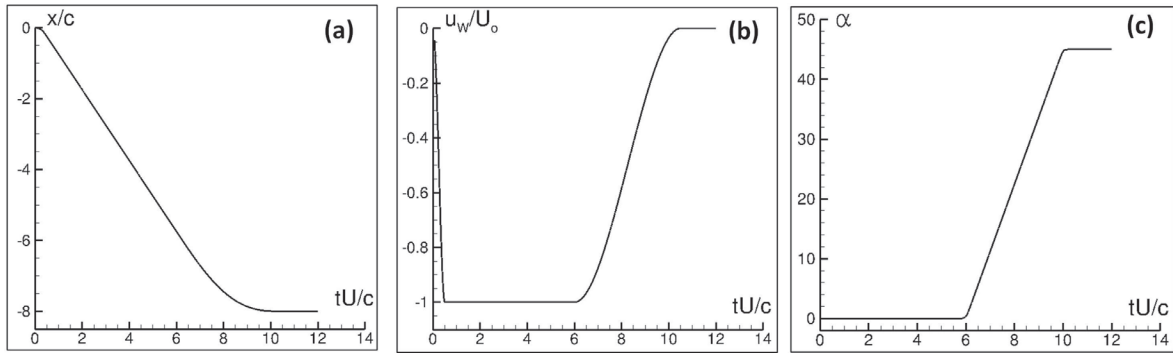


Figure 4. Perching maneuver with $\Omega_o^+ = 0.2$: (a) wing horizontal position, (b) translating velocity and (c) angle of attack

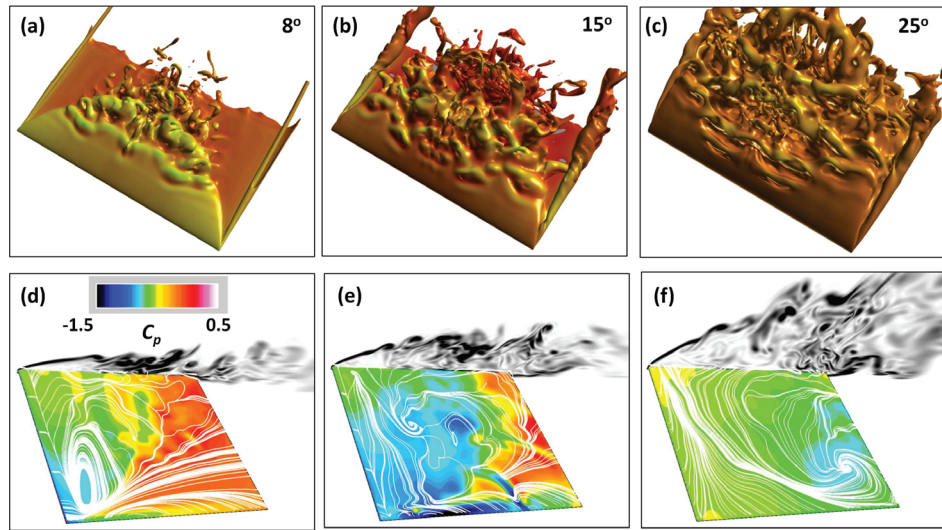


Figure 5. Instantaneous flow structure for stationary wing at $\alpha = 8^\circ, 15^\circ$ and 25° and $Re_c = 10^4$: (a)-(c) iso-surfaces of total pressure, and (d)-(f) surface pressure and vorticity magnitude on symmetry plane

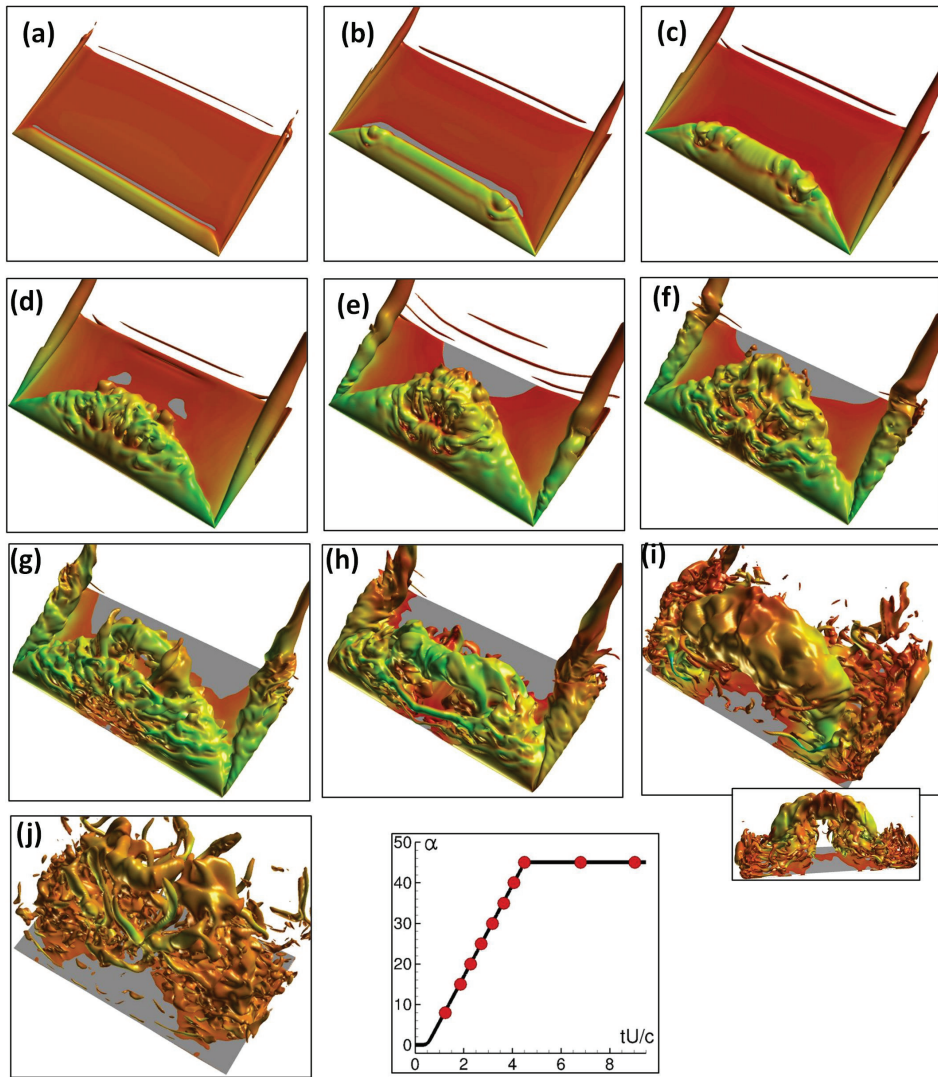


Figure 6. Instantaneous three-dimensional flow structure for pitching wing ($\Omega_o^+ = 0.2$, $Re_c = 10^4$) depicted by an iso-surface of total pressure: (a) 8° , (b) 15° , (c) 20° , (d) 25° , (e) 30° , (f) 35° , (g) 40° , (h) 45° , $t = 4.5$, (i) 45° , $t = 6.8$ (inset shows rear view) and (j) 45° , $t = 9.0$

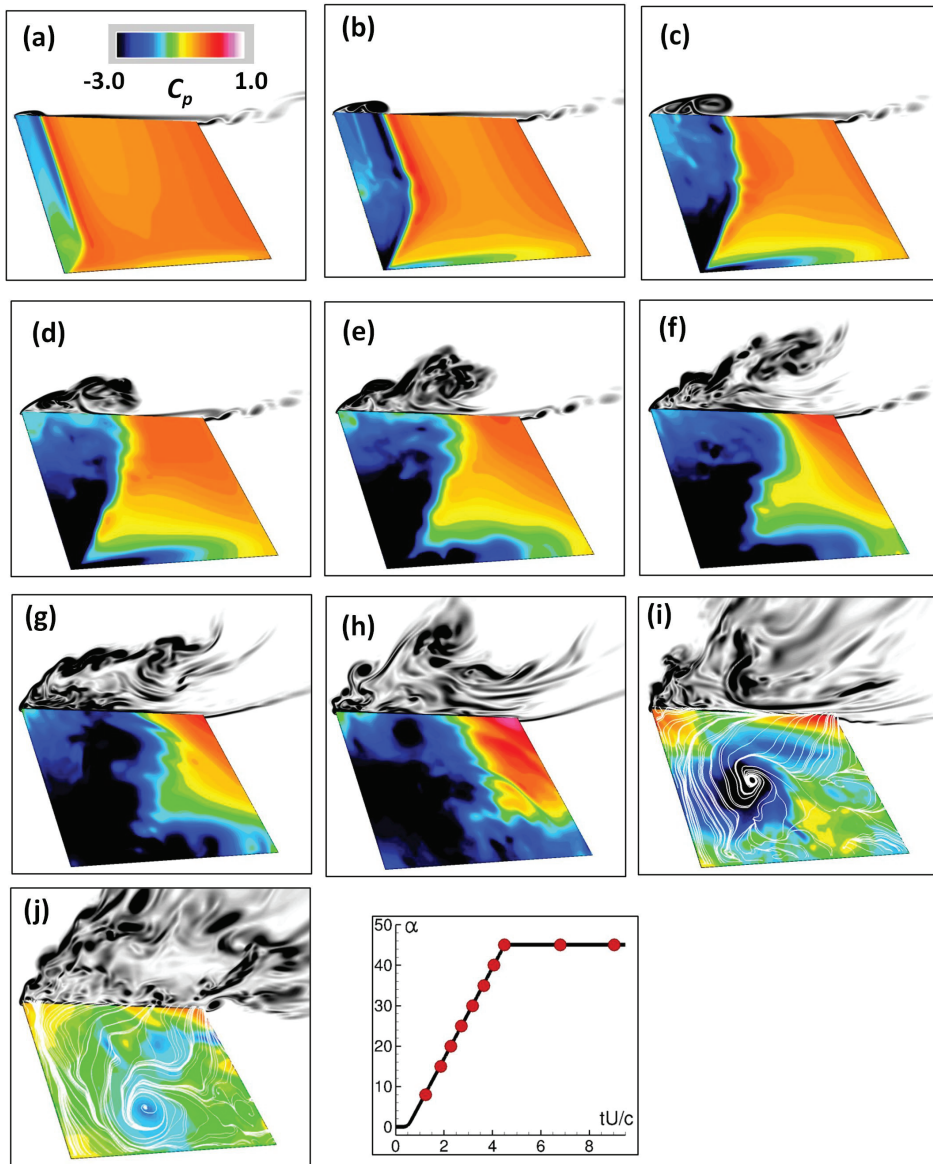


Figure 7. Instantaneous surface pressure and contours of vorticity magnitude on symmetry plane, $\Omega_o^+ = 0.2, Re_c = 10^4$: (a) 8° , (b) 15° , (c) 20° , (d) 25° , (e) 30° , (f) 35° , (g) 40° , (h) $45^\circ, t = 4.5$, (i) $45^\circ, t = 6.8$ and (j) $45^\circ, t = 9.0$

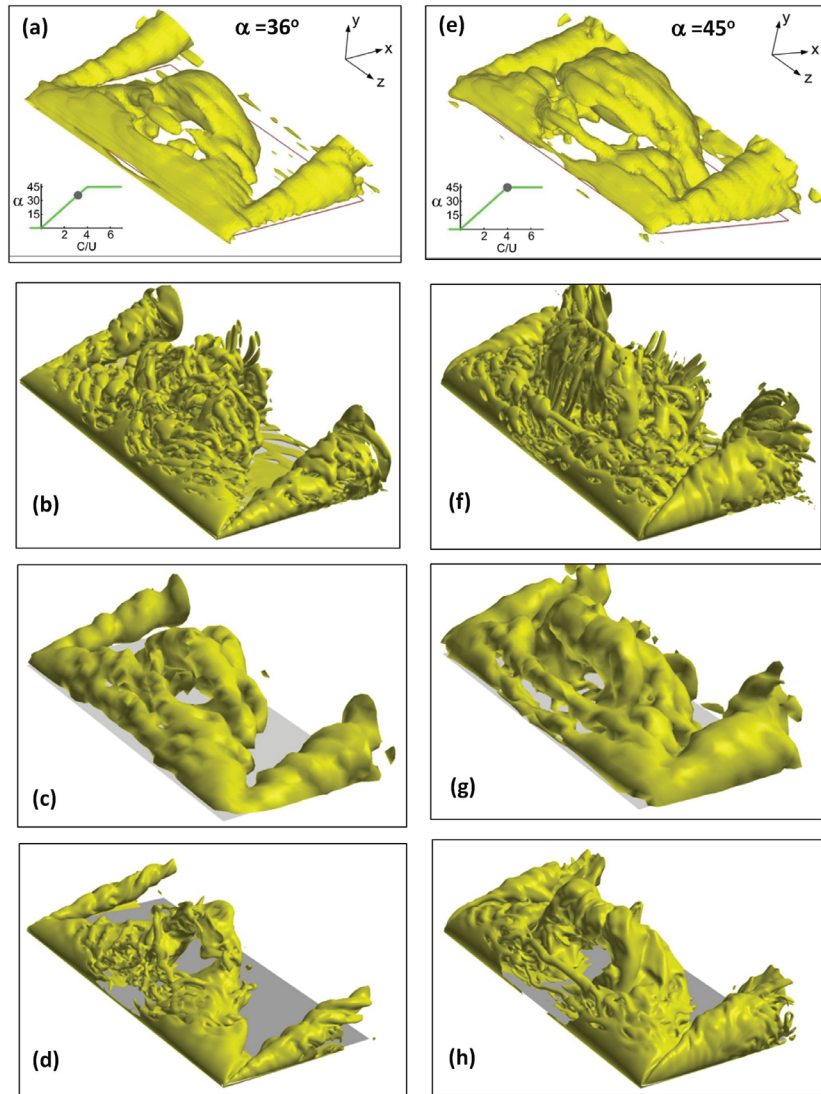


Figure 8. Comparison of computed and experimental²³ three-dimensional instantaneous flow structure for $Re_c = 10^4$ and $\Omega_o^+ = 0.2$. (a,e) experimental Q-criterion iso-surface, (b,f) computed Q-criterion iso-surface, (c,g) computed Q-criterion iso-surface for filtered computational data, and (d,h) computed total pressure iso-surface

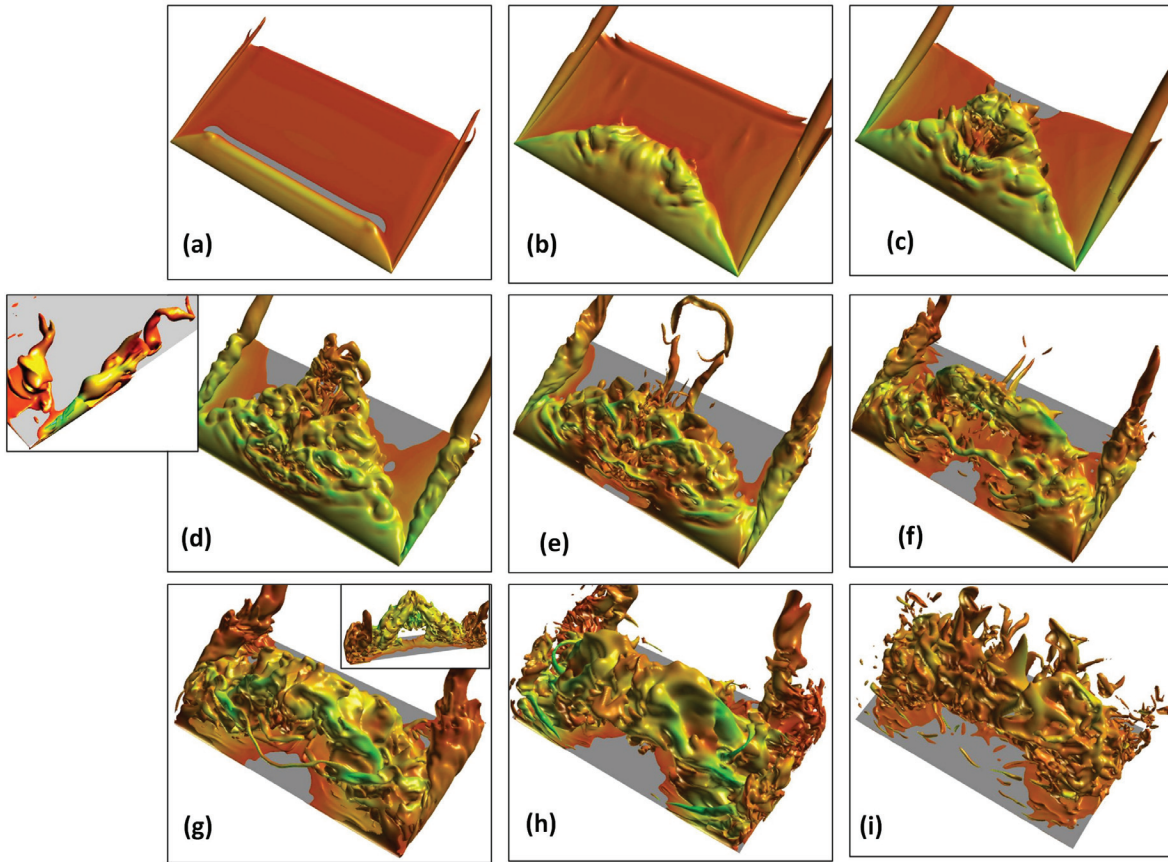


Figure 9. Instantaneous three-dimensional flow structure for pitching wing ($\Omega_o^+ = 0.1, Re_c = 10^4$) depicted by an iso-surface of total pressure: (a) 8° , (b) 15° , (c) 20° , (d) 25° (inset shows tip vortex breakdown), (e) 30° , (f) 35° , (g) 40° (inset shows rear view), (h) $45^\circ, t = 9.0$, and (i) $45^\circ, t = 12.0$

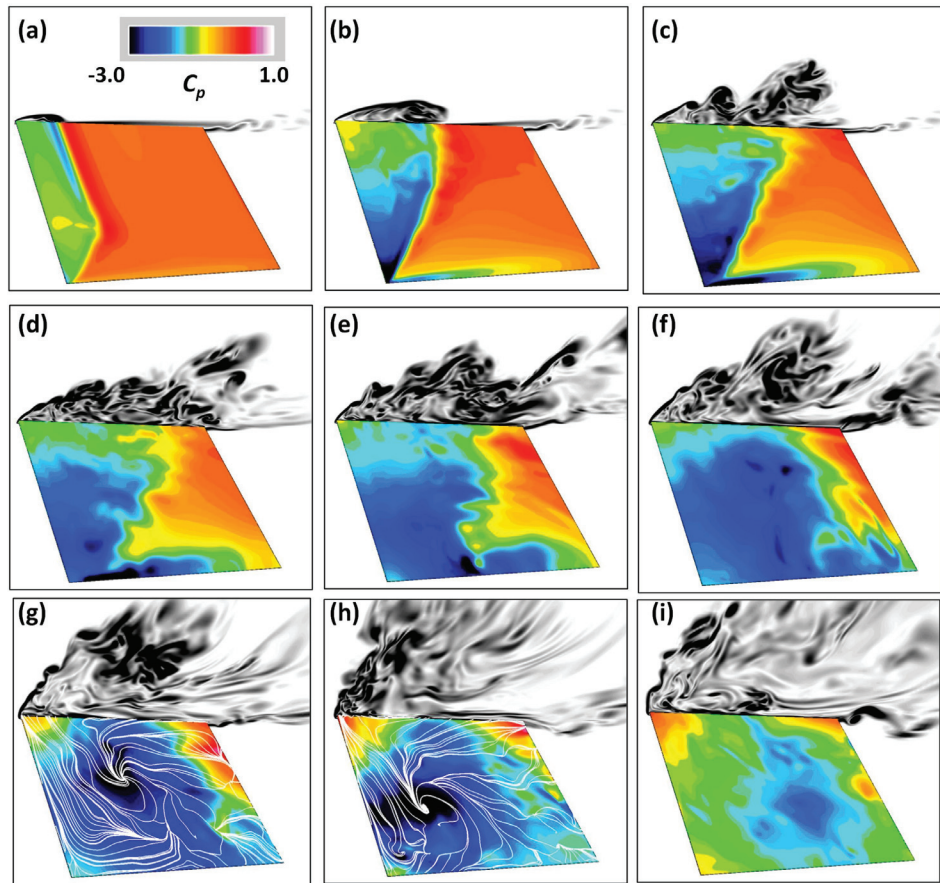


Figure 10. Instantaneous surface pressure and contours of vorticity magnitude on symmetry plane, $\Omega_o^+ = 0.1$, $Re_c = 10^4$: (a) 8° , (b) 15° , (c) 20° , (d) 25° , (e) 30° , (f) 35° , (g) 40° , (h) 45° , $t = 9.0$, and (i) 45° , $t = 12.0$

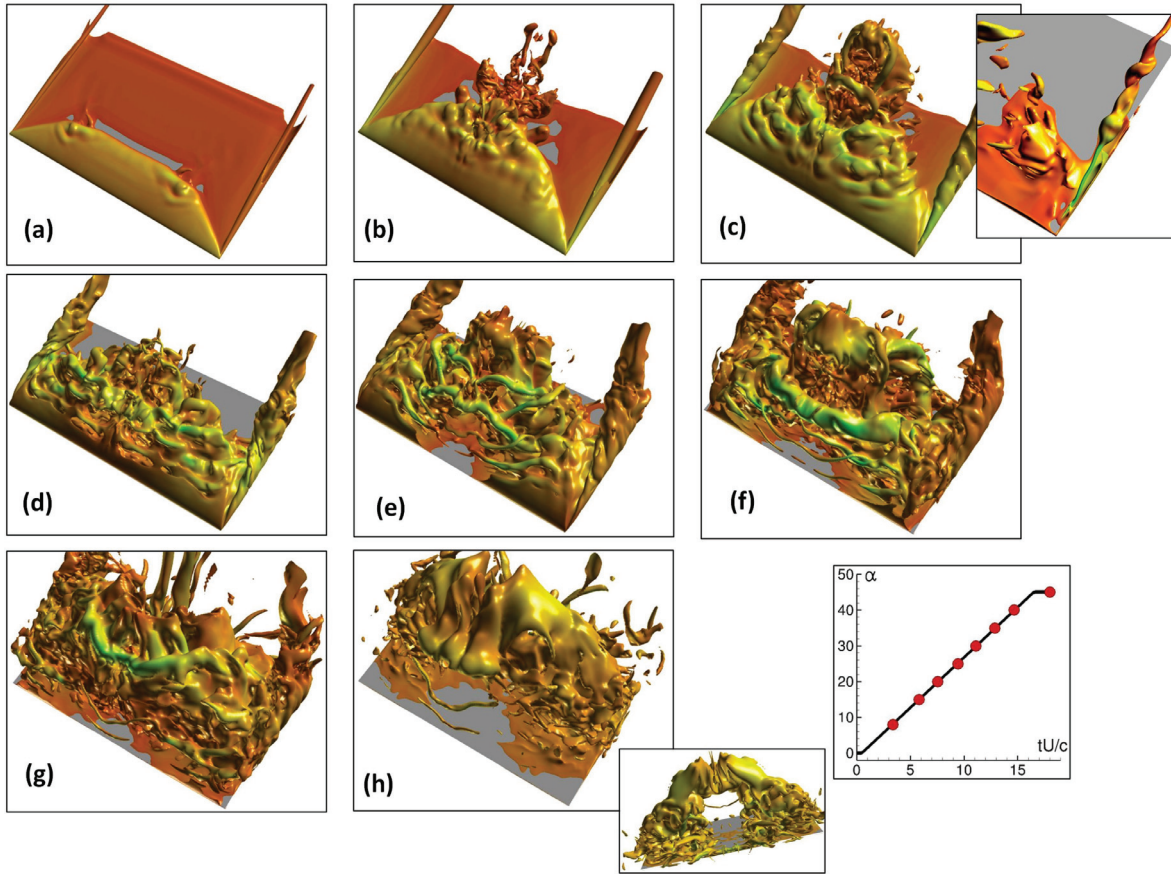


Figure 11. Instantaneous three-dimensional flow structure for pitching wing ($\Omega_o^+ = 0.05$, $Re_c = 10^4$) depicted by an iso-surface of total pressure: (a) 8° , (b) 15° , (c) 20° (inset shows tip vortex breakdown), (d) 25° , (e) 30° , (f) 35° , (g) 40° , and (h) 45° , $t = 9$ (inset shows rear view)

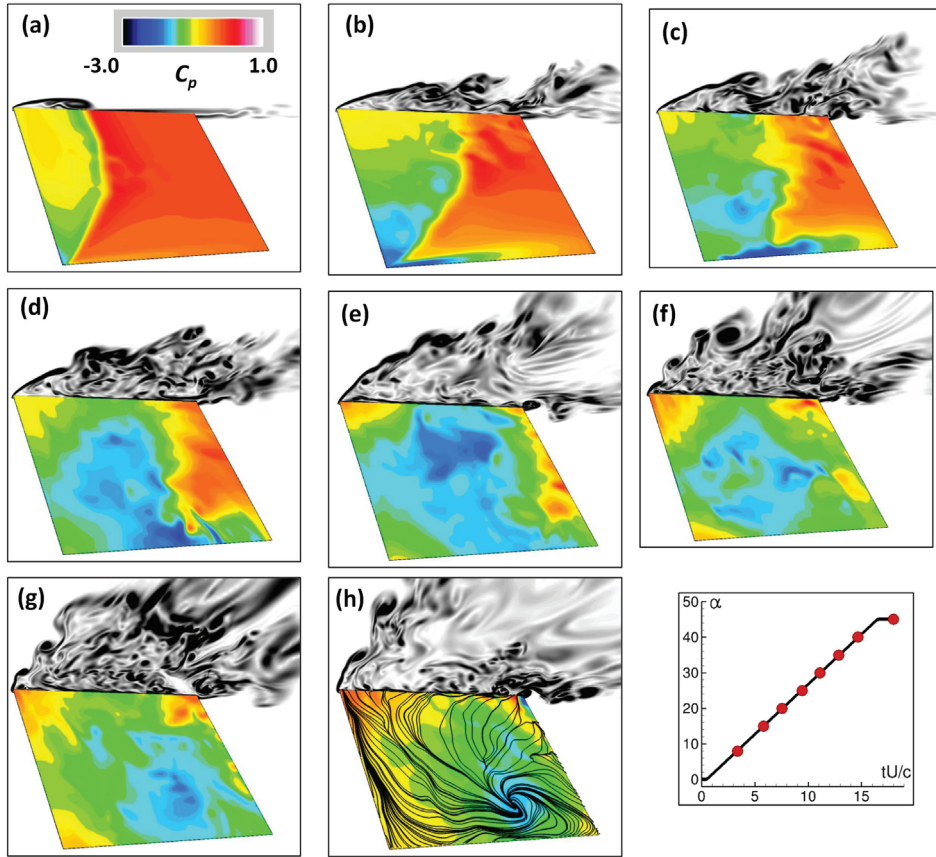


Figure 12. Instantaneous surface pressure and contours of vorticity magnitude on symmetry plane, $\Omega_o^+ = 0.05$, $Re_c = 10^4$: (a) 8° , (b) 15° , (c) 20° , (d) 25° , (e) 30° , (f) 35° , (g) 40° , and (h) 45° , $t = 18.0$

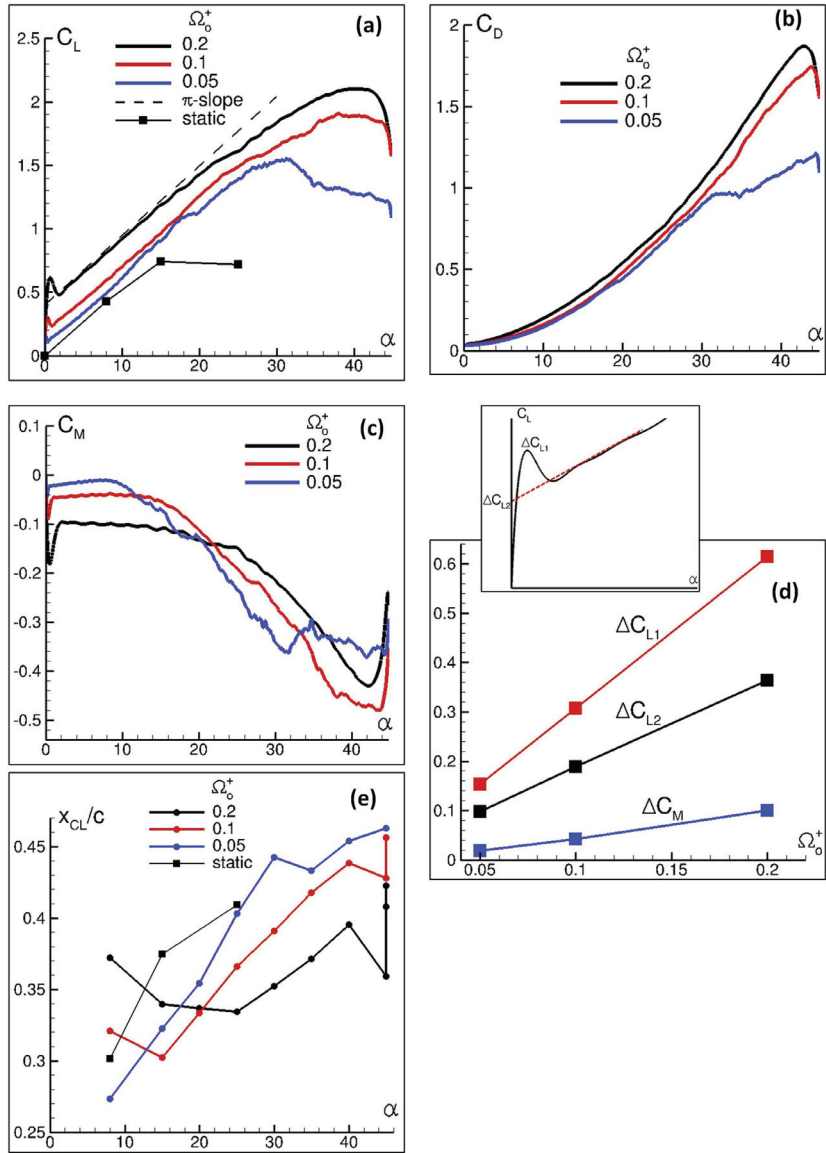


Figure 13. Effect of non-dimensional pitch rate on wing aerodynamic loading for $Re_c = 10^3$: (a-c) lift, drag and quarter-chord pitching moment coefficient histories, (d) offsets in C_L and C_M due to wing rotation and (e) chordwise position of center of lift

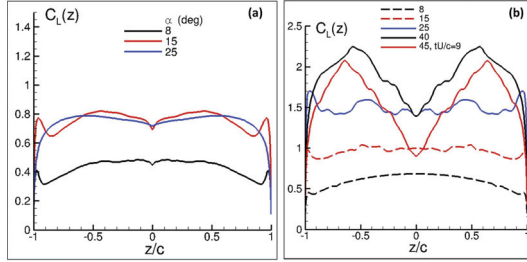


Figure 14. Spanwise distributions of sectional lift for (a) static and (b) pitching wing with $\Omega_o^+ = 0.1$. Note different vertical scales used in (a) and (b)

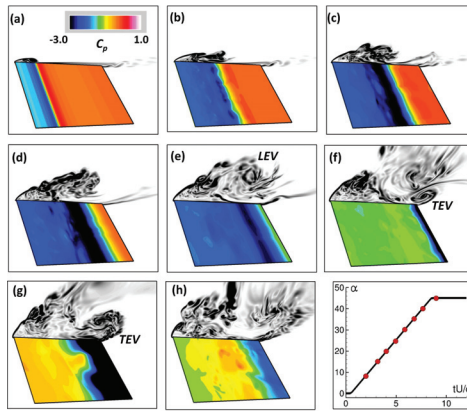


Figure 15. Instantaneous surface pressure and contours of vorticity magnitude on symmetry plane for pitching 2D (infinite aspect ratio) wing, $\Omega_o^+ = 0.1$, $Re_c = 10^4$

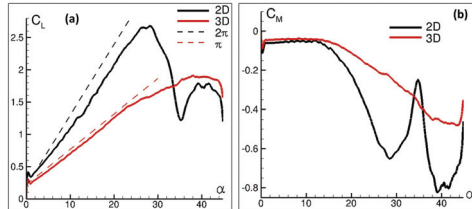


Figure 16. Comparison of (a) lift and (b) pitching moment coefficient histories for pitching 2D and low-aspect-ratio wings, $\Omega_o^+ = 0.1$, $Re_c = 10^4$

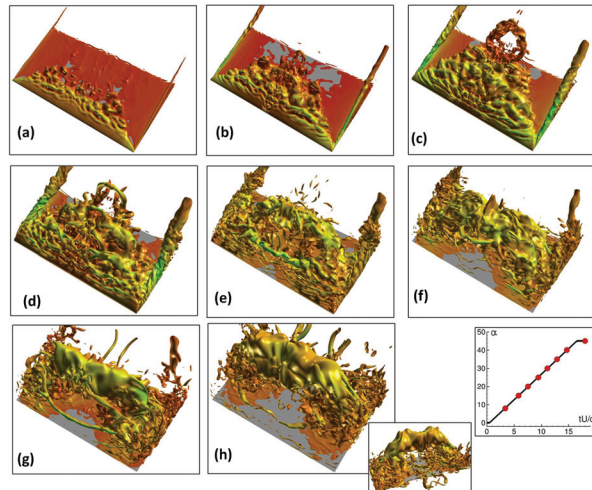


Figure 17. Instantaneous three-dimensional flow structure for pitching wing ($\Omega_o^+ = 0.05$, $Re_c = 4 \times 10^4$) depicted by an iso-surface of total pressure: (a) 8° , (b) 15° , (c) 20° , (d) 25° , (e) 30° , (f) 35° , (g) 40° , and (h) 45° , $t = 18.0$ (inset shows rear view)

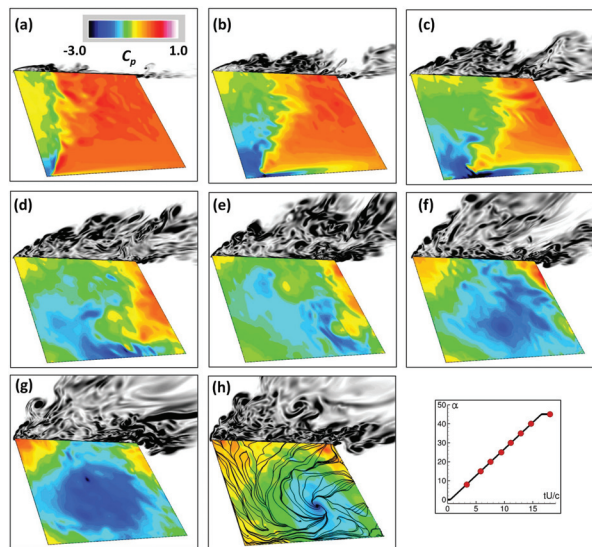


Figure 18. Instantaneous surface pressure and contours of vorticity magnitude on symmetry plane, $\Omega_o^+ = 0.05$, $Re_c = 4 \times 10^4$: (a) 8° , (b) 15° , (c) 20° , (d) 25° , (e) 30° , (f) 35° , (g) 40° , and (h) 45° , $t = 18.0$

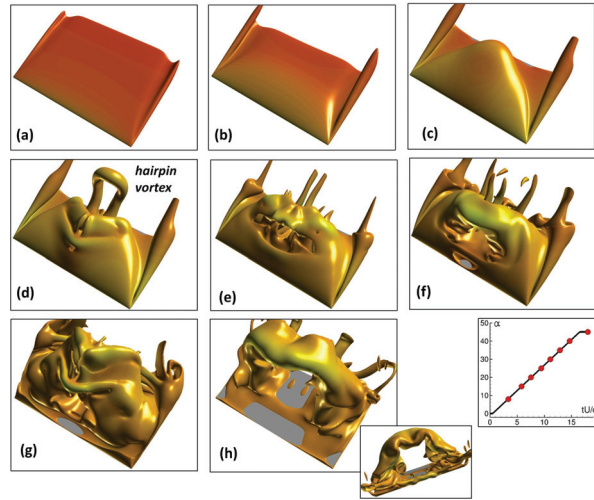


Figure 19. Instantaneous three-dimensional flow structure for pitching wing ($\Omega_o^+ = 0.05$, $Re_c = 10^3$) depicted by an iso-surface of total pressure: (a) 8° , (b) 15° , (c) 20° , (d) 25° , (e) 30° , (f) 35° , (g) 40° , and (h) 45° , $t = 18.0$ (inset shows rear view)

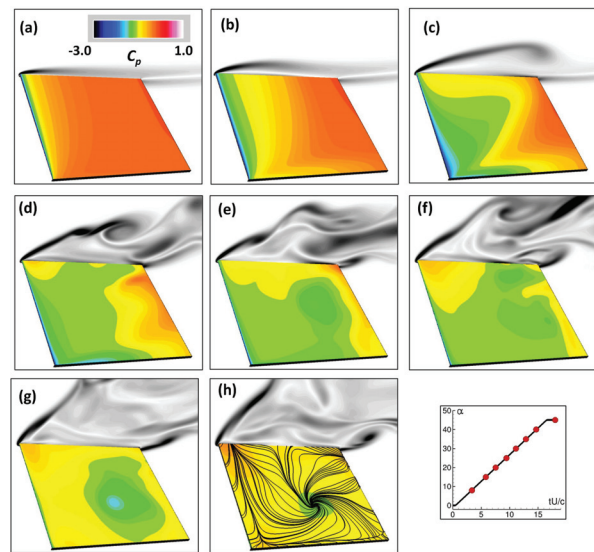


Figure 20. Instantaneous surface pressure and contours of vorticity magnitude on symmetry plane, $\Omega_o^+ = 0.05$, $Re_c = 10^3$: (a) 8° , (b) 15° , (c) 20° , (d) 25° , (e) 30° , (f) 35° , (g) 40° , and (h) 45° , $t = 18.0$

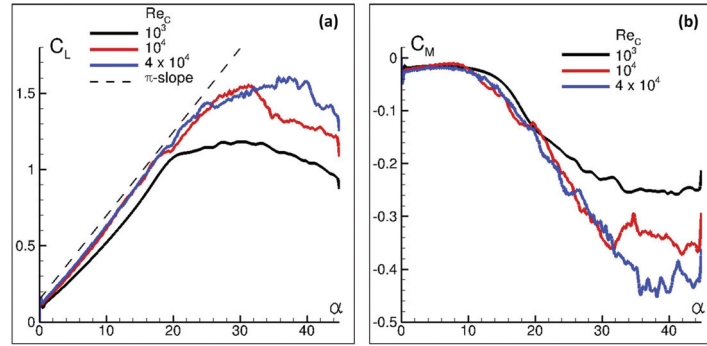


Figure 21. Effect of Reynolds number on (a) lift and (b) pitching moment coefficients, $\Omega_o^+ = 0.05$

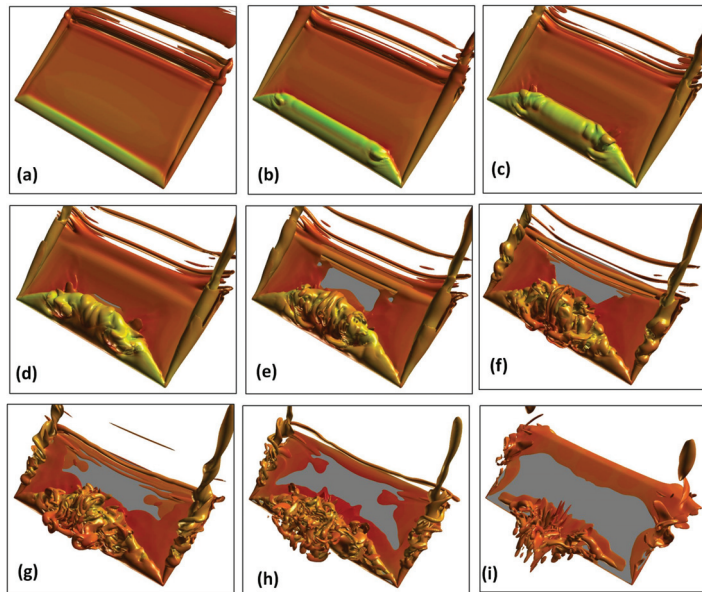


Figure 22. Instantaneous three-dimensional flow structure for perching wing ($\Omega_o^+ = 0.2$, $Re_C = 10^4$) depicted by an iso-surface of vorticity magnitude: (a) 8°, (b) 15°, (c) 20°, (d) 25°, (e) 30°, (f) 35°, (g) 40°, (h) 45°, $t = 4.5$, and (i) 45°, $t = 6.0$

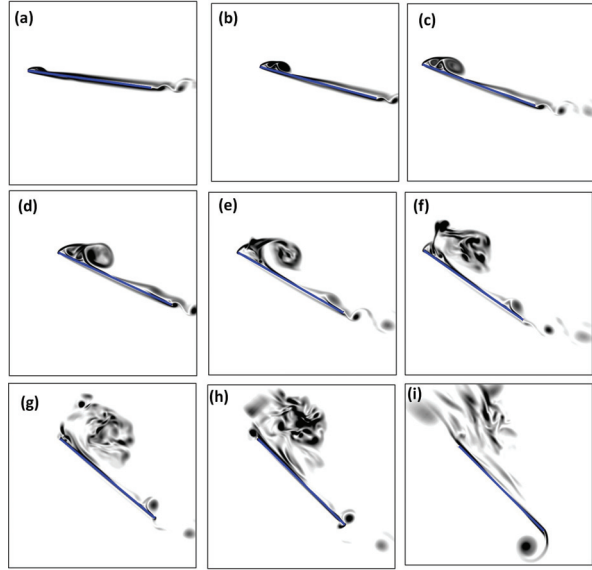


Figure 23. Contours of instantaneous vorticity magnitude on symmetry plane of perching wing ($\Omega_o^+ = 0.2, Re_c = 10^4$): (a) 8° , (b) 15° , (c) 20° , (d) 25° , (e) 30° , (f) 35° , (g) 40° , (h) $45^\circ, t = 4.5$, and (i) $45^\circ, t = 6.0$

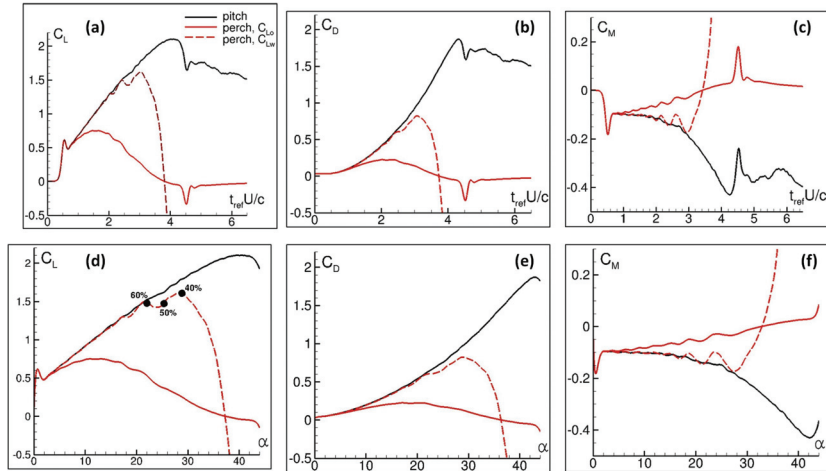


Figure 24. Comparison of aerodynamic loads for perching and pitching wing ($\Omega_o^+ = 0.2, Re_c = 10^4$) as function of time (a-c) and angle of attack (d-f). For perching case, loads are normalized relative to either U_o (solid line) or U_w (dashed line)

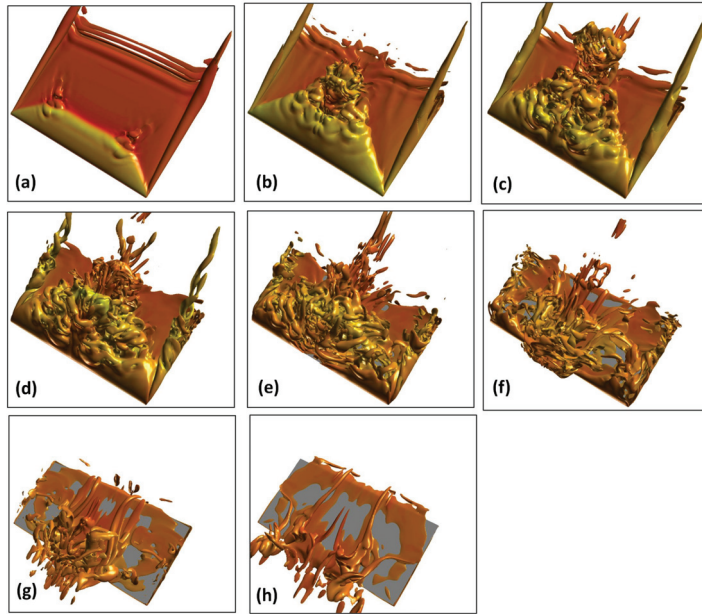


Figure 25. Instantaneous three-dimensional flow structure for perching wing ($\Omega_o^+ = 0.05, Re_c = 10^4$) depicted by an iso-surface of vorticity magnitude: (a) 8° , (b) 15° , (c) 20° , (d) 25° , (e) 30° , (f) 35° , (g) 40° , and (h) 45° , $t = 18.0$

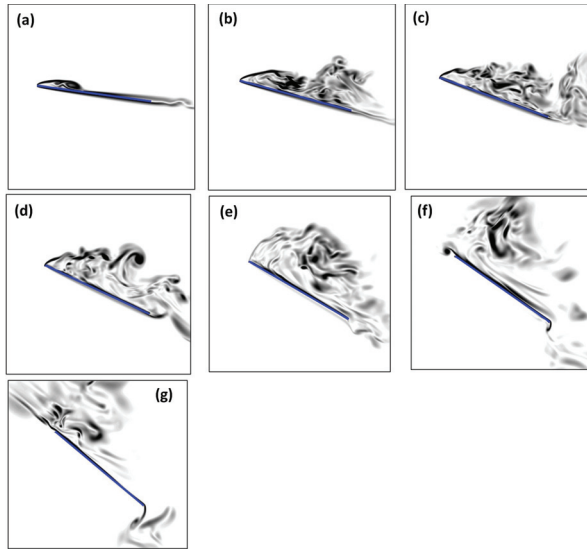


Figure 26. Contours of instantaneous vorticity magnitude on symmetry plane of perching wing ($\Omega_o^+ = 0.05, Re_c = 10^4$): (a) 8° , (b) 15° , (c) 20° , (d) 25° , (e) 30° , (f) 35° , and (g) 40°

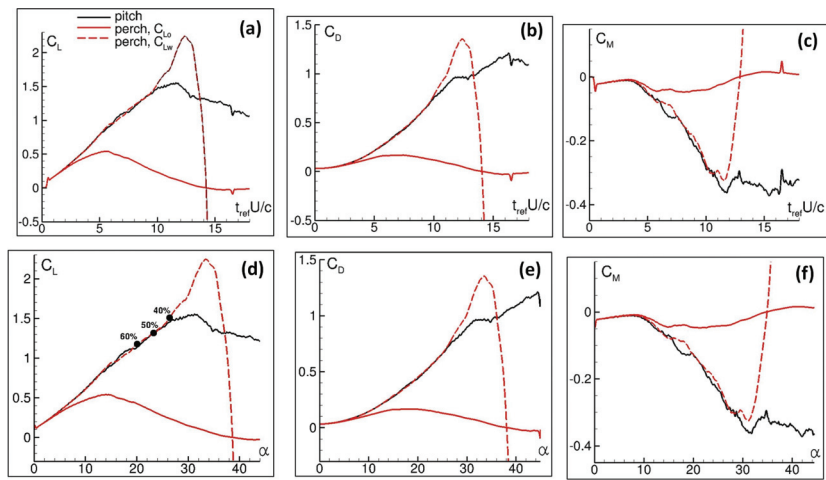


Figure 27. Comparison of aerodynamic loads for perching and pitching wing ($\Omega_o^+ = 0.05$, $Re_c = 10^4$) as function of time (a-c) and angle of attack (d-f). For perching case, loads are normalized relative to either U_o (solid line) or U_w (dashed line)

APPENDIX B

Aeroelastic Simulations of an Aspect Ratio Two Flexible Membrane Wing

Raymond E. Gordnier *

Air Force Research Laboratory, Wright-Patterson AFB, OH 45433-7512

Peter J. Attar †

University of Oklahoma, Norman, OK

Development of an aeroelastic solver with application to flexible membrane wings for micro air vehicles is presented. A high-order (up to 6th order) Navier-Stokes solver is coupled with a geometrically nonlinear p-version Reissner-Mindlin finite element plate model to simulate the highly flexible elastic membrane. An implicit LES approach is employed to compute the mixed laminar/transitional/turbulent flowfields present for the low Reynolds number flows associated with micro air vehicles. Computations are performed for an aspect ratio two membrane wing at an angle of attack, $\alpha = 16^\circ$ and a Reynolds number, $Re = 24,300$. Comparisons of the computational results with experimental PIV and surface deflection measurements demonstrated reasonable agreement. Reduced separation and enhanced lift are obtained due to favorable interactions between the flexible membrane wing and the unsteady flow over the wing. The impact of flexibility on the aerodynamic performance comes primarily from the development of mean camber with some further effects arising from the interaction between the dynamic motion of the membrane and the unsteady flowfield above.

I. Introduction

In order to address the technical challenges associated with MAV development, designers are looking to biological flight for inspiration. Successful development of these biomimetic MAV concepts will require significant advancements in the fundamental understanding of the unsteady aerodynamics of low Reynolds number fliers and the associated fluid-structure interactions. The inherent flexibility in the structural design of lightweight MAVs and the exploitation of that flexibility creates strong coupling between the unsteady fluid dynamics and the airframe structural response giving rise to tightly integrated, multidisciplinary physics. Conventional simplified analytical techniques and empirical design methods, although attractive for their efficiency, may have limited applicability for these complicated, multidisciplinary design problems. Critical insight into the highly complex, coupled MAV physics calls for the exploitation of advanced multidisciplinary computational techniques.

Previous computations for membrane wing applications¹⁻³ have coupled a low-order (2nd order) Navier-Stokes solver with a membrane finite element model based on a hyperelastic Moody-Rivlin model. Computations were performed for a membrane wing with a leading edge spar, rigid centerbody and rigid battens. Persson et al⁴ have coupled a Discontinuous Galerkin method for the Navier-Stokes equations with a hyperelastic Neo-Hookean model for the membrane. They presented simulations for a two-dimensional flexible membrane wing at static angles of attack and undergoing dynamic motion.

The present authors have carried out computations for a flexible membrane airfoil section in References 5 and 6. An implicit LES approach⁷ is employed to compute the mixed laminar/transitional/turbulent flowfields present for the low Reynolds number flows associated with micro air vehicles. The ILES approach exploits the properties of a well validated, robust, sixth-order Navier-Stokes solver.⁸⁻¹⁰ This aerodynamic solver is coupled with a finite element membrane structural model¹¹ suitable for the highly nonlinear structural response associated with a flexible membrane airfoil.

*Senior Research Aerospace Engineer, Computational Sciences Branch, Air Vehicles Directorate, Associate Fellow, AIAA

†Assistant Professor, Department of Mechanical and Aerospace Engineering, Member, AIAA

The focus of this paper will be the simulation and analysis of aeroscience issues associated with an aspect-ratio two flexible membrane wing fixed on all edges. The specific case to be considered corresponds to the experiments of Rojratsirikul, Wang and Gursul.^{12,13} In these experiments a digital image correlation system was used to measure membrane displacements accompanied by PIV measurements of the unsteady flow. Previous computations⁵ and experiments^{14,15} have shown the impact of both mean camber and the dynamic motion of the membrane on the performance of a two-dimensional membrane airfoil. At lower angles of attack the mean camber developed by the membrane airfoil provides for improved airfoil performance and a delay in airfoil stall. At higher angles of attack the dynamic motion of the membrane surface significantly alters the unsteady, separated flow over the membrane airfoil providing an additional enhancement to the airfoil performance. Similar investigations will be performed for the aspect ratio two wing in this work to determine if these favorable fluid-structure interactions remain.

II. Aerodynamic Solver

Governing Equations

The governing equations are the three-dimensional, compressible Navier-Stokes equations. These equations are cast in strong conservative form introducing a general time-dependent curvilinear coordinate transformation $(x, y, z, t) \rightarrow (\xi, \eta, \zeta, \tau)$. In vector notation, and employing non-dimensional variables, the equations are:

$$\frac{\partial}{\partial \tau} \left(\frac{\vec{U}}{J} \right) + \frac{\partial \hat{F}}{\partial \xi} + \frac{\partial \hat{G}}{\partial \eta} + \frac{\partial \hat{H}}{\partial \zeta} = \frac{1}{Re} \left[\frac{\partial \hat{F}_v}{\partial \xi} + \frac{\partial \hat{G}_v}{\partial \eta} + \frac{\partial \hat{H}_v}{\partial \zeta} \right] \quad (1)$$

Here $\vec{U} = \{\rho, \rho u, \rho v, \rho w, \rho E\}$ denotes the solution vector and J is the transformation Jacobian. The inviscid and viscous fluxes, $\hat{F}, \hat{G}, \hat{H}, \hat{F}_v, \hat{G}_v, \hat{H}_v$ can be found, for instance, in Reference 16. The system of equations is closed using the perfect gas law $p = \rho T / \gamma M_\infty^2$, Sutherland's formula for viscosity, and the assumption of a constant Prandtl number, $Pr = 0.72$. In the expressions above, u, v, w are the Cartesian velocity components, ρ the density, p the pressure, and T the temperature. All flow variables have been normalized by their respective freestream values except for pressure which has been nondimensionalized by $\rho_\infty u_\infty^2$.

Spatial Discretization

A finite-difference approach is employed to discretize the flow equations. For any scalar quantity, ϕ , such as a metric, flux component or flow variable, the spatial derivative ϕ' along a coordinate line in the transformed plane is obtained by solving the tridiagonal system:

$$\alpha \phi'_{i-1} + \phi'_i + \alpha \phi'_{i+1} = b \frac{\phi_{i+2} - \phi_{i-2}}{4} + a \frac{\phi_{i+1} - \phi_{i-1}}{2} \quad (2)$$

where $\alpha = \frac{1}{3}$, $a = \frac{14}{9}$ and $b = \frac{1}{9}$. This choice of coefficients yields at interior points the compact five-point, sixth-order algorithm of Lele.¹⁷ At boundary points 1, 2, $IL - 1$ and IL , fourth- and fifth-order one-sided formulas are utilized which retain the tridiagonal form of the interior scheme.^{8,18}

Compact-difference discretizations, like other centered schemes, are non-dissipative and are therefore susceptible to numerical instabilities due to the growth of spurious high-frequency modes. These difficulties originate from several sources including mesh non-uniformity, approximate boundary conditions and nonlinear flow features. In order to ensure long-term numerical stability, while retaining the improved accuracy of the spatial compact discretization, a high-order implicit filtering technique^{10,19} is incorporated. If a component of the solution vector is denoted by ϕ , filtered values $\hat{\phi}$ are obtained by solving the tridiagonal system,

$$\alpha_f \hat{\phi}_{i-1} + \hat{\phi}_i + \alpha_f \hat{\phi}_{i+1} = \sum_{n=0}^N \frac{a_n}{2} (\phi_{i+n} + \phi_{i-n}) \quad (3)$$

Equation 3 is based on templates proposed in Refs. 17 and 20, and with proper choice of coefficients, provides a $2N$ th-order formula on a $2N + 1$ point stencil. The coefficients, a_0, a_1, \dots, a_N , derived in terms of the single parameter α_f using Taylor- and Fourier-series analyses, are given in Ref. 8, along with detailed spectral filter responses. In the present study, an eighth-order filter operator with $\alpha_f = 0.3$ is applied at interior points. For near-boundary points, the filtering strategies described in Refs. 10 and 9 are employed. Filtering is applied to the conserved variables, and sequentially in each coordinate direction.

Time Integration

For wall-bounded viscous flows, the stability constraint of explicit time-marching schemes is too restrictive and the use of an implicit approach becomes necessary. For this purpose, the implicit approximately-factored scheme of Beam and Warming²¹ is incorporated and augmented through the use of Newton-like subiterations in order to achieve second-order temporal and sixth-order spatial accuracy. In delta form, the scheme may be written as

$$\begin{aligned} & \left[J^{-1^{p+1}} + \phi^i \Delta \tau \delta_\xi^{(2)} \left(\frac{\partial \hat{F}^p}{\partial U} - \frac{1}{Re} \frac{\partial \hat{F}^p}{\partial U} \right) \right] J^{p+1} \times \left[J^{-1^{p+1}} + \phi^i \Delta \tau \delta_\eta^{(2)} \left(\frac{\partial \hat{G}^p}{\partial U} - \frac{1}{Re} \frac{\partial \hat{G}_v^p}{\partial U} \right) \right] J^{p+1} \times \\ & \left[J^{-1^{p+1}} + \phi^i \Delta \tau \delta_\zeta^{(2)} \left(\frac{\partial \hat{H}^p}{\partial U} - \frac{1}{Re} \frac{\partial \hat{H}_v^p}{\partial U} \right) \right] \Delta U = -\phi^i \Delta \tau \left[J^{-1^{p+1}} \frac{(1+\phi)U^p - (1+2\phi)U^n + \phi U^{n-1}}{\Delta \tau} \right. \\ & \left. + U^p (1/J)_\tau^p + \delta_\xi \left(\hat{F}^p - \frac{1}{Re} \hat{F}_v^p \right) + \delta_\eta \left(\hat{G}^p - \frac{1}{Re} \hat{G}_v^p \right) + \delta_\zeta \left(\hat{H}^p - \frac{1}{Re} \hat{H}_v^p \right) \right] \end{aligned} \quad (4)$$

where

$$\phi^i = \frac{1}{1 + \phi}, \quad \Delta U = U^{p+1} - U^p. \quad (5)$$

For the first subiteration, $p = 1$, $U^p = U^n$ and as $p \rightarrow \infty$, $U^p \rightarrow U^{n+1}$. The spatial derivatives in the implicit (left-hand-side) operators are represented using standard second-order centered approximations whereas high-order discretizations are employed for the explicit terms (right-hand side). Although not shown in Eqn. 4, nonlinear artificial dissipation terms^{22,23} are appended to the implicit operator to enhance stability. In addition, for improved efficiency, the approximately-factored scheme is recast in diagonalized form.²⁴ Any degradation in solution accuracy caused by the second-order implicit operators, artificial dissipation and the diagonal form are eliminated through the use of subiterations. Typically, two to three subiterations are applied per time step.

Implicit Large Eddy Simulation Methodology

The ILES method to be used in the present computations was first proposed and investigated by Visbal et al.⁷ The underlying idea behind the approach is to capture with high accuracy the resolved part of the turbulent scales while providing for a smooth regularization procedure to dissipate energy at the represented but poorly resolved high wavenumbers of the mesh. In the present computational procedure the 6th-order compact difference scheme provides the high accuracy while the low-pass spatial filters provide the regularization of the unresolved scales. All this is accomplished with no additional sub-grid scale models as in traditional LES approaches. An attractive feature of this filtering ILES approach is that the governing equations and numerical procedure remain the same in all regions of the flow. In addition, the ILES method requires approximately half the computational resources of a standard dynamic Smagorinsky sub-grid scale LES model. This results in a scheme capable of capturing with high-order accuracy the resolved part of the turbulent scales in an extremely efficient and flexible manner.

Boundary Conditions

The boundary conditions for the flow domain are prescribed as follows. At the solid surface, the no slip condition is applied, requiring that the fluid velocity at the wing surface match the surface velocity. In addition, the adiabatic wall condition, $\frac{\partial T}{\partial n} = 0$, and the normal pressure gradient condition $\frac{\partial p}{\partial n} = 0$ are specified. Along the O-grid cut spatial periodicity is imposed by means of a grid overlap region.

The treatment of the farfield boundaries is based on the approach proposed and evaluated previously in Reference 25 for some acoustic benchmark problems. This method exploits the properties of the high-order, low-pass filter in conjunction with a rapidly stretched mesh. As grid spacing increases away from the region of interest, energy not supported by the stretched mesh is reflected in the form of high-frequency modes which are annihilated by the discriminating spatial filter operator. An effective “buffer” zone is therefore created using a few grid points in each coordinate direction to rapidly stretch to the farfield boundary. No further need for the explicit incorporation of complicated boundary conditions or modifications to the governing equations is then required. Freestream conditions are specified along the inflow portion of the farfield boundary, while simple extrapolation of all variables is used on the outflow and side boundaries.

Structural Dynamics Solver

Structural modeling of the elastic membrane will be accomplished using a geometrically nonlinear p-version mixed Reissner-Mindlin plate element. The kinematical assumptions for this model are based on Mindlin's hypothesis that fibers normal to the middle plane of the plate remain straight and do not change length. The kinematic description of the plate deflections (u, v , and w in the x, y and z directions respectively) is given by:

$$\begin{aligned} u &= \hat{u} + z\left(\theta - \frac{1}{6}(\theta^3 + \theta\psi^2)\right) \\ v &= \hat{v} + z\left(\psi - \frac{1}{6}(\theta^2\psi + \psi^3)\right) \\ w &= \hat{w} - \frac{1}{2}z(\theta^2 + \psi^2) \end{aligned} \quad (6)$$

where θ and ψ are rotations of fibers orthogonal to the mid-plane and \hat{u} , \hat{v} , and \hat{w} are the components of the mid-plane deflection vector u_m . Applying Hamilton's principle a variational statement for the problem may be developed with the result being written as follows:

$$\begin{aligned} \int_{t_0}^{t_1} \left[\int_{\Omega} \left(\rho h \delta u_m^T \ddot{u}_m + I_{\rho} \delta \Lambda^T \ddot{\Lambda} + \delta \epsilon^T N + \delta Q^T C_s^{-1} Q + \delta Q^T \gamma^T + \delta \gamma^T Q \right) d\Omega \right] dt = \int_{t_0}^{t_1} \left[\int_{\Omega} \left(h \delta u_m^T b + \delta u_m^T \Phi + z \delta \Lambda^T \Phi - \delta u_m^T h c \dot{u}_m - \delta \Lambda^T \frac{ch^3}{12} \dot{\Lambda} \right) d\Omega + \delta D^T F \right] dt \end{aligned} \quad (7)$$

where $\Lambda = [\theta, \psi, 0]^T$, Φ are the nonconservative surface tractions, b the body loads, F the prescribed concentrated forces with D the corresponding displacements. Q , N and M are the shear, membrane and bending stress resultant vectors. In the present formulation a linear isotropic material is assumed providing a linear relationship between the stress resultants and the strain vectors. A mixed finite element approach to solve the variational problem is developed where hierarchical shape functions of Szabó and Babuška²⁶ are used to interpolate the displacements and rotations and Legendre polynomials are used to interpolate the shear stress variables. The resulting discrete equations are integrated in time using a Newmark acceleration method with the resulting linear equations set being solved using a parallel multifrontal solver in conjunction with a Newton-Raphson predictor-corrector algorithm. A detailed description of the development of this technique may be found in Reference 11.

III. Aerodynamic/Structural Coupling

Coupling of the aerodynamics with the membrane response occurs through the external loads Φ , and by the resulting deflection of the membrane, which is returned to the aerodynamic grid. Interpolation between the aerodynamic and structural meshes is accomplished using the finite element shape functions. Bilinear shape functions are used for this interpolation in the present implementation. In the present computations a one-to-one match is used between the structural and fluid meshes, however.

When solving fluid/structure interactions, the aerodynamic mesh must be allowed to move in accordance with the motion of the structural surface. A simple algebraic method described in Ref. 27 deforms the aerodynamic mesh to accommodate the changing membrane surface position. This grid motion strategy has proved adequate for the membrane motions considered in the present work.

Implicit coupling of these two sets of equations is achieved by a global subiteration strategy. During each subiteration the aerodynamic forces in the membrane equations are updated and the new surface displacements are provided to the aerodynamic solver. Using this approach the temporal lag between the aerodynamic and membrane equations may be eliminated and a complete synchronization of the aerodynamic/structural equation set is achieved. Any factorization or linearization errors introduced in the equations may also be eliminated using this global subiteration procedure. The resulting coupled procedure retains second order temporal accuracy.

IV. Results

The membrane wing to be studied is based on the experimental model of Rojratsirikul et al.¹³ Figure 1. The wing tested was rectangular with an aspect ratio, $AR = 2$. The wing consisted of a rigid frame with an airfoil shaped cross section made from stainless steel and was covered with an attached membrane sheet of latex rubber. The latex sheet had a thickness of $t = 0.2\text{mm}$, Young's modulus of 2.2MPa , and a density, $\rho_m = 1\text{gr/cm}^3$.

A set of 7 overset meshes was used to develop the computational grid around the membrane wing, Figure 2. The main grid consists of an o-mesh with 339 points around the wing in the chordwise direction, 228 points in the spanwise direction, and 151 points normal to the wing. The nominal spacing in the chordwise and spanwise directions is $\Delta x = 0.01$ and $\Delta y = 0.01$ respectively, with appropriate refinement near the leading and trailing edges and wing tips. The initial spacing normal to the surface is $\Delta z = 0.0001$. Cap meshes at the wing tips are used to resolve the wing tip structure. Four additional meshes are then employed to extend the grids to the spanwise boundaries. The total number of grid points employed is 17,638,228. These seven initial meshes are further subdivided into 199 grids to facilitate parallel processing.

The experiments were performed over an angle of attack range from $\alpha = 0$ to 25 degrees and for freestream velocities of $U_\infty = 5, 7.5$ and 10 m/s which corresponds to Reynolds numbers based on chord length of $Re = 24,300, 36,500$, and $48,700$ respectively. Computations for the lowest speed, $U_\infty = 5\text{ m/s}$, and an angle of attack $\alpha = 16^\circ$, are carried out in the present work.

Comparison with Experiment

Figures 3a,b compare the computed results for $\alpha = 16^\circ$ with corresponding experimental PIV measurements¹³ in the mid-span plane of the wing. For this comparison the experimental geometry was a rigid flat-plate wing with leading- and trailing-edges rounded to match the experimental membrane wing. In the computations the rigid geometry is the actual experimental membrane wing geometry with the membrane fixed in a flat position. Figure 3a compares the mean in-plane velocity magnitude. The overall qualitative agreement between the computations and experiment is quite good. The experimental measurements do exhibit a slightly larger separated flow as indicated by the greater extent of the low velocity flow region. Figure 3b displays the computed and measured turbulence intensity. A strong band of turbulence intensity associated with the separated shear layer is noted. The experiment and computations both show the same character but higher levels of turbulence intensity are measured in the experiment, particularly further downstream.

In Figures 4a,b similar comparisons are made for the flexible membrane wing. Figure 4a portrays the mean in-plane velocity on the mid-plane of the wing. The overall agreement between the experiment and computation in this case is again quite good. The comparison of the turbulence intensities is also reasonable albeit with the computations exhibiting a somewhat broader region of high turbulence intensity with the peak levels diminishing further downstream.

Figure 5a plots the maximum mean deflection of the membrane surface for the computation and experiment. The computations underpredict the maximum mean deflection measured in the experiment. The computed mean deflection is primarily in the first mode, Fig. 5b and is symmetric about the mid-plane. The location of maximum deflection occurs on the centerline of the wing and is slightly forward of the mid-chord at $x/c = 0.425$. These observations are consistent with the character of the experimental mean membrane deflection.¹³

Mean Flow Structure

In this section the impact of membrane flexibility on the mean flow structure over the wing is investigated. Previous computations⁵ and experiments^{14,15} have shown the impact of both mean camber and the dynamic motion of the membrane on the performance of a two-dimensional membrane airfoil. In order to delineate the influence of the development of mean camber and the dynamic motion of the membrane surface for the aspect ratio two wing, computational results for a rigid, flat-membrane wing, a rigid, cambered wing with the shape of the mean deflection for the flexible case, and the flexible membrane wing are compared.

An initial understanding of the influence of flexibility is obtained by examining the flow on the mid-plane of the wing. Figures 6a-c plot contours of the normalized total pressure and restricted streamlines on the mid-plane. For the rigid, flat-membrane wing a large separated flow region characterized by lower values

of total pressure and reversed axial flow extends over the full length of the wing, Fig. 6a. When the mean camber is introduced the height of the separated flow region is reduced and the separated flow is split into a larger upstream region and a small, shallow region downstream towards the trailing edge, Fig. 6b. For the flexible case the separated flow region is reduced even further and is located only over the front portion of the wing.

To better understand the three-dimensional structure of the flow, Figures 7a-c show the pressure coefficient and limiting streamline pattern on the upper surface of the membrane wing. For the rigid, flat-membrane wing separated flow covers the majority of the wing with the attachment line reaching the trailing edge over the mid-section of the wing, Fig. 7a. Two stable foci are observed in the separated flow region. Low pressure associated with the separated flow covers a significant portion of the wing with lower pressures located under the two distinct stable foci, Fig. 7a. Two narrow low pressure regions located along the tips of the wing are the low pressure imprint of the tip vortices on the wing surface.

Introducing the mean cambering of the flexible membrane wing results in a decrease in the size of the main separated flow region with primary flow attachment occurring upstream from the trailing edge, Fig. 7b. The two foci observed in Fig. 7a have moved upstream and outboard and are now located in the upstream corners of the wing. Lower values of the pressure coefficient are observed in the separated flow region. Figure 7c presents the results for the flexible case. A further reduction in the size and extent of the separated region is observed with flow attachment now located near the mid-chord of the wing. Even lower values of the pressure coefficient in the separated flow region are observed with strong low pressure in the upstream corners of the wing.

Contours of chordwise and spanwise velocities on a horizontal plane located at $z/c = 0.035$, Fig. 8, provide further insight into how the three-dimensional flow is affected by the membrane flexibility. For the rigid, flat-membrane wing reversed flow associated with the extensive separated flow exists over the majority of the wing and extends beyond the trailing edge over a portion of the mid-span, Fig. 8a. Outward spanwise flow is observed upstream, with inboard flow further downstream. This arises from the swirling flow associated with the two nodes seen in the surface streamlines, Fig. 7a. As mean camber and dynamic membrane motion are introduced the chordwise extent of the reversed axial flow is reduced with positive axial flow now occurring over the full wing span downstream, Figs. 8b,c. This is consistent with the reduction in size of the separated flow. The upstream zones of outward spanwise velocity are diminished in size and strong inboard axial velocity develops downstream of these zones on the outboard portion of the wing. This enhanced inboard velocity is associated with a stronger turning of the flow arising from the reduced size of the separation zone.

The impact of flexibility on the tip vortex is displayed in Figure 9 where contours of the axial component of vorticity are plotted at axial stations $x/c = 0.425$ and $x/c = 0.9$. The addition of mean camber strengthens the tip vortex at each axial location and the vortex moves slightly further away from the surface, Fig. 9b. The tip vortex in the flexible case, Fig. 9c, exhibits a minimal reduction in strength from the mean cambered case. The change in the tip vortex strength and location produces a mild enhancement of the suction pressures on the upper surface of the wing underneath the tip vortex.

The modification of the flow structure due to the flexibility of the membrane wing impacts the aerodynamic performance of the wing. Figure 10 plots the sectional lift coefficient versus the span location for each of the cases considered. For all cases the wing exhibits a fairly uniform lift over the middle portion of the wing ($x/c = -0.5$ to 0.5) with the sectional lift decreasing as the wing tip is approached. This lift results primarily from the low pressures produced by the separated flow over the upper surface of the wing. The lift increases with the inclusion of the mean camber and has its highest values for the flexible membrane wing which produces the most suction under the separated flow region. While the tip vortex produces larger values of sectional lift near the wing tips, these occur over a relatively small portion of the wing (5% of the span). The primary driver of the lift being produced by this wing is the low pressure region associated with the separated flow.

Table 1. Aerodynamic Coefficients

	CL	CD	L/D	Cm_y
Rigid Flat Wing	0.965	0.235	4.112	-0.160
Rigid Cambered Wing	1.020	0.269	3.794	-0.140
Flexible Wing	1.026	0.263	3.903	-0.123

Table 1 lists the aerodynamic coefficients for each of the cases computed. The rigid, cambered wing demonstrates a slight improvement in the total lift coefficient albeit at the cost of increased drag and reduced L/D. The flexible case performs slightly better than the mean cambered airfoil indicating a favorable effect due to the dynamic motion of the membrane. The pitching moment exhibits a continual reduction of the nose down pitching moment when going from the rigid, flat-membrane wing to the flexible membrane wing.

Unsteady Flow Structure and Membrane Wing Dynamics

This section provides a description of the unsteady flow structure and the dynamic structural response for the membrane wing. Figure 11 displays the dynamic response of the membrane surface over approximately one cycle of the structural motion (a-b-c-d-e-a). The upper half of Figure 11 shows the total membrane deflection. From these figures the global structural response is seen to be in the first mode, which is consistent with the mean deflection shown in Fig. 5b. The region of maximum deflection moves downstream and subsequently back upstream over one cycle of the membrane motion. If the mean first mode deflection is subtracted from the total surface deflection, a second streamwise structural mode is more clearly discerned in the lower half of Figure 11. These observations concerning the membrane dynamics are consistent with those made by Rojratsirikul et al¹² for an angle of attack, $\alpha = 17^\circ$.

Figure 12 presents results of a fourier analysis of the time histories of the surface deflection at locations on the centerline of the wing at chordwise stations $x/c = 0.25$, $x/c = 0.5$, and $x/c = 0.75$. This analysis indicates two dominant frequencies in the structural response, $St = 0.66$ and $St = 0.954$. A third peak at the first harmonic of the lower frequency, $St = 1.32$ but with a smaller amplitude is also captured. At the upstream location, $x/c = 0.25$, the dominant frequency is $St = 0.954$. This frequency is associated with the second mode structural response. At the locations further downstream the lower frequency $St = 0.66$ becomes the dominant peak.

The three dimensional, unsteady flow structure over the flexible membrane wing is visualized in Figure 13 by plotting an isosurface of the Q-criterion²⁸ colored by pressure coefficient. The flow separates from the leading edge and the separated shear layer rolls up into a series of longitudinal vortical structures, Fig. 13b. A complex amalgamation of these longitudinal structures is formed, Figs. 13c-d, and is subsequently shed and convects downstream, Figs. 13e-b. These longitudinal vortical structures are subject to spanwise instabilities and breakdown into a complex collection of small scale structures as they convect downstream. This process can be observed further by examining contours of spanwise vorticity in the mid-plane of the wing, Fig. 14. The merging of the vortices, Fig. 14c,d and their subsequent shedding and convection downstream, Figs. 14e-b, are again evident. Such a distinct shedding process is not clearly discerned in the rigid, flat-membrane wing case and results from the influence of the membrane motion on the vortex dynamics of the separated flow. Much larger surface pressure fluctuations, Figure 15c, are observed for this flexible case when compared with either the rigid-flat or mean-cambered wing cases, Figs. 15a,b.

Figure 16 compares the dominant frequencies for the unsteady lift and pitching moment for the flexible wing with those for the rigid-flat membrane wing. For both the lift and pitching moment the rigid, flat-membrane wing exhibits a very low frequency around $St \approx 0.2$ as well as a peak at $St = 0.66$ which corresponds to the low frequency peak observed in the membrane structural response, Fig. 12. For the flexible membrane wing additional higher frequency peaks corresponding to the higher frequencies in the structural response are introduced. For the lift coefficient a peak at $St = 1.32$ is produced while peaks at both $St = 0.954$ and $St = 1.32$ are present for the pitching moment. These results demonstrate the close coupling between the unsteady flow over the wing and the structural response of the wing.

One other interesting difference noted in the flow structure concerns substructures observed in the shear layer that rolls up to form the tip vortex, Fig. 17. For the rigid, flat-membrane wing substructures are observed in the shear layer that rolls up to form the tip vortex over the full chordwise extent of the wing, Fig. 17a. In the case of the flexible membrane wing these substructures only occur downstream towards the trailing edge, Fig. 17b. The origins of these substructures and the differences noted between the rigid and flexible case are a source for further investigation.

V. Conclusions

An aeroelastic solver coupling a high-order computational method for the Navier-Stokes equations with a mixed Reissner-Mindlin finite-element plate model for applications to flexible membrane wing problems has

been developed. An implicit LES scheme is used to accurately capture the laminar/transitional/turbulent flowfields for the low Reynolds number flows considered. Synchronization of the fluid and structural solvers is accomplished by employing subiterations.

Computations were performed for an aspect ratio two membrane wing at an angle of attack, $\alpha = 16^\circ$ and a Reynolds number, $Re = 24,300$. Three different wings were considered: a rigid, flat membrane wing, a rigid, cambered wing with the shape of the mean deflection for the flexible wing, and a flexible membrane wing. Comparisons of the computational results with experimental PIV measurements and surface deflection measurements demonstrated reasonable agreement.

The flexible membrane wing produces a reduced separation region due to the fluid-structure interaction between the structural dynamics of the membrane and the unsteady flow over the wing. The flexible membrane exhibited a mean first mode deflection with a dynamic response in the second streamwise structural mode. Enhanced lift is obtained in the flexible case albeit at the cost of increased drag and a lower lift to drag ratio. The nose down pitching moment is reduced. The impact of flexibility on the aerodynamic performance was demonstrated to come primarily from the development of mean camber with an additional effect arising from the interaction between the dynamic motion of the membrane and the unsteady flowfield above.

VI. Acknowledgment

This work was sponsored by the Air Force Office of Scientific Research under a tasks monitored by Dr. Doug Smith. The authors would like to thank Dr. Ismet Gursul of the University of Bath for providing their experimental measurements. This work was supported in part by a grant of HPC time from the DoD HPC Shared Resource Centers at the Air Force Research Laboratory and the US Army Engineer Research and Development Center.

References

- ¹Lian, Y. and Shyy, W., "Numerical Simulations of Membrane Wing Aerodynamics for Micro Air Vehicle Applications," *Journal of Aircraft*, Vol. 42, No. 4, July-August 2005, pp. 865–873.
- ²Lian, Y. and Shyy, W., "Three-Dimensional Fluid-Structure Interactions of a Membrane Wing for Micro Air Vehicle Applications," AIAA-2003-1726, April 2003.
- ³Lian, Y., Shyy, W., Ifju, P., and Verron, E., "A Computational Model for Coupled Membrane-Fluid Dynamics," AIAA-2002-2972, June 2002.
- ⁴Persson, P.-O., Peraire, J., and Bonet, J., "A High Order Discontinuous Galerkin Method for Fluid-Structure Interaction," AIAA-2007-4327, June 2007.
- ⁵Gordnier, R. E., "High Fidelity Computational Simulation of a Membrane Wing Airfoil," *Journal of Fluids and Structures*, Vol. 25, No. 5, July 2009, pp. 897–917.
- ⁶Gordnier, R. E. and Attar, P. J., "Implicit LES Simulations of a Low Reynolds Number Flexible Membrane Wing Airfoil," AIAA-2009-0579, January 2009.
- ⁷Visbal, M. R., Morgan, P. E., and Rizzetta, D. P., "An Implicit LES Approach Based on High-Order Compact Differencing and Filtering Schemes (Invited)," AIAA-2003-4098, June 2003.
- ⁸Gaitonde, D. and Visbal, M., "High-Order Schemes for Navier-Stokes Equations: Algorithm and Implementation into FDL3DI," Tech. Rep. AFRL-VA-WP-TR-1998-3060, Air Force Research Laboratory, Wright-Patterson AFB, 1998.
- ⁹Gaitonde, D. and Visbal, M., "Further Development of a Navier-Stokes Solution Procedure Based on Higher-Order Formulas," *AIAA Paper 99-0557*, January 1999.
- ¹⁰Visbal, M. and Gaitonde, D., "High-Order Accurate Methods for Complex Unsteady Subsonic Flows," *AIAA Journal*, Vol. 37, No. 10, 1999, pp. 1231–1239.
- ¹¹Attar, P. J., "Some results for approximate strain and rotation tensor formulations in geometrically non-linear Reissner-Mindlin plate theory," *International Journal of Non-Linear Mechanics*, Vol. 43, 2008, pp. 81–99.
- ¹²Rojratsirikul, P., Wang, Z., and Gursul, I., "Unsteady Aerodynamics of Low Aspect Ratio Membrane Wings," AIAA-2010-0729, January 2010.
- ¹³Rojratsirikul, P., Genc, M. S., wang, Z., and Gursul, I., "Flow-induced vibraions of low aspect ratio rectangular membrane wings," *Journal of Fluids and Structures*, Vol. 27, No. 11, 2011, pp. 1296–1309.
- ¹⁴Rojratsirikul, P., Wang, Z., and Gursul, I., "Unsteady Aerodynamics of Membrane Airfoils," AIAA-2008-0613, January 2008.
- ¹⁵Song, A., Tian, X., Israeli, E., Galvao, R., Bishop, K., Swartz, S., and Breuer, K., "The Aero-Mechanics of Low Aspect Ratio Compliant Membrane Wings, with Applications to Animal Flight," AIAA-2008-0517, January 2008.
- ¹⁶Anderson, D., Tannehill, J., and Pletcher, R., *Computational Fluid Mechanics and Heat Transfer*, McGraw-Hill Book Company, 1984.
- ¹⁷Lele, S., "Compact Finite Difference Schemes with Spectral-like Resolution," *Journal of Computational Physics*, Vol. 103, 1992, pp. 16–42.

¹⁸Visbal, M. and Gaitonde, D., "High-Order Accurate Methods for Unsteady Vortical Flows on Curvilinear Meshes," *AIAA Paper 98-0131*, January 1998.

¹⁹Gaitonde, D., Shang, J., and Young, J., "Practical Aspects of High-Order Accurate Finite-Volume Schemes for Electromagnetics," *AIAA Paper 97-0363*, Jan. 1997.

²⁰Alpert, P., "Implicit Filtering in Conjunction with Explicit Filtering," *J. Comp. Phys.*, Vol. 44, 1981, pp. 212–219.

²¹Beam, R. and Warming, R., "An Implicit Factored Scheme for the Compressible Navier-Stokes Equations," *AIAA Journal*, Vol. 16, No. 4, 1978, pp. 393–402.

²²Jameson, A., Schmidt, W., and Turkel, E., "Numerical Solutions of the Euler Equations by a Finite Volume Method Using Runge-Kutta Time Stepping Schemes," *AIAA Paper 81-1259*, 1981.

²³Pulliam, T., "Artificial Dissipation Models for the Euler Equations," *AIAA*, Vol. 24, No. 12, 1986, pp. 1931–1940.

²⁴Pulliam, T. and Chaussee, D., "A Diagonal Form of an Implicit Approximate-Factorization Algorithm," *Journal of Computational Physics*, Vol. 39, No. 2, 1981, pp. 347–363.

²⁵Visbal, M. and Gaitonde, D., "Very High-Order Spatially Implicit Schemes for Computational Acoustics on Curvilinear Meshes," *Journal of Computational Acoustics*, 2001.

²⁶Szabó, B. and Babuška, I., *Finite Element Analysis*, John Wiley & Sons Ltd, 1997.

²⁷Melville, R. B., "Dynamic Aeroelastic Simulation of Complex Configurations Using Overset Grid Systems," *AIAA 2000-2341*, June 2000.

²⁸Jeong, J. and Hussain, F., "On the identification of a vortex," *Journal of Fluid Mechanics*, Vol. 285, 1995, pp. 69–94.

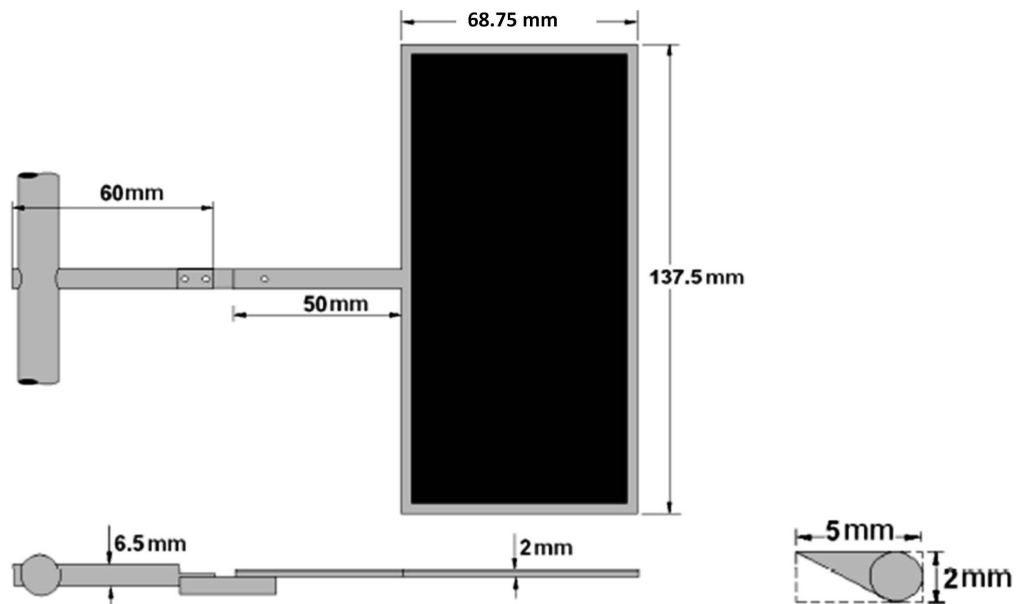


Figure 1. Membrane Wing Geometry¹²

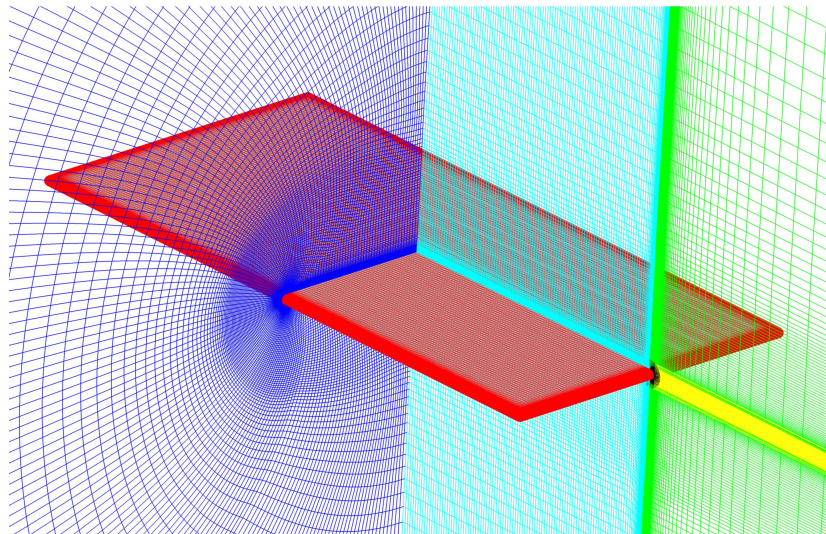


Figure 2. Computational Grid for Membrane Wing

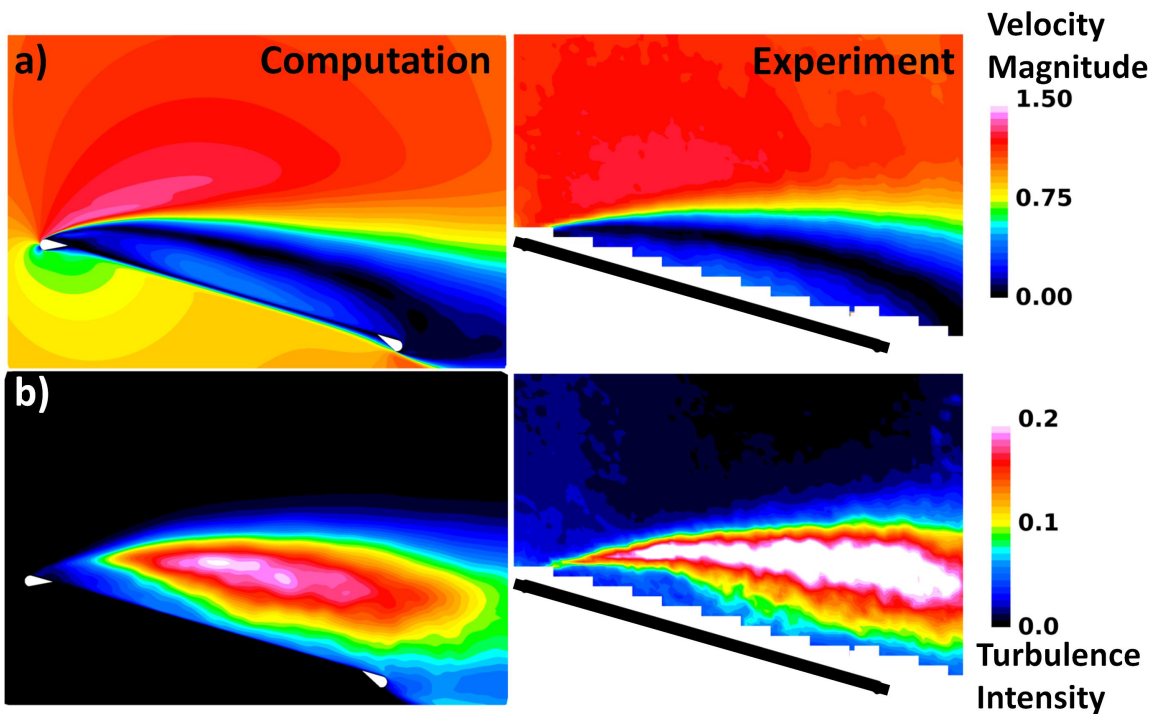


Figure 3. Comparison of computational results for the rigid, flat-membrane wing with experimental measurements¹² at $\alpha = 16^\circ$: a) Mean Velocity Magnitude and b) Turbulence Intensity

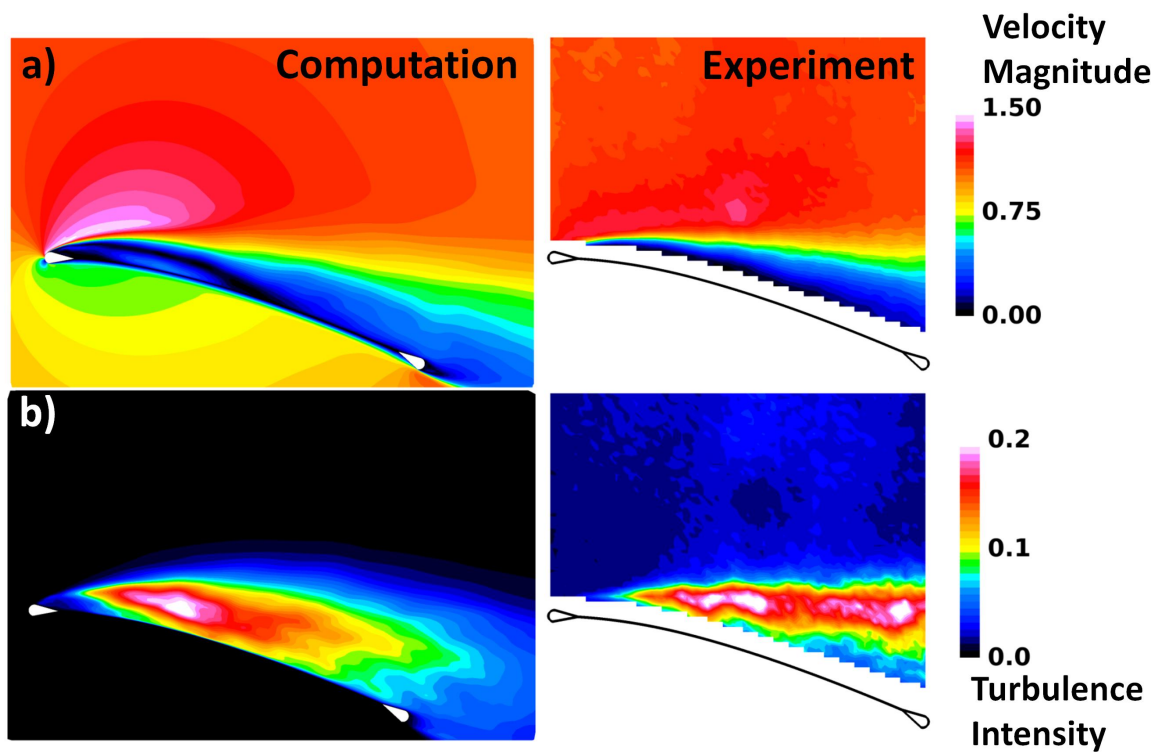


Figure 4. Comparison of computational results for the flexible membrane wing with experimental measurements¹² at $\alpha = 16^\circ$: a) Mean Velocity Magnitude and b) Turbulence Intensity

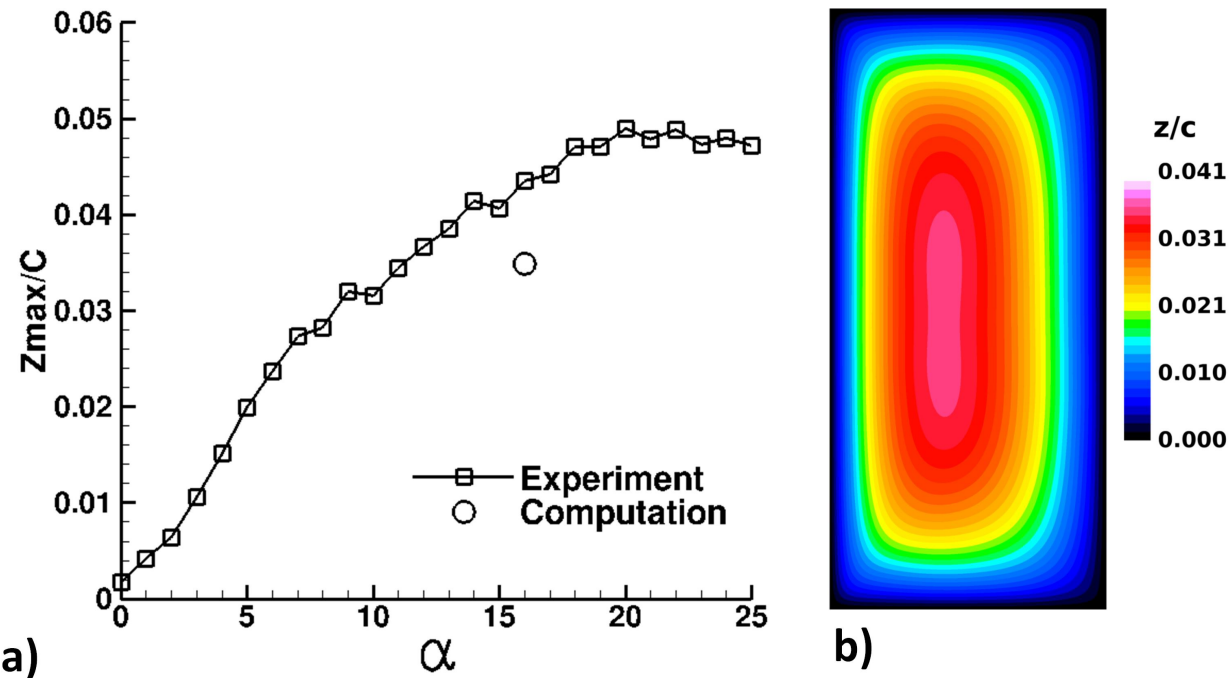


Figure 5. a) Comparison of computational and experimental maximum mean surface deflection and b) computed mean membrane deflection

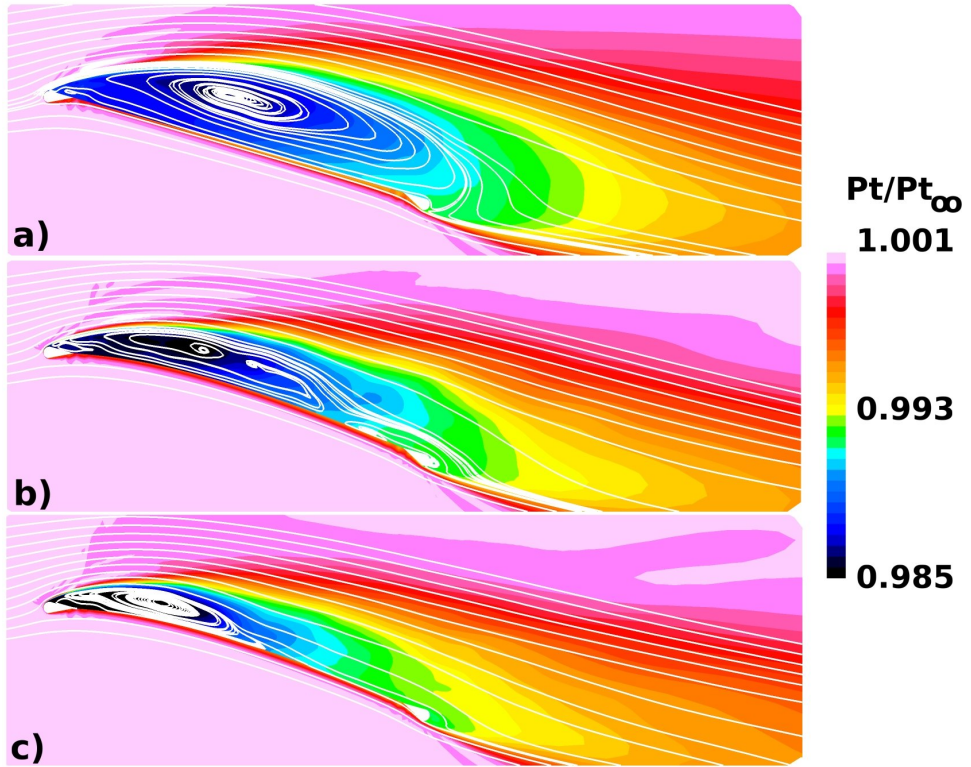


Figure 6. Normalized total pressure and restricted streamlines on the mid-plane of the membrane wing:a) rigid, flat- b) rigid, mean-cambered and c) flexible membrane wing

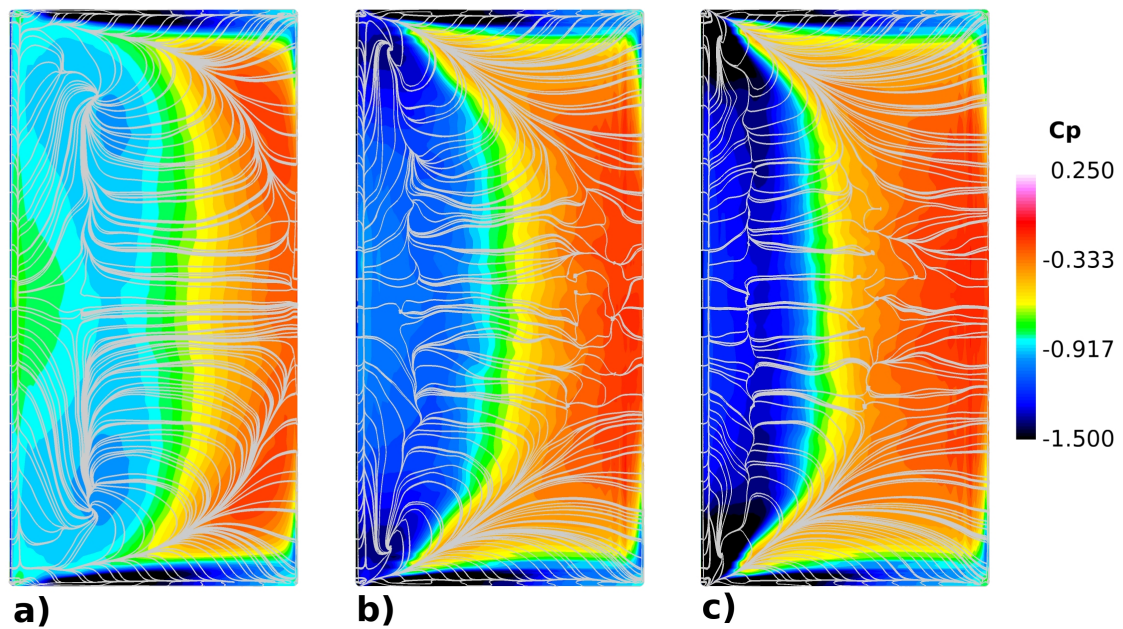


Figure 7. Surface pressure coefficient and limiting streamline pattern:a) rigid, flat- b) rigid, mean-cambered and c) flexible membrane wing

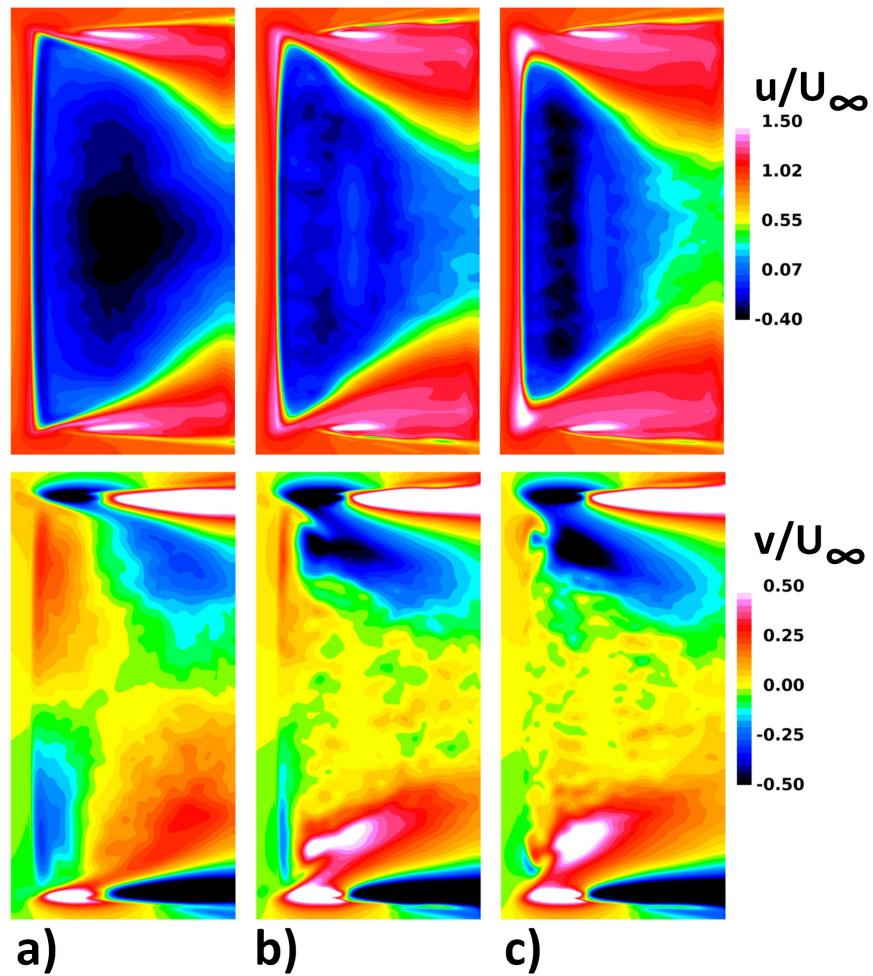


Figure 8. Axial velocity (upper) and spanwise velocity (lower) on a horizontal plane above the wing, $z/c = 0.035$: a) rigid, flat- b) rigid, mean-cambered and c) flexible membrane wing

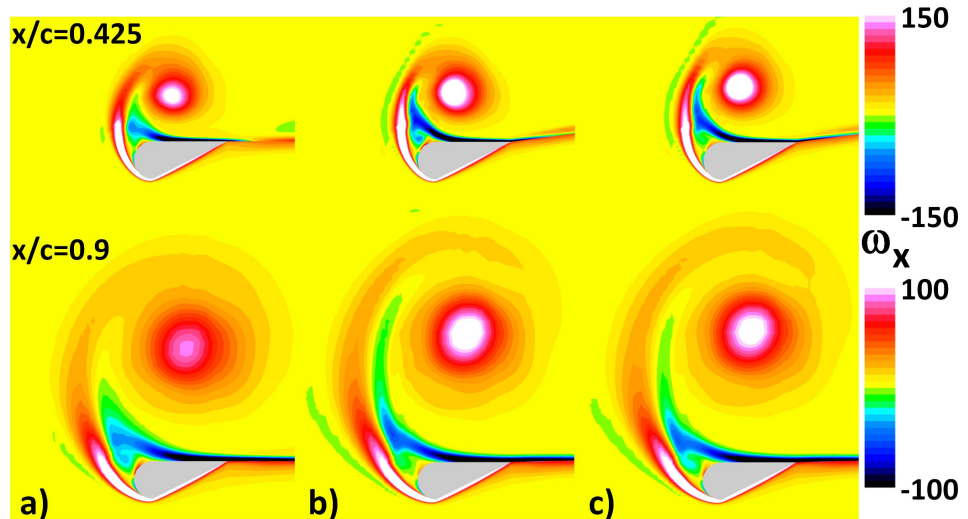


Figure 9. Tip vortex represented via contours of axial vorticity at $x/c = 0.425$ (upper) and $x/c = 0.9$ (lower): a) rigid, flat- b) rigid, mean-cambered and c) flexible membrane wing

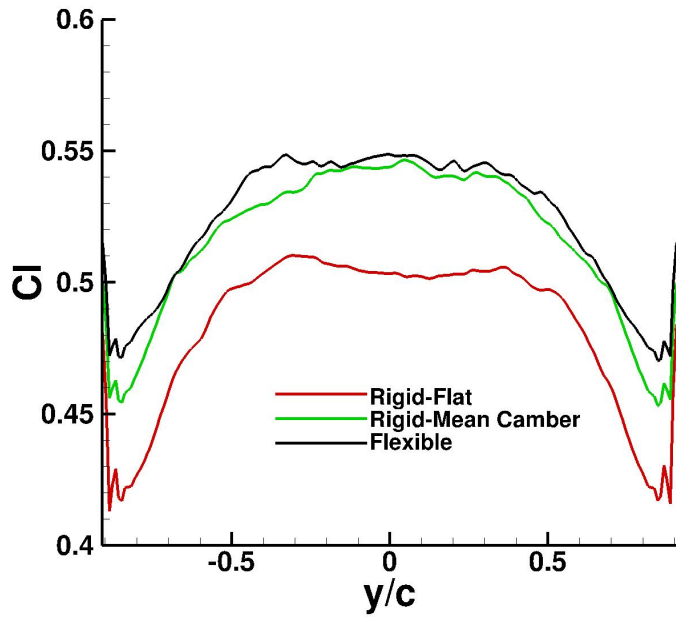


Figure 10. Mean spanwise lift distribution for the rigid, flat-, rigid, mean-cambered and flexible membrane wing

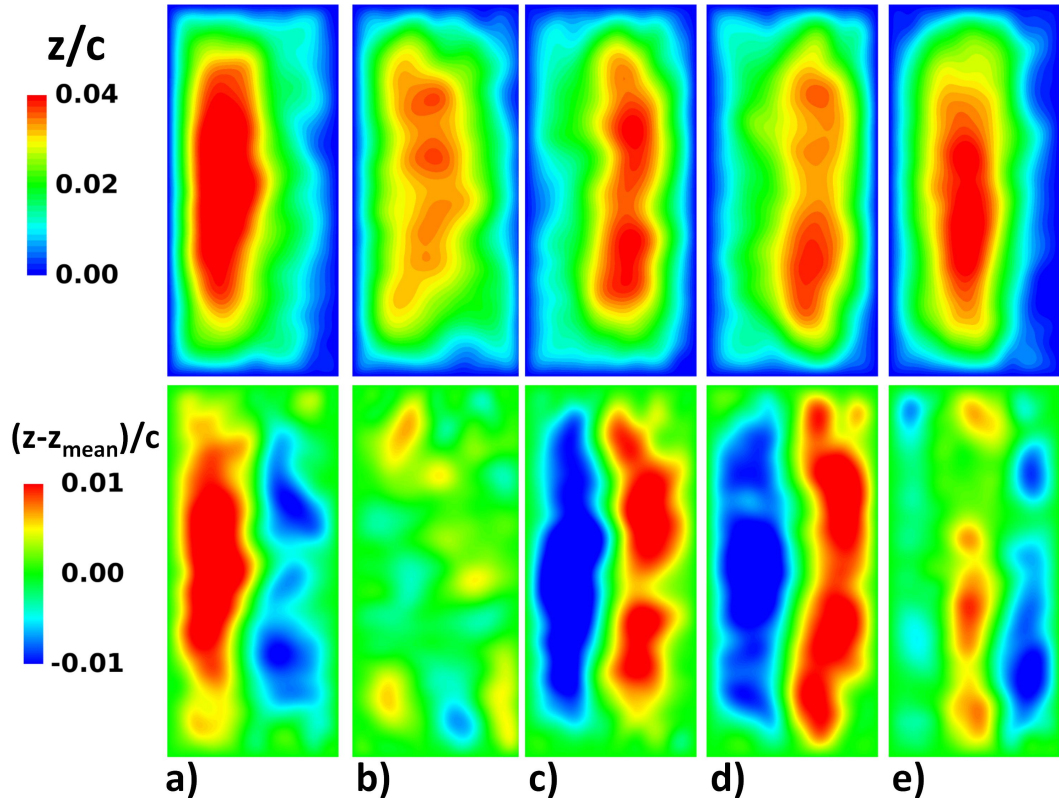


Figure 11. Total surface deflection z/c (upper) and difference from the mean deflection $(z-z_{mean})/c$ (lower): a) $\tau = 0.0$, b) $\tau = 0.25$, c) $\tau = 0.5$, d) $\tau = 0.75$ e) $\tau = 1.0$

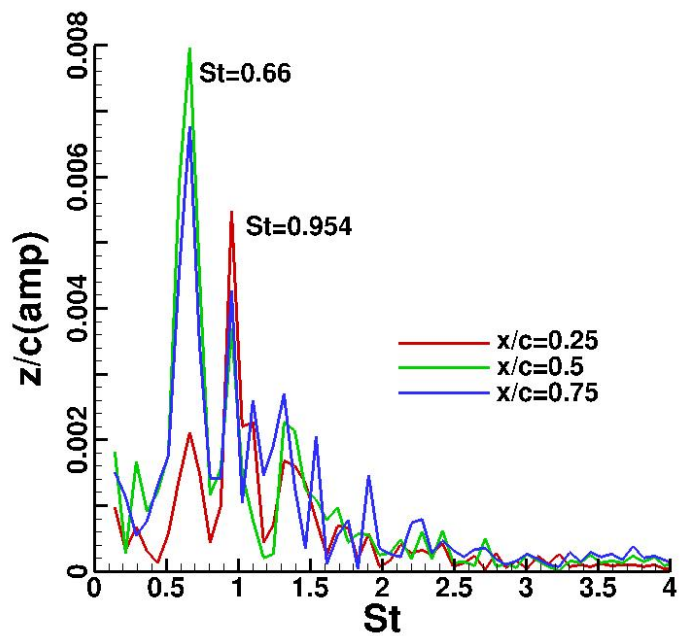


Figure 12. Fourier analysis of the dynamic response of the membrane surface at three axial locations along the centerline of the wing

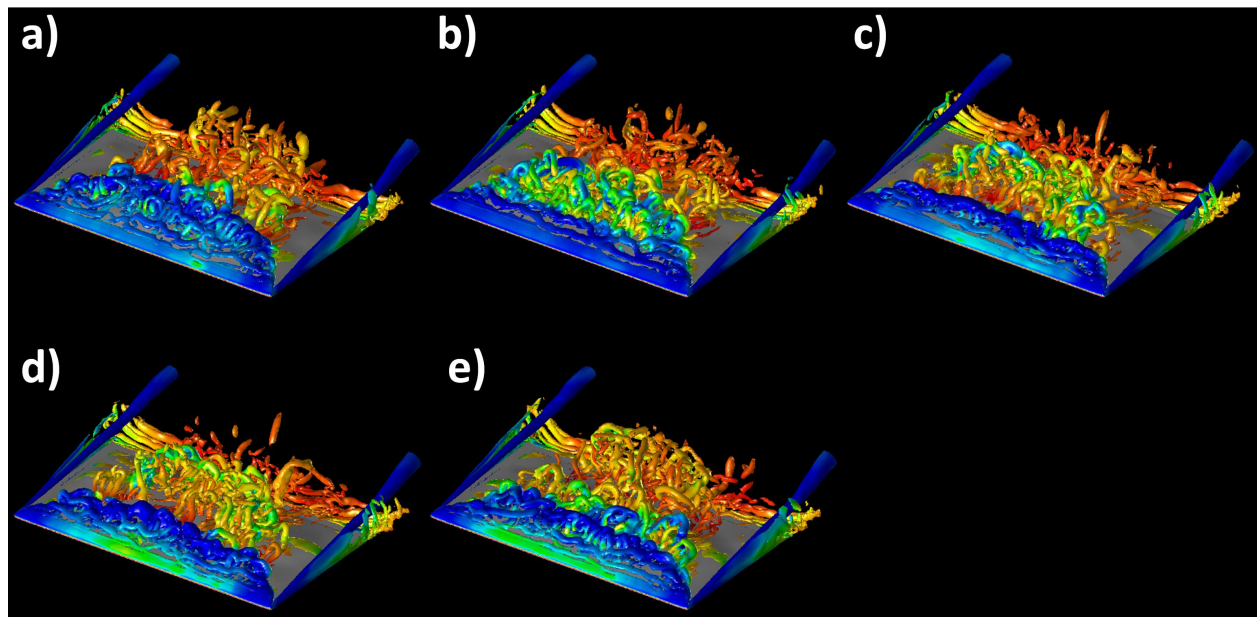


Figure 13. Isosurfaces of Q-criterion colored by pressure coefficient for the flexible membrane wing:a) $\tau = 0.0$, b) $\tau = 0.25$, c) $\tau = 0.5$, d) $\tau = 0.75$ e) $\tau = 1.0$

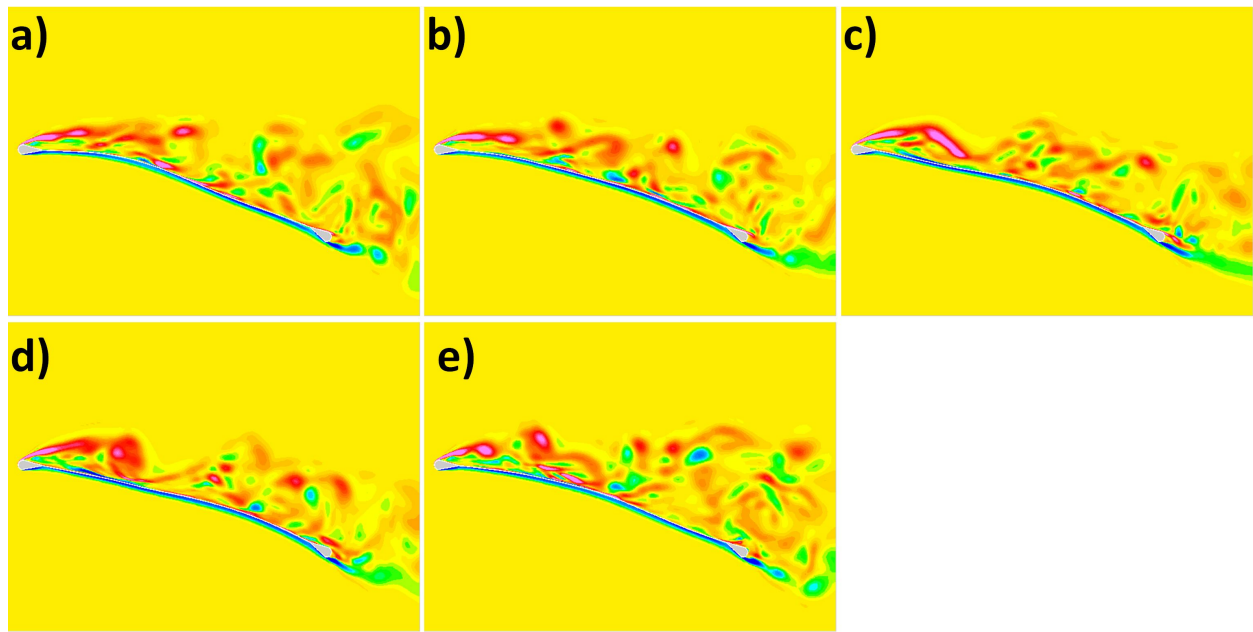


Figure 14. Contours of spanwise vorticity on the mid-plane of the flexible membrane wing:a) $\tau = 0.0$, b) $\tau = 0.25$, c) $\tau = 0.5$, d) $\tau = 0.75$ e) $\tau = 1.0$

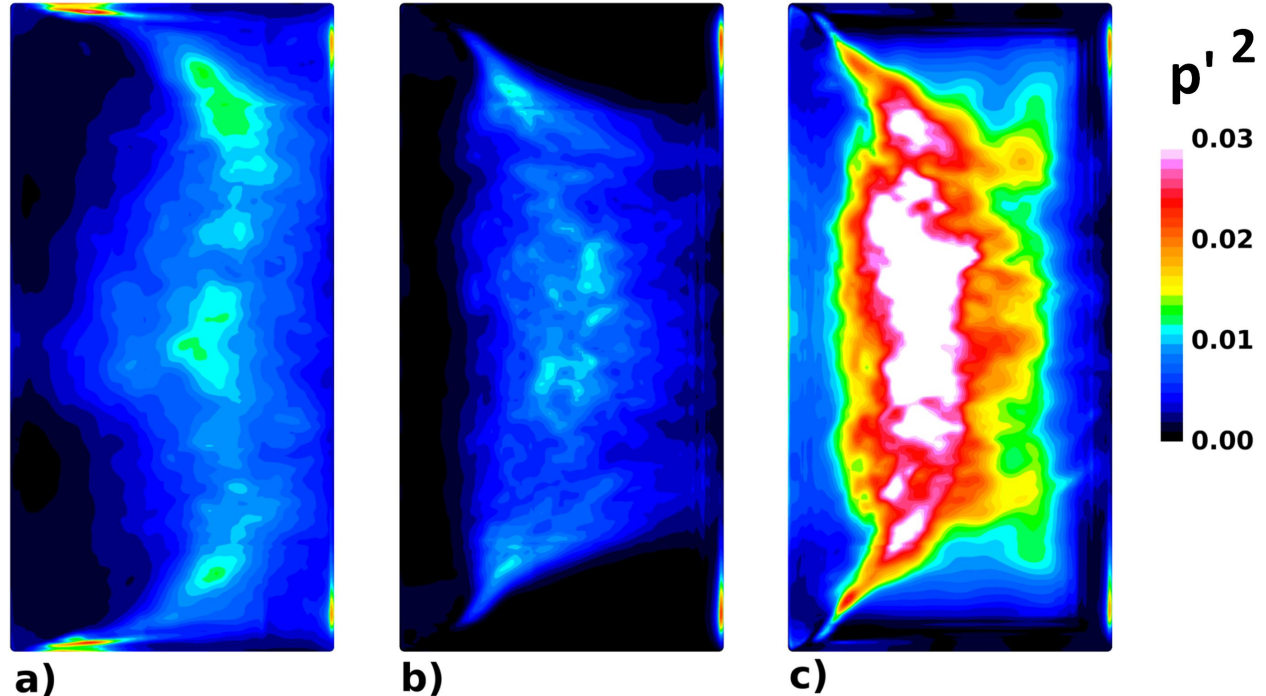


Figure 15. Surface pressure fluctuations on the upper surface of the wing: a) rigid, flat- b) rigid, mean-cambered and c) flexible membrane wing

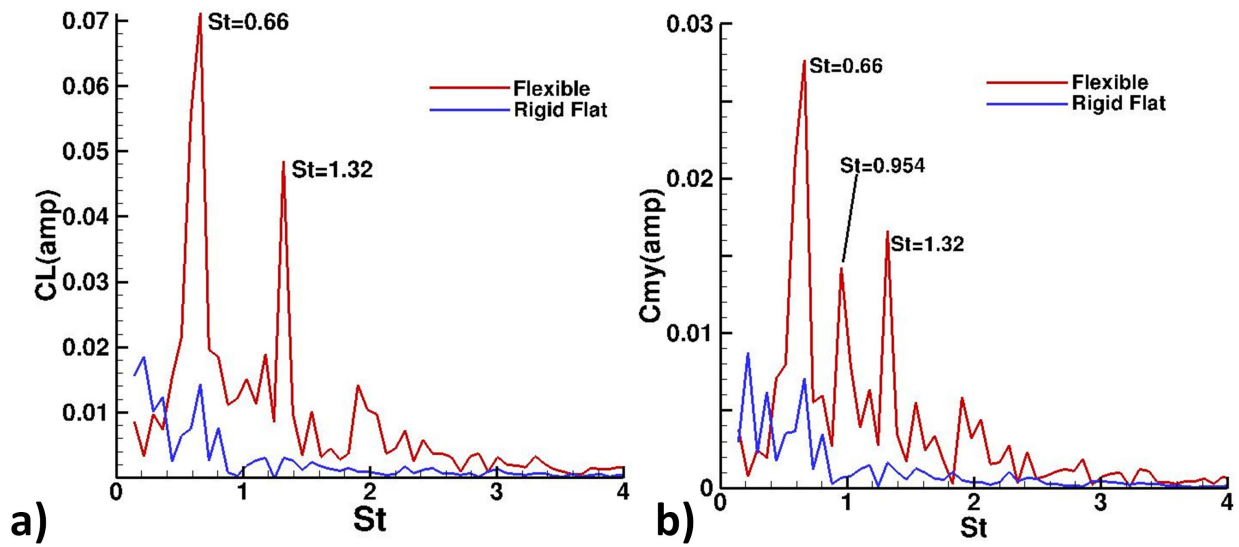


Figure 16. Fourier analysis of a) lift coefficient and b) pitching moment coefficient time histories

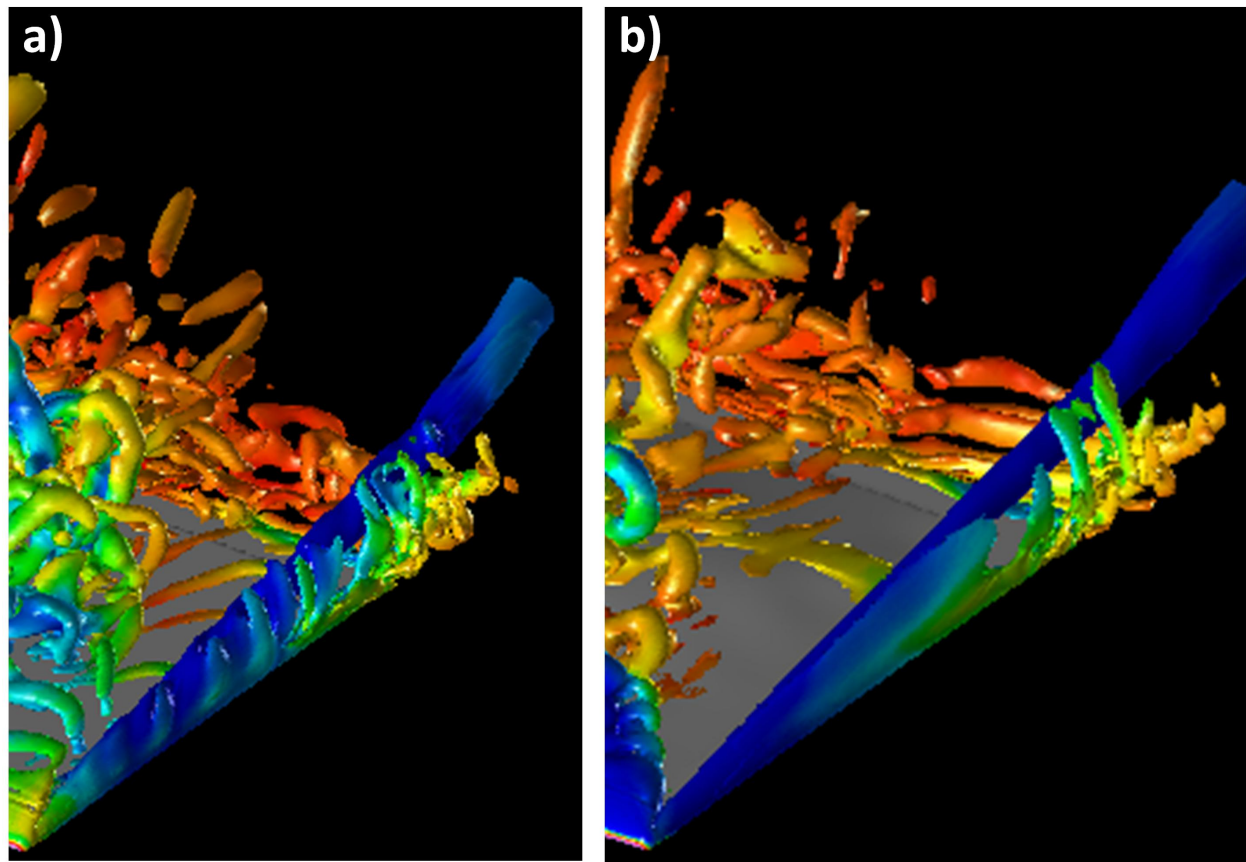


Figure 17. Shear layer substructures in the tip vortex visualized by isosurfaces of the Q-criterion:a)Rigid, flat- and b) flexible membrane wing

APPENDIX C

Numerical exploration of the origin of aerodynamic enhancements in [low-Reynolds number] corrugated airfoils

Caleb J. Barnes^{a)} and Miguel R. Visbal^{b)}

*Wright-Patterson Air Force Base, WPAFB, OH. 45433,
USA*

This paper explores the flow structure of a corrugated airfoil using a high-fidelity implicit large eddy simulation (ILES) approach. The first three-dimensional simulations for a corrugated wing section are presented considering a range of Reynolds numbers of $Re_c = 5 \times 10^3$ to 5.8×10^4 bridging the gap left by previous numerical and experimental studies. Several important effects are shown to result from the corrugations in the leading-edge region. First, interaction between the detached shear layer and the first corrugation peak promotes recirculation upstream and enhances transition to turbulence due to flow instabilities. Thus, early transitional flow develops on the corrugated wing which helps to delay stall even at Reynolds numbers as low as $Re_c = 1 \times 10^4$. Transition is shown to occur as early as $Re_c = 7.5 \times 10^3$ and quickly advances toward the leading-edge as Reynolds number is increased. Modification of the first corrugation peak height produces significantly reduced separation and improved aerodynamic forces demonstrating the sensitivity of flow behavior to leading-edge geometry. Second, the unusual orientation of the corrugated surface and strong suction resulting from rapidly turning fluid over the separated region upstream of the first corrugation produces a new effect which serves to reduce drag. This effect was amplified through the enhanced interaction produced by a modified geometry. Corrugations were found to be most advantageous in the leading-edge region and could be optimized to properly take advantage of the flow field under different operating conditions.

^{a)}Electronic mail: caleb.barnes@wpafb.af.mil;

^{b)}Electronic mail: miguel.visbal@wpafb.af.mil

I. INTRODUCTION

In recent years, the development of small unmanned air systems (UASs) has become an area of great interest for researchers in both civilian and military applications. Design for these small aircraft must overcome a number of challenges including low Reynolds numbers ($Re_c = 1 \times 10^3$ to 1×10^5), low weight requirements, and more challenging aerodynamics^{1,2}. The rising importance of small UAS has spurred the need for the development of high-performance airfoils in low-Reynolds number regimes. Good flight mechanics are difficult to produce for such small-scale conditions due the tendency for flows to contain significant laminar regions^{2,3}. Specifically, low-Reynolds number flows are not very resistant to adverse pressure gradients occurring at moderate angles of attack and are prone to flow separation. Flow separation can either reattach to the body forming a separation bubble or result in aerodynamic stall. While both instances increase the drag, the latter is greatly detrimental to performance. Airfoils on larger aircraft depend on the early transition to turbulent flow seen at higher Reynolds numbers to reduce separation and overcome stall¹.

Many very successful examples of small-scale flight may be found in birds, insects, bats and other species. For this reason, it only makes sense to look to and borrow from nature in order to overcome many of the current challenges. Dragonflies are of particular interest due to their broad range of flight capabilities including hovering and gliding. While gliding is an uncommon flight mode for insects, it is commonly observed in dragonflies as an energy saving technique⁴ and may be useful in small UAS design. Dragonfly wings were found to have among the highest lift coefficients of all insects studied in gliding flight while drag coefficients are similar to those of a flat plate⁴. These wings have a large aspect-ratio and a highly corrugated structure⁵.

Several wind tunnel studies have discussed and shown possible advantages of the corrugations in dragonfly wings. For example, Rees⁶ and Rudolph⁷ concluded that dragonfly wings behave as a smooth airfoil because fluid becomes trapped in the valleys creating an effectively streamlined profile. Rudolph⁷ demonstrated dragonfly wings reduced or delayed flow separation with increasing angle of attack. Wakeling and Ellington⁴ observed an increased lift and Okamoto *et al.*⁸ showed an increase in both maximum lift and lift-to-drag ratio. Both of the latter studies attributed aerodynamic enhancements to the effects of the surface structure.

In addition to aerodynamic benefits, corrugations have been shown to improve spanwise rigidity which is necessary in the high aspect-ratio wings of dragonflies. For instance, Kesel *et al.*⁹ modeled the structure of the forewing from the dragonfly *Aeshna Cyanea* using finite element analysis and determined the corrugated vein network greatly increased the structural strength and rigidity of the wing while using the least possible material. Hord and Lian¹⁰ evaluated the structural benefits of a two-dimensional corrugated wing cross-section and found a greatly improved structural rigidity compared to a flat plate.

In an effort to clarify the impact of the corrugated structure of dragonfly wings, Kesel¹¹ studied a number of wing cross-sections extracted from the forewing of the species *Aeshna Cyanea* and measured aerodynamic forces at chord Reynolds numbers of 7,880 and 10,000 in a wind tunnel experiment. The flow field adhered to a smooth effective geometry around the corrugations due to the formation of vortices in the valleys similar to the conclusions of Rees⁶ and Rudolph⁷. This envelope, referred to as the ‘virtual profile’ by several authors, and in the current work, allowed the corrugated geometry at low Reynolds numbers to behave in a manner similar to a streamlined airfoil at higher Reynolds numbers.

A series of wind tunnel experiments including particle image velocimetry (PIV) on a corrugated airfoil based on Kesel’s are presented in Refs. 12–14 for Reynolds numbers ranging from 34,000 to 125,000. The corrugated profile generated higher lift and delayed stall at higher angles compared to a flat plate and a smooth airfoil, but these benefits reached a limitation around a Reynolds number of 100,000. The PIV measurements provided captured the vortex structure and revealed two mechanisms helping to delay large-scale flow separation: the corrugation peaks tripped turbulence increasing the kinetic energy in the boundary layer, and unsteady vortices formed in the corrugation valleys pull the boundary layer toward the airfoil body.

A number of two-dimensional, low-order numerical studies have been performed using geometries inspired by Kesel’s¹¹ airfoil sections. For instance, Vargas and Mittal¹⁵ modeled a corrugated geometry in two-dimensions at a Reynolds number of 10,000. Shear drag was shown to be very low compared to smooth configurations and gives the corrugated geometry an advantage. Later, Vargas *et al.*¹⁶ continued the study for Reynolds numbers from 500 to 10,000. They deduced the reason for the lower drag was due to a negative shear stress resulting from the recirculation in the valleys. The corrugated geometry was found to perform better than a flat plate at Reynolds numbers exceeding 5,000 concluding that

pleated wings are capable of at least matching conventional airfoil performance under small UAS operating conditions.

Another two-dimensional numerical study was performed by Kim *et al.*¹⁷ on a similar geometry for Reynolds numbers of 150, 1400, and 10,000. This computation focused on the effects of corrugation on lift which was evaluated by closing off upper and lower-surface valleys. While the drag coefficient was not significantly affected by the presence of corrugations, these features resulted in lift enhancement for positive angles of attack. The influence of the corrugations on lift was not found to be dependent on Reynolds number for the cases presented.

Recently, Hord and Lian^{10,18} studied a corrugated wing section at several angles of attack for Reynolds numbers of 500, 1,000 and 2,000 comparing the pleated geometry to a flat plate. They found that the corrugated airfoil produces higher drag and similar lift as the flat plate under these conditions. Structural analysis led to the conclusion that the primary benefit lies in structural considerations for these low Reynolds numbers.

The aforementioned experiments and simulations have shown biomimetic corrugated airfoils generally appear to result in favorable aerodynamics except at very low Reynolds numbers. It should be noted that while all the previous computations and experiments of corrugated airfoil sections are based on those of Kesel¹¹, they are not consistently defined between studies. It would seem that these corrugations, finely tuned by nature, are very sensitive to the specific geometry which could account for some of the inconsistencies in observations at low Reynolds numbers.

Based on the results of previous investigations, the most practical aerodynamic applications for the corrugated geometries appears to lie in the regime of $1 \times 10^4 \leq Re_c \leq 1 \times 10^5$ which has not been sufficiently covered in the literature and is most relevant to small UAS flight. Although a number of two-dimensional numerical experiments highlight the physics of corrugated airfoils at very low Reynolds numbers, detailed high-order, three-dimensional simulations exploring the effect of transition on corrugated airfoils are not available. The current work seeks to address these issues using an implicit large eddy simulation (ILES) approach on the corrugated airfoil section provided in Murphy & Hu¹³. Computations are performed over a range of Reynolds numbers of $5 \times 10^3 \leq Re_c \leq 5.8 \times 10^4$ applicable to small unmanned aircraft. The effects of transition on corrugated wings is explored and the first three-dimensional simulations of a corrugated wing section, to the author's knowledge, are

presented. This paper emphasizes the role of the leading-edge region geometry on the development of flow features and demonstrates the high degree of sensitivity of flow interactions with the corrugation shape.

II. GOVERNING EQUATIONS

The full unsteady Navier-Stokes equations are cast in strong conservation form and transferred from Cartesian coordinates (x, y, z, t) in the physical domain to the computation domain in curvilinear coordinates $(\xi, \eta, \zeta, \tau)^{19,20}$. The system of equations are non-dimensionalized and written in vector form as,

$$\frac{\partial}{\partial \tau} \left(\frac{\vec{U}}{J} \right) + \frac{\partial \hat{F}}{\partial \xi} + \frac{\partial \hat{G}}{\partial \eta} + \frac{\partial \hat{H}}{\partial \zeta} = \frac{1}{Re} \left[\frac{\partial \hat{F}_v}{\partial \xi} + \frac{\partial \hat{G}_v}{\partial \eta} + \frac{\partial \hat{H}_v}{\partial \zeta} \right] \quad (1)$$

where the vector of conservative variables is given as

$$\vec{U} = \left[\rho \ \rho u \ \rho v \ \rho w \ \rho E \right]^T \quad (2)$$

and $J = \partial(\xi, \eta, \zeta, \tau)/\partial(x, y, z, t)$ is the transformation Jacobian²¹.

The inviscid flux vectors are defined by

$$\hat{F} = \frac{1}{J} \begin{bmatrix} \rho U \\ \rho u U + \xi_x p \\ \rho v U + \xi_y p \\ \rho w U + \xi_z p \\ (\rho E + p)U - \xi_t p \end{bmatrix}, \hat{G} = \frac{1}{J} \begin{bmatrix} \rho V \\ \rho u V + \eta_x p \\ \rho v V + \eta_y p \\ \rho w V + \eta_z p \\ (\rho E + p)V - \eta_t p \end{bmatrix}, \hat{H} = \frac{1}{J} \begin{bmatrix} \rho W \\ \rho u W + \zeta_x p \\ \rho v W + \zeta_y p \\ \rho w W + \zeta_z p \\ (\rho E + p)W - \zeta_t p \end{bmatrix} \quad (3)$$

where

$$\begin{aligned} U &= \xi_t + \xi_x u + \xi_y v + \xi_z w \\ V &= \eta_t + \eta_x u + \eta_y v + \eta_z w \\ W &= \zeta_t + \zeta_x u + \zeta_y v + \zeta_z w \end{aligned} \quad (4)$$

are the contravariant velocities and

$$E = \frac{T}{(\gamma - 1)M_\infty^2} + \frac{1}{2}(u^2 + v^2 + w^2) \quad (5)$$

is the internal energy. Here the quantities u , v , and w are the Cartesian velocity components, ρ is the density, p is pressure, and T is temperature.

The viscous flux vectors are given by

$$\hat{F}_v = \frac{1}{J} \begin{bmatrix} 0 \\ \xi_{x_i} \sigma_{i1} \\ \xi_{x_i} \sigma_{i2} \\ \xi_{x_i} \sigma_{i3} \\ \xi_{x_i} (u_j \sigma_{ij} - \Theta_i) \end{bmatrix}, \hat{G}_v = \frac{1}{J} \begin{bmatrix} 0 \\ \eta_{x_i} \sigma_{i1} \\ \eta_{x_i} \sigma_{i2} \\ \eta_{x_i} \sigma_{i3} \\ \eta_{x_i} (u_j \sigma_{ij} - \Theta_i) \end{bmatrix}, \hat{H}_v = \frac{1}{J} \begin{bmatrix} 0 \\ \zeta_{x_i} \sigma_{i1} \\ \zeta_{x_i} \sigma_{i2} \\ \zeta_{x_i} \sigma_{i3} \\ \zeta_{x_i} (u_j \sigma_{ij} - \Theta_i) \end{bmatrix} \quad (6)$$

in indicial notation where the stress tensor (σ_{ij}) and heat flux vector (Θ_i) are defined as

$$\sigma_{ij} = \mu \left(\frac{\partial \zeta_k}{\partial x_j} \frac{\partial u_i}{\partial \xi_k} + \frac{\partial \xi_k}{\partial x_i} \frac{\partial u_j}{\partial \xi_k} - \frac{2}{3} \delta_{ij} \frac{\partial \xi_l}{\partial x_k} \frac{\partial u_k}{\partial \xi_l} \right) \quad (7)$$

and

$$\Theta_i = - \left[\frac{1}{(\gamma - 1) M_\infty^2} \right] \left(\frac{\mu}{Pr} \right) \frac{\partial \xi_j}{\partial x_i} \frac{\partial T}{\partial \xi_j} \quad (8)$$

Here M_∞ , μ , and γ are the free stream Mach number, dynamic viscosity, and ratio of specific heats respectively. Additionally, Stoke's hypothesis was used for the bulk viscosity coefficient where $\lambda = -2/3\mu$ and the perfect gas relationship $p = \rho T / \gamma M_\infty^2$ was assumed. The Prandtl number (Pr) was chosen as a constant value of $Pr = 0.72$ for air.

Each of the flow variables were normalized by the free stream values except pressure which was non-dimensionalized by $\rho_\infty u_\infty^2$ while length scales were non-dimensionalized by the chord length. Sutherland's law and the perfect gas law were used to close the Navier-Stokes equations.

The above form of the Navier-Stokes equations is *unfiltered* and used to solve laminar, transitional, and turbulent flow regions without change using an implicit large-eddy (ILES) simulation procedure. The ILES procedure does not require sub-grid-scale (SGS) models or additional heat flux terms required by the standard large-eddy-simulation (LES) approach. Alternatively, a high-order, low-pass Padé-type filter is applied to the conserved variables of the standard Navier-Stokes equations. This operator is highly-discriminating and selectively damps only the poorly resolved high-frequency content of the solution^{22,23}. The filtering regularization procedure provides an effective alternative to the use of SGS models and has been validated extensively for several canonical turbulent flows. A re-interpretation of this ILES approach in the context of an Approximate Deconvolution Model²⁴ has been presented by Mathew *et al*²⁵. As the grid resolution increases or Reynolds number decreases, the ILES approach is effectively direct numerical simulation (DNS).

III. NUMERICAL PROCEDURE

The high-order Navier-Stokes solver *FDL3DI* was used for all simulations in the present study^{26,27}. Here, spatial derivatives are discretized using high-order compact-differencing schemes²⁸. The computations in this work utilize a sixth-order stencil. High-order one-sided formulas are used at the boundaries that retain the tridiagonal form^{26,27}. Derivatives of the inviscid fluxes are obtained by determining the fluxes at the nodal locations and differentiating each component with the compact differencing scheme. Viscous terms are produced by computing the primitive variable derivatives and then constructing the components of the viscous flux vectors. The components of the viscous fluxes are then differentiated by a second application of the same compact scheme.

In order to eliminate spurious components of the solution, a high-order, low-pass spatial filtering technique^{26,29} is incorporated that is based on templates proposed in Refs. 28 and 30. With proper choice of coefficients, it provides a $2N^{th}$ -order formula on a $2N + 1$ point stencil. These coefficients, along with representative filter transfer functions, can be found in Refs. 27 and 29. The filter is applied to the conserved variables along each transformed coordinate direction once after each time step or sub-iteration. An 8th-order filter is used for the interior points in the present work. For the near-boundary points, the filtering strategies described in Refs. 26 and 29 are used. For transitional and turbulent flows, the high-fidelity spatial algorithmic components provide an effective implicit LES approach in place of traditional SGS models, as demonstrated in Refs. 22 and 23 and more recently in Ref. 31.

Finally, time accurate solutions were obtained using the implicit, approximate-factorization of Beam and Warming³² including the diagonalization of Pulliam and Chaussee³³. Errors can occur due to factorization, linearization, diagonalization, and explicit specification of boundary conditions³⁴. Therefore, temporal accuracy is maintained through the use of Newton-like sub-iterations where three sub-iterations per time step have been found to be sufficient.

IV. DETAILS OF THE COMPUTATIONS

The corrugated airfoil shown in Fig. 1 was based on the cross-sections obtained by Kesel¹¹ and the actual dimensions were provided in Ref. 13. The geometry was meshed using an O-mesh topology shown in Fig. 2(a). The O-mesh was created by extruding a 2D plane from the airfoil surface using a hyperbolic grid generator. In order to accommodate the high order stencils used in *FDL3DI*, the sharp corners were given a small radius of curvature and a denser point distribution. The curvature at the leading and trailing-edges is sharper than some of the other numerical studies^{15–18}, but was chosen to maintain as similar a geometry as possible to that provided in Ref. 13.

An initial mesh was generated using a very fine distribution of 853 points circumferentially around the airfoil surface (ξ -direction) in order to capture the flow structure around the sharp corners of the peaks and valleys and 328 points radially outward (η -direction) to create a 2-dimensional computational plane. This grid was uniformly extruded along the airfoil span (ζ -direction) to include a total of 125 points with a span length of 0.2. In order to capture the physics in the near-body wake region at positive angles of attack, 61% of the points used in the ξ -direction were located on the upper surface of the airfoil.

The mesh was coarsened using a bi-cubic spline interpolation procedure in order to maintain geometric similarity between the different levels of refinement. Table I shows the grid dimensions used in this study. The coarsest mesh was obtained by reducing the number of solution points in the η and ζ -directions to half the nominal value of total points. Because of the complicated geometry of the corrugated airfoil and number of sharp corners, the ξ -direction was left unchanged during refinement in order to preserve the airfoil geometry and maintain consistent flow over the sharp peaks and valleys.

TABLE I: Computational mesh dimensions

Grid	Dimensions	Points	Coarsening Factor
Fine	853x328x125	34,973,000	1.000
Medium	853x284x108	26,163,216	0.748
Coarse	853x232x89	17,612,744	0.504

Two additional geometries, shown in Figs. 2(c) and (d), were studied including a modified corrugated profile and a flat plate where the corresponding grid dimensions for these geometries are provided in Table II. The modified geometry differs from the baseline only in the height of the first corrugation peak which was increased by $y/c = 0.0147$. The flat plate was constructed using the same thickness of the baseline corrugated geometry (4% of chord length) while the leading and trailing-edges were identical to those from the original corrugated profile. Both of the alternate geometries were constructed with similar point distributions to the coarse mesh of the baseline corrugated airfoil.

TABLE II: Alternate geometry mesh dimensions

Grid	Dimensions	Points
Modified corrugated	878x234x89	18,285,228
Flat plate	593x232x89	12,244,264

For the described geometries, boundary conditions were applied in the following manner. The airfoil surface was modeled as a no-slip, adiabatic wall with a fourth-order explicit zero normal pressure gradient. Free stream conditions were imposed at the far field at the specified angle of attack which was located roughly 100 chord lengths away from the airfoil. Here, the low-pass filter of the numerical scheme is used in conjunction with rapidly stretching the mesh outside of the region of interest which serves as a buffer for spurious reflections and has been shown as an effective technique in the past³⁵. Energy not supported as the mesh expands is reflected in the form of high-frequency modes which are eliminated by the highly discriminating filter. The O-grid topology requires a branch-cut where a five-point overlap for spatial periodicity was applied in order to maintain the high-order stencil. Spatial periodic conditions were also applied with a five-point overlap at the ends of the airfoil span to emulate an infinite span wing.

The free stream Mach number for all computations was chosen as a low value of $M_\infty = 0.1$ in order to avoid the effects of compressibility. Each of the static cases were run for 30 convective times using a small nondimensional time step of $\Delta\tau = 0.0001$ in order to remove transients resulting from initialization from uniform flow. Statistical data was then collected for the next 15 convective times.

V. RESULTS

A. Effect of spatial resolution

In order to evaluate the effects of spatial resolution, simulations were conducted for the baseline corrugated wing at $\alpha = 5^\circ$ and $Re_c = 3.4 \times 10^4$ for three grids of successive refinement. The fine, mid, and coarse distributions correspond with roughly 35, 26, and 17 million grid points respectively where dimensions are provided in Table I. Several time-averaged quantities are compared in order to demonstrate grid convergence.

First, the time-mean surface pressure coefficients are shown in Fig. 3(a) and the skin friction coefficients for the suction surface are shown in Fig. 3(b). All three time-mean solutions portray nearly identical phenomena for the pressure and skin friction coefficients. Specifically, the plateaus and jumps resulting from the complicated geometry are equally predicted in each grid indicating excellent agreement.

Next, several streamwise stations (Fig. 4(a)) were chosen along the airfoil surface in order to show velocity profile development. These profiles were extracted normal to the surface at each location. Figure 4(b) shows the time-mean/span-averaged streamwise velocity at each of the selected locations and Fig. 4(c) shows the u -direction rms fluctuations along the same normal lines. Again, the three levels of refinement exhibit excellent agreement in every region.

Finally, velocity probes were placed at ten streamwise stations above the airfoil surface (Fig. 5(a)) along the chord including one on the pressure-side at the trailing-edge. The frequency spectra of each point was computed and then averaged across the span for each chordwise location. The temporal spectra for kinetic energy is displayed at a few of the selected locations in Fig. 5(b). All three meshes produce very similar profiles at each position with small deviations in the highest-frequency content. While the mid and fine mesh values appear to collapse, all three are in excellent agreement in the higher energy regions. Additionally, all the meshes produce nearly identical predictions of the leading-edge vortex shedding frequency visible in Fig. 5(b) at positions one and three. Given the similarities between the three computational meshes, reasonable confidence can be placed in solutions obtained using the coarse grid which was used for all following computations.

B. Effect of spanwise extent

In addition to ensuring sufficient grid resolution, the effect of the spanwise extent is explored for the current spanwise periodic simulations. Spanwise extents of $z/c = 0.1$, 0.2 , and 0.3 were considered for a grid resolution equivalent to the coarse mesh of the previous section. The resulting surface pressure and friction coefficients are shown in Figs. 6(a) and (b) respectively. Here, all three extents show nearly identical solutions for each parameter with excellent agreement on the upper surface. The temporal frequency spectra (Fig. 7(b)) show very similar distributions for each spanwise extent at each chordwise location. The largest deviation is observed just past the leading-edge where the $z/c = 0.1$ airfoil over-predicts the higher-frequency/lower energy content compared to the wider spans. Therefore, a spanwise extent of $z/c = 0.2$ was used for all following cases in this work.

C. Comparison with experiment

A qualitative comparison of the computational solutions with the time-mean PIV measurements of Refs. 12 and 14 for $Re_c = 3.4 \times 10^4$ at $\alpha = 5^\circ$ is presented in this section. Time-mean streamlines and velocity magnitude contours are presented in Figs. 8(a) and (b) along with turbulent kinetic energy (TKE) in Fig. 8(c) for both the simulation and experiment. The PIV measurements show slowly rotating vortices in the corrugation valleys while the high speed flow stream follows the smooth virtual profile generated by these bubbles. This behavior is similar in form to the computational solutions at the same angle of attack. Both cases exhibit a thin shear layer emanating from the leading-edge resulting in a separation region in front of the first peak. Additionally, both demonstrate transition to turbulence within the vicinity of the first two corrugations.

One important distinction can be made between the simulation and experiment in the location of transition to turbulence evidenced by the TKE contours in Fig. 8(c). High values of TKE appear upstream of the first peak in the computation indicating transition to turbulence in this region. As will be discussed in more detail later, transition in the numerical solution appears to be the result of instabilities associated with recirculation (Fig. 8(b)) upstream of the first peak. In the experiment, the separation bubble upwind of the first corrugation is smaller and reattaches to the inclined surface of the first corrugation.

Transition in the experiment occurs as the flow separates from the first peak and the detached shear layer interacts with recirculation upwind of the second peak in a manner similar to that of the computation although at a different location. The apparent effect of the corrugations and the associated mechanisms sparking transition are inherently the same for both cases.

A number of factors can significantly contribute to, and help explain, these variations such as wall effects, presence of free stream turbulence, uncertainty in the angle of attack, and small differences in the actual geometry. For instance, the presence of free stream turbulence, has been shown to decrease the size of separation bubbles and delay aerodynamic stall³⁶. Additionally, as will be shown later, the airfoil behavior is particularly sensitive to the leading-edge region geometry. Minor differences in the corrugations can have a significant impact on the overall flow field. Differences between the two solutions cannot be attributed to grid resolution as excellent agreement was observed between the three meshes used for all parameters considered.

D. Effect of angle of attack

In order to investigate the effect of angle of attack on the aerodynamic forces and flow structure, simulations were obtained over a range of α between 5° and 10° at $Re_c = 3.4 \times 10^4$. This section investigates the role of the corrugated geometry on flow development and large-scale flow separation with changing angle of attack.

For the lower angles of attack, $\alpha = 5^\circ$ to 8° , the free stream tends to conform to the general outline of the corrugated body forming a virtual profile similar to that observed in past studies. In a general sense, this effective shape, characterized by large, slowly rotating time-averaged vortices which form in the corrugation valleys, remains relatively unchanged for these angles, but quickly transforms as the α is increased. For example, at $\alpha = 9^\circ$, the virtual profile begins to deteriorate with a series of large time-mean recirculation bubbles along the suction-surface. A further increase in the angle of attack, $\alpha = 10^\circ$, results in a rather abrupt transition to large-scale separation.

Looking at the time-averaged streamlines at the leading-edge region in more detail, Fig. 9(b), differences in the flow structure at each angle are more clearly elucidated. At the lowest angle of attack, $\alpha = 5^\circ$, flow separates from the leading-edge due to the relatively sharp corners. The first dividing streamline emanating from the leading-edge travels sufficiently

close to the first corrugation inducing a roll-up of the shear layer (not shown in this section) and produces a small time-mean recirculation bubble just upwind of the peak. Raising the angle of attack decreases this shear layer-corrugation interaction as the first dividing streamline emanating from the leading-edge travels further away from the wing surface. Consequently, this bubble shrinks, $\alpha = 8^\circ$, and eventually merges with the larger bubble in the first corrugation valley, $\alpha = 9^\circ$. At the highest angles of attack, $\alpha = 9^\circ$ and 10° , the small leading-edge region recirculation bubble has completely merged with the first corrugation valley corresponding with the observation of large-scale separation.

Next, time-averaged contours of the pressure coefficient for the leading-edge region of the airfoil are provided in Fig. 10(a) and the pressure coefficient is plotted along the upper surface for each angle of attack in Fig. 10(b). Rapidly turning fluid over the leading-edge at $\alpha \leq 9^\circ$ produces a region of strong suction upstream of the first corrugation. The C_p contours appear to be lowest just upstream of the first corrugation peak demonstrating the intensity of the recirculation in this region. This low pressure region appears to strengthen up to $\alpha = 7^\circ$ where the recirculation due to the shear layer-corrugation interaction is most intense and the local distribution of surface pressure in Fig. 10(b) between $0.066 \leq x/c \leq 0.124$ is lowest. The presence of this enhanced suction implies improved lift and, due to the forward-facing orientation of the corrugation surface, reduced drag; an effect that will be explored in more detail in the next section. Higher angles of attack reveal an attenuated leading-edge region suction resulting from a weakened interaction of the flow field with the first corrugation.

Influence of suction from the first two corrugations is apparent due to the formation of time-averaged vortices in the respective valleys. For example, the low pressure in the second valley (Fig. 10(a)) at $\alpha = 5^\circ$ results in a corresponding local decrease in the surface pressure coefficient (Fig. 10(b), $0.271 \leq x/c \leq 0.398$). At higher angles of attack, the first valley plays a greater role where the local surface pressure is lowest at $\alpha = 8^\circ$ for $0.124 \leq x/c \leq 0.271$. Downstream of the second valley, $x/c > 0.398$, there is little difference between the surface pressure coefficient distributions at pre-stall angles of attack showing that the influence of the leeward wing geometry appears to be relatively benign.

In the experimental work of Murphy and Hu¹³, corrugations were identified as mechanisms that serve to promote transition to turbulence. The role of turbulent flow is evaluated for the corrugated wing simulations at the current Reynolds number using contours of turbulence kinetic energy (TKE), which is a measurement of energy associated with root-mean-

square velocity fluctuations. This quantity helps to identify regions of unsteady laminar flow contributions and turbulence by visualizing how energy associated with unsteadiness is concentrated and is depicted for the corrugated wing section at several angles of attack in Fig. 11. Highly unsteady flow is apparent at the lowest angle of attack, $\alpha = 5^\circ$, indicated by the high levels of TKE upwind of the first corrugation. As the angle of attack increases toward the post-stall regime, concentrations of TKE, shown more clearly in Fig. 12, appear to march away from the leading-edge corrugation. This movement of TKE away from the wing body correlates with decreased shear layer-body interaction and the formation of large-scale separation. Adjusting the wing's orientation to sufficiently large α appears to remove the turbulence tripping-mechanism of the first corrugation peak, delays transition, and consequently the flow separates.

Finally, the time-mean force coefficients are presented in Table III where the drag coefficient is separated into its pressure and shear stress contributions. For this Reynolds number, pressure forces appear to be the dominant contribution to drag and can be expected to produce the greatest effects. Therefore, the strong influence of the first two corrugations on the surface pressure coefficient can be expected to have a large effect on the time-averaged forces. For instance, the highest lift-to-drag ratio occurs at $\alpha = 7^\circ$ which corresponds with the lowest pressure along the forward-facing surface of the first corrugation. Lift coefficients increase to a maximum value at $\alpha = 8^\circ$ indicating aerodynamic stall for higher angles of attack which is consistent with observations of the time-averaged streamlines in Fig. 9(a).

TABLE III: Time-mean aerodynamic forces with angle of attack ($Re_c = 3.4 \times 10^4$)

α	\bar{C}_L	\bar{C}_D	\bar{C}_{D_p}	\bar{C}_{D_s}	\bar{L}/\bar{D}
5°	0.6016	0.0795	0.0763	0.0031	7.567
7°	0.7601	0.0959	0.0931	0.0027	7.926
8°	0.8279	0.1132	0.1113	0.0019	7.314
9°	0.7943	0.1447	0.1432	0.0015	5.489
10°	0.7290	0.1802	0.1776	0.0027	4.046

True to the conclusions in Ref. 13, the presence of wing corrugations appears to serve as a mechanism to promote transition to turbulence which can be advantageous in the presence

of adverse pressure gradients and help to delay stall. This interaction also results in a strong suction region on the forward-facing surface of the first corrugation peak which can be expected to enhance lift and reduce drag due to the local upstream orientation. Clearly, the effect of the leading-edge geometry is an important factor for defining flow characteristics and could be manipulated for improved performance. The effects of flow interaction with the leading-edge geometry on transition to turbulence and aerodynamic forces are more thoroughly explored and better explained in the following section.

E. Effect of leading-edge region corrugations

In the previous section we explored the effect of angle of attack on the flow field for the baseline corrugated airfoil at $Re_c = 3.4 \times 10^4$ and observed that the flow behavior at the leading-edge is particularly sensitive to interaction between the shear-layer and the first corrugation peak. In this section we further investigate the effect of the first peak by considering a case where the interaction has been removed (flat plate) and one in which the interaction with the peak has been enhanced (modified corrugated wing). As mentioned before, the modified geometry is identical to the baseline with the exception of the first corrugation peak which has been raised by $y/c = 0.0147$ as shown in Fig. 13.

First, the baseline geometry is compared with the flat plate at $\alpha = 8^\circ$ which was the highest angle of attack preserving body-conforming flow for the original corrugated airfoil. Observing the time-mean streamlines in Fig. 14 shows that large-scale separation has already occurred for the flat plate at this angle. Consistent with observations by Murphy and Hu¹³, the corrugated geometry can help to delay separation compared to a flat plate. The physics associated with this phenomenon is examined further here.

The result of shear layer-body interaction is demonstrated in the contours of instantaneous spanwise vorticity in Fig. 15 were the vortex sheet of the baseline corrugated airfoil rolls-up much earlier than the flat plate and exhibits the formation of small-scale structures upstream of the first peak. These small structures are then pulled into the first valley as they pass over the peak through the recirculation formed in this region. Alternatively, the flat plate vortex sheet rolls up further away from the wing body and small-scale structures develop further away from the surface. The general location of transition is better depicted using the contours of time-mean TKE in Fig. 16. Here, highly unsteady flow appears up-

wind of the first peak close to the corrugated wing surface whereas high levels of TKE form far away from the flat plate and further downstream. Without the leading-edge corrugation mechanism which promotes shear-layer instabilities, the flat plate is not capable of effectively utilizing turbulence to prevent large-scale separation at this low Reynolds number.

Time-averaged aerodynamic forces for the flat plate are compared to the baseline geometry in Table IV. Compared to the flat plate at $\alpha = 8^\circ$, the baseline corrugated airfoil has a much higher lift and a smaller drag. The improved aerodynamics of the corrugated airfoil results in a much higher lift-to-drag ratio indicating favorable performance compared to the flat plate at this particular angle of attack and is a direct consequence of delayed aerodynamic stall. In order to better understand the role of surface stresses on the drag of a corrugated wing, the time-averaged drag coefficient was decomposed into its pressure, \bar{C}_{D_p} , and shear, \bar{C}_{D_s} , components which are also provided in Table IV. Similar to the observations presented in Vargas *et al.*¹⁶, recirculation in the corrugation valleys appears to reduce the shear stress component of drag for the corrugated wing. However, this particular drag-reducing effect is relatively minor compared to that observed in Ref. 16 in which the smaller Reynolds number used can be expected to result in more significant shear stress contributions. Overall, the consistently larger values of \bar{C}_{D_p} demonstrates the dominance of pressure stresses on airfoil drag at this higher Reynolds number.

TABLE IV: Time-mean aerodynamic forces of alternate geometries compared to baseline airfoil ($Re_c = 3.4 \times 10^4$)

Geometry	α	\bar{C}_L	\bar{C}_D	\bar{C}_{D_p}	\bar{C}_{D_s}	\bar{L}/\bar{D}
Flat plate	8°	0.6788	0.1381	0.1313	0.0068	4.915
Baseline corrugated	8°	0.8279	0.1132	0.1113	0.0019	7.314
Flat Plate	10°	0.7053	0.1726	0.1645	0.0080	4.089
Baseline corrugated	10°	0.7290	0.1802	0.1776	0.0027	4.046
Modified corrugated	10°	0.9705	0.1154	0.1141	0.0013	8.410

The effects due to interaction between the shear layer and corrugation peaks is further demonstrated by removing shear layer-corrugation interaction using a higher angle of attack ($\alpha = 10^\circ$) which is a post-stall regime for both the baseline corrugated wing and the flat

plate. Here, separation at the leading-edge has moved the shear layer sufficiently far away from the corrugation peaks due to the higher angle of attack. See, for instance, the first dividing streamline emanating from the leading-edge in Fig. 17 which largely overshoots the first corrugation peak. At the current angle of attack, both airfoils exhibit flow structure that is exceptionally similar for all quantities presented in Figs. 17-20. In fact, the gliding ratios are essentially the same (Table IV) indicating no benefit from the corrugation mechanisms. Consequently, any advantage gained by shear layer-corrugation interaction is diminished and the baseline geometry behaves as if it were a flat plate.

Shear layer-corrugation interaction can be reproduced at this larger α by simply increasing the height of the first corrugation peak, as in the modified geometry. For example, the steeper first peak of the modified corrugated airfoil penetrates further into the separated region above the leading-edge and reduces the distance between the shear layer and the airfoil body, Fig. 17. The contours of instantaneous spanwise vorticity in Fig. 18 show that the leading-edge vortex sheet directly interacts with the modified first corrugation peak. This enhanced level of interaction recovers the strong time-averaged recirculation region upwind of the first peak shown in Fig. 17 for the modified airfoil which contributes to spanwise instabilities. Consequently, this effect produces an earlier onset of turbulence shown in Fig. 19 and an enhanced ability to prevent aerodynamic stall at this angle of attack.

Such a simple difference in geometry produces significant changes in the general flow structure that can be very beneficial. The advantage of raising the first corrugation peak can be further illustrated by comparing the time-averaged aerodynamic forces of the three geometries in Table IV at $\alpha = 10^\circ$. While the flat plate and baseline corrugated airfoil are very similar, the lift and drag coefficients produced by the modified geometry are markedly advantageous resulting in a significantly enhanced lift-to-drag ratio. In fact, adjusting the first corrugation peak increased lift to the largest value observed in this study and reduced the drag to a value comparable to the baseline geometry at 8° .

In the previous section, suction contained between the leading-edge and first corrugation peak was shown to be related to the recirculation upstream of the first corrugation surface. The combination of this low pressure and the unusual orientation of the first corrugation surface produces a new effect that is a beneficial consequence of shear layer-corrugation interaction. Due to the forward orientation of this surface, the local distribution of normal forces imposed by the suction are tilted upstream and serve to reduce drag. Table V shows

the contribution to drag due to pressure forces along forward-facing surface of the first corrugation. This quantity, denoted as $\bar{C}_{D_p,partial}$, is defined by integrating the streamwise component of the pressure coefficient along the first corrugation's upstream-oriented surface between $0.066 \leq x/c \leq 0.124$. Values for the baseline geometry at all angles of attack studied are presented in addition to the modified profile at $\alpha = 10^\circ$. $\bar{C}_{D_p,partial}$ is shown to be negative for both wings at all angles of attack presented demonstrating a local drag-reducing effect along this surface. As expected, the minimum values of $\bar{C}_{D_p,partial}$ for the baseline airfoil occurs at $\alpha = 7^\circ$ which corresponds with the lowest pressure (Fig. 10) and the largest gliding-ratio (Table III). The magnitude of the upstream-oriented force, imposed by the leading-edge region suction, decreases rapidly for post-stall angles of attack corresponding with two factors: a reduced shear-layer corrugation interaction and a reorientation of the forward-facing surface that becomes less favorable with increasing angle of attack.

Although the baseline profile demonstrates a drag-reducing effect along the first inclined surface, this mechanism is hardly utilized to its fullest capacity. Simple modifications in the leading-edge geometry can better optimize shear layer-corrugation interaction and improve lift-to-drag ratios. For example, at $\alpha = 10^\circ$ the raised corrugation height of the modified airfoil retains the shear layer-corrugation interaction and produces enhanced suction (Fig. 20) exceeding the strongest low-pressure region observed for the baseline airfoil at any angle of attack (Fig. 10). Furthermore, the steeper peak of the modified corrugation elicits a more favorable forward-facing orientation of the airfoil surface which amplifies the local drag-reducing effect. As a result, $\bar{C}_{D_p,partial}$ for the modified wing is 80% larger than the best value produced by the baseline airfoil.

TABLE V: Contribution to the time-mean drag coefficient from pressure along the forward-facing surface of the first peak ($Re_c = 3.4 \times 10^4$)

Geometry	α	$\bar{C}_{D_p,partial}$
Baseline corrugated	5°	-0.0390
	7°	-0.0484
	8°	-0.0439
	9°	-0.0325
	10°	-0.0208
	Modified corrugated	10° -0.0875

The simple geometric modification investigated in the present section further demonstrates that flow behavior can be strongly affected by the leading-edge configuration. Corrugated geometries could be optimized for different operating conditions to produce the most favorable results. For instance, increasing corrugation peaks by the proper amount at higher angles of attack can delay separation and produce high gliding ratios by improving lift and reducing drag. Since there is no large-scale separation at lower angles of attack, the corrugations can be lowered to decrease drag by reducing the wake size. These effects of wing geometry could be actively exploited in flight for different angles of attack by contracting or extending leading-edge corrugations through a morphing wing configuration.

F. Effect of Reynolds number

In order to more clearly understand the effects of transition for corrugated wings, computations were performed for the baseline corrugated airfoil at a fixed angle of attack, $\alpha = 5^\circ$, for a large range of Reynolds numbers, $5 \times 10^3 \leq Re_c \leq 5.8 \times 10^4$. Additional results for a higher angle of attack, $\alpha = 10^\circ$, are provided in Ref. 37. The instantaneous flow field is visualized for several Reynolds numbers using iso-surfaces of the Q-criterion in Fig. 21 and instantaneous contours of spanwise vorticity in Fig. 22 which qualitatively show how the general flow structure changes for each case. For the lowest Reynolds number, $Re_c = 5 \times 10^3$, the shear layer is shown to roll up into large spanwise coherent vortices close to the trailing-edge.

Here, the flow field is essentially laminar and exhibits no three-dimensionality of the flow structure in the Q-criterion iso-surfaces. Raising the Reynolds number to $Re_c = 7.5 \times 10^3$ increases the shear layer roll-up frequency and advances the shear layer roll-up upstream to the second corrugation valley. As these coherent vortices shed downstream, spanwise instabilities begin to appear near the trailing-edge where three-dimensional effects become apparent. The authors have previously shown the effects of three-dimensionality become significant in computations as early as $Re_c = 7.5 \times 10^3$ in Ref. 37.

At a slightly higher Reynolds number, $Re_c = 1 \times 10^4$, spanwise instabilities appear much further upstream beginning in the first corrugation valley. These instabilities result in a break down of the coherent vortices into smaller-scale structures as they traverse the second valley. When the Reynolds number is further increased, $Re_c = 2 \times 10^4$, transition continues to advance toward the leading-edge of the airfoil beginning at the first valley. Eventually, turbulence appears in front of the first corrugation peak at $Re_c = 3.4 \times 10^4$. Beginning at $Re_c = 2.0 \times 10^4$ the flow appears to be fully turbulent everywhere past transition with small-scale structures reducing in size as the Reynolds number increases. Similar unsteady features appear on the pressure surface beginning at $Re_c = 2 \times 10^4$ and move toward the leading-edge with increasing Reynolds number. However, this upstream advancement of lower-surface turbulence occurs slowly compared to that observed on the upper surface.

Contours of TKE are shown in Fig. 23 which provide for a clearer visualization of the onset of transition for each case. At the lowest Reynolds number, $Re_c = 5 \times 10^3$, the TKE shows little energy along the upper surface of the airfoil corresponding with the lack of transitional flow for this case. An increased level of TKE near the trailing-edge at $Re_c = 7.5 \times 10^3$ is indicative of the instabilities in the coherent vortices observed previously from the Q-criterion iso-surfaces. The presence of corrugations appears to promote the formation of spanwise instabilities in coherent vortices, even at this low Reynolds number. This effect is further demonstrated due to a rapid advancement of transitional flow toward the leading-edge with increase in Reynolds number. For instance, transition to turbulence is apparent in the TKE following the second valley for $Re_c = 1 \times 10^4$ while these instabilities quickly advance toward the leading-edge at $Re_c = 3.4 \times 10^4$. Beyond $Re_c \geq 3.4 \times 10^4$, only insignificant changes in both the location of transition and the form of the TKE are apparent which shows a decreasing dependence on Reynolds number beyond this point. In fact, all quantities evaluated in Figs. 21-25 are nearly identical for the two highest Reynolds

numbers. This observation of Reynolds number saturation is consistent with that presented in Murphy and Hu¹³ for $Re_c \geq 5.8 \times 10^4$.

Next, time-averaged streamlines and velocity magnitude contours are depicted in Fig. 24 which demonstrate the change in flow field with Reynolds number. At the lowest values, $Re_c = 5 \times 10^3$ and 7.5×10^3 , the laminar flow is not as capable of advancing against the adverse pressure gradient and a shallow separation bubble spans the aft-portion of the airfoil. This bubble decreases with increasing Reynolds number and disappears as transition develops allowing the flow field to better advance against the adverse pressure gradient and adhere to the corrugated airfoil's virtual profile. The free stream begins following the virtual profile everywhere at $Re_c = 1 \times 10^4$ correlating with the advancement of transition to the second valley. Very little difference is observed in the time-mean streamlines as the flow consistently adheres to the effective shape at the higher Reynolds numbers considered, $Re_c \geq 1 \times 10^4$. Clearly, the influence of corrugations near the leading-edge in promoting early transition to turbulence plays an important role in preventing stall for these airfoils and appears to be the dominant factor. The particular downstream geometry of the present corrugated wing appears to provide little to no observable aerodynamic benefit.

In the previous section, suction along the upstream surface of the first corrugation was shown to be a favorable drag-reducing consequence of the unusual geometry. The change in this effect with Reynolds number is explored here by looking at the time-mean pressure coefficient contours in the leading-edge region for several Reynolds numbers in Fig. 25. For $Re_c = 5 \times 10^3$, suction in the leading-edge region is very weak, but quickly increases with Reynolds number. It appears that benefits from low pressure over the leading-edge are diminished at very low Reynolds numbers. Hence, in addition to the lack of transition, very low Reynolds number conditions fail to elicit a second favorable effect of corrugations. Absence of these features helps to explain the unfavorable performance of corrugated airfoil sections observed by Hord and Lian¹⁰ at very low Reynolds numbers in which laminar flow prevails.

Finally, the aerodynamic forces for the corrugated airfoil at each Reynolds number are provided in Table VI. Here, drag coefficients are highest at the lowest Reynolds number due in part to the larger effective profile generated by the aft-region separation bubble and the reduced effect of suction in the leading-edge region. These factors serve to reduce drag coefficients with increasing Reynolds number until $Re_c = 1 \times 10^4$ where the highest gliding-

ratio occurs among the Reynolds numbers considered. Lift coefficients are shown to increase with Re_c with the exception of a local maximum at $Re_c = 7.5 \times 10^3$. The drag coefficient increases for $Re_c \geq 2 \times 10^4$ corresponding with the appearance of transition on the lower surface.

TABLE VI: Aerodynamic forces with Reynolds number at $\alpha = 5^\circ$

Re_c	\bar{C}_L	\bar{C}_D	\bar{L}/\bar{D}
5.0×10^3	0.5262	0.0822	6.401
7.5×10^3	0.6517	0.0681	9.570
1.0×10^4	0.5880	0.0600	9.800
2.0×10^4	0.6008	0.0675	8.901
3.4×10^4	0.6016	0.0795	7.567
5.8×10^4	0.6172	0.0804	7.677

VI. CONCLUSIONS

A numerical study was conducted on a bio-inspired corrugated airfoil using the high-fidelity ILES research code *FDL3DI*. The effects of angle of attack and Reynolds number were studied over the ranges of $\alpha = 5^\circ$ to 10° and $Re_c = 5 \times 10^3$ to 5.8×10^4 respectively. This work is the first three-dimensional computational study of bio-inspired corrugated wing sections to the authors' knowledge and considers Reynolds numbers bridging the low values considered in previous numerical investigations with higher values presented in recent detailed experiments.

Two significant findings resulted from this work. First, a new drag-reducing effect was demonstrated as a consequence of the unique corrugated geometry. The separation region between the leading-edge and first corrugation promotes rapid turning of fluid around the leading-edge. A strong suction region forms as a result along the forward-facing surface of the first corrugation. Due to the unusual orientation of the corrugation surface, the local pressure forces not only enhance lift but also reduce drag. Gliding ratios were shown to improve with the strength of this low pressure region. This effect appears to be most effectively employed for Reynolds numbers where transitional flow is apparent. Further

exploration into improved geometries is likely to result in more optimal benefits for low Reynolds number wings.

Second, interaction between the shear layer and the leading-edge corrugations plays an important role in promoting early transition to turbulence. The presence of corrugations induces recirculation near the first peak promoting instabilities in the vortex sheet emanating from the leading-edge. Shear layer-corrugation interaction can be reduced by either removing the corrugations or increasing the angle of attack. In both cases, transition is delayed and aerodynamic stall ensues. Interaction can be enhanced and exploited by raising the first corrugation peak to capture the shear layer at higher angles of attack further delaying stall.

The importance of transition, which is strongly influenced by corrugations, is shown to be a dominant factor in delaying stall for these airfoils, even at Reynolds numbers as low as $Re_c = 1 \times 10^4$. Large separation bubbles form for the lowest Reynolds numbers at the lowest angle of attack considered. Because transitional flow is more resistent to adverse pressure gradients it can delay or reduce flow separation. This effect is demonstrated by the disappearance of a large separation bubble coinciding with transition as Reynolds number is increased. Previous studies have generally found corrugated wings provide little benefit compared to a flat plate in very low Reynolds number regimes in which laminar flow prevails. However, these bio-inspired geometries can employ early transition to turbulence at Reynolds numbers practical for small unmanned air systems.

The present work demonstrates that flow behavior for the current bio-inspired wing sections is highly sensitive to the leading-edge configuration. Such a simple modification as raising the first corrugation peak results in further stall delay and greatly enhanced gliding ratios compared to a flat plate. The leading-edge corrugations are of particular importance and could be optimized to properly manipulate flow at higher angles of attack and improve gliding ratios. These could be further exploited for changing flow conditions in flight through a morphing wing configuration.

ACKNOWLEDGMENTS

This work was supported in part by AFOSR under a task monitored by Dr. D. Smith. This project was also supported in part by a grant of HPC time from the DoD HPC Major Shared Resource Center at AFRL, WPAFB. The authors are also grateful to Dr. Hui Hu

for providing experimental data.

REFERENCES

¹M. Gad-el-Hak, "Micro-air-vehicles: Can they be controlled better?," *J. Aircraft* **38**, 419–429 (2001).

²D. J. Pines and F. Bhorquez, "Challenges facing future micro-air-vehicle development," *J. Aircraft* **43**, 290–305 (2006).

³J. H. McMasters and M. L. Henderson, "Low speed single element airfoil synthesis," *Technical Soaring* **6**, 1–21 (1980).

⁴J. M. Wakeling and C. P. Ellington, "Dragonfly flight i. gliding flight and steady-state aerodynamic forces," *J. Exp. Biol.* **200**, 543–556 (1997).

⁵B. G. Newman, S. B. Savage, and D. Schouella, "Model test on a wing section of a aeshna dragonfly," *Scale Effects in Animal Locomotion*, 445–477(1977).

⁶C. J. C. Rees, "Aerodynamic properties of an insect wing section and a smooth aerofoil compared," *Nature* **258**, 141–142 (1975).

⁷R. Rudolph, "Aerodynamics properties of libellula quadrimaculata l. (anisoptera: Libellulidae), and the flow around smooth and corrugated wing section models during gliding flight," *Odonatologica* **7**, 49–58 (1977).

⁸M. Okamoto, K. Yasuda, and A. Azuma, "Aerodynamic characteristics of the wings and body of a dragonfly," *J. Theor. Biol.* **199**, 281–294 (1996).

⁹A. B. Kesel, U. Philippi, and W. Nachtigall, "Biomechanical aspects of the insect wing: An analysis using the finite element method," *Comput. Biol. and Med.* **28**, 423–437 (1998).

¹⁰K. Hord and Y. Lian, "Numerical investigation of the aerodynamic and structural characteristics of a corrugated airfoil," *J. Aircraft* **49**, 749–757 (2012).

¹¹A. B. Kesel, "Aerodynamic characteristics of the wings and body of a dragonfly," *J. Exp. Biol.* **203**, 3125–3135 (2000).

¹²H. Hu and M. Tamai, "Bioinspired corrugated airfoil at low reynolds numbers," *J. Aircraft* **45**, 2068–2077 (2008).

¹³J. T. Murphy and H. Hu, "An experimental study of a bio-inspired corrugated airfoil for micro air vehicle applications," *Exp. Fluids* **49**, 531–546 (2010).

¹⁴M. Tamai, Z. Wang, G. Rajagopalan, H. Hu, and G. He, "Aerodynamic performance of

a corrugated dragonfly airfoil compared with smooth airfoils at low reynolds numbers,” AIAA Paper 2007-483 (AIAA, 2007).

¹⁵A. Vargas and R. Mittal, “Aerodynamic performance of biological airfoils,” AIAA Paper 2004-2319 (AIAA, 2004).

¹⁶A. Vargas, R. Mittal, and H. Dong, “A computational study of the aerodynamic performance of a dragonfly wing section in gliding flight,” *Bioinspir. Biomim.* **3**, 1–13 (2008).

¹⁷W. Kim, J. Ko, H. Park, and D. Byun, “Effects of corrugation of the dragonfly wing on gliding performance,” *J. Theor. Biol.* **26**, 523–530 (2009).

¹⁸K. Hord and Y. Lian, “Numerical investigation of the aerodynamic and structural characteristics of a corrugated airfoil,” AIAA Paper 2010-4624 (AIAA, 2010).

¹⁹M. Vinokur, “Conservation equations of gasdynamics in curvilinear coordinate systems,” *J. Comput. Phys.* **14**, 105–125 (1974).

²⁰J. L. Steger, “Implicit finite-difference simulation of flow about arbitrary two-dimensional geometries,” *AIAA J.* **16**, 679–686 (1978).

²¹D. A. Anderson, J. C. Tannehill, and R. H. Pletcher, *Computational Fluid Mechanics and Heat Transfer* (McGraw-Hill Book Company, 1984).

²²M. R. Visbal and D. P. Rizzetta, “Large-eddy simulation on curvilinear grids using compact differencing and filtering schemes,” *J. of Fluids Eng.* **124**, 836–847 (2002).

²³M. R. Visbal, P. E. Morgan, and D. P. Rizzetta, “An implicit les approach based on high-order compact differencing and filtering schemes,” AIAA Paper 2003-4098 (AIAA, 2003).

²⁴S. Stolz and N. Adams, “An approximate deconvolution procedure for large-eddy simulation,” *Phys. Fluids* **11**, 1699–1701 (1999).

²⁵J. Mathew, R. Lechner, H. Foysi, J. Sesterhenn, and R. Friedrich, “An explicit filtering method for les of compressible flows,” *Phys. Fluids* **15**, 2279–2289 (2003).

²⁶M. R. Visbal and D. V. Gaitonde, “High-order accurate methods for complex unsteady subsonic flows,” *AIAA J.* **37**, 1231–1239 (1999).

²⁷D. V. Gaitonde and M. R. Visbal, “High-order schemes for navier-stokes equations: Algorithm and implementation into FDL3DI,” Technical Report AFRL-VI-WP-TR-1998-3060 (Air Force Research Laboratory, Wright-Patterson AFB, 1998).

²⁸S. Lele, “Compact finite difference schemes with spectral-like resolution,” *J. Comput. Phys.* **103**, 16–42 (1992).

²⁹D. Gaitonde and M. Visbal, “Further development of a navier-stokes solution procedure based on higher-order formulas,” AIAA Paper 1999-0557 (AIAA, 1999).

³⁰P. Alpert, “Implicit filtering in conjunction with explicit filtering,” *J. Comput. Phys.* **44**, 212–219 (1981).

³¹D. J. Garmann, M. R. Visbal, and P. D. Orkwis, “Comparative study of implicit and subgrid-scale model large-eddy simulation techniques for low-reynolds number airfoil applications,” *Int. J. Numer. Methods Fluids* **71**, 1546–1565 (2012).

³²R. Beam and R. Warming, “An implicit factored scheme for the compressible navier-stokes equations,” *AIAA J.* **16**, 393–402 (1978).

³³T. Pulliam and D. Chaussee, “A diagonal form of an implicit approximate-factored algorithm,” *J. Comput. Phys.* **17**, 347–363 (1981).

³⁴D. P. Rizzetta, M. R. Visbal, and P. E. Morgan, “A high-order compact finite-difference scheme for large-eddy simulation of active flow control (invited),” AIAA Paper 2008-526 (AIAA, 2008).

³⁵M. R. Visbal and D. V. Gaitonde, “Very high-order spatially implicit schemes for computational acoustics on curvilinear meshes,” *J. Comput. Acoust.* **9**, 1259–1286 (2001).

³⁶D. A. Olson, *Facility and Flow Dependence Issues Influencing the Experimental Characterization of a Laminar Separation Bubble at Low Reynolds Number*, Master’s thesis, Michigan State University (2011).

³⁷C. Barnes and M. Visbal, “High fidelity simulations of a corrugated airfoil,” AIAA Paper 2012-0753 (AIAA, 2012).

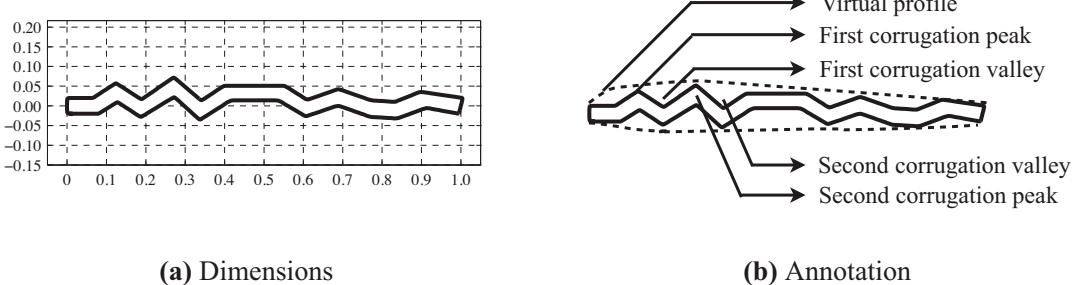


FIG. 1: Corrugated airfoil geometry dimensions and terminology

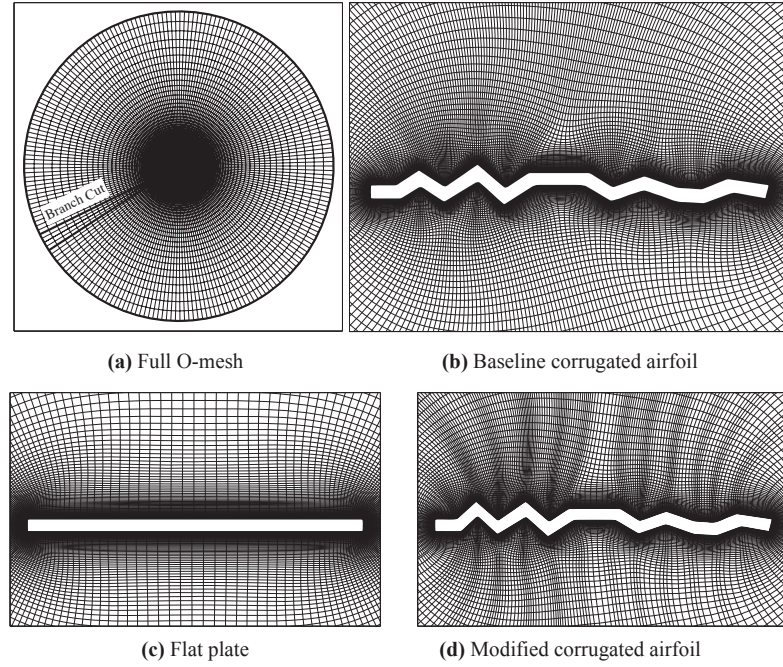


FIG. 2: Selected views of the computational meshes

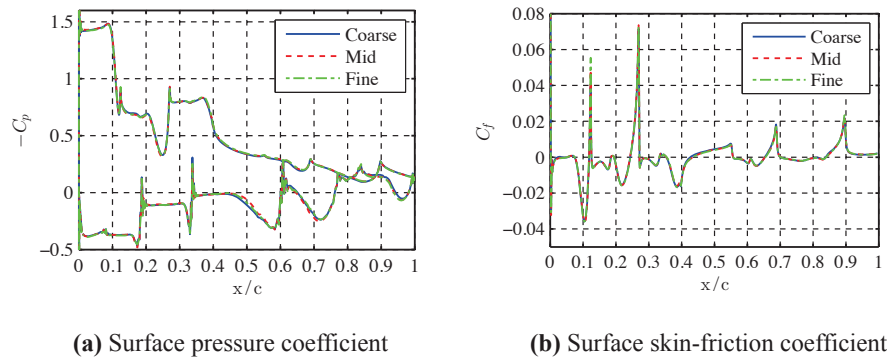


FIG. 3: Effect of grid resolution on surface forces at $Re_c = 3.4 \times 10^4$ and $\alpha = 5^\circ$, (a) time-mean surface C_p and (b) time-mean suction-side C_f .

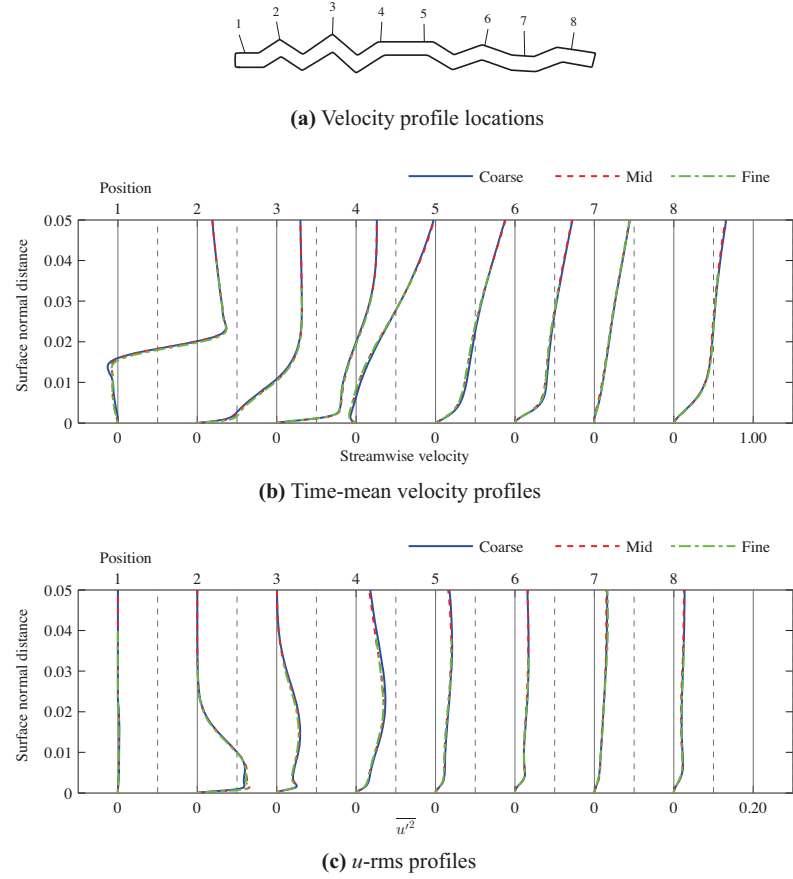
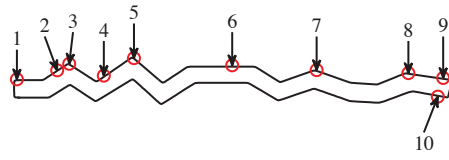
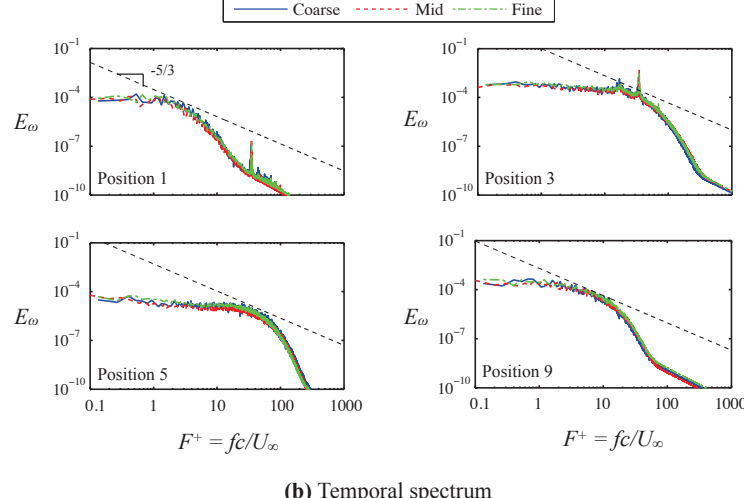


FIG. 4: Effect of grid resolution at (a) selected profile lines normal to the wing surface for (b) time-mean streamwise velocity profiles and (c) mean-squared fluctuation u -velocity profiles at $Re_c = 3.4 \times 10^4$ and $\alpha = 5^\circ$



(a) Velocity probe locations



(b) Temporal spectrum

FIG. 5: Effect of grid resolution at (a) selected velocity probe locations for (b) temporal energy spectra at selected chord-wise positions for $Re_c = 3.4 \times 10^4$ and $\alpha = 5^\circ$

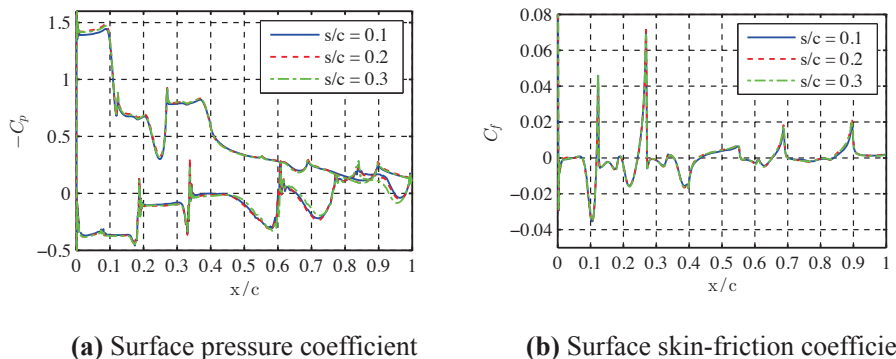


FIG. 6: Effect of spanwise extent at $Re_c = 3.4 \times 10^4$ and $\alpha = 5^\circ$ for (a) time-mean surface C_p and (b) time-mean suction-side C_f

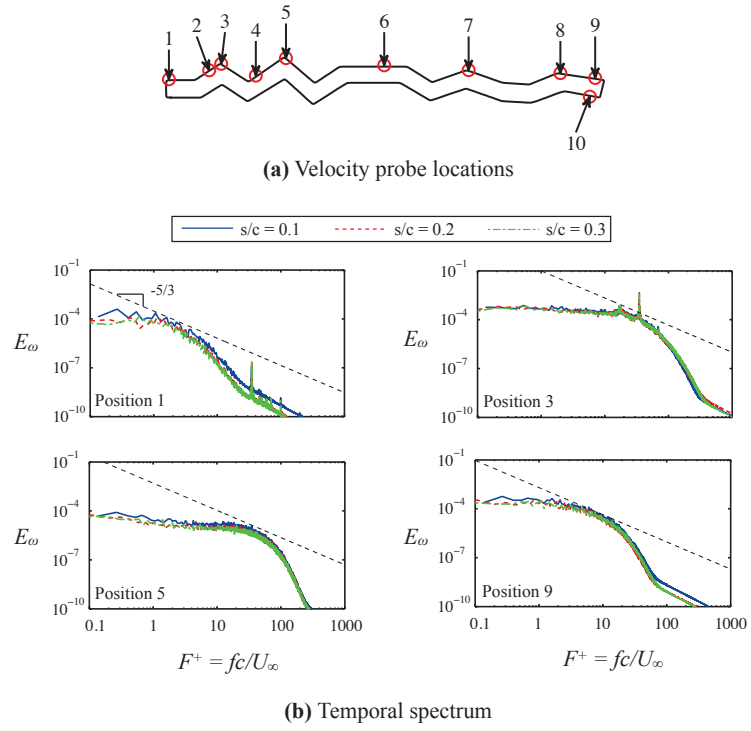


FIG. 7: Effect of span-wise extent at (a) selected velocity probe locations for (b) kinetic energy temporal frequency spectra at $Re_c = 3.4 \times 10^4$ and $\alpha = 5^\circ$

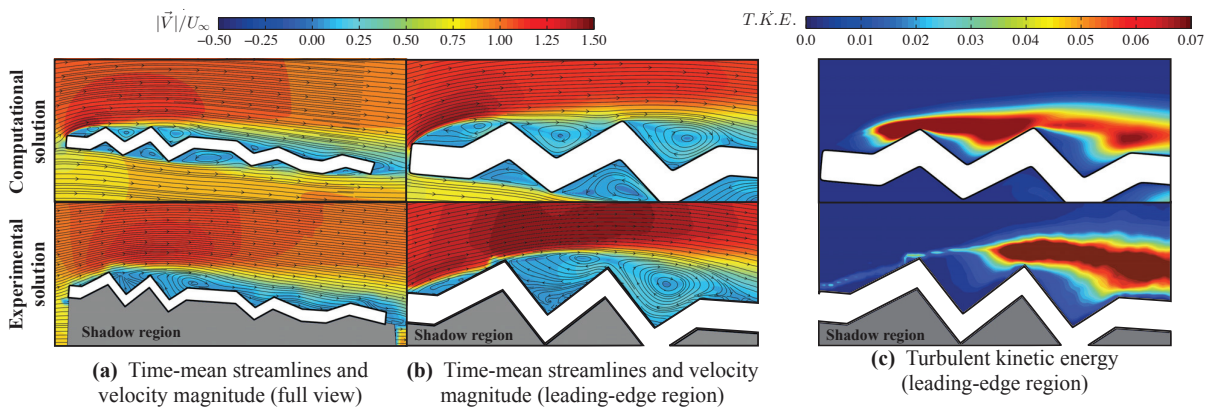
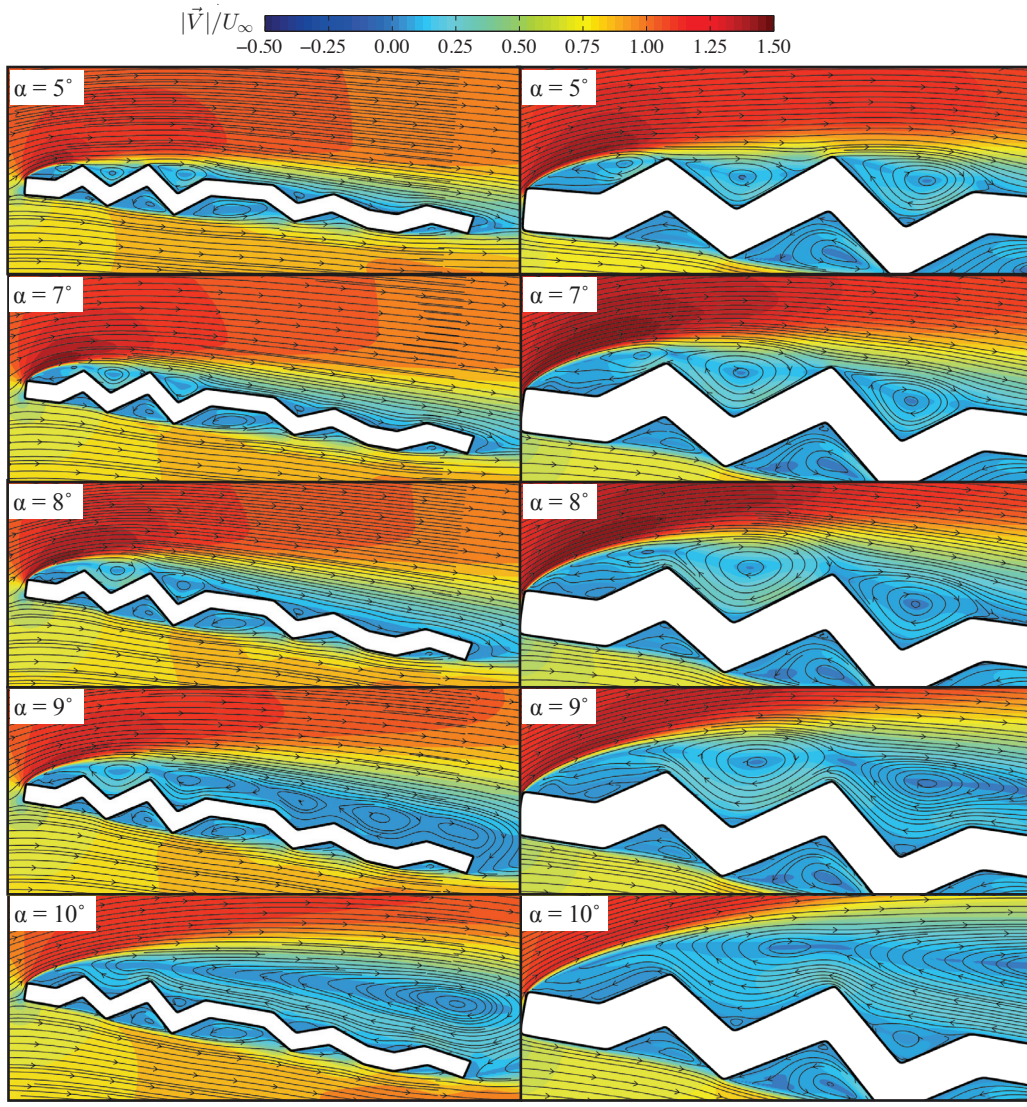


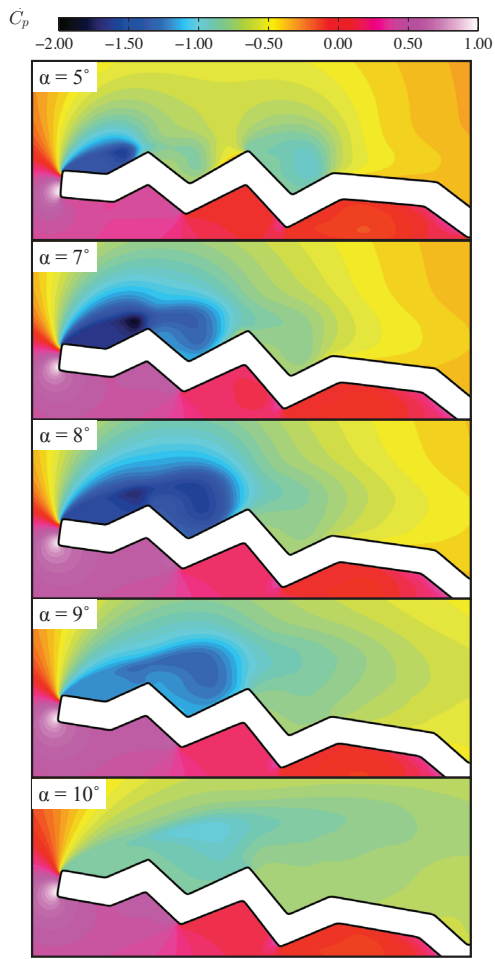
FIG. 8: Comparison of (a) time-mean streamlines and velocity magnitude contours and (b) TKE between computation and experiment at $Re_c = 3.4 \times 10^4$ and $\alpha = 5^\circ$



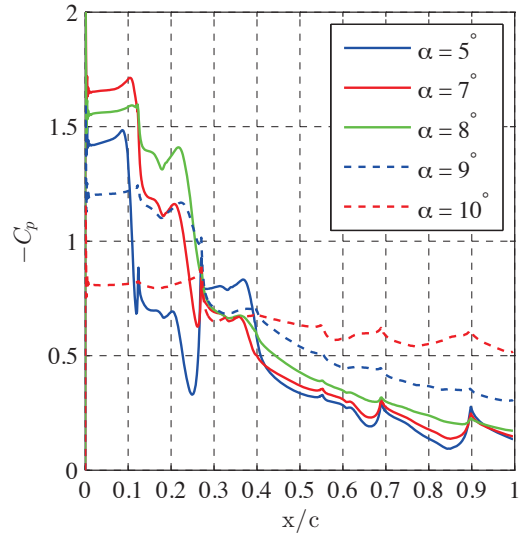
(a) Full airfoil view

(b) Close view of leading-edge

FIG. 9: Time-mean streamlines and velocity magnitude contours with increasing angle of attack showing (a) transformation of the virtual profile and large-scale separation and (b) flow structure near the leading-edge at $Re_c = 3.4 \times 10^4$



(a) Pressure coefficient contours



(b) Upper-surface pressure coefficient

FIG. 10: Time-mean (a) pressure coefficient contours and (b) pressure coefficient along the upper surface for various angles of attack at $Re_c = 3.4 \times 10^4$

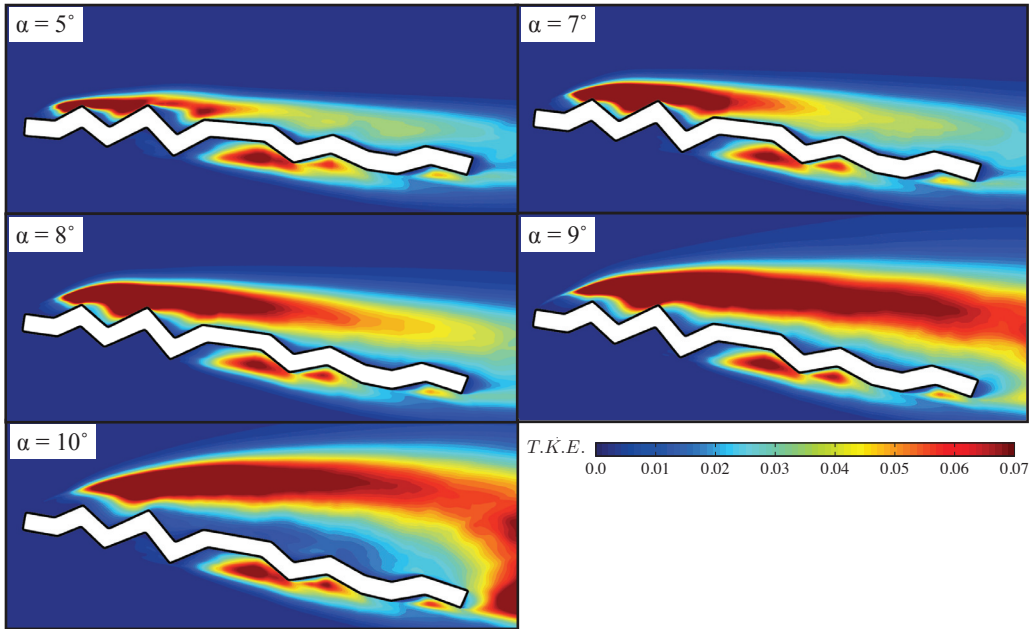


FIG. 11: Transformation of time-mean turbulent kinetic energy contours at the leading-edge with angle of attack at $Re_c = 3.4 \times 10^4$

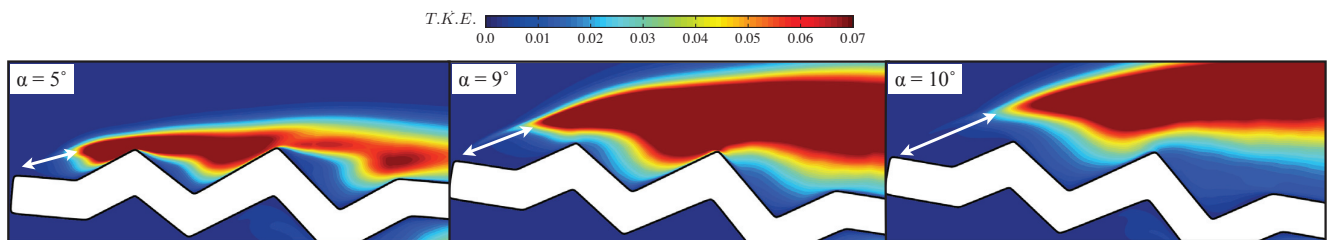


FIG. 12: Detailed view of TKE at $Re_c = 3.4 \times 10^4$ near the leading-edge for several angles of attack

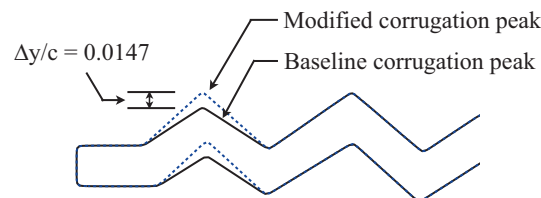


FIG. 13: Modification to the first corrugation peak

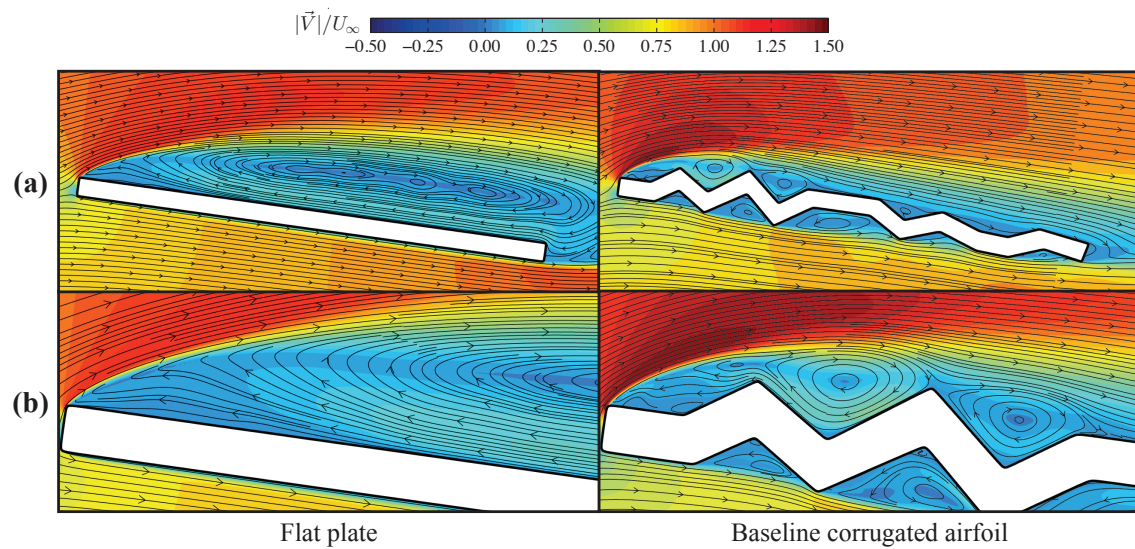


FIG. 14: Comparison of time-mean streamlines and velocity magnitude contours for (left) flat plate and (right) baseline corrugated airfoil at $Re_c = 3.4 \times 10^4$ and $\alpha = 8^\circ$

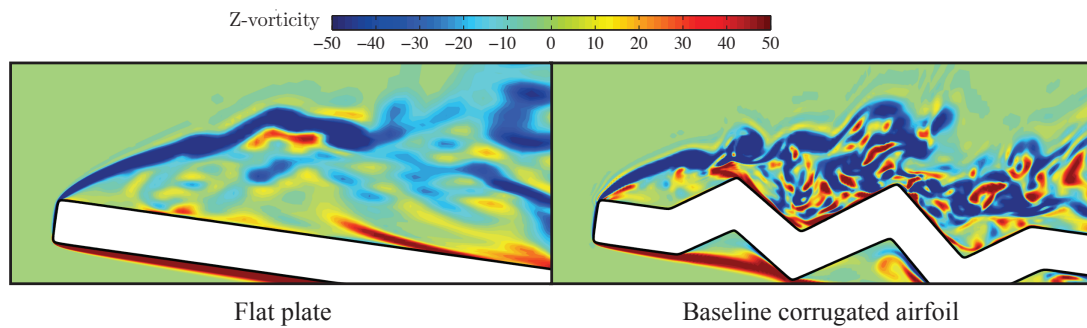


FIG. 15: Comparison of instantaneous spanwise vorticity contours for (left) flat plate and (right) baseline corrugated airfoil at $Re_c = 3.4 \times 10^4$ and $\alpha = 8^\circ$

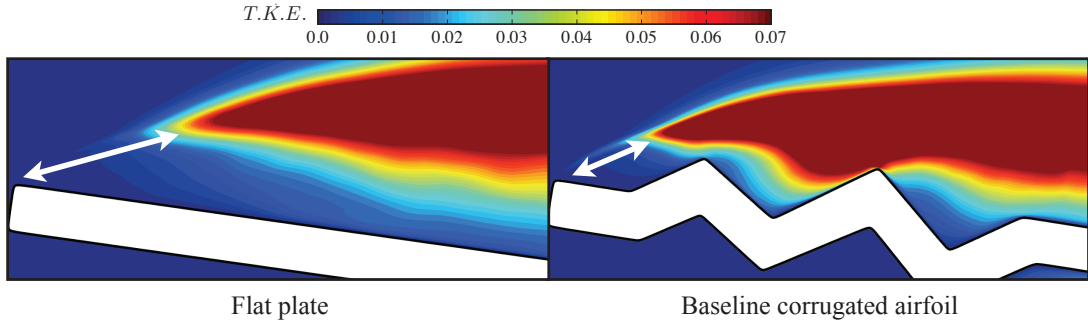


FIG. 16: Comparison of time-mean turbulent kinetic energy contours for (left) flat plate and (right) baseline corrugated at $Re_c = 3.4 \times 10^4$ and $\alpha = 8^\circ$

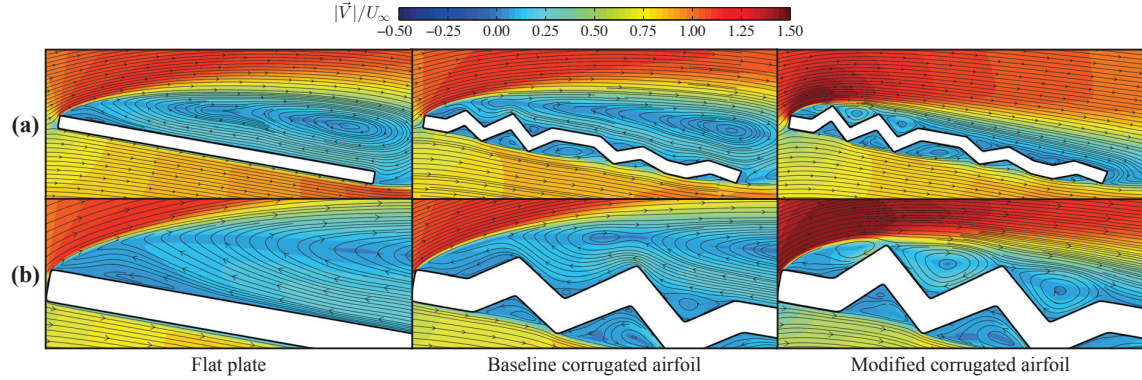


FIG. 17: Comparison of time-mean streamlines and velocity magnitude contours for (left) flat plate, (center) baseline corrugated airfoil, and (right) modified corrugated airfoil at $Re_c = 3.4 \times 10^4$ and $\alpha = 10^\circ$

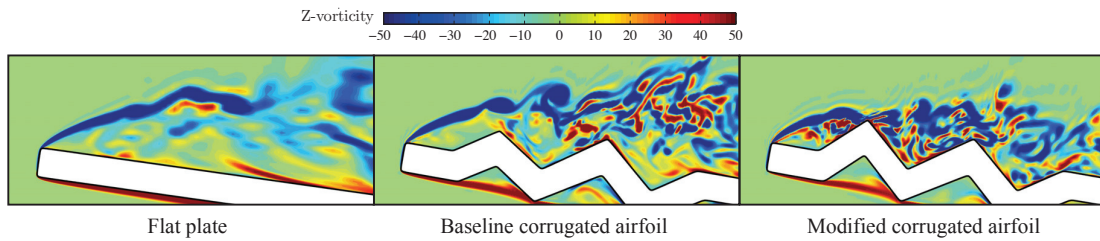


FIG. 18: Comparison of instantaneous spanwise vorticity contours for (left) flat plate, (center) baseline corrugated airfoil, and (right) modified corrugated airfoil at $Re_c = 3.4 \times 10^4$ and $\alpha = 10^\circ$

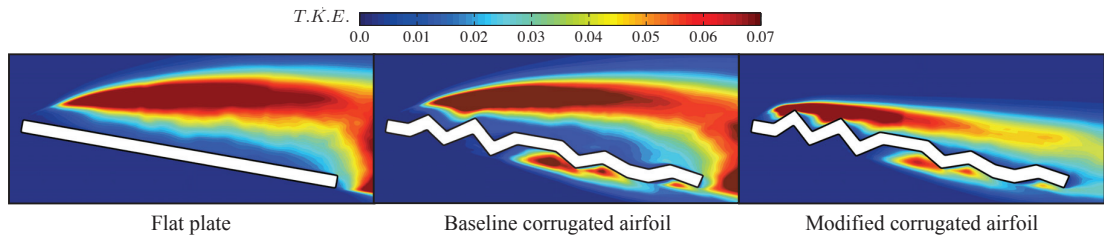


FIG. 19: Comparison of time-mean turbulent kinetic energy contours for (left) flat plate, (center) baseline corrugated airfoil, and (right) modified corrugated airfoil at $Re_c = 3.4 \times 10^4$ and $\alpha = 10^\circ$

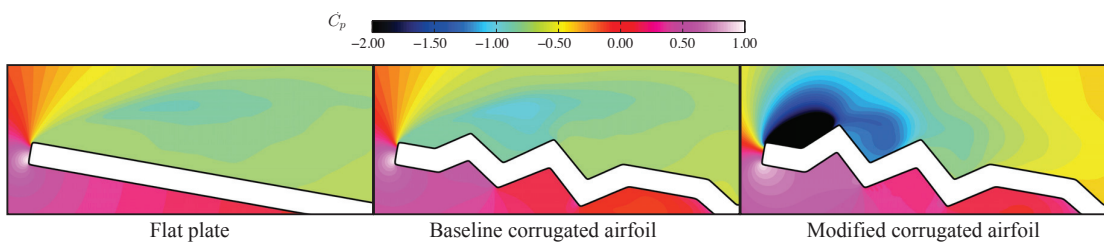


FIG. 20: Comparison of time-mean pressure coefficient contours for (left) flat plate, (center) baseline corrugated airfoil, and (right) modified corrugated airfoil at $Re_c = 3.4 \times 10^4$ and $\alpha = 10^\circ$

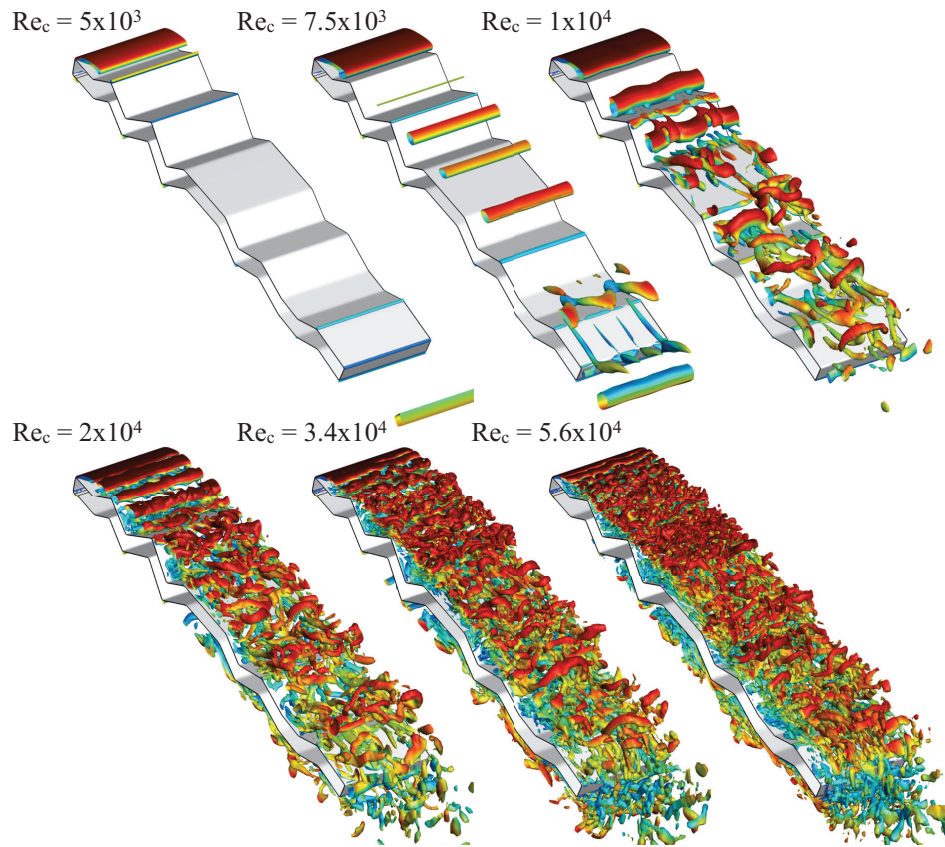


FIG. 21: Effect of Reynolds number on 3-D instantaneous iso-surfaces of Q-criterion ($Q = 200$, $\alpha = 5^\circ$), iso-surfaces colored by velocity magnitude.

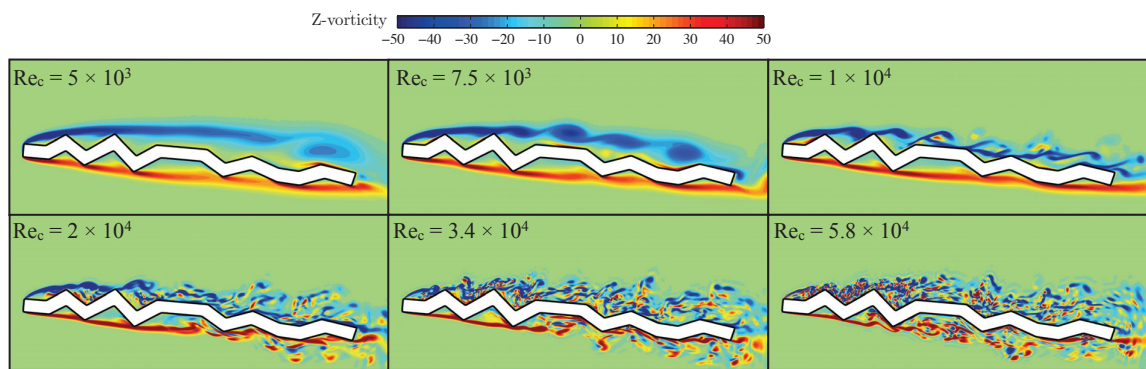


FIG. 22: Instantaneous spanwise-vorticity contours over $5 \times 10^3 \leq Re_c \leq 5.8 \times 10^4$ at $\alpha = 5^\circ$

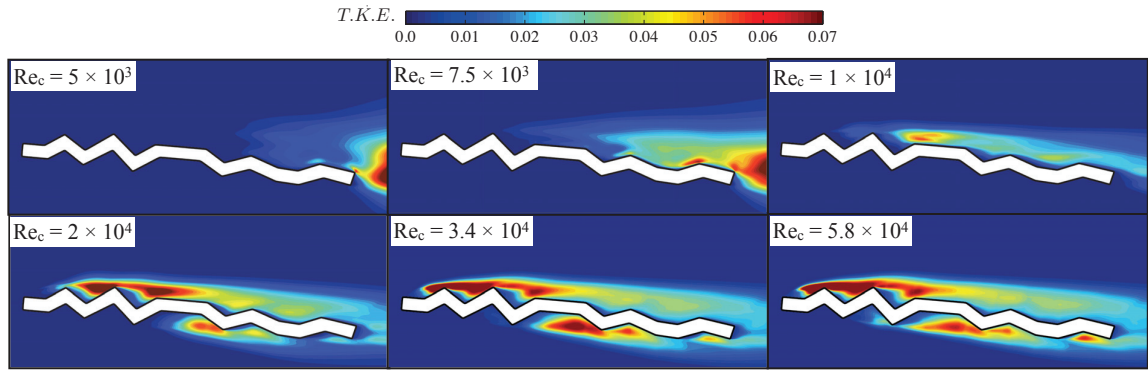


FIG. 23: Effect of Reynolds number on time-mean turbulent kinetic energy contours at $\alpha = 5^\circ$

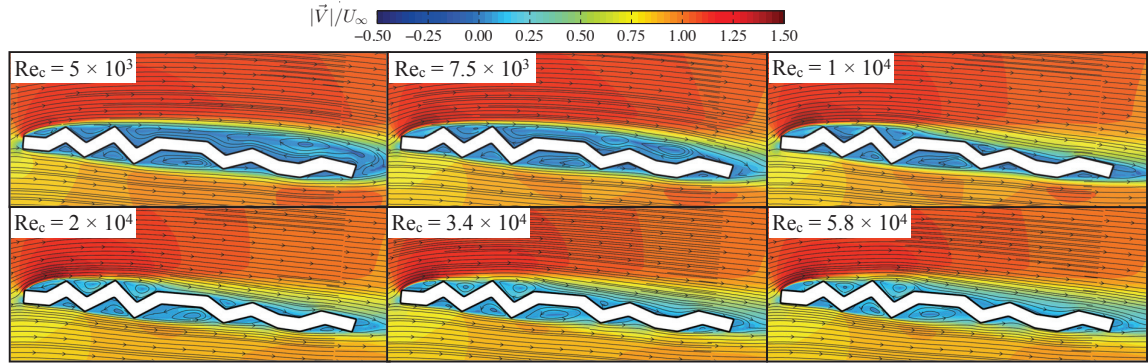


FIG. 24: Effect of Reynolds number on time-mean streamlines and velocity magnitude contours at $\alpha = 5^\circ$

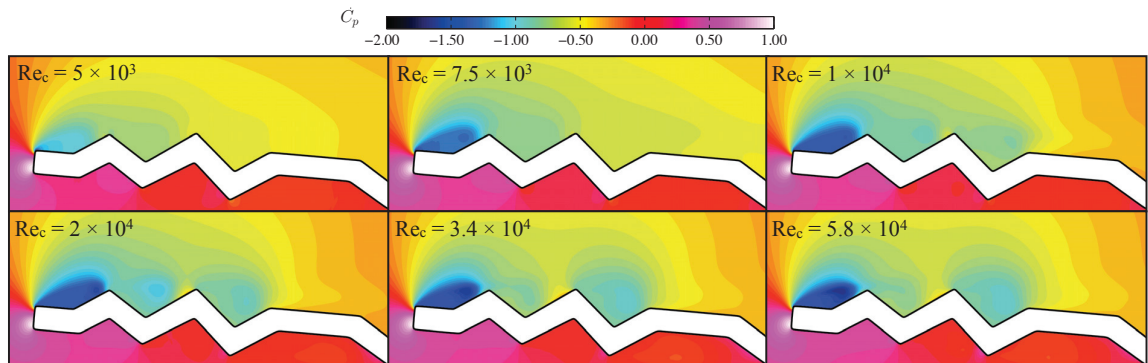


FIG. 25: Effect of Reynolds number on time-mean pressure coefficient contours at $\alpha = 5^\circ$

APPENDIX D

Investigation of aspect ratio and dynamic effects due to rotation for a revolving wing using high-fidelity simulation

Daniel J. Garmann* and Miguel R. Visbal†

Air Force Research Laboratory, Wright-Patterson AFB, OH 45433

Paul D. Orkwis‡

University of Cincinnati, Cincinnati, OH 45220

A numerical study is conducted to examine the vortex structure and aerodynamic loading on a unidirectionally revolving wing. Wings with aspect ratios of one, two, and four are simulated, and each wing is shown to generate a stable and coherent vortex system shortly after the onset of the motion. The proximity of the vortex to the surface of the wing promotes a strong region of suction along the leading edge that persists to the mid-span, regardless of aspect ratio. Past mid-span, the vortex lifts off the surface into an arch-type structure as it reorients itself along the tip. The highest aspect ratio wing promotes the development of substructures in the feeding sheet of the leading edge vortex. The origins of these features have been traced back to the eruption of near-wall vorticity underneath the vortex that disrupts the shear layer, causing the feeding sheet to roll-up into discrete substructures. For a fixed root-based Reynolds number of 1,000, the lower aspect ratio wings do not have sufficient spans for these transitional elements to manifest. The leading edge vortex grows proportionally to the distance from the rotational axis, so with higher aspect ratios, the chord-wise extent of the vortex becomes constrained by the trailing edge, leading to saturation of the aerodynamic loads. With $AR = 1$, the extent of the vortex never reaches the trailing edge, leading to a slight increase of the lift and drag coefficients throughout the motion. The centrifugal, Coriolis, and pressure gradient forces are also analyzed at several span-wise locations across each wing, where the centrifugal and pressure gradient forces are shown to be responsible for the span-wise flow around the suction side of the wing. The Coriolis force is observed to have a contribution at the base of the leading edge vortex directed away from the surface, indicating that Coriolis does not promote attachment of the vortex. As a means of emphasizing the importance of the centrifugal force on a revolving wing, the aspect-ratio-two wing is simulated with the addition of a source term in the governing equations to oppose and eliminate the centrifugal force near the wing surface. The initial formation and development of the leading edge vortex is unhindered by the absence of this force; however, later in the motion, the lifted-off portion of the vortex moves inboard. Without the opposing outboard centrifugal force to keep the separation past mid-span, the entire vortex eventually separates and moves away from the surface resulting in stall.

I. Introduction

The idea of a small, autonomous aircraft to perch, hover, or move inconspicuously through virtually any terrain has brought vast new possibilities to the areas of intelligence, surveillance, and reconnaissance. Along with these new possibilities, however, come many challenges in order to mimic the physics of biological flight of birds and insects. At relatively low speeds or even hover, flapping flight exhibits extremely unsteady and three-dimensional flow structure. The extensive range of pitching and plunging amplitudes of the flapping

*Aerospace Engineering Graduate Student and AIAA Member.

†Technical Area Leader. AIAA Fellow.

‡Professor, Aerospace Engineering. AIAA Associate Fellow.

wing induces the formation of large vortical structures, whose interactions can severely impact flight stability and performance without the use of a dynamic and responsive control system. In an attempt to quantify the complex aerodynamics of insect flight, several experimental reviews have been presented by, but not limited to, Ellington,¹ Dickinson,² Sane,³ Birch and Dickinson,⁴ Lehmann,⁵ and Lehmann and Pick.⁶ These reviews provide insight into the dominant mechanisms of lift enhancement for flapping wing flight produced from leading edge and tip vortex formation coupled with wing-wake/wing-wing interactions to create dynamic stall-like effects and favorable up-/down-wash that allow biological fliers such as birds and insects to sustain flight and maneuver.

Insect-type flight has been examined experimentally by many researchers for a range of motions including forward flight^{7,8} and maneuvering.⁹ Particular attention has been paid to the aerodynamics of hover through several experimental studies in recent years. Early experiments by Dickinson² suggest that the unsteady mechanisms generated by simple wing flips at the end of a flapping stroke provide a significant performance benefit to insect flight. This claim was reiterated in the work of Dickinson *et al.*,¹⁰ where direct force measurements of a wing undergoing a flapping motion suggest that the basis of insect flight can be generalized through three dynamic mechanisms: delayed stall, rotational circulation, and wake capture. Birch *et al.*¹¹ examined the delayed stall effect of a wing undergoing a swinging motion. Their results show the formation of an attached leading-edge vortex (LEV) with no trailing-edge shedding at very large angles of rotation (270°). This was observed over a range of Reynolds numbers (120 \leq Re \leq 1400) despite differences in flow structure, where increased Reynolds number promotes a spiral flow pattern in the axial direction within the core of the leading-edge vortex. Poelma *et al.*¹² found similar results in their experiments, where spanwise flow was not localized within the leading-edge vortex core. Instead, it was observed behind the wing suggesting that it leads to stability of the leading-edge vortex by draining circulation from the wing and balancing the vorticity generated by the leading-edge. The more recent works of Lentink and Dickinson^{13,14} further hypothesize that Coriolis acceleration is equally important for the attachment of the LEV. Their findings correlated the Rossby number (Ro), not the Reynolds number, with LEV attachment. Additionally, their results suggest that spanwise flow balances the formation of vorticity at the leading-edge by transporting it towards the tip. Ozen and Rockwell¹⁵ offer detailed experimental measurements of the flow structure around a rotating plate following the work of Lentink and Dickinson.¹⁴ Excellent flow visualizations about a revolving wing are provided in the experimental works of Carr *et al.*^{16,17} for various aspect ratio wings.

In each of the afore-mentioned studies, the attachment of the leading-edge vortex encountered on a rotating wing closely resembles the flow structure observed about a swept delta wing. A review of delta wing dynamics is provided, for example, by Lee and Ho¹⁸ and the references therein. Additionally, the works of Visbal^{19,20} give very detailed descriptions of the onset of unsteady vortex breakdown encountered by stationary and pitching delta wings. Visbal and Gordnier²¹ go on to identify the substructures found in the shear layer above delta wings.

Much of the previous numerical work pertaining to MAV aerodynamics with high-fidelity methods has focused primarily on nominally two-dimensional wing planforms by enforcing spanwise periodic boundary conditions across a simple wing section, and, thus, are restricted to rectilinear motions. Computational simulations of this nature range from those that examine transitional effects from perching-type motions,^{22,23,24,25} to investigations of deep dynamic stall induced by a purely plunging wing section,^{26,27} to plasma-based flow control methods for a pitching and plunging wing section.²⁸ Gordnier *et al.*²⁹ went even further and performed high-order solutions of a rigid and flexible wing section employing an implicit, large eddy simulation approach coupled with a nonlinear structural dynamics solver. These tests have provided a solid foundational understanding of the unsteady aerodynamics associated with MAV flight and have detailed significant findings that may be extrapolated to large aspect ratio wing and/or low-Reynolds number flows. However, detailed, a broader range of high-resolution experimental and computational studies of finite aspect ratio wings must still be performed to provide insight into the complex, three-dimensional vortical interactions and transitional processes incurred from the addition of wing tips and out-of-plane rotation, which can produce span-wise flow across the wing that can significantly affect aerodynamic performance.

Recent high-fidelity computations by Visbal³⁰ offered extremely detailed characterizations of the three-dimensional flow structure about a static and heaving low aspect ratio, rectangular wing at a constant angle of attack. For a stationary wing, a completely laminar structure was found at a Reynolds number of 1000, but the flow becomes highly unsteady and transitional for Re = 5000. For the heaving case, the computations were found to be in good agreement with experimental flow measurements at a Reynolds number of 10,000, where the flow is characterized by the formation of a leading edge vortex system which is pinned at the front

corners, producing intense transverse flow toward the centerline of the wing at the onset of its formation. Later in the motion, the vortex detaches from the corners and forms an arch-type structure with legs attached to the upper surface of the wing that move toward the centerline before reconnecting into a ring-like vortex structure. Similar features were also found experimentally by Yilmaz and Rockwell³¹ for the heaving wing configuration.

A revolving-wing configuration of an aspect-ratio-one wing was simulated using high-fidelity, ILES by Garmann *et al.*³² This work detailed the vortex formation and attachment across a broad range of rotational-based Reynolds numbers and the accompanying aerodynamic loads. It was determined that for the Reynolds numbers examined, the overall vortex structure including the attachment of a leading edge vortex was mostly insensitive to transitional effects despite the apparent vortex breakdown and shear layer instabilities observed at higher Reynolds numbers. The higher Reynolds number flows did augment force production on the wing, although the growth of the force components became saturated at the highest Reynolds numbers. Several angles of attack of the revolving wing configuration were also simulated for a Reynolds number of 500. The leading edge vortex was found to weaken with increased angle of attack but still remain attached to the wing surface. Comparisons of the mid-span velocity and vorticity contours at several rotational angles were made with available experimental PIV measurements¹⁵ for a mid-span rotational Reynolds number of 3,600. Very favorable agreement was found with the experimental measurements throughout the wing motion.

The purpose of the present computational study is to examine the three-dimensional flow structure and aerodynamic loading generated by revolving wings of various aspect ratios to build upon the recent work by the current authors that detailed the flow over an aspect-ratio-one wing. A high-order, ILES approach will be utilized to examine the role of the wing-tip proximity on the attachment and transition of the leading edge vortex generated by a revolving wing. Wings with aspect ratios of AR = 1, 2, and 4 will be simulated to determine if the findings from Ref. 32 hold for larger-span wings. Additionally, as a means of isolating dynamic effects due to rotation, the aspect-ratio-two wing is simulated with the addition of a source term in the governing equations to oppose and eliminate the centrifugal force near the wing surface. This is in an effort to assess the importance of centrifugal force on leading edge vortex attachment and development for revolving wings.

II. Governing equations

The governing equations for the current work correspond to the compressible, three-dimensional Navier-Stokes equations. These equations in curvilinear coordinates, (ξ, η, ζ) , can be expressed in strong conservation form³³ as follows:

$$\frac{\partial}{\partial t} \left(\frac{\vec{U}}{J} \right) + \frac{\partial \hat{F}}{\partial \xi} + \frac{\partial \hat{G}}{\partial \eta} + \frac{\partial \hat{H}}{\partial \zeta} = \frac{1}{\text{Re}} \left[\frac{\partial \hat{F}_v}{\partial \xi} + \frac{\partial \hat{G}_v}{\partial \eta} + \frac{\partial \hat{H}_v}{\partial \zeta} \right] \quad (1)$$

The solution vector is $\vec{U} = [\rho, \rho u, \rho v, \rho w, \rho E]^T$, $J = \partial(\xi, \eta, \zeta, \tau) / \partial(x, y, z, t)$ is the Jacobian of the transformation, and the inviscid flux vectors, \hat{F} , \hat{G} , and \hat{H} , are

$$\hat{F} = \frac{1}{J} \begin{bmatrix} \rho U \\ \rho u U + \xi_x p \\ \rho v U + \xi_y p \\ \rho w U + \xi_z p \\ (\rho E + p) U - \xi_t p \end{bmatrix} \quad \hat{G} = \frac{1}{J} \begin{bmatrix} \rho V \\ \rho u V + \eta_x p \\ \rho v V + \eta_y p \\ \rho w V + \eta_z p \\ (\rho E + p) V - \eta_t p \end{bmatrix} \quad \hat{H} = \frac{1}{J} \begin{bmatrix} \rho W \\ \rho u W + \zeta_x p \\ \rho v W + \zeta_y p \\ \rho w W + \zeta_z p \\ (\rho E + p) W - \zeta_t p \end{bmatrix} \quad (2)$$

where u , v , and w are the Cartesian velocity components, ρ is the density, p is the pressure, T is the temperature, U , V , and W are the contravariant velocities given as

$$\begin{aligned} U &= \xi_t + \xi_x u + \xi_y v + \xi_z w \\ V &= \eta_t + \eta_x u + \eta_y v + \eta_z w \\ W &= \zeta_t + \zeta_x u + \zeta_y v + \zeta_z w \end{aligned} \quad (3)$$

and the internal energy, E , is

$$E = \frac{T}{(\gamma - 1) M_{\text{ref}}^2} + \frac{1}{2} (u^2 + v^2 + w^2) \quad (4)$$

The viscous fluxes, \hat{F}_v , \hat{G}_v , and \hat{H}_v , written in indicial notation are

$$\hat{F}_v = \frac{1}{J} \begin{bmatrix} 0 \\ \xi_{x_i} \sigma_{i1} \\ \xi_{x_i} \sigma_{i2} \\ \xi_{x_i} \sigma_{i3} \\ \xi_{x_i} (u_j \sigma_{ij} - \Theta_i) \end{bmatrix} \quad \hat{G}_v = \frac{1}{J} \begin{bmatrix} 0 \\ \eta_{x_i} \sigma_{i1} \\ \eta_{x_i} \sigma_{i2} \\ \eta_{x_i} \sigma_{i3} \\ \eta_{x_i} (u_j \sigma_{ij} - \Theta_i) \end{bmatrix} \quad \hat{H}_v = \frac{1}{J} \begin{bmatrix} 0 \\ \zeta_{x_i} \sigma_{i1} \\ \zeta_{x_i} \sigma_{i2} \\ \zeta_{x_i} \sigma_{i3} \\ \zeta_{x_i} (u_j \sigma_{ij} - \Theta_i) \end{bmatrix} \quad (5)$$

with components of the stress tensor and heat flux vector given as

$$\sigma_{ij} = \mu \left(\frac{\partial \xi_k}{\partial x_j} \frac{\partial u_i}{\partial \xi_k} + \frac{\partial \xi_k}{\partial x_i} \frac{\partial u_j}{\partial \xi_k} - \frac{2}{3} \delta_{ij} \frac{\partial \xi_l}{\partial x_k} \frac{\partial u_k}{\partial \xi_l} \right) \quad (6)$$

and

$$\Theta_i = - \left[\frac{1}{(\gamma - 1) M_{\text{ref}}^2} \right] \left(\frac{\mu}{\text{Pr}} \right) \frac{\partial \xi_j}{\partial x_i} \frac{\partial T}{\partial \xi_j} \quad (7)$$

where M_{ref} is the reference Mach number, μ is the dynamic viscosity, γ is the ratio of specific heats, and $x_i (\equiv x, y, z)$, $\xi_i (\equiv \xi, \eta, \zeta)$ and $u_i (\equiv u, v, w)$ for $i = 1, 2, 3$. Stokes' hypothesis is assumed for the bulk viscosity coefficient ($\lambda = -2/3\mu$), and the governing equations are also supplemented with the perfect gas equation, $p = \rho T / \gamma M_{\text{ref}}^2$, Sutherland's viscosity law, and a constant Prandtl number ($\text{Pr} = 0.72$ for air). All velocity components are non-dimensionalized by the maximum velocity achieved at the wing root during rotation, $U_{r_g} = r_{\text{root}} \dot{\phi}_{\text{max}}$, where r_{root} is the distance to the wing root and $\dot{\phi}_{\text{max}}$ is the maximum rotational rate of the revolving wing. All length scales are scaled by the chord, and pressure is normalized by $\rho_{\text{ref}} U_{r_{\text{root}}}^2$.

This set of equations corresponds to the *unfiltered* Navier-Stokes equations and is used without change in laminar, transitional or fully turbulent regions of the flow for the ILES procedure. Unlike the standard LES approach, no additional subgrid-scale (SGS) model or heat flux terms are appended. Instead, a high-order, low-pass filter operator, which will be discussed later, is applied to the conserved variables during the solution of the standard Navier-Stokes equations. This highly-discriminating, Padé-type filter selectively dampens only the evolving, poorly resolved high-frequency content of the solution.^{34,35} The filtering regularization procedure provides an attractive alternative to the use of standard SGS models, and has been found to yield suitable results for several turbulent and transitional flows on LES level grids.³⁶ A reinterpretation of this ILES approach in the context of an Approximate Deconvolution Model³⁷ has been provided by Matthew *et al.*³⁸ For low Reynolds numbers and/or high spatial resolutions, the ILES approach is effectively direct numerical simulation (DNS).

III. Numerical Procedure

All simulations are performed with the extensively validated high-order, Navier-Stokes solver, FDL3DI.^{39,40} In this code, a finite-difference approach is employed to discretize the governing equations, and all spatial derivatives are obtained with high-order compact-differencing schemes.⁴¹ At boundary points, higher-order one sided formulas are utilized that retain the tridiagonal form of the scheme.^{39,40} The derivatives of the inviscid fluxes are obtained by forming the fluxes at the nodes and differentiating each component with the compact differencing scheme. Viscous terms are obtained by first computing the derivatives of the primitive variables. The components of the viscous fluxes are then constructed at each node and differentiated by a second application of the same scheme.

In order to eliminate spurious components of the solution, a high-order, low-pass spatial filtering technique^{39,42} is incorporated that is based on templates proposed in References 41 and 43. With proper choice of coefficients, it provides a $2N^{\text{th}}$ -order formula on a $2N + 1$ point stencil. These coefficients, along with representative filter transfer functions, can be found in References 40 and 42. The filter is applied to the conserved variables along each transformed coordinate direction one time after each time step or sub-iteration. For the near-boundary points, the filtering strategies described in References 39 and 42 are used. For transitional and turbulent flows, the high-fidelity spatial algorithmic components provide an effective implicit LES approach in lieu of traditional SGS models, as demonstrated in References 34 and 35 and more recently in Ref. 36. All computations presented here are performed with a sixth-order interior discretization scheme coupled with an eighth-order accurate implicit filter.

Time marching of the governing equations is achieved through the iterative, implicit approximately-factored integration method of Beam and Warming.⁴⁴ This method has been simplified through the diagonalization of Pulliam and Chaussee⁴⁵ and supplemented with the use of Newton-like sub-iterations to achieve second-order accuracy.^{34,35} Sub-iterations are commonly used to reduce errors due to factorization, linearization, diagonalization, and explicit specification of boundary conditions.⁴⁶ Fourth-order, nonlinear dissipation terms^{47,48} are also appended to the implicit operator to augment stability.

In the case of a maneuvering wing, the grid is moved in a rigid fashion using the prescribed kinematics. The time-metric terms are evaluated employing the procedures described in detail in Ref. 49 to ensure the geometric conservation law (GCL) is satisfied.

IV. Details of the computations

A. Geometry and kinematic definitions

The geometry considered in this study is a rectangular wing of varying aspect ratio and thickness of $0.041c$. The root of the wing is extended out a distance of $r_{\text{root}} = 0.5c$ from the axis of rotation with the chord oriented at an angle of $\alpha = 30^\circ$ relative to the axis as depicted in Fig. 1(a). The wing, initially at rest, accelerates to a constant rotational rate as it revolves around its axis as shown in Fig. 1(b). The angle of rotation, $\phi(\tau)$, is given by

$$\phi(\tau) = \frac{\dot{\phi}_{\max}^*}{2a} \ln \left[\frac{\cosh(a(\tau - \tau_1))}{\cosh(a(\tau - \tau_2))} \right] + \frac{1}{2}\phi_0 \quad (8)$$

where the dimensionless time is $\tau = tU_{\text{ref}}/c$, the maximum angle of rotation is ϕ_{\max} , and $\dot{\phi}_{\max}^* = \dot{\phi}_{\max}c/U_{r_{\text{root}}}$ is the normalized rotational rate. The parameter, a , controls the smoothness of the function with smaller values reducing the maximum angular acceleration and causing more smoothing. If no smoothing were present, τ_1 is the time until the sharp start-up of the unsmoothed motion and τ_2 is the end time of the motion, $\tau_2 = \tau_1 + \phi_0/\dot{\phi}_{\max}^*$. Equation (8) is a modified form of a function described by Eldredge *et al.*⁵⁰ which allows for a continuous motion that is sufficiently differentiable, thereby avoiding discontinuities in the angular acceleration. This simple, unidirectional revolving motion of the wing provides a means of examining, for example, a single stroke of hovering or a take-off motion for a biological flier.

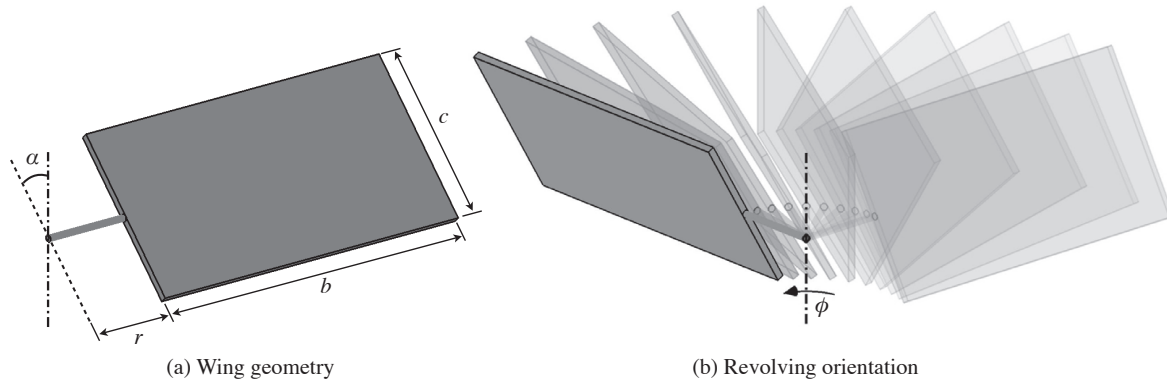


Figure 1: Geometry definition and revolving configuration

As mentioned earlier, the maximum velocity of the root of the wing, $U_{r_{\text{root}}} = r_{\text{root}}\dot{\phi}_{\max}$, is used as the reference speed for normalization. This results in a purely geometric rotational rate given as

$$\dot{\phi}_{\max}^* = \frac{\dot{\phi}_{\max}c}{U_{r_{\text{root}}}} = \frac{\dot{\phi}_{\max}c}{(r_{\text{root}}\dot{\phi}_{\max})} = \frac{c}{r_{\text{root}}} = \frac{c}{0.5c} = 2.0 \quad (9)$$

where $r_{\text{root}} = 0.5c$ is the distance the wing root to the rotational axis. In a non-Newtonian frame, $\dot{\phi}_{\max}^*$ is similar to the inverse of the Rossby number (Ro) which appears in some non-dimensionalizations of the fictitious body forces,⁵¹ leading to $\text{Ro} = 0.5$.

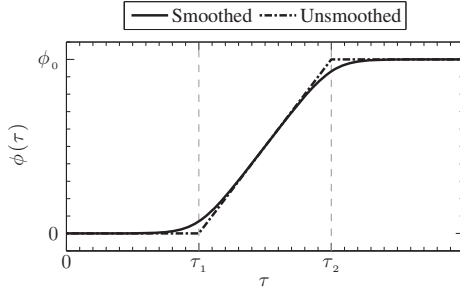


Figure 2: Rotational angle in time

All simulations presented in this work use a maximum angle of $\phi_{\max} = 2\pi$ radians (360°), a rotational rate of $\dot{\phi}_{\max}^* = 2.0$, and a smoothing parameter of $a = 5.2$. The start time is set as $\tau_1 = 0.75$ leading to $\tau_2 = 3.89$. The time-step for all computations is set as $\Delta\tau = 5.0 \times 10^{-5}$.

B. Computational mesh and boundary conditions

While the geometry of the current study is very simple, the sharp edges of the rectangular wing actually cause complications with the meshing topology. The Chimera overset method⁵² with high-order interpolation⁵³ is used to construct a mesh that maintains sufficient near-body and wake resolution around the wing. A generic depiction of the multi-block near-field domain used in this study can be seen in Fig. 3 for reference. Each block actually extends outward to 30 chords from the body using 81 points with increased stretching. The wing surface is discretized with 131 points distributed across the chord (ξ -direction) and 41 points across the thickness (η -direction). The number of span-wise points (ζ -direction) varies with aspect ratio: 131, 261, or 391 points are used for aspect ratios of $AR = 1, 2$, or 4 , respectively. The initial off-body spacing and corner surface spacing is $\Delta n_i = 0.0005$ chords. Grid clustering immediately off the body and around the wing edges is maintained throughout the domain. The resulting sizes of each block are listed in Table 1 for each aspect-ratio wing.

The upper and lower surface meshes extend four grid planes into the leading and trailing edge blocks and into the root and tip sections to provide point-to-point communication between the adjacent blocks. The root and tip blocks similarly extend into the leading and trailing edge sections. Note that these extended planes of data are overwritten each sub-iteration with the values obtained from the adjacent block. In the case of the maneuvering wing, the entire domain rotates at the prescribed motion with varying kinematics.

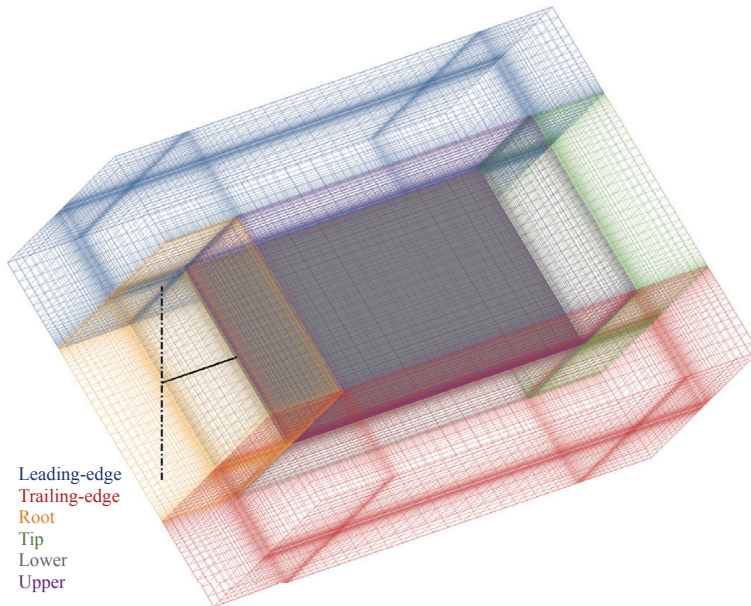
The boundary condition on the wing surface is specified as a no-slip, adiabatic moving wall with zero-normal pressure gradient approximated by a fourth-order accurate extrapolation. The far-field boundary in each block, which is located 30 chords from the wing surface, is set as a zero-velocity condition with the reference temperature and density each as unity. Near this boundary, each mesh is stretched quite rapidly. This, in conjunction with the low-pass filter, provides a buffer-type treatment of the boundary that eliminates spurious reflections associated with the imposed flow condition. The reference Mach number for all computations is selected as 0.1 to avoid compressibility effects, which results in a normalized pressure at the far-field boundaries of $p = 71.43$.

The revolving, aspect-ratio-one wing was simulated at a Reynolds number of $Re_{\text{root}} = 7,250$ on the mesh described above along with two other meshes of successive refinement in Ref. 32. The current grid was found to provide sufficient spatial resolution of the three-dimensional flow structure when compared to the other resolutions. The unsteady aerodynamic loads that were produced throughout the motion also showed only slight sensitivity to spatial resolution. Additionally, comparisons of the baseline mesh solution with experimental PIV measurements¹⁵ showed remarkably favorable agreement throughout the motion. The refinement study and experimental comparisons in Ref. 32 provide a high level of confidence in the choice of resolutions for the meshes used in the current study.

Table 1: Computational mesh sizes for the various aspect-ratio wings

Block	n_ξ	n_η	AR = 1		AR = 2		AR = 4	
			n_ζ	Points	n_ζ	Points	n_ζ	Points
Leading edge	81	201	291	4,737,771	421	6,854,301	681	11,087,361
Trailing edge	81	201	291	4,737,771	421	6,854,301	681	11,087,361
Root	137	201	81	2,230,497	81	2,230,497	81	2,230,497
Tip	137	201	81	2,230,497	81	2,230,497	81	2,230,497
Lower surface	137	81	137	1,520,289	267	2,962,899	527	5,848,119
Upper surface	137	81	137	1,520,289	267	2,962,899	527	5,848,119
				16,977,114		24,095,394		38,331,954

n_ξ , n_η , n_ζ correspond to the number of points in the ξ -, η -, and ζ -directions, respectively

**Figure 3:** Near-field computational mesh

V. Effect of aspect ratio

The effects of aspect ratio on the three-dimensional flow structure and aerodynamic loads are examined in this section. Three wings are considered with aspect ratios of AR = 1, 2, and 4, respectively. The Reynolds number based on the maximum rotational velocity achieved at the *root* is selected as $Re_{root} = 1,000$ for all cases. This allows the variation of Reynolds number along the span to remain consistent for all aspect ratios considered, which means that the higher aspect-ratio wings operate as if they are extensions of the aspect-ratio-one wing. The corresponding mid-span and tip Reynolds numbers for the different aspect ratios are listed in Table 2 for reference. For comparison purposes, most components of interest are re-normalized by the maximum *mid-span* velocity, which varies with aspect ratio.

Table 2: Reynolds numbers based on the maximum root, mid-span, and tip rotational velocities

AR	Re _{root}	Re _{r_g}	Re _{tip}
1	1,000	2,000	3,000
2	1,000	3,000	5,000
4	1,000	5,000	9,000

A. Description of unsteady flow structure

The three-dimensional flow structure is shown in Fig. 4 for rotational angles of $\phi = 45^\circ$, 90° , and 135° through iso-surfaces of relative total pressure. Two surfaces are shown to highlight the inner core and outer shell of the vortex system. Representation of the solution through the total pressure has been shown to remove many of the smaller scales associated with transition and vortex breakdown while leaving the coherence of the vortex core.^{30,32}

Shortly after the onset of the motion, each wing produces vortices emanating from the four edges and pinned at the corners. By $\phi = 45^\circ$, the leading edge, tip, and trailing edge vortices unpin from the outboard corners of the wing and undergo a reconnection process to form a continuous vortex loop. The root and trailing edge vortices also reconnect just off their adjacent corner. The vortex loop increases in size with aspect ratio since the travel distance of the tip also increased with aspect ratio. The leading edge portion of the vortex lifts off slightly from the outboard section of the wing and forms an arch-type structure as it reorients itself with the tip. This evolution has been closely detailed for an aspect-ratio-one wing across a broad range of Reynolds numbers in Ref. 32.

The evolution of the vortex core for $22.5^\circ \leq \phi \leq 135^\circ$ can be seen in Fig. 5 through another iso-surface of relative total pressure and the surface pressure distribution on the suction side of the wing. Note that the pressure coefficient is normalized by the maximum *mid-span* velocity, $U_{r_g}^2$, for comparison between the different aspect-ratio wings. The proximity of the vortex to the surface of the wing promotes a strong region of suction along the leading edge that persists to the mid-span, regardless of aspect ratio. Past mid-span, the vortex lifts off the surface into an arch-type structure as it reorients itself along the tip, which diminishes its imprint on the surface pressure and reduces the suction near the tip. At $\phi = 90^\circ$, the inboard pressure is largely established for all aspect ratios. At this same instant, an expansion of the vortex core is identifiable for each wing around mid-span (denoted as (1)), which is indicative of vortex breakdown. At $\phi = 112.5^\circ$ and 135.0° , spiraling undulations of the vortex core can be seen with the higher aspect-ratio-wings. The spiraling winds in the direction opposite the sense of rotation, which is another sign of breakdown. The size of the LEV scales with the distance from the rotational axis, and for the higher aspect ratios, the LEV grows larger than the chord of the wing, causing it to be obstructed by the trailing edge. Once this occurs, the tip unloads and the edge of the suction region moves inboard slightly.

Contours of the relative span-wise velocity around the suction side of each wing at $\phi = 90^\circ$ are shown in Fig. 6 at several locations across the span. A single contour line of relative total pressure ($p_0/p_{0,\text{ref}} = 0.99$) is superimposed in each image as well to highlight the leading edge vortex, and the view is directed from root to tip. The velocity is normalized by the maximum speed achieved at the mid-span of the wing during rotation, U_{r_g} . For each aspect ratio, the size of the LEV scales with distance from the root of the wing until the effects of the tip force the LEV to lift-off and reorient in the chord-wise direction. Additionally, there is a large region of strong outboard flow present behind the LEV regardless of aspect ratio at each span-wise location. At a distance of 0.25 chords from the wing root, all solutions show a similarly sized LEV with a strong outboard jet present in its core that is on the order of the mid-span velocity. A portion of the root vortex is present in these images as well due to the proximity of the viewing plane to the wing root. At 0.50 chords from the root, the aspect-ratio-one wing produces a relatively enlarged LEV with a region of reversed flow present its feeding sheet off the leading edge. Just past this location for AR = 1, the jet in the vortex core encounters an abrupt flow reversal due to breakdown. Interestingly, this same phenomenon occurs around the mid-span location for each wing, despite aspect ratio. In all cases, the LEV is lifted-off the surface as it approaches the tip around the 75%-span location. Regions of reversed flow are also present underneath the LEV at these sections, which allow effects from the tip to propagate inboard.

The evolution of the LEV along the span of the aspect-ratio-four wing at $\phi = 67.5^\circ$ is shown in Fig. 7

through contours of span-wise vorticity at several slices along the wing that dissect the leading edge vortex. An iso-surface of total pressure is also shown to highlight the three-dimensionality of the vortex system. Initially off the root of the wing, the LEV appears as a tight and coherent vortex. A secondary vortex is formed from the wall-induced vorticity generated between the LEV and its feeding sheet. The size of the LEV and secondary vortex grows proportionally with distance from the rotational axis. At a distance of 1.5 chords from the wing root, the secondary vortex erupts from the surface and penetrates the feeding sheet of the LEV. The disrupted shear layer rolls up under self-induction and forms substructures that rotate in the same direction as the LEV. The finger-like substructures are apparent off the leading edge in the span-wise vorticity and in the three-dimensional iso-surface of total pressure at a distance greater than 1.75 chords from the root. Similar transitional elements have been described in detail for swept delta wings in Ref. 21 and have been seen experimentally for a revolving wing by Carr *et al.*¹⁷ The lower aspect ratio wings in this study do not show the formation of these substructures, indicating that it is an effect of the Reynolds number based on distance along the span. The other wings do not have sufficient span for the LEV to develop these features before the flow is overcome by the influence of the tip.

Between $\phi = 67.5^\circ$ and 90° , the outer portion of the LEV and its feeding sheet substructures undergo transition and breakdown into much smaller scales. This is shown in the Q -criterion iso-surfaces of Fig. 8. The wings with $AR = 1$ and 2 are also shown for comparison. The lower aspect-ratio wings also show transitional elements of the LEV, but they do not have the same feeding-sheet substructures that are present with $AR = 4$. The finer-scale features increase with the Reynolds number based on the distance from the rotational axis.

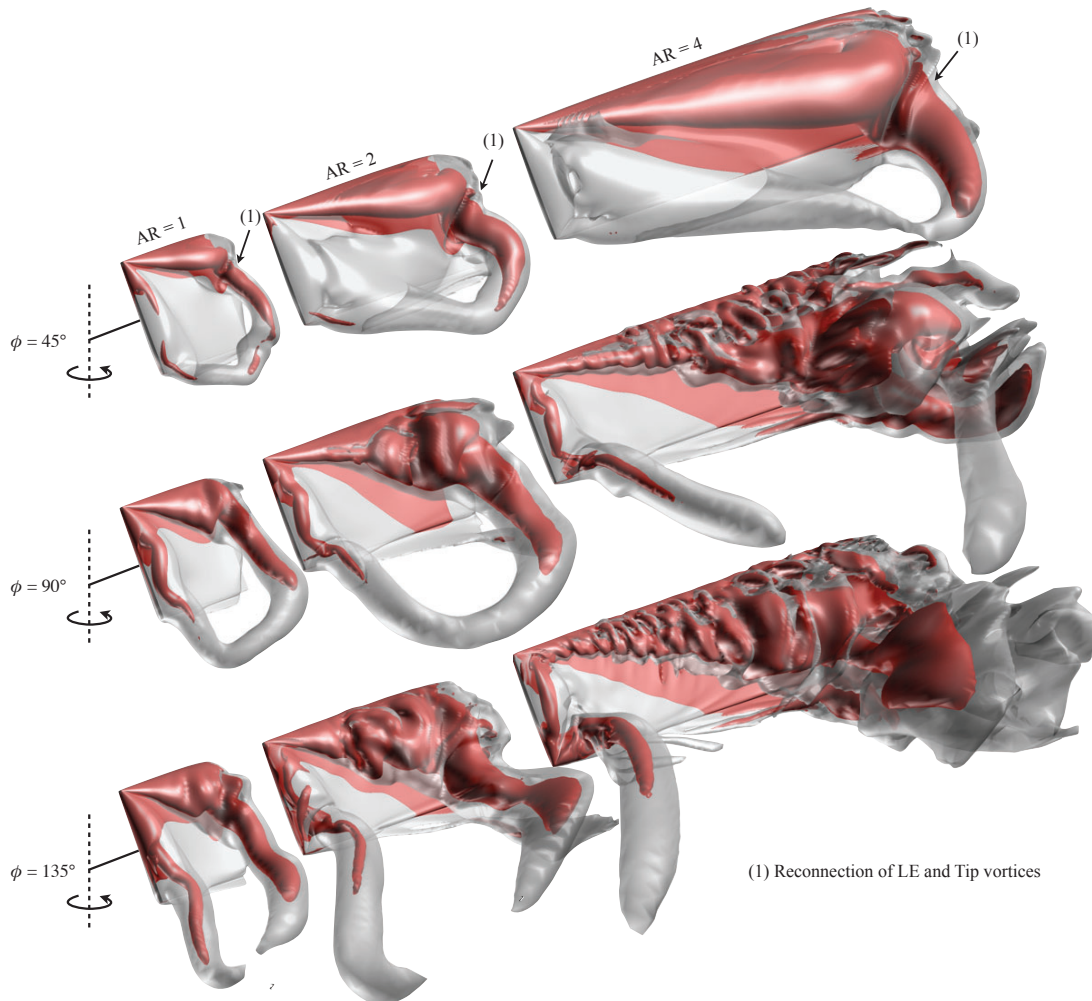


Figure 4: Iso-surfaces of relative total pressure

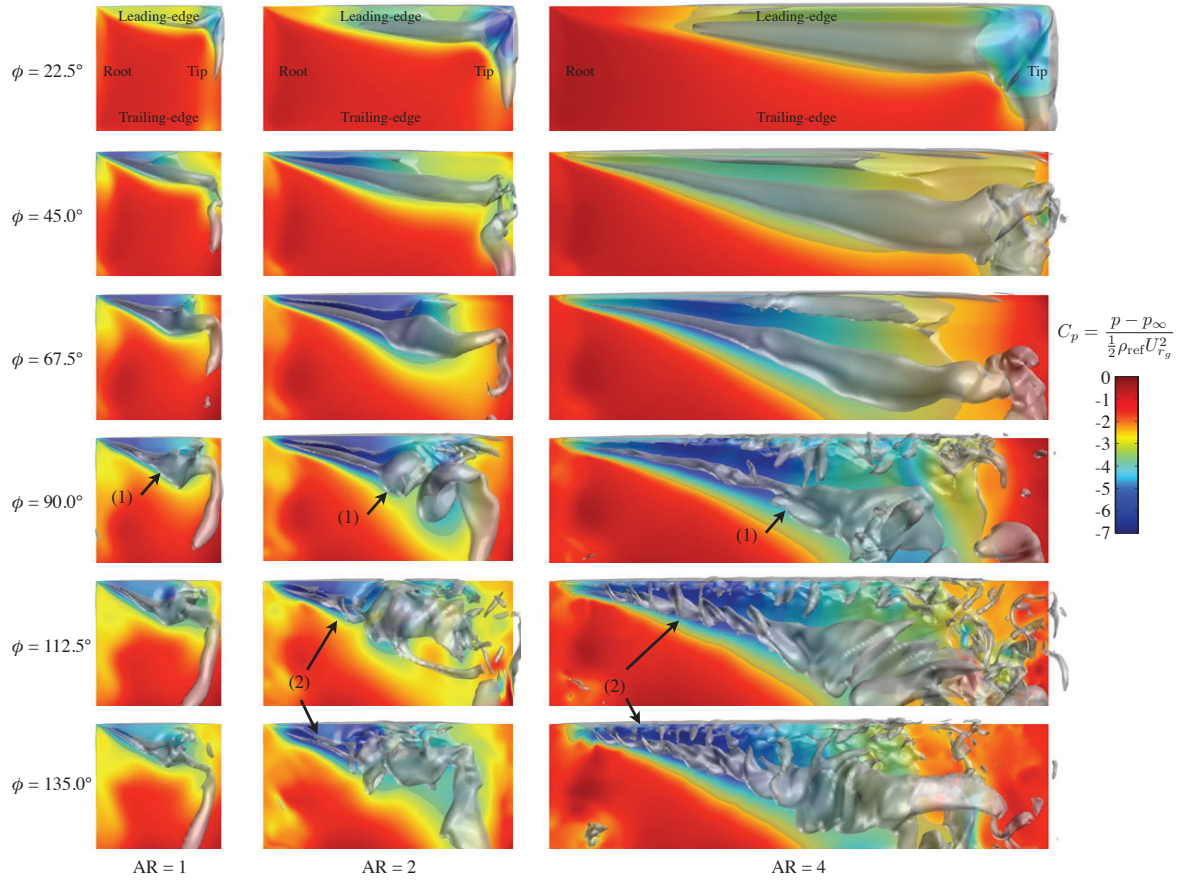


Figure 5: Evolution of the surface pressure distribution on the suction side of the wing with overlaid iso-surface of relative total pressure highlighting the vortex core along the leading edge. (1) Denotes the expansion of the vortex core due to breakdown. (2) Indicates the undulation of the vortex core for higher aspect ratios.

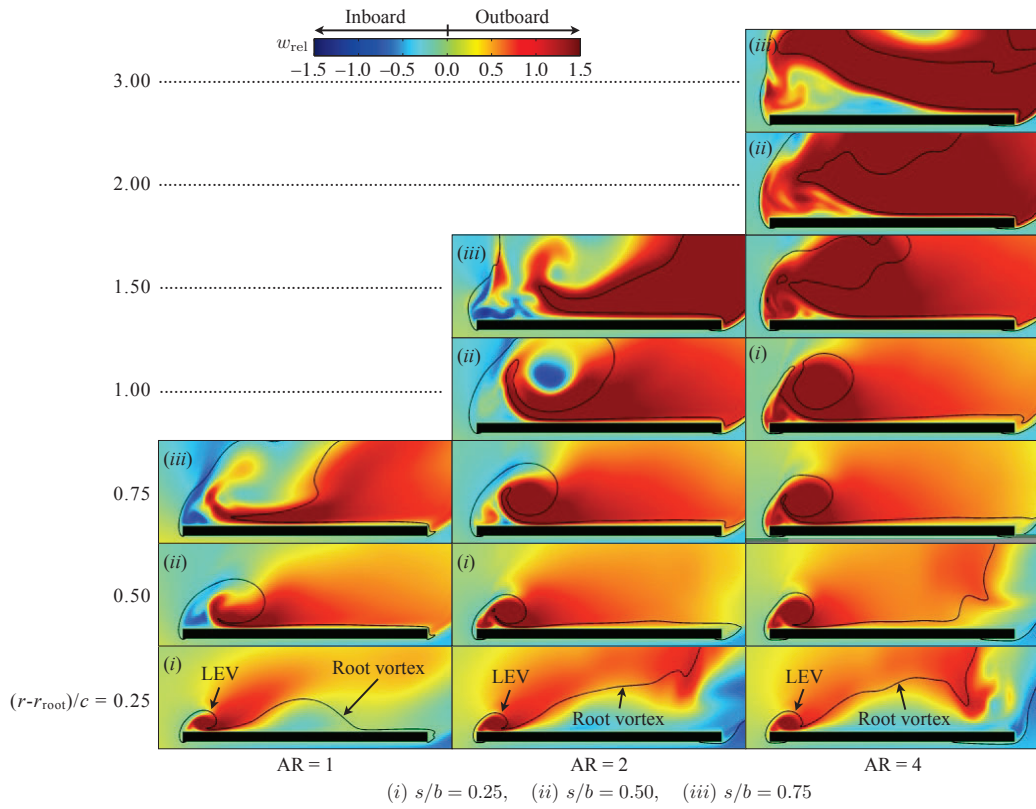


Figure 6: Contours of relative span-wise velocity around the suction side of the wing. A single contour line of relative total pressure ($p_0/p_{0,\text{ref}} = 0.99$) is superimposed to highlight the leading edge vortex. View is directed from root to tip, and all components are normalized by the maximum velocity of the wing at the mid-span. Images of corresponding (i), (ii), or (iii) span-normalized locations of 25%, 50%, and 75%, respectively.

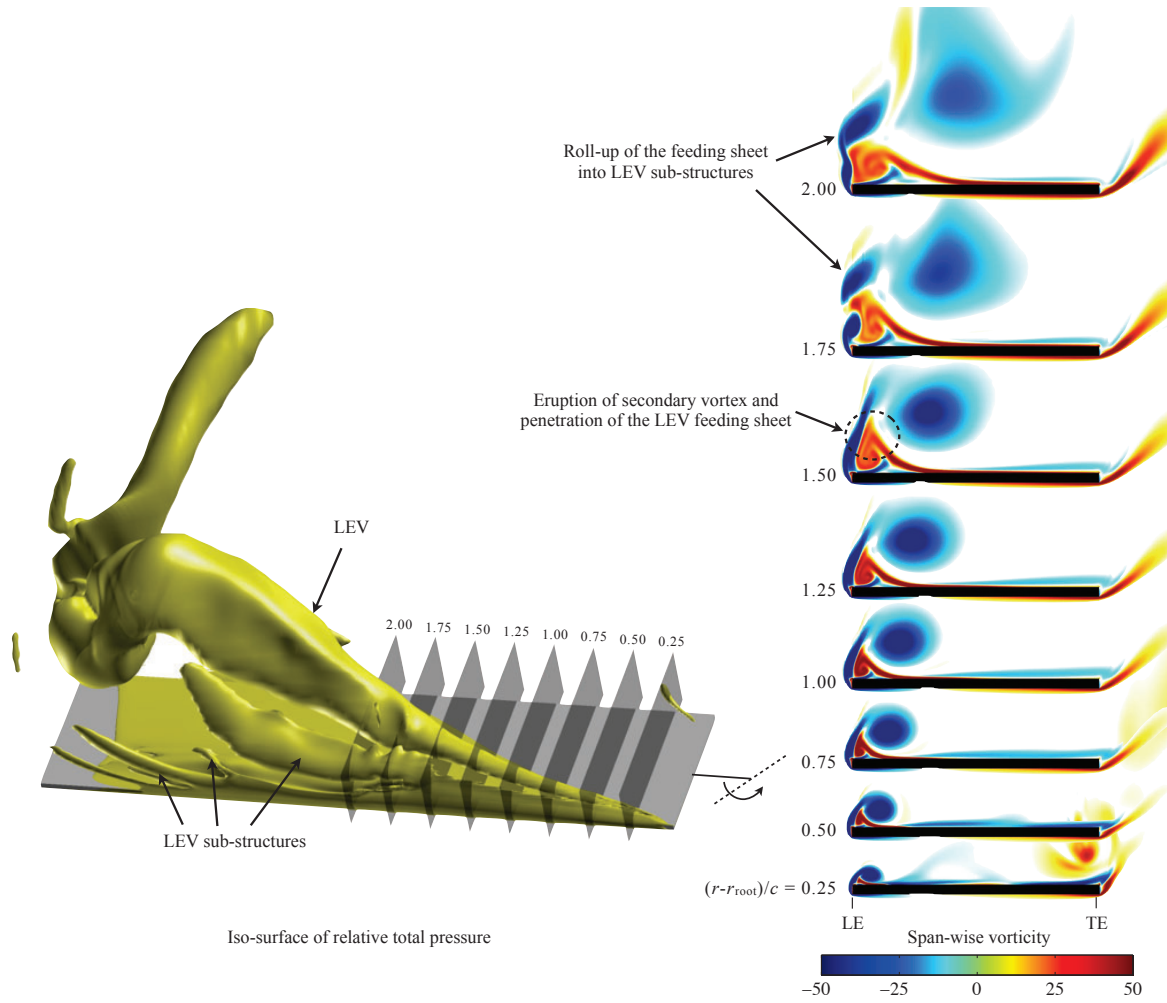


Figure 7: Evolution of the leading edge vortex along the span of the aspect-ratio-four wing. Solution corresponds to a rotational angle of $\phi = 67.5^\circ$.

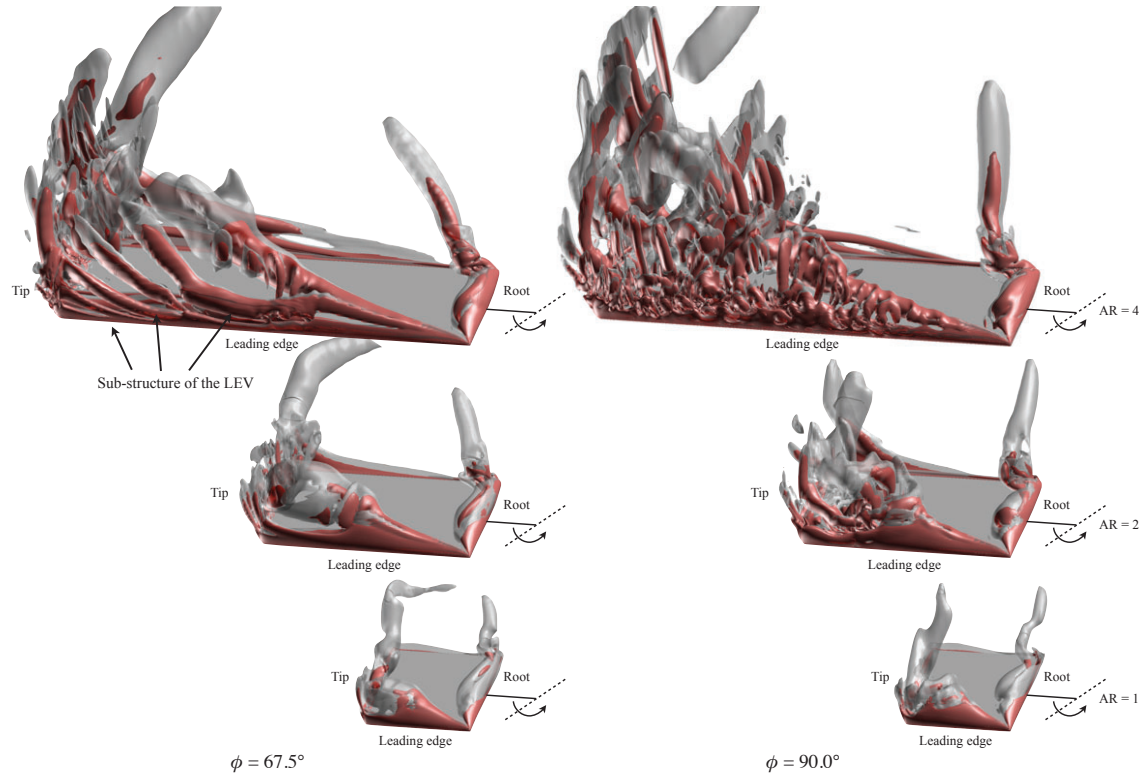


Figure 8: Q -criterion iso-surfaces showing the evolution of the leading edge vortex along the span for each aspect ratio. Solutions correspond to rotational angles of $\phi = 67.5^\circ$ and 90.0° .

B. Aerodynamic loads

The lift, drag, and radial force coefficients are shown in Fig. 9. It is important to note that these coefficients have been renormalized by the *mid-span* velocity, U_{r_g} , for comparison and use the wetted area of the chord times the span, $S = cb$. Relative to the other components, the radial forces are insignificant throughout the motion for each aspect ratio. The lift and drag coefficients increase very quickly at the onset of the motion due to the angular acceleration of the plate. Shortly thereafter, the coefficients plateau and then increase at a much lower rate as the vortex system strengthens and grows. By $\phi = 90$, where the inboard surface pressure was seen to be largely established, the forces from the higher aspect ratio wings mostly level off and exhibit unsteady fluctuations around nearly the same mean value. At this point, the chord-wise extent of the LEV for the higher aspect ratio wings has grown to a size that covers the entire chord. It cannot grow past the trailing edge, so the lift and drag saturate. For $AR = 1$, the lift and drag continue to rise slightly throughout the motion but do not quite reach the higher peak values of the other aspect ratio wings. At this aspect ratio, the extent of the LEV never encompasses the entire chord of the wing, so its development is unhindered by the trailing edge.

The sectional lift coefficient, $C_l = L'/(1/2\rho_{ref}U_{r_g}^2 c)$, plotted against the normalized span-wise location is shown in Fig. 9 for several rotational angles. For $AR = 1$, the majority of the lift is biased towards the tip for the duration of the motion. The higher aspect-ratio-wings initially show the same bias at $\phi = 45^\circ$, but later in the motion, they move to a more normalized distribution. Some unsteadiness is observed in the distributions of the higher aspect-ratio-wings, as well.

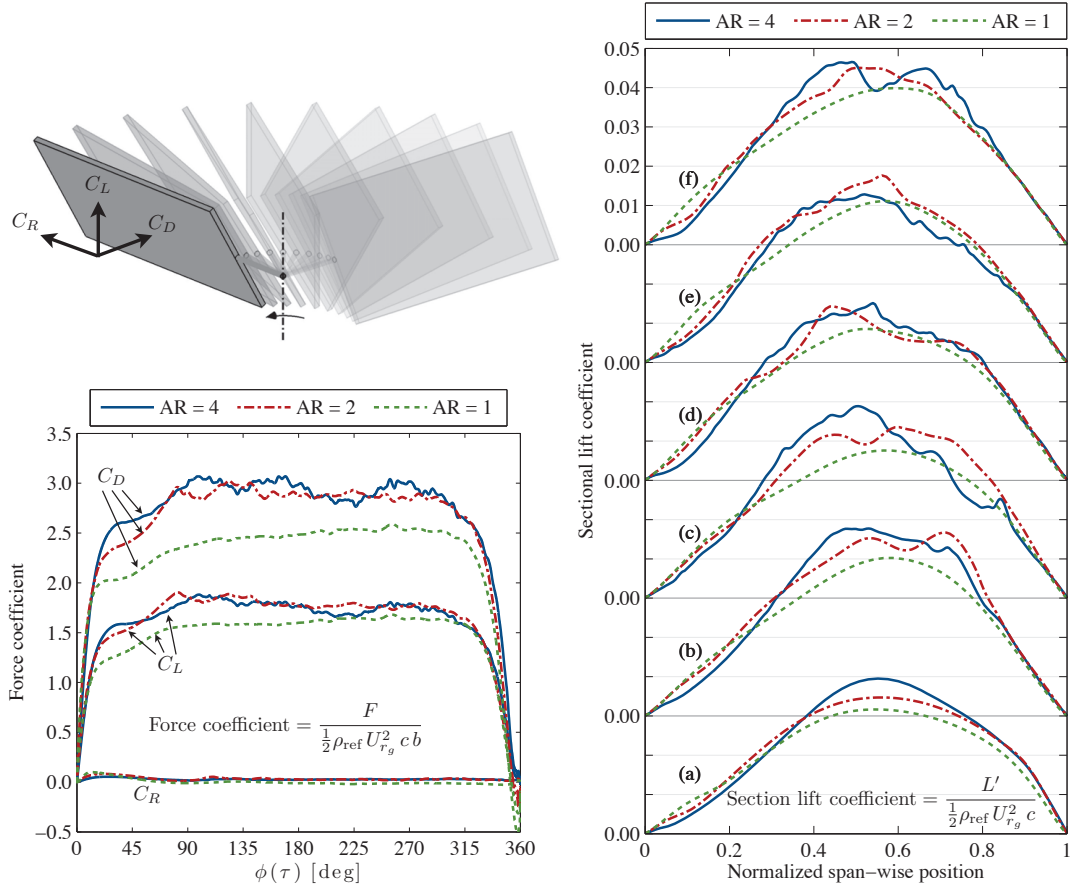


Figure 9: Lift, drag, and radial force coefficients and the sectional lift coefficient across the span for the various aspect-ratio-wings at rotational angles of $\phi = 45^\circ$ (a), 90° (b), 135° (c), 180° (d), 225° (e), and 270° (f).

C. Separation of dynamic forces for the revolving wing

When the nondimensionalized Navier-Stokes equations are cast into a rotating frame of reference, the apparent angular, centrifugal, and Coriolis forces appear on the right-hand-side of the equations as source terms. These forces, when summed with the pressure gradient force and neglecting the viscous forces, form the total dynamic force seen by the fluid measured in the moving reference frame. This force is formulated as follows:

$$\mathbf{F}_{\text{dyn}} = -\nabla p - \underbrace{\rho \dot{\Omega} \times \mathbf{r}}_{\mathbf{F}_{\text{ang}}} - \underbrace{\rho \Omega \times (\Omega \times \mathbf{r})}_{\mathbf{F}_{\text{cen}}} - \underbrace{2\rho (\Omega \times \mathbf{u})}_{\mathbf{F}_{\text{Cor}}} \quad (10)$$

where \mathbf{r} is the radius from the rotational axis, $\mathbf{u} = \mathbf{V} - (\Omega \times \mathbf{r})$ is the relative velocity, and Ω is the rotational rate of the system. The angular, centripetal, and Coriolis forces are designated as \mathbf{F}_{ang} , \mathbf{F}_{cen} and \mathbf{F}_{Cor} , respectively. The Rossby number, which appears in some nondimensionalizations of rotational forces, does not appear in this normalization since the dimensional form of Ω is normalized by U_{ref}/c and the radius, r , is normalized by the chord.

The total dynamic force is decomposed into its centrifugal, Coriolis, and pressure gradient contributions. The span-wise components of these forces are shown in Fig. 10 at the 25%-span location for each aspect ratio. The forces are normalized by the mid-span velocity, $U_{r_g}^2$. For each wing, the centrifugal force is consistently directed outboard and on the order of unity, but scales with distance from the rotational axis. The component of Coriolis force operates mostly on the edges of the LEV with an outboard contribution on the rearward side, and an inboard contribution on the forward and upper edge. It is also on the order of unity but has a diminishing magnitude with aspect-ratio. The pressure gradient force acts in a dipole-like distribution that is an order of magnitude greater than the other two forces in the span-wise direction. A large region of outboard forcing encompasses the rear and upper portions of the LEV that prevails to the wing surface. A smaller region of inboard forcing is present in the forward section of the LEV core. This force is responsible for the deceleration and eventual flow reversal of the coherent jet in the vortex core. The span-wise total dynamic force in the vortex core is quite obviously dominated by the pressure gradient, but also has a strong component of centrifugal force ahead of and behind the LEV. The outboard flow that was shown in Fig. 6 around almost the entirety of the area surrounding the wing is largely due to the centrifugal and pressure gradient forces.

Next, the surface-normal components of the total dynamic force and its decomposed forces are shown in Fig. 11 at the 25%-span locations of each wing. On a span-wise plane, the centrifugal force in the normal direction is negligible in these regions since it is a radially-directed force. The Coriolis force shows moderate contributions in the normal direction with an *upward* force in the core and at the base of the LEV. The upward direction suggests that Coriolis does not contribute to leading edge vortex attachment, but rather, quite the opposite. The pressure gradient force is also directed upward at the base of the vortex, where the vortex is still close to the surface. However, it also has a larger region of downward force around the upper edge of the LEV. The pressure gradient, again, dominates the other two forces by an order of magnitude and is almost indistinguishable from the total dynamic force.

The span-wise and surface-normal components of the forces are integrated across a sectional area at each span-wise location along the wing in order to quantify each forces' net contribution. The area selected extends from the wing surface to a normal distance of half a chord and also from 0.1c ahead of the leading edge to 0.1c behind the trailing edge. Figure 12 shows the integrated values at each span-wise location for all the forces discussed above. Each component is plotted against the span-normalized distance from the wing root.

A strong similarity is seen between the integrated span-wise components of the different aspect-ratio-wings with the distributions scaling as a function of aspect ratio. The centrifugal, pressure gradient, and total dynamic forces show a mostly outboard-directed (positive) distribution across the span, while the Coriolis net effect is comparable in magnitude but is directed inboard (negative) across the entirety of the wing. The sectional pressure gradient force is directed outboard along much of the span, but does switch signs on either side of the wing due to the interactions of the leading edge vortex with the root and tip vortices. The pressure gradient force is, again, shown to be the major contributor to the total dynamic force.

The integrated surface-normal forces (Fig. 12(b)) reveal an upward (positive) net force from the Coriolis across the span for each aspect ratio. The sectional pressure gradient and total dynamic forces have a net effect directed downward (negative) initially near the wing root for all aspect ratios. The total dynamic force remains negative until 81%, 51%, and 31%-span locations for the aspect ratios of one, two, and four,

respectively. These distances correspond to 0.81, 1.02, and 1.25 chords from the wing root. The contribution of this force continues to increase until reaching a maximum at 0.96, 1.71, and 2.10 chords, respectively, for each aspect ratio. This distance appears to saturate with aspect ratio, indicating that the leading edge vortex development is reaching a critical Reynolds number along the span, which will promote the feeding sheet substructures discussed earlier. The integrated surface-normal component of the centrifugal force is negligible across the wing due to its radial orientation.

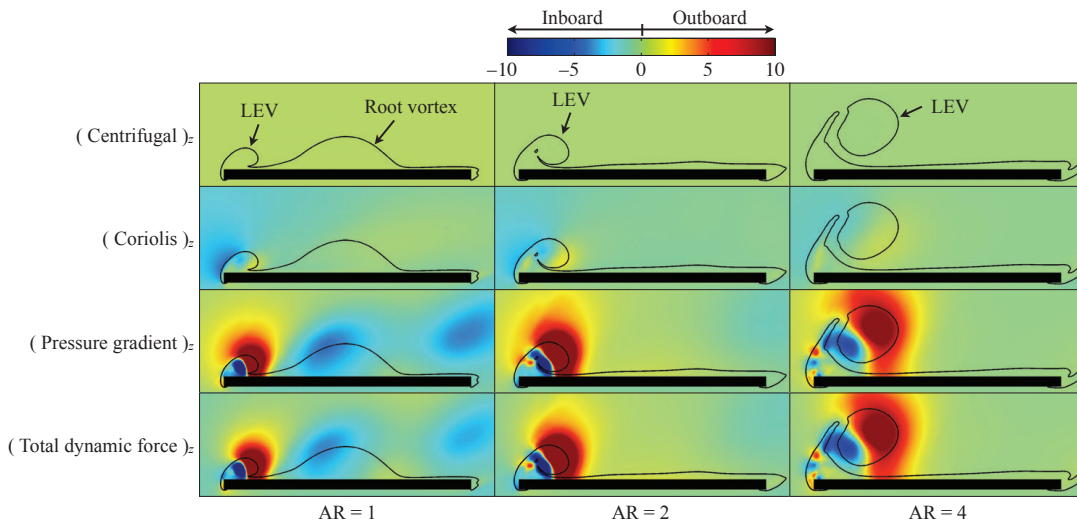


Figure 10: Contours of the span-wise components of the centrifugal, Coriolis, pressure gradient forces and total dynamic forces at the 25% span-location. A single contour line of relative total pressure ($p_0/p_{0,\text{ref}} = 0.99$) superimposed to highlight the leading edge vortex. View is directed from root to tip, and all components are normalized by the maximum velocity of the wing at the mid-span.

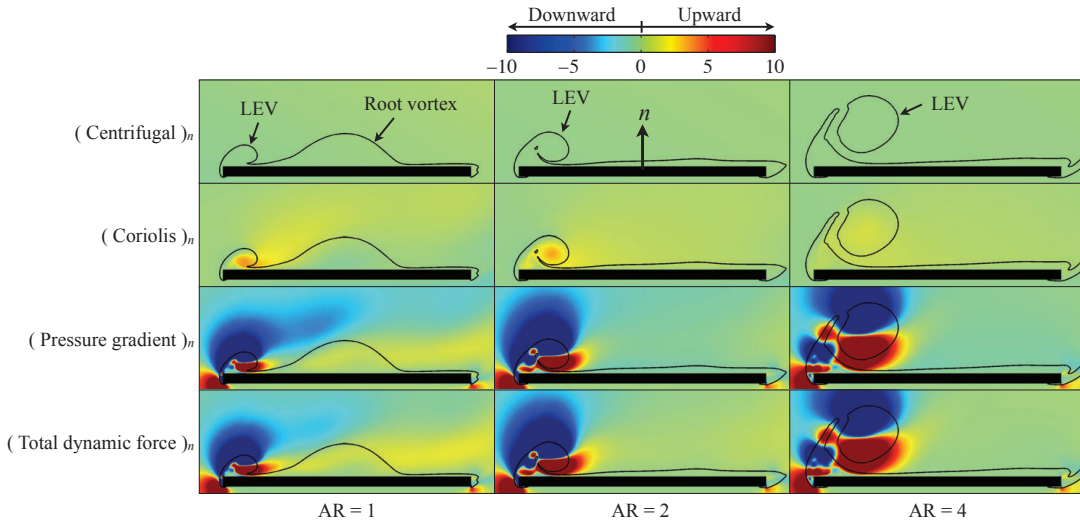


Figure 11: Contours of the surface-normal components of the centrifugal, Coriolis, pressure gradient forces and total dynamic forces at the 25% span-location. A single contour line of relative total pressure ($p_0/p_{0,\text{ref}} = 0.99$) superimposed to highlight the leading edge vortex. View is directed from root to tip, and all components are normalized by the maximum velocity of the wing at the mid-span.

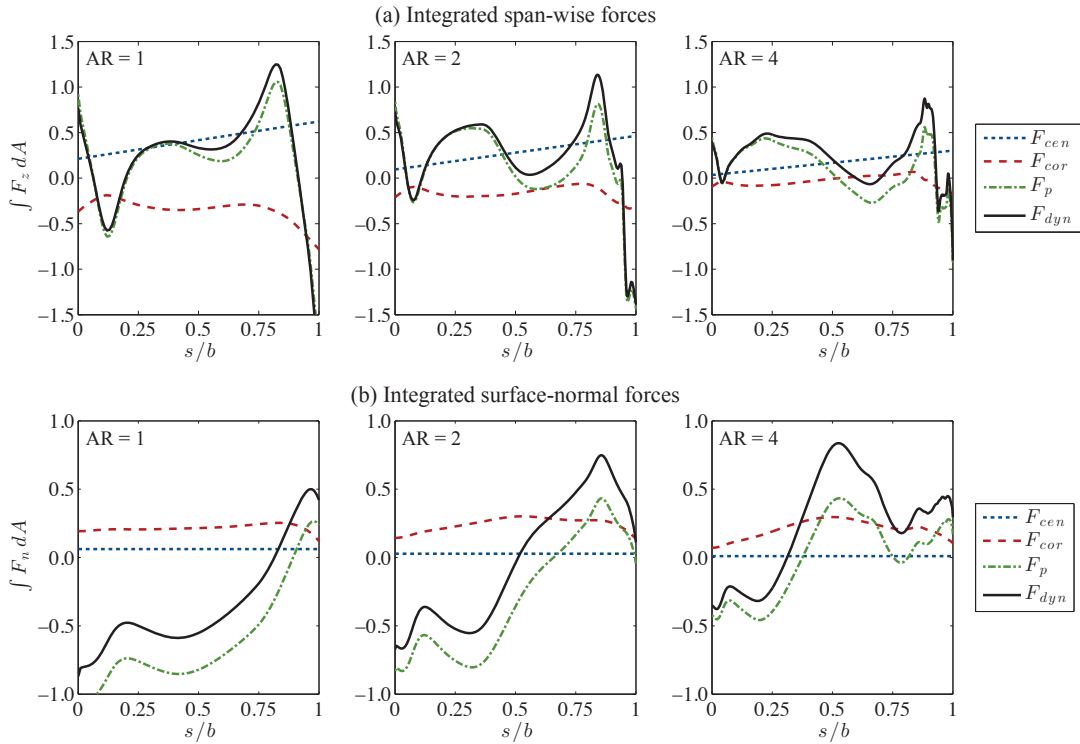


Figure 12: Net contributions of (a) the span-wise and (b) the surface-normal forces across the span. At each span-wise location, the force components are integrated across an area that extends from the wing surface to half a chord off the suction side and 0.1 chords off the leading and trailing edges.

VI. Isolation of dynamic effects due to rotation

In an attempt to separate and quantify the dominant mechanisms of leading edge vortex attachment, the aspect-ratio-two wing ($AR = 2$) is simulated with the addition of a source term in the governing equations to oppose and eliminate the centrifugal force around the wing. This is in an effort to assess the importance of the centrifugal force to vortex attachment for revolving wings. The wing is revolved in the same manner as before, but the inboard oriented source term eliminates the contribution of the outboard centrifugal force around the wing. While this simulation cannot be represented by a physical experiment, it does provide a means of isolating effects of rotation to emphasize their importance.

Iso-surfaces of relative total pressure are depicted in Fig. 13 for the wing without centrifugal force to highlight the overall vortex structure and the inner core at rotational angles of $\phi = 45^\circ, 90^\circ, 135^\circ$, and 180° . For $\phi \leq 45^\circ$, the flow field develops almost identically to the previous simulation with the centrifugal force included. This is not surprising since the wing is accelerating up until this point and has not reached its constant rotational rate, indicating that the initial vortex formation and development is due to the acceleration of the wing. The leading edge, tip, and root vortices produced at the edges unpin from the outboard corners and reconnect as before. The leading edge portion of the vortex lifts off the surface past mid-span as it reorients itself with the wing tip. At $\phi = 90$, however, the flow field starts to show differences. Without the outboard centrifugal force, the lifted-off section of the leading edge vortex progresses inboard causing spiraling undulations of the core near the wing root. The root vortex also moves towards the rotational axis and separates from the wing. For $\phi > 90^\circ$, the root vortex and the separation of the leading edge portion of the vortex continue to move inboard and eventually cause the entire vortex system to eject from the wing surface. At $\phi = 180^\circ$, only remnants of the vortex system are evident around the wing.

The relative span-wise velocities from the original solution and a solution with the absence of centrifugal force are depicted at several span-wise locations in Fig. 14. The rotational angle is $\phi = 90^\circ$. While there is a strong outboard flow present in the core of the LEV for both solutions, there is also a large inboard flow ahead of the leading edge in the absence of centrifugal force, which leads to increased shearing in the feeding sheet of the LEV. Additionally, a smaller region of outboard flow is present behind the leading edge without centrifugal force. The decreased span-wise flow around the vortex could lead to its eventual separation from the wing.

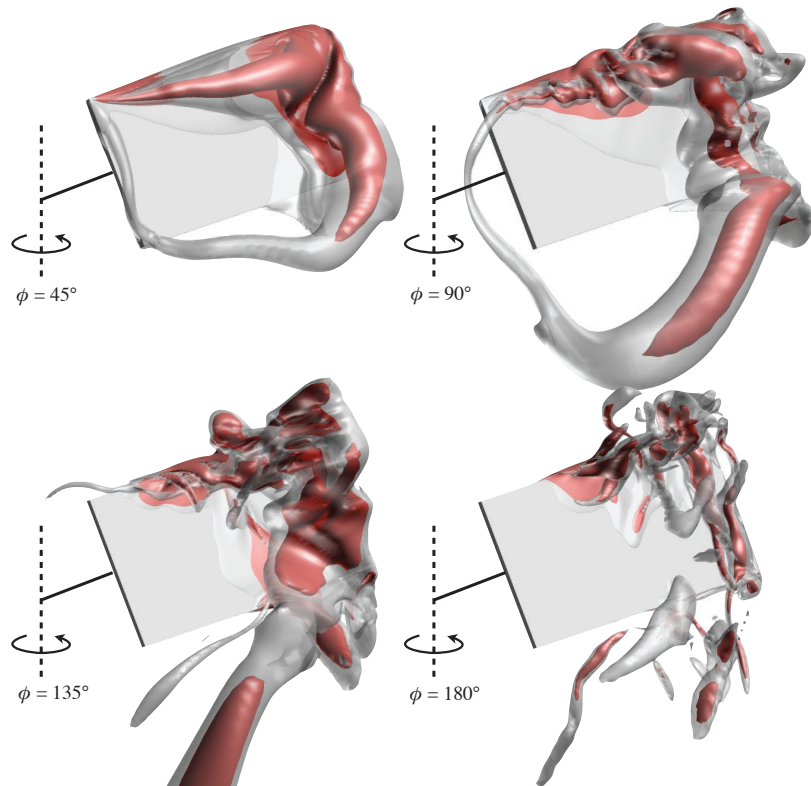


Figure 13: Evolution of the vortex structure about the revolving wing in the absence of centrifugal force.

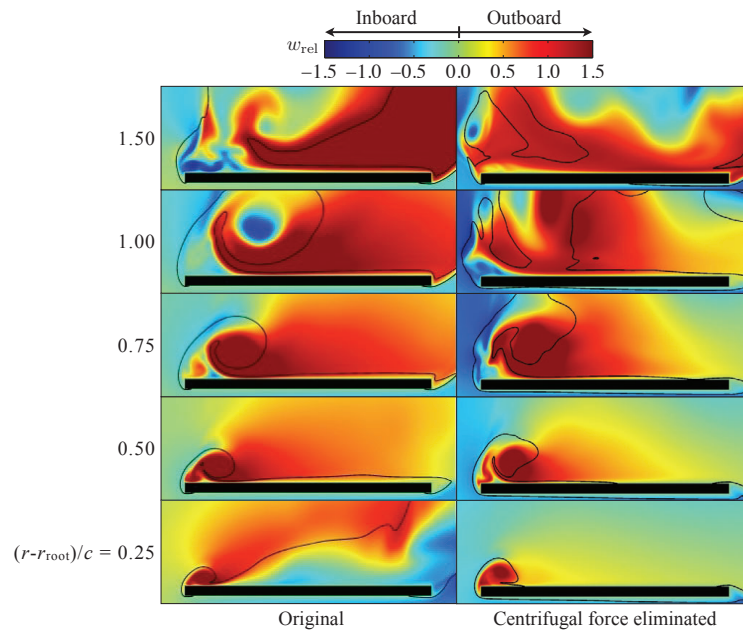


Figure 14: Relative span-wise velocity contours from the original solution and a solution with the centrifugal force eliminated. The rotational angle is $\phi = 90^\circ$, and a single contour of total pressure is superimposed to highlight the leading edge vortex.

VII. Summary and conclusions

A numerical study has been conducted to examine the vortex structure and aerodynamic loading on a unidirectionally revolving wing using high-fidelity, implicit large-eddy simulation. Several aspect ratio wings (AR = 1, 2, and 4) were simulated at a root-based Reynolds number of 1,000. A stable and coherent vortex system was observed emanating from the edges of the wing shortly after the onset of the motion. The proximity of the vortex to the surface of the wing promotes a strong region of suction along the leading edge that persists to the mid-span, regardless of aspect ratio. Past mid-span, the vortex lifts off the surface into an arch-type structure as it reorients itself along the tip. The highest aspect ratio wing promotes the development of substructures in the feeding sheet of the leading edge vortex. The origins of these features have been traced back to the eruption of near-wall vorticity underneath the vortex that disrupts the feeding sheet, causing it to roll-up into discrete substructures. For a fixed root-based Reynolds number of 1,000, the lower aspect ratio wings do not have sufficient spans for these transitional elements to manifest. Since the leading edge vortex grows proportionally to the distance from the rotational axis, the chord-wise extent of the vortex becomes constrained by the trailing edge with increased aspect ratio, leading to saturation of the aerodynamic loads. With AR = 1, the extent of the vortex never reaches the trailing edge, leading to a slight increase of the lift and drag coefficients throughout the motion.

The size and eventual breakdown of the leading edge vortex was shown to be sensitive to the distance from the rotational axis, indicating that a Reynolds number based on span-wise position may be appropriate for comparisons of wings of differing aspect ratio. Matching of the root-based Reynolds numbers between different wing planforms ensures that the variation of Reynolds number along the span is kept consistent. This is much like the scaling used for swept delta wings.

Additionally, the centrifugal, Coriolis, and pressure gradient forces were analyzed for each wing. The normal and span-wise components of the pressure gradient force at the 25% span-location were shown to dominate the other two forces by an order of magnitude in the core of the LEV regardless of aspect ratio. However, the centrifugal force was found to be equally important outside the vortex core, and the two, together, are responsible for the large regions of outboard flow around the suction side of the wing. The normal component of the Coriolis force was observed to be directed away from the wing surface at the base and in the core of the leading edge vortex indicating that it does not promote attachment of the vortex system, but rather, the opposite.

As a means of isolating dynamic effects due to rotation, the aspect-ratio-two wing was simulated with the addition of a source term in the governing equations to oppose and eliminate the centrifugal force near the wing surface. The initial formation and development of the leading edge vortex was unhindered by the absence of this force; however, later in the motion, the separation of the leading edge vortex near the tip was able to propagate inboard. Without the opposing outboard centrifugal force to keep the separation past mid-span, the vortex eventually separated and moved away from the surface much like that of a translating wing undergoing stall. The relative span-wise velocity revealed a reduction of outboard flow behind the LEV and a strong region of inboard flow ahead of the LEV when the centrifugal force was eliminated. This results in increased span-wise shearing of the vortex and could destabilizing the system.

Future studies will investigate the addition of a centrifugal-like source term in the governing equations for simulation of a translating wing to see if the addition of a span-wise force can augment leading edge vortex attachment and prevent separation during translation. An investigation of the flow structure about revolving wings undergoing reciprocating motions is also planned for future study.

Acknowledgements

This work is supported in part by AFOSR under a task monitored by Dr. D. Smith and also by a grant of HPC time from the DoD HPC Shared Resource Centers at AFRL and ERDC.

References

¹Ellington, C., "The Novel Aerodynamics of Insect Flight: Applications to Micro-Air Vehicles," *The Journal of Experimental Biology*, Vol. 202, 1999, pp. 3439–3448.

²Dickinson, M., "The Effects of Wing Rotation on Unsteady Aerodynamic Performance at Low Reynolds Numbers," *The Journal of Experimental Biology*, Vol. 192, 1994, pp. 179–206.

³Sane, S., "The aerodynamics of insect flight," *The Journal of Experimental Biology*, Vol. 206, No. 23, 2003, pp. 4191–4208.

⁴Birch, J. and Dickinson, M., "The influence of wing-wake interactions on the production of aerodynamic forces in flapping flight," *The Journal of Experimental Biology*, Vol. 206, 2003, pp. 2257–2272.

⁵Lehmann, F., "The mechanisms of lift enhancement in insect flight," *Naturwissenschaften*, Vol. 91, 2004, pp. 101–122.

⁶Lehmann, F. and Pick, S., "The aerodynamic benefit of wing-wing interaction depends on stroke trajectory in flapping insect wings," *The Journal of Experimental Biology*, Vol. 210, 2007, pp. 1362–1377.

⁷Dudley, R. and Ellington, C., "Mechanics of Forward Flight in Bumblebees: I. Kinematics and Morphology," *The Journal of Experimental Biology*, Vol. 148, 1990, pp. 19–52.

⁸Dudley, R. and Ellington, C., "Mechanics of Forward Flight in Bumblebees: II. Quasi-Steady Lift and Power Requirements," *The Journal of Experimental Biology*, Vol. 148, 1990, pp. 53–88.

⁹Fry, S., Sayaman, R., and Dickinson, M., "The Aerodynamics of Free-Flight Maneuvers in *Drosophila*," *Science*, Vol. 300, No. 495, 2003.

¹⁰Dickinson, M., Lehmann, F., and Sane, S., "Wing Rotation and the Aerodynamic Basis of Insect Flight," *Science*, Vol. 284, No. 1954, 1999.

¹¹Birch, J., Dickson, W., and Dickinson, M., "Force production and flow structure of the leading edge vortex on flapping wings at high and low Reynolds numbers," *The Journal of Experimental Biology*, Vol. 207, 2004, pp. 1063–1072.

¹²Poelma, C., Dickson, W., and Dickinson, M., "Time-resolved reconstruction of the full velocity field around a dynamically-scaled flapping wing," *Experiments in Fluids*, Vol. 41, 2006, pp. 213–225.

¹³Lentink, D. and Dickinson, M., "Biofluiddynamic scaling of flapping, spinning and translating fins and wings," *The Journal of Experimental Biology*, Vol. 212, 2009, pp. 2691–2704.

¹⁴Lentink, D. and Dickinson, M., "Rotational accelerations stabilize leading edge vortices on revolving fly wings," *The Journal of Experimental Biology*, Vol. 212, 2009, pp. 2705–2719.

¹⁵Ozen, C. and Rockwell, D., "Flow structure on a rotating plate," *Experiments in Fluids*, Vol. 52, No. 1, 2012, pp. 207–223.

¹⁶Carr, Z., Chen, C., and Ringuette, M., "The Effect of Aspect Ratio on the Three-Dimensional Vortex Formation of Rotating Flat-Plate Wings," AIAA Paper AIAA-2012-912, AIAA, 2012.

¹⁷Carr, Z., Chen, C., and Ringuette, M., "Development of the Three-Dimensional Vortex Structure and Forces of Low-Aspect Ratio, Rotating Flat-Plate Wings at Low Reynolds Numbers," AIAA Paper AIAA-2012-3280, AIAA, 2012.

¹⁸Lee, M. and Ho, C.-M., "Lift Force of Delta Wings," *Applied Mechanics Reviews*, Vol. 43, No. 9, 1990, pp. 209–221.

¹⁹Visbal, M., "Computed Unsteady Structure of Spiral Vortex Breakdown on Delta Wings," AIAA Paper 1996-2074, AIAA, 1996.

²⁰Visbal, M., "Onset of Vortex Breakdown Above a Pitching Delta Wing," *AIAA Journal*, Vol. 32, No. 8, 1994, pp. 1568–1575.

²¹Visbal, M. and Gordnier, R., "On the Structure of the Shear Layer Emanating from a Swept Leading Edge at Angle of Attack," AIAA Paper 2003-4016, AIAA, 2003.

²²Garman, D. and Visbal, M., "High-Fidelity Simulations of Transitional Flow Over Pitching Airfoils," AIAA Paper 2009-3693, AIAA, 2009.

²³Garman, D. and Visbal, M., "Implicit LES Computations for a Rapidly Pitching Plate," AIAA Paper AIAA-2010-4282, AIAA, 2010.

²⁴Garman, D., *High-Fidelity Simulations of Transitional Flow Over Pitching Airfoils*, Master's thesis, University of Cincinnati, 2010.

²⁵Garman, D. and Visbal, M., "Numerical investigation of transitional flow over a rapidly pitching plate," *Physics of Fluids*, Vol. 23, No. 9, 2011.

²⁶Visbal, M., "High-Fidelity Simulations of Transitional Flow past a Plunging Airfoil," *AIAA Journal*, Vol. 47, No. 11, 2009, pp. 2685–2697.

²⁷Visbal, M., "Numerical Investigation of Deep Dynamic Stall of a Plunging Airfoil," AIAA Paper 2010-4458, AIAA, 2010.

²⁸Rizzetta, D. and Visbal, M., "Effect of Plasma-Based Control for Low-Reynolds Number Flapping Airfoil Performance," AIAA Paper 2011-0735, AIAA, 2011.

²⁹Gordnier, R., Attar, P., Chimakurthi, S., and Cesnik, C., "Implicit LES Simulations of a Flexible Flapping Wing," AIAA Paper 2010-2960, AIAA, 2010.

³⁰Visbal, M., "Three-Dimensional Flow Structure on a Heaving Low-Aspect Ratio Wing," AIAA Paper 2011-0219, AIAA, 2011.

³¹Yilmaz, T. and Rockwell, D., "Three-dimensional flow structure on a maneuvering wing," *Experiments in Fluids*, Vol. 48, 2010, pp. 539–544.

³²Garman, D., Visbal, M., and Orkwis, P., "Three-dimensional flow structure and aerodynamic loading on a low-aspect-ratio, revolving wing," AIAA Paper 2012-3277, AIAA, 2012.

³³Tannehill, J., Anderson, D., and Pletcher, R., "Computational Fluid Mechanics and Heat Transfer," *Series in computational and physical processes in mechanics and thermal sciences*, Taylor & Francis, 2nd ed., 1997.

³⁴Visbal, M. and Rizzetta, D., "Large-Eddy Simulation on Curvilinear Grids Using Compact Differencing and Filtering Schemes," *Journal of Fluids Engineering*, Vol. 124, 2002, pp. 836–847.

³⁵Visbal, M., Morgan, P., and Rizzetta, D., "An Implicit LES Approach Based on High-Order Compact Differencing and Filtering Schemes," AIAA Paper 2003-4098, AIAA, June 2003.

³⁶Garman, D., Visbal, M., and Orkwis, P., "Comparative study of implicit and subgrid-scale model large-eddy simulation techniques for low-Reynolds number airfoil applications," *International Journal for Numerical Methods in Fluids*, 2012.

³⁷Stolz, S. and Adams, N., "An Approximate Deconvolution Procedure for Large-Eddy Simulation," *Physics of Fluids*, Vol. 11, No. 7, 1999, pp. 1699–1701.

³⁸Matthew, J., Lechner, R., Foysi, H., Sesterhenn, J., and Friedrich, R., "An Explicit Filtering Method for LES of Compressible Flows," *Physics of Fluids*, Vol. 15, No. 8, 2003, pp. 2279–2289.

³⁹Visbal, M. and Gaitonde, D., "High-Order Accurate Methods for Complex Unsteady Subsonic Flows," *AIAA Journal*, Vol. 37, No. 10, 1999, pp. 1231–1239.

⁴⁰Gaitonde, D. and Visbal, M., "High-Order Schemes for Navier-Stokes Equations: Algorithm and Implementation into FDL3DI," Technical Report AFRL-VA-WP-TR-1998-3060, Air Force Research Laboratory, Wright-Patterson AFB, 1998.

⁴¹Lele, S., "Compact Finite Difference Schemes with Spectral-like Resolution," *Journal of Computational Physics*, Vol. 103, 1992, pp. 16–42.

⁴²Gaitonde, D. and Visbal, M., "Further Development of a Navier-Stokes Solution Procedure Based on Higher-Order Formulas," AIAA Paper 99-0557, AIAA, 1999.

⁴³Alpert, P., "Implicit Filtering in Conjunction with Explicit Filtering," *Journal of Computational Physics*, Vol. 44, 1981, pp. 212–219.

⁴⁴Beam, R. and Warming, R., "An Implicit Factored Scheme for the Compressible Navier-Stokes Equations," *AIAA Journal*, Vol. 16, No. 4, 1978, pp. 393–402.

⁴⁵Pulliam, T. and Chaussee, D., "A Diagonal Form of an Implicit Approximate-Factorization Algorithm," *Journal of Computational Physics*, Vol. 17, No. 10, 1981, pp. 347–363.

⁴⁶Rizzetta, D., Visbal, M., and Morgan, P., "A High-Order Compact Finite-Difference Scheme for Large-Eddy Simulation of Active Flow Control (Invited)," AIAA Paper 2008-526, AIAA, 2008.

⁴⁷Jameson, A., Schmidt, W., and Turkel, E., "Numerical Solutions of the Euler Equations by Finite Volume Methods Using Runge-Kutta Time Stepping Schemes," AIAA Paper 1981-1259, AIAA, 1981.

⁴⁸Pulliam, T., "Artificial Dissipation Models for the Euler Equations," *AIAA Journal*, Vol. 24, No. 12, Dec. 1986, pp. 1931–1940.

⁴⁹Visbal, M. and Gaitonde, D., "On the Use of High-Order Finite-Difference Schemes on Curvilinear and Deforming Meshes," *Journal of Computational Physics*, Vol. 181, 2002, pp. 155–185.

⁵⁰Eldredge, J., Wang, C., and Ol, M., "A Computational Study of a Canonical Pitch-up, Pitch-down, Wing Maneuver," AIAA Paper 2009-3687, AIAA, 2009.

⁵¹Visbal, M., "On Some Physical Aspects of Airfoil Dynamic Stall," *Proceedings of the International Symposium on Non-Steady Fluid Dynamics*, edited by J. Miller and D. Telionis, Vol. 92, American Society of Mechanical Engineers, 1990.

⁵²Steger, J., Dougherty, F., and Benek, J., "A Chimera Grid Scheme," *Advances in Grid Generation*, edited by K. Ghia and U. Ghia, Vol. 5, American Society of Mechanical Engineers, 1983, pp. 59–69.

⁵³Sherer, S. and Scott, J., "High-Order Compact Finite-Difference Methods on General Overset Grids," *Journal of Computational Physics*, Vol. 210, No. 2, 2005, pp. 459–496.

APPENDIX E

Numerical Simulation of Excrescence Generated Transition

Donald P. Rizzetta* and Miguel R. Visbal†

Air Force Research Laboratory, Wright-Patterson Air Force Base, Ohio 45433-7512, USA

Large-eddy simulations (LES) are carried out in order to predict transition generated by excrescence on a plate-like geometry in subsonic flow. Both forward-facing and rearward-facing steps of small roughness height are considered in the investigation. These are representative of joints and other surface imperfections on wing sections that disrupt laminar flow, thereby increasing skin friction and drag. Solutions are obtained via a high-fidelity numerical scheme and an implicit LES approach, on an overset mesh system that is used to represent the steps. Very small-amplitude numerical forcing is employed to generate perturbations, which are amplified by the geometric disturbances, similar to the physical situation. Details of the simulation procedure are summarized, features of the flowfields are described, and the process of transition is elucidated. Comparisons are made with available experimental data in terms of time-mean skin-friction measurements. Locations of transition and skin friction levels predicted by the LES are in close correspondence with experiments. A grid resolution study was carried out to confirm accuracy of the computations. In the fully turbulent region downstream of transition, calculations agree with the expected behavior, but have not yet evolved to the high-Reynolds number asymptotic form.

Nomenclature

C_f	= time-mean skin friction coefficient
C_p	= time-mean surface pressure coefficient
E	= total specific energy
E_{k_z}, E_ω	= spanwise wave number and frequency spectral amplitudes
$\mathbf{F}, \mathbf{G}, \mathbf{H}$,	= inviscid vector fluxes
$\mathbf{F}_v, \mathbf{G}_v, \mathbf{H}_v$	= viscous vector fluxes
h	= dimensional plate thickness, 2.0in (0.00508m)
k	= dimensional excrescence step height, 0.04in (0.001m)
k_z	= nondimensional wave number
K	= turbulent kinetic energy, $0.5(\bar{u}'\bar{u}' + \bar{v}'\bar{v}' + \bar{w}'\bar{w}')$
K_i	= integrated turbulent kinetic energy, $\int K dy$
\mathcal{J}	= Jacobian of the coordinate transformation
M	= Mach number
p	= nondimensional static pressure
Pr	= Prandtl number, 0.73 for air
\mathbf{Q}	= vector of dependent variables
Q_i	= components of the heat flux vector
Re	= reference Reynolds number, $\rho_\infty u_\infty h / \mu_\infty$
Re_k	= roughness-based Reynolds number, $Re u_k h$
R_{11}, R_{22}, R_{33}	= spanwise correlation coefficients of the fluctuating velocity components
s	= nondimensional arc length along the plate surface
t	= nondimensional time
T	= nondimensional static temperature

*Senior Research Aerospace Engineer, Aerodynamic Technology Branch, AFRL/RQVA, Associate Fellow AIAA.

†Technical Area Leader, Aerodynamic Technology Branch, AFRL/RQVA, Fellow AIAA.

u, v, w	= nondimensional Cartesian velocity components in the x, y, z directions
u_1, u_2, u_3	= u, v, w
u_k	= nondimensional streamwise velocity of undisturbed flow evaluated at $x = x_k, y = k/h$
U, V, W	= contravariant velocity components
x, y, z	= nondimensional Cartesian coordinates in the streamwise, vertical, and spanwise directions
x_1, x_2, x_3	= x, y, z
x_d	= nondimensional downstream location of resolved region
x_k	= nondimensional streamwise step location
z_s	= nondimensional spanwise extent
γ	= specific heat ratio, 1.4 for air
δ	= nondimensional boundary-layer thickness
δ_{ij}	= Kronecker delta function
$\delta_{\xi 2}, \delta_{\eta 2}, \delta_{\zeta 2}$	= 2nd-order and 6th-order finite-difference operators in ξ, η, ζ
$\delta_{\xi 6}, \delta_{\eta 6}, \delta_{\zeta 6}$	
δ^*	= nondimensional displacement thickness
ΔQ	= $Q^{p+1} - Q^p$
Δt	= time step size
μ	= nondimensional molecular viscosity coefficient
ξ, η, ζ	= nondimensional body-fitted computational coordinates
$\xi_t, \xi_x, \xi_y, \xi_z$	= metric coefficients of the coordinate transformation
$\eta_t, \eta_x, \eta_y, \eta_z$	
$\zeta_t, \zeta_x, \zeta_y, \zeta_z$	
ρ	= nondimensional fluid density
τ_{ij}	= components of the viscous stress tensor
ω	= nondimensional frequency
ω_f	= nondimensional forcing frequency

Subscripts

r	= rescaled variable
s	= evaluated at the surface
∞	= dimensional reference value

Superscripts

n	= time level
p	= subiteration level
$\hat{}$	= filtered value
$'$	= fluctuating component
$\bar{}$	= time-mean quantity
$+$	= law-of-the-wall variable

I. Introduction

One of the principal considerations in the design and construction of aircraft is that of configuration drag. This is especially true for unmanned air systems (UAS) and high altitude long endurance (HALE) vehicles, which are primarily used for intelligence, surveillance, and reconnaissance missions requiring extensive loiter times at altitude. An approach for reducing drag in such applications is the use of wings devised to maintain laminar flow. Through a judicious design process, wings may be constructed so that the boundary layer can have a transition location which is significantly downstream of that in a conventional situation. This results in a smaller fraction of the vehicle wetted surface being exposed to turbulent flow and a reduction in drag, leading directly to lower fuel consumption, energy efficiency, longer range, larger payloads, or increased flight times.

The exploitation of laminar flow on air vehicles requires stringent manufacturing tolerances in the production of aerodynamic surfaces. Specifically, the heights of steps, the width of gaps, and the undulations

of surfaces must be minimized. In order to define allowable variations in these properties, they must first be quantified with regard to their ability to generate transition. It is the purpose of this investigation to assist in characterizing allowable sizes of surface imperfections on laminar-flow wings to preclude premature transition to turbulence. This will aid in development of criteria for manufacturing tolerances during the design and fabrication of long-endurance air vehicles.

Studies on effects of surface imperfections upon aerodynamic performance have been carried out for many years. As early as 1939, Hood¹ investigated waves on the surface of a NACA 23012 airfoil. It was reported that sinusoidal undulations of the leading-edge region could result in premature transition, thereby increasing skin friction drag. Subsequently, Fage² conducted experiments on flat plates and airfoil models with geometric shapes that were similar to those of Hood. He judged that the size of the surface perturbations required to generate transition, was essentially independent of pressure gradient. This presumption is now generally considered to be incorrect. In contrast to a smooth surface variation, effects of isolated surface excrescences were examined by Gregory et al.³ Flight test were conducted, and criteria for permissible "pimple" heights were reported.

Smith and Clutter⁴ investigated flows over wire trips, and quantified critical roughness Reynolds numbers capable of producing transition. They also decided that the transition process appeared to be insensitive to pressure gradient. Braslow⁵ compiled an early summary on the transition of boundary-layers due to surface roughness effects. It was found that roughness formed by integrated forward or rearward-facing steps had a critical roughness-based Reynolds number of approximately 200. Flight experiments conducted by Drake et al.⁶ explored effects of integral steps and gaps on boundary-layer transition for a wing with a favorable pressure gradient.

The advent of long-endurance air vehicles has more recently spawned a current series experimental studies devoted to the investigation of excrescence effects on transition.⁷⁻¹⁴ While early work of these studies focussed on zero pressure gradient flows,^{7,8} the long term goal was examination of excrescence generated transition in conditions typical of laminar flow wings.⁹⁻¹⁴ It was generally determined that laminar flow continued to exist for excrescence heights that were larger than previously thought possible. And although the probability of maintaining laminar flow for long-endurance air vehicles appears quite probable, it is still necessary to quantify excrescence effects in order to develop required criteria for manufacturing tolerances.

Surface imperfections have two dominant effects. They produce a local enhancement of receptivity to freestream disturbances due to geometry, and they result in a local modification of the time-mean flowfield and its stability properties. One purpose of the present investigation was to determine the possibility of predicting transition for the flow past steps of moderate roughness-based Reynolds number, through the use of large-eddy simulation. Although the computations are carried out using a high-order numerical method, many simulations of this type commonly require small-amplitude numerical forcing in order to create perturbations that are amplified by the geometric disturbances. The process is similar to that of the physical situation, which is receptive to freestream non-uniformities or other perturbations which eventually evolve into fully turbulent flows. In addition to providing insight into transition calculations, this effort also complements existing experimental data documenting excrescence-based transition, and increases understanding of the fundamental physical issues involved in the process. It may ultimately aid in development of criteria for manufacturing tolerances during the design and fabrication of UAS and HALE vehicles.

The large-eddy simulations are carried out for flow past a flat-plate configuration, which duplicates that of the experimental arrangement. Forward-facing and rearward-facing steps of small heights are imposed in the plate surface downstream of the leading edge. These can be considered representative of mismatched panels, which arise during the fabrication of aerodynamic surfaces. In the sections that follow, the governing equations are defined, the numerical method and LES approach are described, and details of the computations are outlined. Results of the simulations are summarized, features of the transition process are elucidated, and comparisons between the computations and experiments are provided.

II. The Governing Equations

The governing fluid equations are taken as the unsteady three-dimensional compressible unfiltered Navier-Stokes equations. Although these computations are considered to be large-eddy simulations, it will be subsequently explained why, unlike more traditional approaches, the unfiltered equations are solved. After introducing a generalized time-dependent curvilinear coordinate transformation to a body-fitted system, the

equations are cast in the following nondimensional conservative form

$$\frac{\partial}{\partial t} \left(\frac{1}{\mathcal{J}} \mathbf{Q} \right) + \frac{\partial}{\partial \xi} \left(\mathbf{F} - \frac{1}{Re} \mathbf{F}_v \right) + \frac{\partial}{\partial \eta} \left(\mathbf{G} - \frac{1}{Re} \mathbf{G}_v \right) + \frac{\partial}{\partial \zeta} \left(\mathbf{H} - \frac{1}{Re} \mathbf{H}_v \right) = 0. \quad (1)$$

Here t is the time, ξ, η, ζ the computational coordinates, \mathbf{Q} the vector of dependent variables, $\mathbf{F}, \mathbf{G}, \mathbf{H}$ the inviscid flux vectors, and $\mathbf{F}_v, \mathbf{G}_v, \mathbf{H}_v$ the viscous flux vectors. The vector of dependent variables is given as

$$\mathbf{Q} = \begin{bmatrix} \rho & \rho u & \rho v & \rho w & \rho E \end{bmatrix}^T \quad (2)$$

the vector fluxes by

$$\mathbf{F} = \frac{1}{\mathcal{J}} \begin{bmatrix} \rho U \\ \rho u U + \xi_x p \\ \rho v U + \xi_y p \\ \rho w U + \xi_z p \\ \rho E U + \xi_{x_i} u_i p \end{bmatrix}, \quad \mathbf{G} = \frac{1}{\mathcal{J}} \begin{bmatrix} \rho V \\ \rho u V + \eta_x p \\ \rho v V + \eta_y p \\ \rho w V + \eta_z p \\ \rho E V + \eta_{x_i} u_i p \end{bmatrix}, \quad \mathbf{H} = \frac{1}{\mathcal{J}} \begin{bmatrix} \rho W \\ \rho u W + \zeta_x p \\ \rho v W + \zeta_y p \\ \rho w W + \zeta_z p \\ \rho E W + \zeta_{x_i} u_i p \end{bmatrix} \quad (3)$$

$$\mathbf{F}_v = \frac{1}{\mathcal{J}} \begin{bmatrix} 0 \\ \xi_{x_i} \tau_{i1} \\ \xi_{x_i} \tau_{i2} \\ \xi_{x_i} \tau_{i3} \\ \xi_{x_i} (u_j \tau_{ij} - \mathcal{Q}_i) \end{bmatrix}, \quad \mathbf{G}_v = \frac{1}{\mathcal{J}} \begin{bmatrix} 0 \\ \eta_{x_i} \tau_{i1} \\ \eta_{x_i} \tau_{i2} \\ \eta_{x_i} \tau_{i3} \\ \eta_{x_i} (u_j \tau_{ij} - \mathcal{Q}_i) \end{bmatrix}, \quad \mathbf{H}_v = \frac{1}{\mathcal{J}} \begin{bmatrix} 0 \\ \zeta_{x_i} \tau_{i1} \\ \zeta_{x_i} \tau_{i2} \\ \zeta_{x_i} \tau_{i3} \\ \zeta_{x_i} (u_j \tau_{ij} - \mathcal{Q}_i) \end{bmatrix} \quad (4)$$

where

$$U = \xi_t + \xi_{x_i} u_i, \quad V = \eta_t + \eta_{x_i} u_i, \quad W = \zeta_t + \zeta_{x_i} u_i \quad (5)$$

$$E = \frac{T}{\gamma(\gamma-1)M_\infty^2} + \frac{1}{2} (u^2 + v^2 + w^2). \quad (6)$$

In the preceding expressions, u, v, w are the Cartesian velocity components, ρ the density, p the pressure, and T the temperature. All length scales have been nondimensionalized by the plate thickness h , and dependent variables have been normalized by reference values except for p which has been nondimensionalized by $\rho_\infty u_\infty^2$. Components of the heat flux vector and stress tensor are expressed as

$$\mathcal{Q}_i = - \left[\frac{1}{(\gamma-1)M_\infty^2} \right] \left(\frac{\mu}{Pr} \right) \frac{\partial \xi_j}{\partial x_i} \frac{\partial T}{\partial \xi_j} \quad (7)$$

$$\tau_{ij} = \mu \left(\frac{\partial \xi_k}{\partial x_j} \frac{\partial u_i}{\partial \xi_k} + \frac{\partial \xi_k}{\partial x_i} \frac{\partial u_j}{\partial \xi_k} - \frac{2}{3} \delta_{ij} \frac{\partial \xi_l}{\partial x_k} \frac{\partial u_k}{\partial \xi_l} \right). \quad (8)$$

The Sutherland law for the molecular viscosity coefficient μ and the perfect gas relationship

$$p = \frac{\rho T}{\gamma M_\infty^2} \quad (9)$$

were also employed, and Stokes' hypothesis for the bulk viscosity coefficient has been invoked.

III. The Numerical Method

Time-accurate solutions to Eq. (1) were obtained numerically by the implicit approximately-factored finite-difference algorithm of Beam and Warming¹⁵ employing Newton-like subiterations,¹⁶ which has evolved as an efficient tool for generating solutions to a wide variety of complex fluid flow problems, and may be written as follows

$$\left[\frac{1}{\mathcal{J}} + \left(\frac{2\Delta t}{3} \right) \delta_{\xi 2} \left(\frac{\partial \mathbf{F}^p}{\partial \mathbf{Q}} - \frac{1}{Re} \frac{\partial \mathbf{F}_v^p}{\partial \mathbf{Q}} \right) \right] \mathcal{J} \times \left[\frac{1}{\mathcal{J}} + \left(\frac{2\Delta t}{3} \right) \delta_{\eta 2} \left(\frac{\partial \mathbf{G}^p}{\partial \mathbf{Q}} - \frac{1}{Re} \frac{\partial \mathbf{G}_v^p}{\partial \mathbf{Q}} \right) \right] \mathcal{J} \times$$

$$\left[\frac{1}{\mathcal{J}} + \left(\frac{2\Delta t}{3} \right) \delta_{\zeta^2} \left(\frac{\partial \mathbf{H}^p}{\partial \mathbf{Q}} - \frac{1}{Re} \frac{\partial \mathbf{H}_v^p}{\partial \mathbf{Q}} \right) \right] \Delta \mathbf{Q} = - \left(\frac{2\Delta t}{3} \right) \left[\left(\frac{1}{2\Delta t} \right) \left(\frac{3\mathbf{Q}^p - 4\mathbf{Q}^n + \mathbf{Q}^{n-1}}{\mathcal{J}} \right) \right. \\ \left. + \delta_{\xi^6} \left(\mathbf{F}^p - \frac{1}{Re} \mathbf{F}_v^p \right) + \delta_{\eta^6} \left(\mathbf{G}^p - \frac{1}{Re} \mathbf{G}_v^p \right) + \delta_{\zeta^6} \left(\mathbf{H}^p - \frac{1}{Re} \mathbf{H}_v^p \right) - D_c q_c \mathbf{S}^p \right]. \quad (10)$$

In this expression, which is employed to advance the solution in time, \mathbf{Q}^{p+1} is the $p+1$ approximation to \mathbf{Q} at the $n+1$ time level \mathbf{Q}^{n+1} , and $\Delta \mathbf{Q} = \mathbf{Q}^{p+1} - \mathbf{Q}^p$. For $p=1$, $\mathbf{Q}^p = \mathbf{Q}^n$. Second-order-accurate backward-implicit time differencing was used to obtain temporal derivatives.

The implicit segment of the algorithm (left-hand side of Eq. 10) incorporates second-order-accurate centered differencing for all spatial derivatives, and utilizes nonlinear artificial dissipation¹⁷ to augment stability. For simplicity, the dissipation terms are not shown in Eq. (10). Efficiency is enhanced by solving this implicit portion of the factorized equations in diagonalized form.¹⁸ Temporal accuracy, which can be degraded by use of the diagonal form, is maintained by utilizing subiterations within a time step. This technique has been commonly invoked in order to reduce errors due to factorization, linearization, diagonalization, and explicit application of boundary conditions. It is useful for achieving temporal accuracy on overset zonal mesh systems, and for a domain decomposition implementation on parallel computing platforms. Any deterioration of the solution caused by use of artificial dissipation and by lower-order spatial resolution of implicit operators is also reduced by the procedure. Three subiterations per time step have been applied in the current simulations to preserve second-order temporal accuracy.

The compact difference scheme employed on the right-hand side of Eq. 10 is based upon the pentadiagonal system of Lele,¹⁹ and is capable of attaining spectral-like resolution. This is achieved through the use of a centered implicit difference operator with a compact stencil, thereby reducing the associated discretization error. For the present computations, a sixth-order tridiagonal subset of Lele's system is utilized, which is illustrated here in one spatial dimension as

$$\alpha_d \left(\frac{\partial \mathbf{F}}{\partial \xi} \right)_{i-1} + \left(\frac{\partial \mathbf{F}}{\partial \xi} \right)_i + \alpha_d \left(\frac{\partial \mathbf{F}}{\partial \xi} \right)_{i+1} = a \left(\frac{\mathbf{F}_{i+1} - \mathbf{F}_{i-1}}{2} \right) + b \left(\frac{\mathbf{F}_{i+2} - \mathbf{F}_{i-2}}{4} \right) \quad (11)$$

with $\alpha_d = 1/3$, $a = 14/9$, and $b = 1/9$. The scheme has been adapted by Visbal and Gaitonde²⁰ as an implicit iterative time-marching technique, applicable for unsteady vortical flows, and has been used to obtain the spatial derivative of any scalar, flow variable, metric coefficient, or flux component. It is used in conjunction with a low-pass Pade-type non-dispersive spatial filter developed by Gaitonde et al.,²¹ which has been shown to be superior to the use of explicitly added artificial dissipation for maintaining both stability and accuracy on stretched curvilinear meshes.²⁰ The filter is applied to the solution vector sequentially in each of the three computational directions following each subiteration, and is implemented in one dimension as

$$\alpha_f \hat{\mathbf{Q}}_{i-1} + \hat{\mathbf{Q}}_i + \alpha_f \hat{\mathbf{Q}}_{i+1} = \sum_{n=0}^4 \frac{a_n}{2} (\mathbf{Q}_{i+n} + \mathbf{Q}_{i-n}) \quad (12)$$

where $\hat{\mathbf{Q}}$ designates the filtered value of \mathbf{Q} . It is noted that the filtering operation is a post processing technique, applied to the evolving solution in order to regularize features that are captured but poorly resolved. Equation 12 represents a one-parameter family of eighth-order filters, where numerical values for the a_n 's may be found in Ref. 22. The filter coefficient α_f is a free adjustable parameter which may be selected for specific applications, where $|\alpha_f| < 0.5$. The value of α_f determines sharpness of the filter cutoff and has been set to 0.40 for the present simulations.

The aforementioned features of the numerical algorithm are embodied in a parallel version of the time-accurate three-dimensional computer code FDL3DI,²² which has proven to be reliable for steady and unsteady fluid flow problems, including vortex breakdown,^{23,24} transitional wall jets,²⁵ synthetic jet actuators,²⁶ roughness elements,²⁷ plasma flows,²⁸⁻³⁶ and direct numerical and large-eddy simulations of subsonic^{37,38} and supersonic flowfields.^{39,40}

IV. The LES Approach

In the LES approach, physical dissipation at length scales smaller than those in the inertial range is not resolved, thereby allowing for less spatial resolution and a savings in computational resources. For

nondissipative numerical schemes, without use of subgrid-scale (SGS) models, this leads to an accumulation of energy at high mesh wave numbers, and ultimately to numerical instability. Traditionally, explicitly added SGS models are then employed as a means to dissipate this energy. In the present methodology, the effect of the smallest fluid structures is accounted for by a high-fidelity implicit large-eddy simulation (HFILES) technique, which has been successfully utilized for a number of turbulent and transitional computations. The present HFILES approach was first introduced by Visbal et al.^{41,42} as a formal alternative to conventional methodologies, and is predicated upon the high-order compact differencing and low-pass spatial filtering schemes, without the inclusion of additional SGS modeling. This technique is similar to monotonically integrated large-eddy simulation (MILES)⁴³ in that it relies upon the numerical solving procedure to provide the dissipation that is typically supplied by conventional SGS models. Unlike MILES however, dissipation is contributed by the aforementioned high-order Pade-type low-pass filter only at high spatial wavenumbers where the solution is poorly resolved. This provides a mechanism for the turbulence energy to be dissipated at scales that cannot be accurately represented on a given mesh system, in a fashion similar to subgrid modeling. For purely laminar flows, filtering may be required to maintain numerical stability and preclude a transfer of energy to high-frequency spatial modes due to spurious numerical events. The HFILES methodology thereby permits a seamless transition from large-eddy simulation to direct numerical simulation as the resolution is increased. In the HFILES approach, the unfiltered governing equations may be employed, and the computational expense of evaluating subgrid models, which can be substantial, is avoided. This procedure also enables the unified simulation of flowfields where laminar, transitional, and turbulent regions simultaneously coexist. For the present situation, the range of fluid scales in the transition region is limited and thus may be fully resolve by the HFILES formulation. Here, the solution can be consider a direct numerical simulation, which may not be true if lower-order numerical methods are employed.

It should also be noted that the HFILES technique may be interpreted as an approximate deconvolution SGS model,⁴⁴ which is based upon a truncated series expansion of the inverse filter operator for the unfiltered flowfield equations. Mathew et al.⁴⁵ have shown that filtering provides a mathematically consistent approximation of unresolved terms arising from any type of nonlinearity. Filtering regularizes the solution, and generates virtual subgrid model terms that are equivalent to those of approximate deconvolution.

V. Details of the Computations

A. The Computational Configurations

The configurations to be considered in the computations correspond to that of experimental arrangements detailed in Refs. 7–14, and illustrated schematically in Fig. 1. The model geometry consists of 2.0in (0.00508m) thick flat plate with a rounded leading edge. The thickness h was employed as a reference quantity to nondimensionalize all spatial lengths. For the purpose of these simulations, a Cartesian coordinate system was established with its origin located at the inboard leading edge of the plate. The shape of the leading edge was prescribed by a superellipse having the following functional form:

$$\left| \frac{(x_s - a)}{a} \right|^m + \left| \frac{(y_s)}{b} \right|^m = 1 \quad (13)$$

where a and b are the semi-diameters and $m = 2.2$. The aspect ratio of the ellipse was 6:1 such that $a/b = 6$, and $b = h/2$. In experiments, forward-facing and rearward-facing steps of 0.04in (0.001m) in height ($k = 0.02$), were located 18.85in (0.48m) downstream of the plate leading edge ($x_k = 9.42$). Simulations resolved the region for $x < x_d$ with $x_d = 42.0$. The spanwise extent of the computational was taken equal to the plate thickness ($z_s = 1.0$). It was estimated that in the fully turbulent region downstream of steps, this distance would be adequate to capture relevant physical properties.

B. Computational Meshes

The overset computational mesh systems employed for the simulations are displayed in Fig. 2. Because the plate configuration is symmetric about $y = 0$ and the angle of attack is 0 deg, only the upper half of the geometry is represented in the computations. Shown in frame a) of the figure is the overall flowfield representation, where only a fraction of the total grid lines appear. The planar C-grid construct was generated using automated software,⁴⁶ such that the outer boundaries were stretched to a distance of 100 plate thicknesses from the leading edge. The planar grid structure was then distributed uniformly in the z direction, due to

Table 1. Computational mesh sizes

configuration	designation	upstream grid	downstream grid	total points
baseline		(1741 \times 301)		524,041
forward-facing step		(421 \times 399 \times 205)	(1425 \times 305 \times 205)	123,533,820
rearward-facing step	fine	(325 \times 301 \times 205)	(1421 \times 401 \times 205)	136,867,430
rearward-facing step	medium	(245 \times 226 \times 155)	(1066 \times 301 \times 155)	58,316,580
rearward-facing step	coarse	(165 \times 151 \times 105)	(711 \times 201 \times 105)	17,621,730

spanwise homogeneity of the configuration. The nondimensional grid spacing in the wall-normal direction at the surface was 0.0002. Downstream of the steps, a uniform distribution of $\Delta x = 0.025$ was employed. Seen in frame b) of Fig. 2 is the overset grid structure for the forward-facing step, and that of the rearward-facing step is found in frame c). Because mesh points in the respective grids upstream and downstream of the step locations (x_k) coincide in the overlap region, no interpolation between the systems is required. The number of points for each mesh is given in Table 1.

Besides the mesh systems described above, additional grids were developed for the rearward-facing step in order to assess the effects of spatial resolution on computed results. For both grids, the same regions of clustering and mesh spacing ratios were maintained. This was achieved by fitting a cubic spline to each coordinate, and then redistributing the grid points. In each coordinate direction, approximately 75% of the number of grid points in the fine grid system were utilized for the medium mesh, and 50% for the coarse mesh. Unless specifically stated otherwise, all results to be subsequently described will have been obtained on the finest computational meshes.

C. Boundary Conditions

On all solid surfaces, the no slip condition was enforced, along with an adiabatic wall and vanishing normal pressure gradient, that were implemented with third-order spatial accuracy. At the farfield boundaries (upstream, downstream, and upper), freestream conditions were specified for dependent variables. Grid stretching in farfield regions transferred information to high spatial wave numbers, and it was then dissipated by the low-pass numerical filter.⁴⁷ This technique prevents any spurious reflections, particularly in the outflow area of the computational domain. Periodic conditions were specified at the spanwise boundaries, where a five-grid plane overlap of the mesh systems was employed.

D. Preliminary Computations

The freestream Mach number M_∞ was set to 0.1, and preliminary computations were carried out for the baseline flat-plate configuration without steps. These two-dimensional calculations utilized the mesh system indicated in Table 1. The value of Re was varied parametrically until an appropriate roughness-based Reynolds number was determined. For $Re = 90,000$, it was established that $Re_k = 1013$, where $Re_k = Re u_k k$. Here, u_k is the value of the streamwise velocity u evaluated at $x = x_k$ and $y = k/h$, in the undisturbed flow without a step. This roughness Reynolds number is similar to that seen experimentally, and was shown to produce transition. In the subsequent LES, the value $Re = 90,000$ was employed.

Found in Fig. 3 are computed results for the baseline case, which indicate the global appearance of the flowfield. Contours of the u -velocity component are visible in frame a) of the figure, and those of the pressure coefficient in frame b). The spanwise extent of the configuration is only for visual effect. Expansion over the elliptic leading edge is evident in the figure, and downstream the solution is essentially that of a flat plate in the absence of incoming freestream disturbances.

VI. The Numerical Forcing Methodology

It was originally envisioned that it might be possible to simulate transition without use of any numerical perturbations. There are a number of sources in any numerical scheme which can produce perturbations. And, due to the inherent stability properties of the boundary layer, it was thought that the geometric

step disturbances would then promote growth of instabilities, reinforcing the perturbations, and lead to transition. Computations were carried out on the coarse-mesh system for the rearward-facing step. Although a development of fine-scale fluid structures did occur, its appearance was sporadic. Thus in the time-mean flowfield, transition was much further downstream than that observed experimentally. Furthermore, as the grid was refined, the regions of fine-scale structures became more erratic. Forcing was then applied at a frequency within the unstable range of that associated with the boundary layer upstream of the step. This was ineffective. It was noted from an examination of the resultant turbulent kinetic energy frequency spectra (to be discussed later), that a dominant mode existed downstream of the step. This mode had a lower frequency and was found to be associated with the increase in displacement thickness generated by the step. As noted in the Introduction, the geometric disturbance modified the stability properties of the boundary layer. When forcing was applied at the lower frequency, the transition process was regularized. The location of transition was brought into correspondence with experimental measurements, and it was rendered largely insensitive to grid refinement.

Numerical forcing was implemented as an imposed vertical velocity at the surface, and has the following specified form

$$v = AF_f(x)G_f(t) \quad (14)$$

where

$$F_f(x) = \sin \theta(1 - \cos \theta), \quad \theta = 2\pi \left(\frac{x - x_b}{x_e - x_b} \right) \quad (15)$$

$$G_f(t) = \sin(2\pi\omega_f t) \quad (16)$$

The locations x_b and x_e correspond to the beginning and end of the forcing region. The length $x_e - x_b$ was selected as a wave length within the unstable region based upon the stability diagram for the upstream flat-plate boundary layer,⁴⁸ and was taken as 0.12 (this length is equal to 6 times the step height). Equation (14) represents a blowing/suction slot, which adds no mass to the flow. It results in the generation of vorticity waves that may be amplified by the geometric disturbances. This form is identical to that utilized by others for both subsonic⁴⁹ and supersonic^{50,51} transition applications. The forcing slot was positioned at the edges of the steps, and its length and location is represented schematically in Fig. 4. The non-dimensional frequency ω_f was taken as 0.5, whose choice was dictated by the stability diagram.⁴⁸ This frequency was within the unstable range based upon displacement thickness generated by the step. The amplitude A could be varied to increase or decrease the magnitude of the perturbation. For the rearward-facing step, the value $A = 0.0001$ was sufficient to generate transition. However, with the forward-facing step, sustainable transition could not be achieved with this magnitude. Some coarse-grid investigations indicated that slightly higher values could produce transition, but because the computations were resource intensive, the more reliable specification $A = 0.0005$ was selected. Note that this small amplitude is 0.05% of the freestream velocity, and is probably lower than common freestream turbulence levels. Results to follow for the LES will explain the difference in transition behavior for the respective steps, and why a larger value of A was required for the forward-facing case.

VII. Numerical Results

Simulations were carried out with nondimensional time increments of $\Delta t = 0.000125$ for the forward-facing step, and $\Delta t = 0.000250$ for the rearward-facing step. These values were dictated by stability restrictions for the overset mesh systems, and were unrelated to numerical forcing. The time increments provided 16,000 and 8,000 steps per cycle of the forcing frequency for the respective cases. Mesh systems indicated in Table 1 were partitioned for parallel processing, and distributed across 1535 computing cores for the forward-facing step and 1640 for the rearward-facing step (fine mesh). After initializing forcing and attaining equilibrium flowfields, all solutions were evolved for a minimum of 650,000 time steps in order to acquire time-mean and statistical information.

A. Features of the Time-Mean Flowfields

Features of the time-mean flowfields are represented in Figs. 5-12. Unless explicitly stated otherwise, these results have been averaged in the homogeneous spanwise direction, as well as in time. To assess the effect of grid resolution, solutions were obtained on three different mesh systems (see Table 1) for the rearward-facing

step. Presented in Fig. 5 are time-mean distributions of the pressure along the plate surface. Here, s is the nondimensional arc length of the surface geometry starting from the leading edge. As demonstrated in the figure, there is an expansion about the leading edge, followed by an adverse pressure gradient up to the step. A fairly constant pressure level is attained in the downstream region. Little sensitivity is seen with regard to grid density. Corresponding distributions of the time-mean skin friction appear in Fig. 6. As reference levels, laminar and turbulent theoretical distributions are also shown. The laminar distribution corresponds to the Blasius solution, while that for the turbulent distribution represents the result for a 1/7 power law profile. Here, there is a notable dependence upon grid resolution, but results appear to be collapsing to a grid independent state. The dependence is probably dominated by the normal grid spacing at the surface. That notwithstanding, the location of transition at $x \approx 12.0$, is relatively insensitive to grid spacings. It should also be noted that the coarse mesh system has less than 13% of the grid points as that of its fine counterpart (see Table 1). Because of the leading-edge expansion, adverse pressure gradient, and associated evolution of the displacement thickness, the skin friction does not correspond with the theoretical zero-pressure gradient level. This is particularly true downstream of transition. Even though the flow is fully turbulent, it exists in a different state from that of the high-Reynolds number flat-plate equilibrium situation.

Time-mean surface pressure distributions for the forward-facing and rearward-facing steps are exhibited in Fig. 7. One of the major differences between these two results is visible in the region of the step location. With the forward-facing step, the pressure gradient just ahead of the corner is adverse. For the rearward-facing step, there is a region of favorable pressure gradient, as the flow passes over the step to the lower surface downstream. Corresponding distributions of the skin friction for both cases are shown in Fig. 8. Apart from small differences at the step locations, the distributions are quite similar. In particular, the transition location is approximately the same for both cases. Distributions of the time-mean displacement thickness are displayed in Fig. 9. The displacement thickness is related to both pressure gradient and skin friction through the momentum integral equation. The observed differences in δ^* for the respective steps is consistent with results indicated in Figs. 7 and 8. Abrupt changes of δ^* in the step region are responsible for altering the boundary-layer stability properties. Values of the displacement thickness for the forward-facing step just upstream of the corner are similar to that of the rearward-facing step downstream of the corner. However, there is a large decrease in δ^* for the forward-facing step downstream of the corner. This results in a shift of the unstable frequency range to higher values. In retrospect, perhaps a larger value of the forcing frequency could have been applied for the forward-facing step case. Nevertheless, there is a wide range of unstable frequencies along the flow path, and transition transition was also achieved by increasing the forcing amplitude.

Time-mean skin friction distributions from the large-eddy simulations are compared to experimental data⁹ in Figs. 10 and 11. Experimental measurements were made for a range of roughness-based Reynolds numbers. Comparisons in the figures consist of cases for which Re_k was both above and below those of the simulations, and represent values that most closely approximated those of the computations. For each experimental value of Re_k , data was obtained at two different spanwise locations, both of which are found in the figures. Results for the forward-facing step are given in Fig. 10. The location of transition predicted by the LES compares reasonably well with the experiment. Downstream levels of C_f following transition are below the flat-plate high Reynolds number equilibrium theoretical prediction, for reasons previously mentioned. Because the flow for small roughness heights may be very sensitive to any minute perturbations which can be present in the experiment due to freestream disturbances, vibration, or other factors, and in the simulation to a number of numerical causes, the comparison is generally considered to be quite favorable. A similar comparison for the rearward-facing step is provided in Fig. 11. Here too, the comparison is favorable. And as was the case for the forward-facing step, C_f levels downstream of transition are somewhat below those of the experiment.

Streamlines of the time-mean flowfield and planar contours of the u -velocity component are pictured in Fig. 12. For the forward-facing step, a small region of reversed flow extends upstream of the corner, a distance of approximately 5 step heights. It is indicated for the rearward-facing step, that a long separation region exists, for an extended distance of 44 step heights downstream of the corner.

B. Features of the Instantaneous Flowfields

Instantaneous planar contours and iso-surfaces of the v -velocity component are depicted in Fig. 13. In this representation, the spanwise coordinate (z) has been stretched by a factor of 2.0 in order to facilitate viewing of the flowfield. Note that the magnitude of the contours and iso-surfaces is quite small, indicating

that the observed structures are rather weak. These structures are initially very coherent. Non-uniformities begin to develop at around $x = 13.85$ for the rearward-facing step, which is a distance of 4.43 downstream of the corner. This is a length of approximately 220 step heights. For the forward-facing step, the non-uniformity starts to occur further downstream at $x = 14.4$. These structures evolved from the geometric disturbances produced by the steps, and were evident in solutions even without numerical forcing. They convect downstream at a frequency that lies within the unstable region of the boundary-layer stability diagram. Because that region has a fairly wide range of frequency, the generation of the structures was not uniform. This resulted in a sporadic production of turbulence downstream. Forcing regularized the evolution of these structures, resulting in a consistent transition process.

Presented in Fig. 14 are instantaneous planar contours of the spanwise vorticity at the inboard boundary, and planar contours of the u -velocity in the near-wall region. In this view, the y -coordinate has been scaled by a factor of 5.0, so that the flowfield features are more easily seen. Fine-scale structures in the near-wall region and the hairpin vortices represented by the spanwise vorticity, are characteristic of the fully turbulent flow which develops downstream of transition. An additional portrayal of these characteristics is demonstrated by instantaneous iso-surfaces of the Q -criterion vortex identification function⁵² seen in Fig. 15. The Q -criterion has commonly been utilized to represent vortical fluid structures, and has been colored by the streamwise velocity in the figure, where the spanwise coordinate (z) has been stretched by a factor of 5.0. Downstream of transition in the fully turbulent region, the flows for both steps is quite similar.

Certain aspects of the transition process can be quantified by integrating the turbulent kinetic energy in the wall normal direction (y), and plotting the result as a function of streamwise distance. Distributions of the integrated turbulent kinetic energy appear in Fig. 16, where

$$K_i = \int K dy, \quad \text{and} \quad K = 0.5(\bar{u}'\bar{u}' + \bar{v}'\bar{v}' + \bar{w}'\bar{w}'). \quad (17)$$

In Eq. (17), the integration in y takes place from the surface to the outer boundary, and K has been averaged in the homogeneous spanwise direction (z). For $x < 12.0$, the small magnitude of K_i corresponds to the coherent structures. In the transition region ($x \approx 15.0$), a local maximum of K_i occurs, which coincides with a similar behavior seen in the skin friction (see Figs. 10 and 11). Following the maximum, K_i decays until $x \approx 18.0$, and then consistently grows in the downstream fully turbulent region. Note that the levels of K_i for the rearward-facing step are slightly higher than those of the forward-facing step, even though a greater magnitude of forcing was applied for the latter.

Shown in Fig. 17 are turbulent kinetic energy frequency spectra for the rearward-facing step in the transition region just downstream of x_k (9.42). These and all other spectra to follow (E_{k_z}, E_ω) were collected at a normal distance from the surface of one half the step height (0.02). At $x = 13.9$, spectra are provided for solutions both with and without numerical forcing. The frequency range indicated as ① in the figure, represents the extent of the stability diagram in the unstable region, based on the displacement thickness of the upstream, undisturbed boundary layer. As is visible in the figure, the spectral amplitude in this range is quite low. The frequency range designated ② corresponds to the unstable region, after the displacement thickness has been modified by presence of the step. In the unforced solution, the spectral amplification is found to be nonuniform. When forcing is applied, the spectral magnitude is substantially increased, and the amplification frequency becomes discrete. The forcing frequency $\omega_f = 0.5$ was selected as a convenient choice within the unstable range. Higher harmonics of the fundamental mode are observed in the spectra. Further downstream at $x = 17.9$, remnants of the forcing are not seen in the spectra following transition.

C. The Downstream Turbulent Region

Mesh spacings in wall units at $x = 40.0$ are given in Table 2, and indicate that the boundary layer and near-wall region are adequately resolved for both steps. The spacings in all three directions fall within the commonly accepted range for large-eddy simulations.^{53,54} Features of the fully turbulent region downstream of transition are illustrated in Figs. 18-23. Turbulent kinetic energy spanwise wave number spectra are exhibited in Fig. 18 at $x = 40$. For the rearward-facing step, solutions are displayed from results on all three mesh systems. As the grid density is increased, the spectra is resolved for higher wave numbers, as expected. On the finest grids, it is evident that the inertial range is captured

Displayed in frame a) of Fig. 19 are profiles of the time-mean streamwise velocity u , plotted in law-of-the-wall variables. Results for the forward-facing and rearward-facing steps are in close agreement with each other, but both differ from the high-Reynolds number asymptotic profile in the logarithmic region. The

Table 2. Mesh spacings in the downstream region

configuration	Δx^+	Δy_s^+	Δz^+	no. pts. for $\Delta y^+ < 10$	no. pts. in boundary layer
forward-facing step	80.1	0.64	16.0	11	199
rearward-facing step	81.1	0.65	16.2	16	293

behavior depicted in the figure is often associated with a lack of spatial resolution in numerical simulations. In the present situation however, that is not the case. The circumstance here, is that the flow has been modified by the displacement effect due to the step, and following transition has not yet evolved to the high-Reynolds number equilibrium state. To provide some evidence of this assertion, the profiles in frame a) of the figure have been rescaled using the skin friction from the high-Reynolds number formulation (1/7 power law profile). In Figs. 10 and 11, the computations did not quite achieved the asymptotic limit. Profiles in the rescaled variables are pictured in frame b) of Fig. 19. In this formulation, the profiles cannot satisfy the proper linear near-wall behavior. As seen in the figure, the asymptotic limit is still not attained in the logarithmic region.

A representation of the streamwise evolution of the flowfield is indicated by time-mean profiles of the turbulent kinetic energy for the rearward-facing at several x -stations in Fig. 20. The profiles have been averaged in the homogeneous spanwise direction, as well as temporally. Results for the forward-facing step are very similar. For each location, the origin of the x -axis has been translated for clarity. As the flow evolves in the streamwise direction, the peak value of the turbulent kinetic energy (K) decreases. This occurs even though total energy increases, as was seen in Fig. 16. In addition to growth of K_i , there is a redistribution of the energy from the near-wall layer to the outer region. Also shown in the figure at $x = 40.0$, is the classic high-Reynolds number flat-plate experimental data of Klebanoff.⁵⁵ The LES appears to be approaching the high-Reynolds situation, but varies appreciably from it in the logarithmic region. Corresponding time-mean streamwise velocity profiles and Klebanoff's⁵⁵ data are found in Fig. 21. These also demonstrate that the flow has not yet fully evolved to the high-Reynolds number equilibrium state.

One aspect of LES that can preclude correct physical behavior, is the length of the homogeneous extent (z -direction). If this distance is not sufficient, the solution may be over constrained due to application of periodic boundaries. To determine adequacy of the homogeneous extent, spanwise correlation coefficients of the fluctuating velocity components were computed, and are exhibited for the rearward-facing step in Fig. 22. The coefficients are defined as

$$R_{ii} = \frac{\overline{u'_{ia} u'_i}}{\sqrt{\overline{u'_{ia}^2}} \sqrt{\overline{u'_i^2}}} \quad (18)$$

where $i = 1, 2, 3$, $u'_1, u'_2, u'_3 = u', v', w'$ and u'_{ia} is evaluated at $z = 0.5$.

Distributions appearing in Fig. 22 were evaluated at a distance from the surface equal to one half of the step height (0.02), similar to spectral data. A rapid decay in the amplitude of the coefficients away from $z = 0.5$ signifies that there is no anomalous behavior due to inadequacy of the homogeneous distance. Results for the forward-facing step were similar. Turbulent kinetic energy frequency spectra in the downstream region are presented in Fig. 23. The spectra are characterized by the broadband content typical of fully turbulent flows. The inertial range is apparent, and there is no evidence of the upstream imposed forcing at a discrete frequency. At this location ($y - y_s = 0.02$), the energy magnitude of the forward-facing step is greater than that of the rearward-facing step, even though this behavior is opposite that of the integrated energy K_i (see Fig. 16).

VIII. Summary and Conclusion

Large-eddy simulations were performed in order to simulate the flow past a flat-plate configuration with forward-facing and rearward-facing steps downstream of the leading edge. The steps were representative of excrescences generated during fabrication of aerodynamic surfaces, which disrupt laminar flow, leading to a premature transition to turbulence. The configuration and roughness-based Reynolds number for the steps

were similar to that of an experimental investigation. Solutions were obtained using a high-fidelity numerical scheme and implicit LES approach, in order to replicate the observed transition. When the computations were conducted without use of numerical perturbations, transition did not occur in a consistent manner. This situation was overcome by applying small amplitude numerical forcing of the normal surface velocity, in the step region. The forcing frequency was selected as a value within the unstable range based upon the stability diagram for the boundary layer, whose properties were modified by the step. Use of forcing regularized the transition process, making the transition location rather insensitive to spatial resolution.

A grid sensitivity study was carried out, and indicated that solutions obtained on the finest computational meshes were reasonably well resolved. Results of the simulations elucidated some aspects of the flow evolution to turbulence. As predicted by theory, the process initially consists of very small coherent two-dimensional structures, which are amplified by the geometric disturbances, and convect downstream of the step. Eventually, these structures lose their coherence, breakdown into more complex forms, and evolve to a chaotic state. Skin friction distributions and transition locations resulting from the simulations were found to agree well with measurements from the experiment. In the most downstream region of the computational domain, it was found that the solution had not yet evolved to the high-Reynolds number asymptotic form.

The large-eddy simulations were found to be computational resource intensive. This resulted not only because of the large mesh systems required for adequate spatial resolution, but also because of the small time step restriction and lengthy computing times necessary for temporal development to attain converged statistical information. Several approaches were identified to reduce these demands for future investigations. First, two-dimensional simulations can be carried out to obtain a reasonable representation of the displacement thickness distribution. This can be used to identify the range of unstable frequency for a given Reynolds number, which is then employed for numerical forcing. Because this range is somewhat broad, details of the numerical solution are not critical. Not only are the two-dimensional calculations inexpensive to perform, but the physical flow has no three-dimensional effects upstream of the step. Second, coarse-mesh three-dimensional large-eddy simulations may then be performed to predict the transition location. It would only be necessary to conduct more spatially resolved computations to obtain correct information regarding skin friction and turbulent statistics.

Acknowledgments

The work presented here was sponsored by the U. S. Air Force Office of Scientific Research, under a task monitored by D. Smith. The authors wish to thank G. Dale for assistance with this effort. They are also especially grateful to A. Bender for supplying many details of the experimental work. Computational resources were supported in part by a grant of supercomputer time from the U. S. Department of Defense Supercomputing Resource Centers at the Stennis Space Center, MS and Wright-Patterson AFB, OH.

References

- ¹Hood, M. J., "The Effects of Surface Waviness and of Rib Stitching on Wing Drag," Technical Note 724, NACA, Aug. 1939.
- ²Fage, A., "The Smallest Size of a Spanwise Surface Corugation which Affects Boundary-Layer Transition on an Aerofoil," Reports and Memoranda 2120, Aeronautical Research Council, Jan. 1943.
- ³Gregory, N., Walker, W. S., and Johnson, D., "Part I: The Effect on Transition of Isolated Surface Excrescences in the Boundary Layer; Part II: Brief Flight Tests on a *Vampire I* Aircraft to Determine the Effect of Isolated Surface Pimples on Transition," Reports and Memoranda 2779, Aeronautical Research Council, Oct. 1951.
- ⁴Smith, A. M. O. and Clutter, D. W., "The Smallest Height of Roughness Capable of Affecting Boundary-Layer Transition in Low-Speed Flow," Engineering Report ES26803, Douglas Aircraft Company, 1954.
- ⁵Braslow, A. L., "The Effect of Distributed Surface Roughness on Boundary-Layer Transition," AGARD Report 254, North Atlantic Treaty Organization, Jan. 1960.
- ⁶Drake, A., Westphal, R. V., Zuniga, F. A., Kennelly, R. A., and Koga, D. J., "Wing Leading Edge Joint Laminar Flow Tests," Technical Memorandum 4762, NASA, Mar. 1997.
- ⁷Drake, A., Bender, A. M., Solomom, W. D., and Vavra, A. J., "Prediction of Manufacturing Tolerances for Laminar Flow," Technical Report AFRL-VA-WP-TR-2005-3060, Wright-Patterson AFB, OH, Jun. 2005.
- ⁸Bender, A. M. and Drake, A., "Manufacturing Tolerances for Laminar Flow," Technical Report AFRL-VA-WP-TR-2007-3086, Air Force Research Laboratory, Wright-Patterson AFB, OH, Sep. 2006.
- ⁹Drake, A. and Bender, A., "Surface Excrescence Transition Study," Technical Report AFRL-RB-WP-TR-2009-3109, Wright-Patterson AFB, OH, Apr. 2009.
- ¹⁰McKeon, B. J., Bender, A. M., Westphal, R. V., and Drake, A., "Transition in Incompressible Boundary Layers with Two-Dimensional Excrescences," AIAA Paper 2008-589, Jan 2008.

¹¹Bender, A. M., Elliot, J. R., Shinagawa, Y., Korntheuer, A. J., Drake, A., Westphal, R. V., Gerashchenko, S., McKeon, B. J., and Yoshioka, S., "An Approach to Measuring Step Excrescence Effects in the presence of a Pressure Gradient," AIAA Paper 2010-373, Jan. 2010.

¹²Gerashchenko, S., McKeon, B. J., Westphal, R. V., Bender, A. M., and Drake, A., "Hot-Wire Measurements of the Influence of Surface Steps on Transition in Favorable Pressure Gradient Boundary Layers," AIAA Paper 2010-374, Jan. 2010.

¹³Drake, A., Bender, A. M. and Korntheuer, A. J., Westphal, R. V., McKeon, B. J., Gerashchenko, S., Rohe, W., and Dale, G., "Step Excrescence Effects for Manufacturing Tolerances on Laminar Flow Wings," AIAA Paper 2010-375, Jan. 2010.

¹⁴Bender, A., Harris, C., and Hawkins, B., "Boundary Layer Excrescence Examination Study," Technical Report AFRL-RB-WP-TR-2012-0027, Air Force Research Laboratory, Wright-Patterson AFB, OH, May 2012.

¹⁵Beam, R. and Warming, R., "An Implicit Factored Scheme for the Compressible Navier-Stokes Equations," *AIAA Journal*, Vol. 16, No. 4, Apr. 1978, pp. 393-402.

¹⁶Gordnier, R. E. and Visbal, M. R., "Numerical Simulation of Delta-Wing Roll," AIAA Paper 93-0554, Jan. 1993.

¹⁷Jameson, A., Schmidt, W., and Turkel, E., "Numerical Solutions of the Euler Equations by Finite Volume Methods Using Runge-Kutta Time Stepping Schemes," AIAA Paper 81-1259, Jun. 1981.

¹⁸Pulliam, T. H. and Chaussee, D. S., "A Diagonal Form of an Implicit Approximate-Factorization Algorithm," *Journal of Computational Physics*, Vol. 39, No. 2, Feb. 1981, pp. 347-363.

¹⁹Lele, S. A., "Compact Finite Difference Schemes with Spectral-like Resolution," *Journal of Computational Physics*, Vol. 103, No. 1, Nov. 1992, pp. 16-42.

²⁰Visbal, M. R. and Gaitonde, D. V., "High-Order-Accurate Methods for Complex Unsteady Subsonic Flows," *AIAA Journal*, Vol. 37, No. 10, Oct. 1999, pp. 1231-1239.

²¹Gaitonde, D., Shang, J. S., and Young, J. L., "Practical Aspects of High-Order Accurate Finite-Volume Schemes for Electromagnetics," AIAA Paper 97-0363, Jan. 1997.

²²Gaitonde, D. and Visbal, M. R., "High-Order Schemes for Navier-Stokes Equations: Algorithm and Implementation into FDL3DI," Technical Report AFRL-VA-WP-TR-1998-3060, Air Force Research Laboratory, Wright-Patterson AFB, OH, Aug. 1998.

²³Gordnier, R. E., "Computation of Delta-Wing Roll Maneuvers," *Journal of Aircraft*, Vol. 32, No. 3, May 1995, pp. 486-492.

²⁴Visbal, M. R., "Computational Study of Vortex Breakdown on a Pitching Delta Wing," AIAA Paper 93-2974, Jul. 1993.

²⁵Visbal, M., Gaitonde, D., and Gogineni, S., "Direct Numerical Simulation of a Forced Transitional Plane Wall Jet," AIAA Paper 98-2643, Jun. 1998.

²⁶Rizzetta, D. P., Visbal, M. R., and Stanek, M. J., "Numerical Investigation of Synthetic-Jet Flowfields," *AIAA Journal*, Vol. 37, No. 8, Aug. 1999, pp. 919-927.

²⁷Rizzetta, D. P. and Visbal, M. R., "Direct Numerical Simulation of Flow Past an Array of Distributed Roughness Elements," AIAA Paper 2006-3527, Jun. 2006.

²⁸Gaitonde, D. V., Visbal, M. R., and Roy, S., "Control of Flow Past a Wing Section with Plasma-Based Body Forces," AIAA Paper 2005-5302, Jun. 2005.

²⁹Visbal, M. R. and Gaitonde, D. V., "Control of Vortical Flows Using Simulated Plasma Actuators," AIAA Paper 2006-0505, Jan. 2005.

³⁰Visbal, M. R., Gaitonde, D. V., and Roy, S., "Control of Transitional and Turbulent Flows Using Plasma-Based Actuators," AIAA Paper 2006-3230, Jun. 2006.

³¹Rizzetta, D. P. and Visbal, M. R., "Numerical Investigation of Plasma-Based Flow Control for Transitional Highly Loaded Low-Pressure Turbine," *AIAA Journal*, Vol. 45, No. 10, Oct. 2007, pp. 2554-2564.

³²Rizzetta, D. P. and Visbal, M. R., "Plasma-Based Flow Control Strategies for Transitional Highly Loaded Low-Pressure Turbines," *Journal of Fluids Engineering*, Vol. 130, No. 4, Apr. 2008, pp. 041104-1-041104-12.

³³Rizzetta, D. P. and Visbal, M. R., "Large Eddy Simulation of Plasma-Based Control Strategies for Bluff Body Flow," *AIAA Journal*, Vol. 47, No. 3, Mar. 2009, pp. 717-729.

³⁴Rizzetta, D. P. and Visbal, M. R., "Large-Eddy Simulation of Plasma-Based Turbulent Boundary-Layer Separation Control," *AIAA Journal*, Vol. 48, No. 12, Dec. 2010, pp. 2793-2810.

³⁵Rizzetta, D. P. and Visbal, M. R., "Effect of Plasma-Based Control on Low-Reynolds Number Flapping Airfoil Performance," AIAA Paper 2011-735, Jan. 2011.

³⁶Rizzetta, D. P. and Visbal, M. R., "Numerical Investigation of Plasma-Based Control for Low-Reynolds Number Airfoil Flows," *AIAA Journal*, Vol. 49, No. 2, Feb. 2011, pp. 411-425.

³⁷Rizzetta, D. P. and Visbal, M. R., "Numerical Investigation of Transitional Flow Through a Low-Pressure Turbine Cascade," AIAA Paper 2003-3587, Jun. 2003.

³⁸Rizzetta, D. P., Visbal, M. R., and Blaisdell, G. A., "A Time-Implicit High-Order Compact Differencing and Filtering Scheme for Large-Eddy Simulation," *International Journal for Numerical Methods in Fluids*, Vol. 42, No. 6, Jun. 2003, pp. 665-693.

³⁹Rizzetta, D. P. and Visbal, M. R., "Application of Large-Eddy Simulation to Supersonic Compression Ramps," *AIAA Journal*, Vol. 40, No. 8, Aug. 2002, pp. 1574-1581.

⁴⁰Rizzetta, D. P. and Visbal, M. R., "Large-Eddy Simulation of Supersonic Cavity Flowfields Including Flow Control," *AIAA Journal*, Vol. 41, No. 8, Aug. 2003, pp. 1452-1462.

⁴¹Visbal, M. R. and Rizzetta, D. P., "Large-Eddy Simulation on Curvilinear Grids Using Compact Differencing and Filtering Schemes," *Journal of Fluids Engineering*, Vol. 124, No. 4, Dec. 2002, pp. 836-847.

⁴²Visbal, M. R., Morgan, P. E., and Rizzetta, D. P., "An Implicit LES Approach Based on High-Order Compact Differencing and Filtering Schemes," AIAA Paper 2003-4098, Jun. 2003.

⁴³Fureby, C. and Grinstein, F. F., "Monotonically Integrated Large Eddy Simulation," *AIAA Journal*, Vol. 37, No. 5, May 1999, pp. 544–556.

⁴⁴Stoltz, S. and Adams, N. A., "An Approximate Deconvolution Procedure for Large-Eddy Simulation," *Physics of Fluids*, Vol. 11, No. 7, Jul. 1999, pp. 1699–1701.

⁴⁵Matthew, J., Lechner, R., Foysi, H., Sesterhenn, J., and Friedrich, R., "An Explicit Filtering Method for Large Eddy Simulation of Compressible Flows," *Physics of Fluids*, Vol. 15, No. 8, Aug. 2003, pp. 2279–2289.

⁴⁶Steinbrenner, J. P., Chawner, J. P., and Fouts, C. L., "The GRIDGEN 3D Multiple Block Grid Generation System, Volume II: User's Manual," Technical Report WRDC-TR-90-3022, Wright Research and Development Center, Wright-Patterson AFB, OH, Feb. 1991.

⁴⁷Visbal, M. R. and Gaitonde, D. V., "Very High-Order Spatially Implicit Schemes for Computational Acoustics on Curvilinear Meshes," *Journal of Computational Acoustics*, Vol. 9, No. 4, Dec. 2001, pp. 1259–1286.

⁴⁸Schlichting, H., *Boundary-Layer Theory*, McGraw-Hill, New York, 4th ed., 1960.

⁴⁹Fasel, H. and Konzelmann, U., "Non-parallel Stability of a Flat-Plate Boundary Layer Using the Complete Navier-Stokes Equations," *Journal of Fluid Mechanics*, Vol. 221, Dec. 1990, pp. 311–347.

⁵⁰Rai, M. M. and Moin, P., "Direct Numerical Simulation of Transition and Turbulence in a Spatially Evolving Boundary Layer," *Journal of Computational Physics*, Vol. 109, No. 2, Dec. 1993, pp. 169–192.

⁵¹Rizzetta, D. P. and Visbal, M. R., "Large-eddy Simulation of Supersonic Boundary-layer Flow by a High-order Method," *International Journal of Computational Fluid Dynamics*, Vol. 18, No. 1, Jan. 2004, pp. 15–27.

⁵²Jeong, J. and Hussain, F., "On the Identification of a Vortex," *Journal of Fluid Mechanics*, Vol. 285, Feb. 1995, pp. 69–94.

⁵³Piomelli, U. and Balaras, E., "Wall-Layer Models for Large-Eddy Simulations," *Annual Review of Fluid Mechanics*, Vol. 34, Jan. 2002, pp. 349–374.

⁵⁴Georgiadis, N. J., Rizzetta, D. P., and Fureby, C., "Large-Eddy Simulation: Current Capabilities, Recommended Practices, and Future Research," *AIAA Journal*, Vol. 48, No. 8, Aug. 2010, pp. 1772–1784.

⁵⁵Klebanoff, P. S., "Characteristics of Turbulence in a Boundary Layer with Zero Pressure Gradient," NACA Technical Report 1247, National Advisory Committee for Aeronautics, 1955.

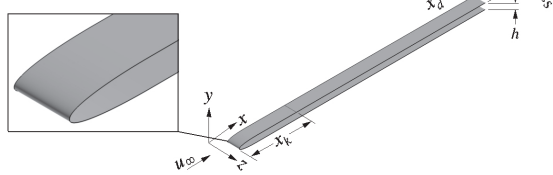


Figure 1. Flat-plate geometry configuration.

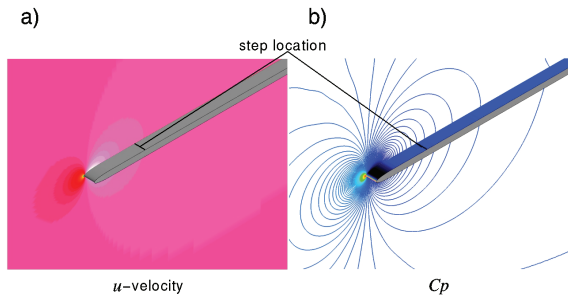


Figure 3. Features of the baseline case without steps:
a) planar contours of the u -velocity in the flowfield,
b) planar contours of C_p in the flowfield and on the configuration surface.

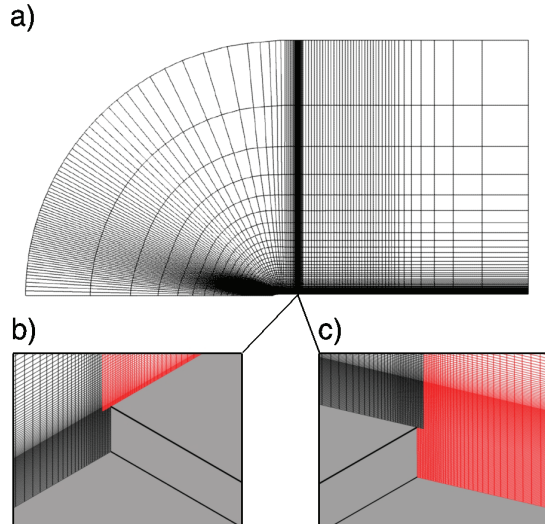


Figure 2. Computational mesh system: a) overall flow field domain structure, b) overset grid structure for the forward-facing step, c) overset grid structure for the rearward-facing step.

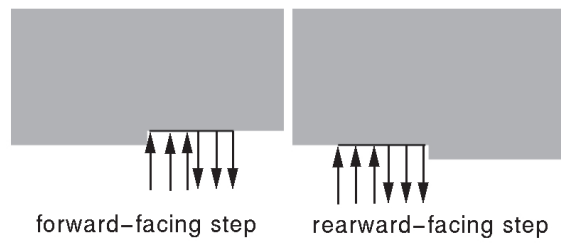


Figure 4. Blowing/suction boundary locations.

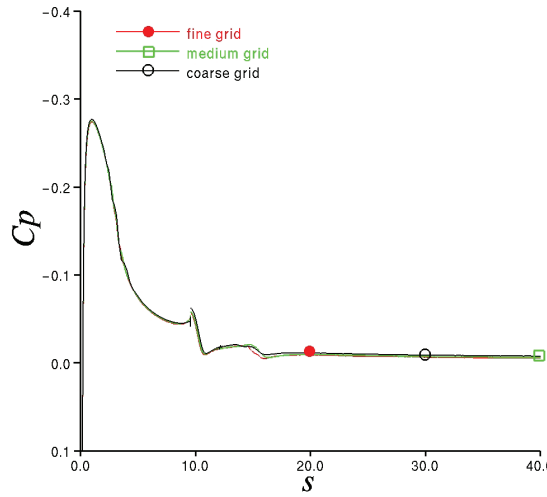


Figure 5. Time-mean surface pressure distributions for the rearward-facing step on various mesh systems.

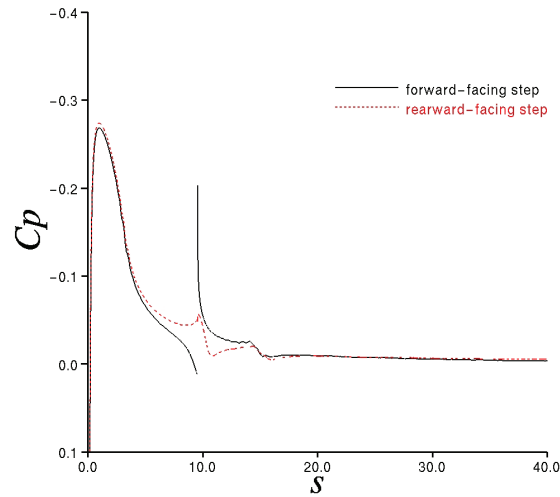


Figure 7. Time-mean surface pressure distributions for the forward-facing and rearward-facing steps.

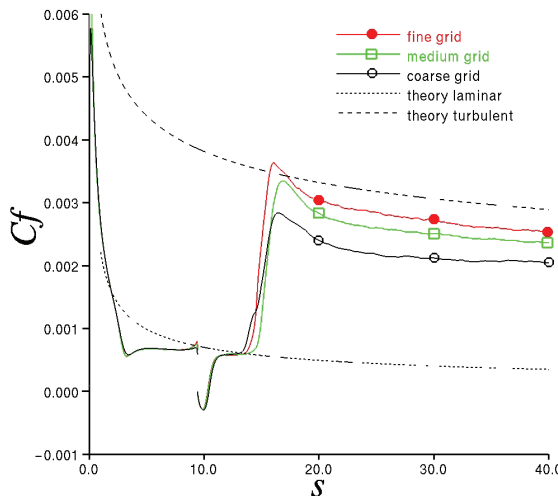


Figure 6. Time-mean skin friction distributions for the rearward-facing step on various mesh systems.

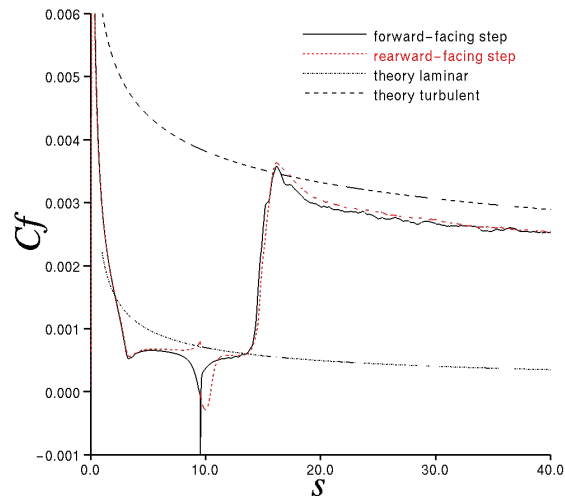


Figure 8. Time-mean skin friction distributions for the forward-facing and rearward-facing steps.

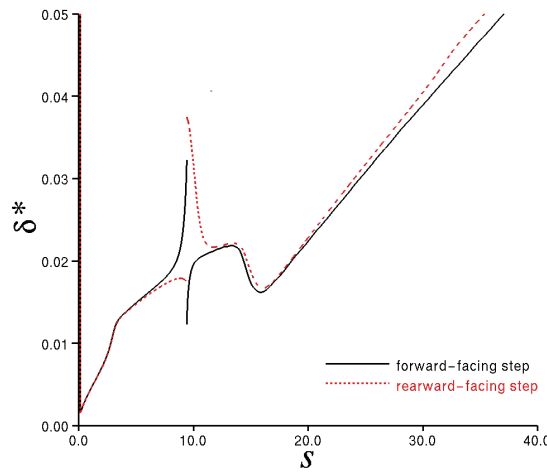


Figure 9. Time-mean displacement thickness distributions for the forward-facing and rearward-facing steps.

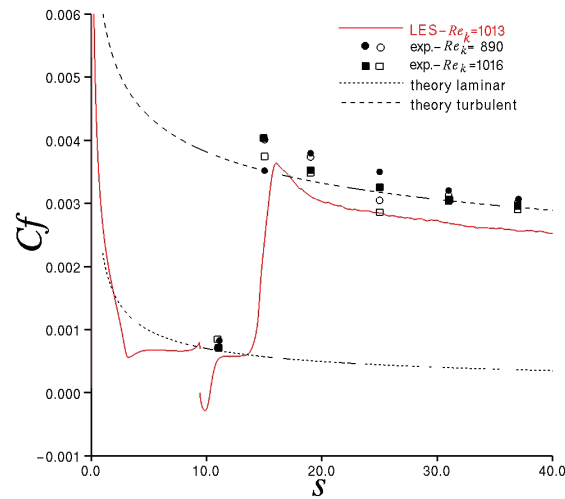


Figure 11. Time-mean skin friction distribution for the rearward-facing step compared with experimental data.

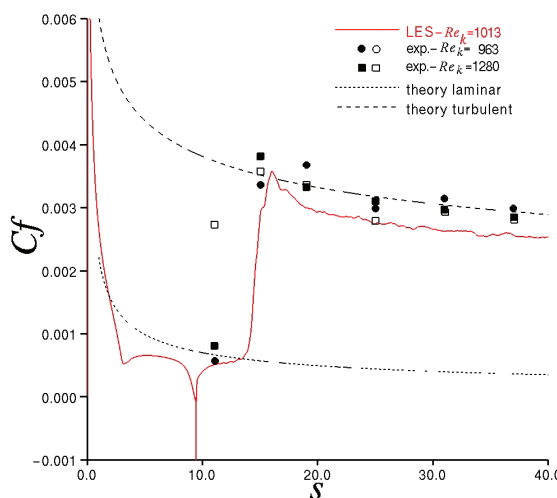


Figure 10. Time-mean skin friction distribution for the forward-facing step compared with experimental data.

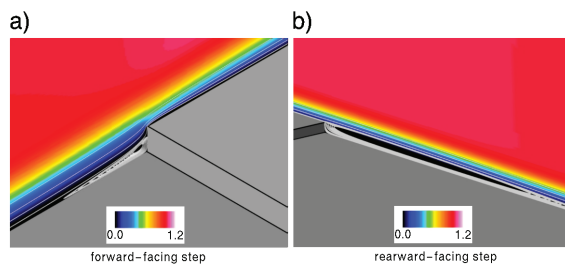


Figure 12. Time-mean streamlines and planar contours of the u -velocity: a) forward-facing step, b) rearward-facing step.

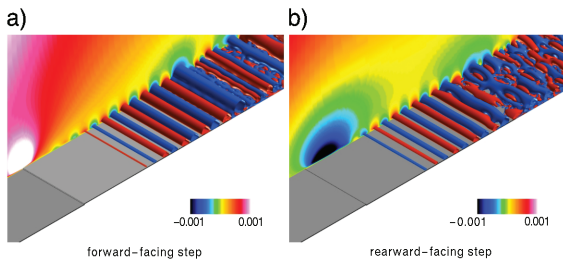


Figure 13. Instantaneous planar contours at the inboard boundary and iso-surfaces of the v -velocity: a) forward-facing step, b) rearward-facing step. z -coordinate stretch by a factor of 2.0.

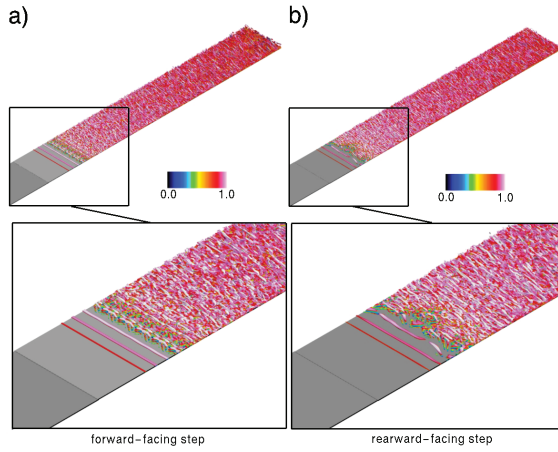


Figure 15. Instantaneous iso-surfaces of the Q -criterion colored by the u -velocity: a) forward-facing step, b) rearward-facing step. z -coordinate stretch by a factor of 5.0.

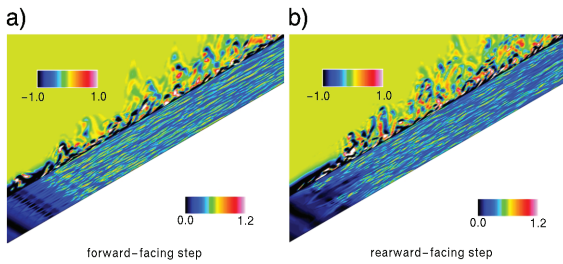


Figure 14. Instantaneous planar contours of the spanwise vorticity at the inboard boundary, and planar contours of the u -velocity in the near-wall region: a) forward-facing step, b) rearward-facing step. y -coordinate stretch by a factor of 5.0 in the planar contours of spanwise vorticity.

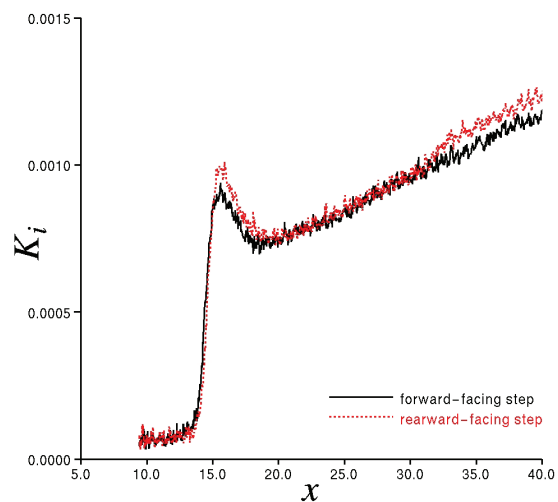


Figure 16. Distributions of the integrated turbulent kinetic energy for the forward-facing and rearward-facing steps.

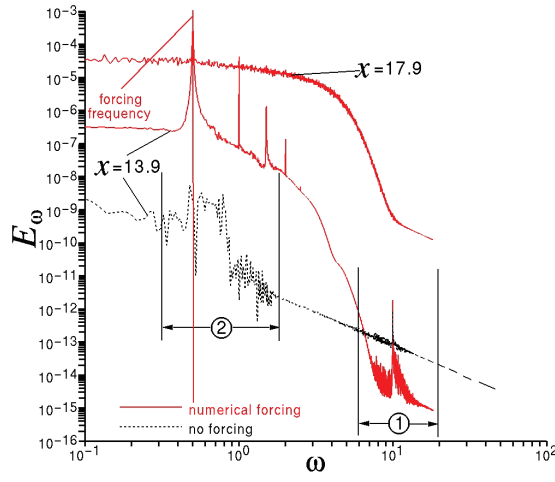


Figure 17. Turbulent kinetic energy frequency spectra for the rearward-facing step in the transition region.

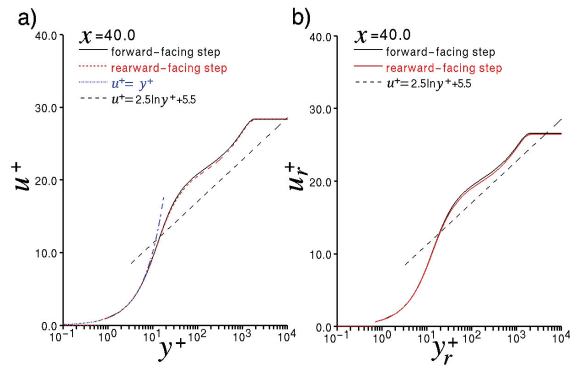


Figure 19. Time-mean streamwise velocity profiles in law-of-the-wall variables for the forward-facing and rearward-facing steps in the fully turbulent downstream region: a) normal variables, b) rescaled variables.

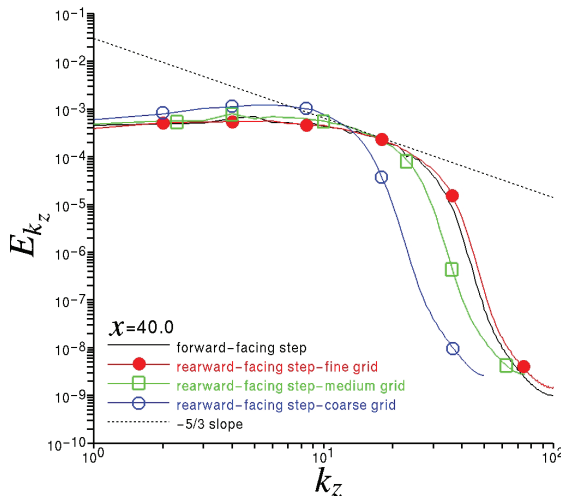


Figure 18. Turbulent kinetic energy spanwise wave-number spectra for the forward-facing and rearward-facing steps in the fully turbulent downstream region.

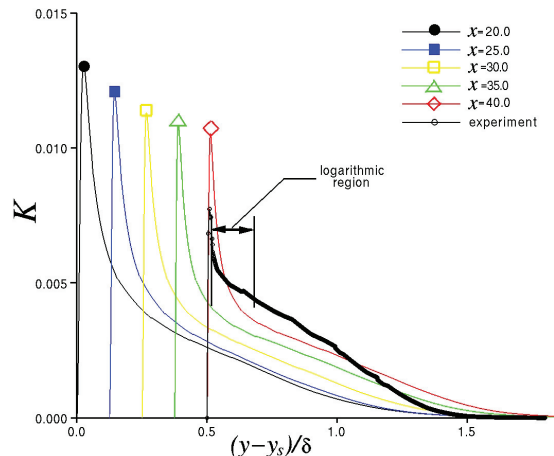


Figure 20. Time-mean turbulent kinetic energy profiles for the rearward-facing step at several streamwise locations.

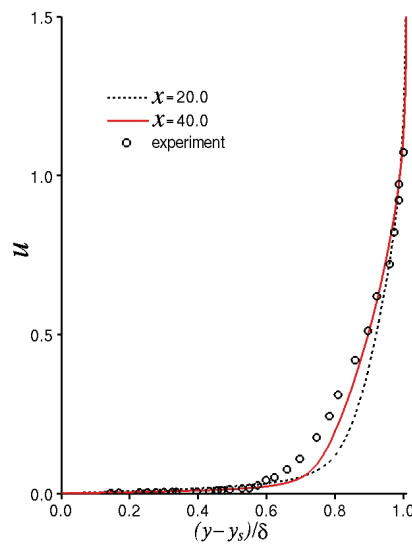


Figure 21. Time-mean streamwise velocity profiles for the rearward-facing step.

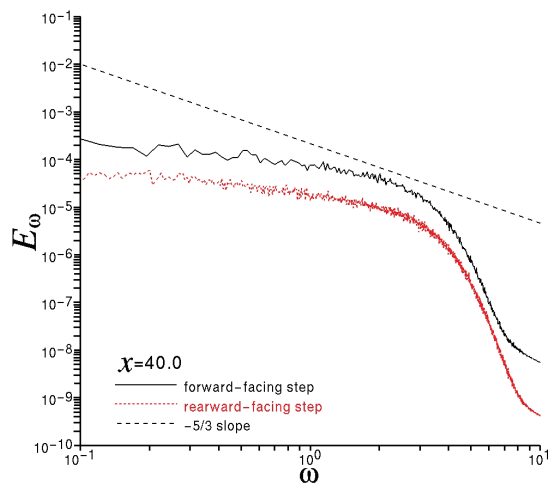


Figure 23. Turbulent kinetic energy frequency spectra for the forward-facing and rearward-facing steps in the fully turbulent downstream region.

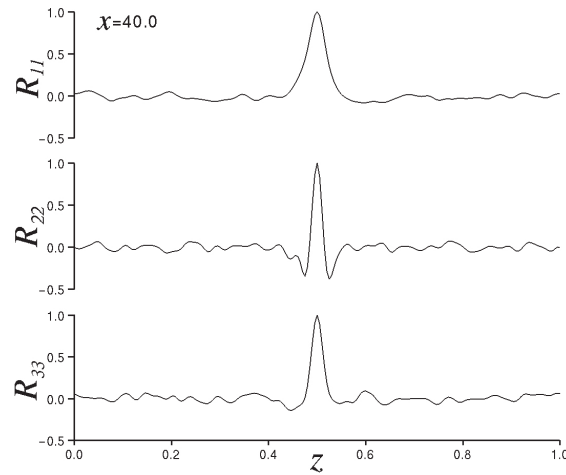


Figure 22. Spanwise correlation coefficients of the fluctuating velocity components for the rearward-facing step in the fully turbulent downstream region.

APPENDIX F

Shock/Boundary Layer Interaction Over a Flexible Panel

Miguel R. Visbal *

Air Force Research Laboratory, Wright-Patterson AFB, OH 45433

The dynamics of a flexible panel subjected to an impinging oblique shock is considered numerically. Both inviscid and viscous 2D computations have been performed for a freestream Mach number equal to two and for several shock strengths employing a previously validated fluid-structural approach. Results show for the first time that for a sufficiently strong shock limit-cycle oscillations arise in the coupled system, even in the absence of viscous separated flow effects. For the inviscid situation, depending upon shock strength, either supercritical or subcritical bifurcations emerge at a value of dynamic pressure which can be considerably lower than that corresponding to standard panel flutter (i.e., in the absence of a shock). This observation suggests that a new aeroelastic instability (distinct from regular panel flutter) is at play and arises from the complex interaction of the incident and reflected wave system with the panel flexural modes. In addition to the incident and reflected oblique shocks, the unsteady flows are characterized by a shock at the plate leading edge and by a strong recompression and subsequent expansion near the trailing edge. Significant changes in panel dynamics were found as a function of the shock impingement point. For viscous laminar flow above the panel without a shock, high-frequency periodic oscillations are observed which appear to result from the coupling of boundary-layer instabilities with high-mode flexural deflections. For a separated shock laminar boundary layer interaction, non-periodic self-excited oscillations arise which can result in a significant reduction in the extent of the time-averaged separation region. This finding suggests the potential use of an aeroelastically-tailored flexible panel as a means of passive flow control. Forced panel oscillations, induced by a specified variable cavity pressure underneath the panel, were also found to be effective in reducing separation. For both inviscid and viscous interactions, the significant unsteadiness generated by the fluttering panel propagates along the complex reflected expansion/recompression wave system with potential structural implications not only for the panel but for opposing surfaces in internal flow applications.

Nomenclature

a	= panel length
b	= panel width
Cp	= pressure coefficient
D	= flexural stiffness, $E_s h^3 / 12(1 - \nu^2)$
E	= total specific energy
E_s	= Young's modulus
$\hat{F}, \hat{G}, \hat{H}$	= inviscid vector fluxes
$\hat{F}_v, \hat{G}_v, \hat{H}_v$	= viscous vector fluxes
h	= panel thickness
J	= transformation Jacobian
$l.e., t.e.$	= leading and trailing edge of flexible panel
M_∞, M_1	= freestream Mach number
N'_x, N'_y, N'_z	= membrane stresses
p	= pressure
Re_a	= Reynolds number, $Re_a = \frac{\rho_\infty u_\infty a}{\mu_\infty}$
St	= Strouhal number, $St = \frac{f a}{u_\infty}$

*Technical Area Leader, Computational Aero-Physics Branch. Associate Fellow AIAA

t, τ	=	non-dimensional time $\frac{\bar{t}u_\infty}{a}$
u, v, w	=	velocity components in x, y and z
x, y, z	=	physical coordinates
δ	=	boundary layer thickness
δ^*	=	displacement thickness
$\delta u, \delta v, \delta w$	=	structural displacements
ξ, η, ζ	=	computational coordinates
λ	=	dynamic pressure, $\frac{\rho_\infty u_\infty^2 a^3}{D}$; also wavelength
f	=	frequency
K_f	=	linear free vibration frequency
ρ	=	density
ρ_s	=	panel density
μ	=	viscosity coefficient
μ_s	=	mass ratio, $\frac{\rho_\infty a}{\rho_s h}$

I. INTRODUCTION

The complex flow-acoustic-structural interactions which arise in flow over flexible panels are of importance when considering structural integrity, fatigue and sound radiation. The well-known phenomena of panel flutter and divergence of an elastic plate have been investigated for a number of years and excellent reviews of the subject have been provided by Dowell¹ and Mei et al.² Potential flow theories aimed at providing predictions across the subsonic to supersonic Mach number range have been given by Dowell.³ Davis and Bendiksen^{4,5} have considered the nonlinear inviscid case by solving the 2-D Euler equations coupled with a non-linear finite-element model for a semi-infinite panel. Nydick et al.⁶ provided panel flutter solutions in the hypersonic regime employing a compressible Navier-Stokes solver, and compared their results with those obtained using third-order piston theory. Gordnier and Visbal^{7,8} further extended panel flutter simulations by considering both inviscid and viscous (laminar and turbulent) three-dimensional flow employing a Navier-Stokes solver coupled, via an iterative implicit strategy, with a finite-difference structural module for the nonlinear (von Karman) plate equations. The same Navier-Stokes flow solver was coupled with a finite-element structural solver by Gordnier and Fithen.⁹ Visbal and Gordnier¹⁰ studied the case of a transitional boundary layer above a flexible panel using a very high-order flow solver and demonstrated the emergence of travelling wave flutter due to the coupling of Tollmien-Schilchting waves with the panel higher-mode flexural deflections.

In this paper, consideration is given for the first time to the case of supersonic flow over a flexible panel in the presence of an impinging (and reflecting) oblique shock, as depicted in the schematic of Fig. 1. Oblique shock reflection is a common feature encountered both in external and internal supersonic flow applications. Attention is given first to the inviscid case. This is done in order to demonstrate that beyond just buffeting due to unsteady separation, a true aeroelastic (inviscid) instability can arise from the coupling of the oblique shock reflection system with the elastic deflections of the panel. For this purpose, the dynamics of the panel is explored as a function of shock strength for a fixed freestream Mach number ($M_\infty = 2.0$). A limited investigation of the effect of shock impingement location relative to the edges of the flexible panel is also provided for the inviscid situation. Inclusion of viscous effects is considered next. First, the case of a laminar boundary layer flowing over the elastic panel without an impinging shock is examined to explore the potential coupling of instability modes with flexural waves. Finally, the case of a separated shock laminar boundary layer interaction is considered to describe the coupling of the panel deflections with the separated shear layer and reattachment process.

The present fluid-structure interaction is studied by solving the compressible Navier-Stokes equations coupled to a von Karman plate model for large transverse panel deflections. The flow fields are computed by means of an extensively validated time-implicit Navier-Stokes solver which incorporates both standard second-order, as well as high-order spatial discretizations. Solutions to the plate equations are obtained employing a previously developed structural solver.⁷ The aerodynamic and structural equations are coupled via a sub-iteration strategy required to avoid spurious panel dynamics.

II. Governing Equations

A. Flow Equations

In order to properly account for the complex unsteady viscous flow arising over a dynamically deforming surface, the full compressible Navier-Stokes equations are selected. These equations are cast in strong conservative form introducing a general time-dependent curvilinear coordinate transformation $(x, y, z, t) \rightarrow (\xi, \eta, \zeta, \tau)$. In vector notation, and employing non-dimensional variables, the equations are:

$$\frac{\partial}{\partial \tau} \left(\frac{\vec{U}}{J} \right) + \frac{\partial \hat{F}}{\partial \xi} + \frac{\partial \hat{G}}{\partial \eta} + \frac{\partial \hat{H}}{\partial \zeta} = \frac{1}{Re} \left[\frac{\partial \hat{F}_v}{\partial \xi} + \frac{\partial \hat{G}_v}{\partial \eta} + \frac{\partial \hat{H}_v}{\partial \zeta} \right] \quad (1)$$

Here $\vec{U} = \{\rho, \rho u, \rho v, \rho w, \rho E\}$ denotes the solution vector and J is the transformation Jacobian, which in general is a function of time. The inviscid fluxes \hat{F} , \hat{G} and \hat{H} are:

$$\hat{F} = \frac{1}{J} \begin{bmatrix} \rho U \\ \rho u U + \xi_x p \\ \rho v U + \xi_y p \\ \rho w U + \xi_z p \\ (\rho E + p) U - \xi_t p \end{bmatrix} \quad (2)$$

$$\hat{G} = \frac{1}{J} \begin{bmatrix} \rho V \\ \rho u V + \eta_x p \\ \rho v V + \eta_y p \\ \rho w V + \eta_z p \\ (\rho E + p) V - \eta_t p \end{bmatrix} \quad (3)$$

$$\hat{H} = \frac{1}{J} \begin{bmatrix} \rho W \\ \rho u W + \zeta_x p \\ \rho v W + \zeta_y p \\ \rho w W + \zeta_z p \\ (\rho E + p) W - \zeta_t p \end{bmatrix} \quad (4)$$

where

$$U = \xi_t + \xi_x u + \xi_y v + \xi_z w \quad (5)$$

$$V = \eta_t + \eta_x u + \eta_y v + \eta_z w \quad (6)$$

$$W = \zeta_t + \zeta_x u + \zeta_y v + \zeta_z w \quad (7)$$

$$E = \frac{T}{(\gamma - 1)M_\infty^2} + \frac{1}{2}(u^2 + v^2 + w^2). \quad (8)$$

The viscous fluxes, F_v , G_v and H_v can be found, for instance, in Ref. 11. In the expressions above, u, v, w are the Cartesian velocity components, ρ the density, p the pressure, and T the temperature. The perfect gas relationship $p = \rho T / \gamma M_\infty^2$ is also assumed. All flow variables have been normalized by their respective freestream values except for pressure which has been nondimensionalized by $\rho_\infty u_\infty^2$.

B. Structural Equations for Flexible Panel

The deformations of the flexible surface are assumed to be governed by the (non-linear) von Karman plate equations for large plate deflections. Derivation of these equations may be found in a number of sources.^{12,13} For the von Karman theory the plate is assumed to be isotropic, of uniform small thickness and initially flat. The normal deflection of the plate is assumed to be on the order of the thickness of the plate, while the tangential displacements are assumed infinitesimal. Finally, Kirchoff's hypothesis is employed with tractions on surfaces parallel to the middle surface assumed negligible and strains varying linearly with the plate thickness.

Using these assumptions the governing equations for the plate motion may be written in nondimensional form as

$$\frac{\lambda}{\mu_s} \frac{\partial^2 \delta w}{\partial t^2} + \nabla^4 \delta w - \lambda N'_x \frac{\partial^2 \delta w}{\partial x^2} - 2.0 \lambda N'_{xy} \frac{\partial^2 \delta w}{\partial x \partial y} - \lambda N'_y \frac{\partial^2 \delta w}{\partial y^2} = \frac{\lambda}{h} [p^u(x, y, t) - p_c] \quad (9)$$

$$\frac{\partial N'_x}{\partial x} + \frac{\partial N'_{xy}}{\partial y} = 0 \quad (10)$$

$$\frac{\partial N'_{xy}}{\partial x} + \frac{\partial N'_y}{\partial y} = 0 \quad (11)$$

where

$$N'_x = \frac{12.0}{\lambda} \left(\frac{\partial \delta u}{\partial x} + \nu \frac{\partial \delta v}{\partial y} + \frac{1}{2} \left[\left(\frac{\partial \delta w}{\partial x} \right)^2 + \nu \left(\frac{\partial \delta w}{\partial y} \right)^2 \right] \right) \quad (12)$$

$$N'_y = \frac{12.0}{\lambda} \left(\frac{\partial \delta v}{\partial y} + \nu \frac{\partial \delta u}{\partial x} + \frac{1}{2} \left[\left(\frac{\partial \delta w}{\partial y} \right)^2 + \nu \left(\frac{\partial \delta w}{\partial x} \right)^2 \right] \right) \quad (13)$$

$$N'_{xy} = \frac{12.0}{\lambda} \left(\frac{1 - \nu}{2} \left(\frac{\partial \delta u}{\partial y} + \frac{\partial \delta v}{\partial x} + \frac{\partial \delta w}{\partial x} \frac{\partial \delta w}{\partial y} \right) \right) \quad (14)$$

The previous equations are written in a Lagrangian reference frame where x, y and z refer to the original undeflected plate location, and $\delta u, \delta v$ and δw are the corresponding displacements from the undeflected position. The term $p^u(x, y, t)$ denotes the instantaneous fluid pressure acting on the upper surface of the plate, whereas p_c represents the pressure underneath the panel, which is typically assumed to be constant.³ These equations have been nondimensionalized based on the freestream density, freestream velocity and the length of the plate. The relevant non-dimensional parameters are the panel aspect ratio a/b , the thickness ratio h/a , the mass ratio μ_s and the dynamic pressure λ (see Nomenclature).

Equations 9-11 form a coupled set of nonlinear equations for the plate deflections. The terms N'_x, N'_y , and N'_{xy} in Eq. (9) are the so called membrane stresses. These nonlinear terms arise due to the stretching of the middle surface of the plate.

It should be noted that the above structural equations could be easily extended to the more general case of a “Kramer-type” compliant surface or for a panel with a continuous elastic support. This can be accomplished through the addition of a structural damping term (of the form $\sim d \frac{\partial \delta w}{\partial t}$) and/or a restoring term ($\sim k \delta w$). Finally, the inclusion of externally applied axial forces could be accounted for by straight-forward modification of the membrane stresses N'_x, N'_y, N'_{xy} .

III. Numerical Methodology

A. Flow Solver

For wall-bounded viscous flows, the stability constraint of explicit time-marching schemes is too restrictive and the use of an implicit approach becomes necessary. For this purpose, the implicit approximately-factored scheme of Beam and Warming¹⁴ is incorporated and augmented through the use of Newton-like subiterations in order to achieve second-order time accuracy. In delta form, the scheme may be written as

$$\begin{aligned} & \left[J^{-1^{p+1}} + \phi^i \Delta \tau \delta_\xi^{(2)} \left(\frac{\partial \hat{F}^p}{\partial U} - \frac{1}{Re} \frac{\partial \hat{F}_v^p}{\partial U} \right) \right] J^{p+1} \times \\ & \left[J^{-1^{p+1}} + \phi^i \Delta \tau \delta_\eta^{(2)} \left(\frac{\partial \hat{G}^p}{\partial U} - \frac{1}{Re} \frac{\partial \hat{G}_v^p}{\partial U} \right) \right] J^{p+1} \times \\ & \left[J^{-1^{p+1}} + \phi^i \Delta \tau \delta_\zeta^{(2)} \left(\frac{\partial \hat{H}^p}{\partial U} - \frac{1}{Re} \frac{\partial \hat{H}_v^p}{\partial U} \right) \right] \Delta U \\ & = -\phi^i \Delta \tau \left[J^{-1^{p+1}} \frac{(1+\phi)U^p - (1+2\phi)U^n + \phi U^{n-1}}{\Delta \tau} \right. \\ & \quad \left. + U^p (1/J) \tau^p + \delta_\xi \left(\hat{F}^p - \frac{1}{Re} \hat{F}_v^p \right) + \right. \\ & \quad \left. \delta_\eta \left(\hat{G}^p - \frac{1}{Re} \hat{G}_v^p \right) + \delta_\zeta \left(\hat{H}^p - \frac{1}{Re} \hat{H}_v^p \right) \right] \end{aligned} \quad (15)$$

where

$$\phi^i = \frac{1}{1 + \phi}, \quad \Delta U = U^{p+1} - U^p. \quad (16)$$

For the first subiteration, $p = 1$, $U^p = U^n$ and as $p \rightarrow \infty$, $U^p \rightarrow U^{n+1}$. Although not shown in Eq. (15), nonlinear artificial dissipation terms^{15,16} are appended to the implicit operator to enhance stability. In addition, for improved efficiency, the approximately-factored scheme is recast in diagonalized form.¹⁷ Typically, three subiterations are applied per time step. All spatial derivatives on the implicit operators are discretized using standard second-order approximations.

For the explicit terms, two approaches are utilized. The first employs second-order central discretizations in conjunction with standard non-linear dissipation terms.¹⁶ This method was previously validated and applied to viscous and inviscid panel flutter simulations by Gordnier and Visbal.^{7,8} The second approach is based on 6th-order compact schemes and very high-order (up to 10th-order) Pade-type filters. This high-fidelity methodology has been adapted and validated extensively for unsteady viscous flows.¹⁸⁻²⁰ This approach has also been employed for the simulation of transitional boundary-layer flow over a flexible panel in the subsonic regime.¹⁰ For the present supersonic flows, the high-order scheme is augmented with the shock-capturing procedures introduced in Ref. 21 incorporating a WENO-type shock sensor and adaptive filtering. Unless noted otherwise, computations were performed using the more robust and efficient second-order approach.

B. Structural Dynamics Solver

The structural equations (Eqs. (9)-(11)) are solved using standard finite-difference procedures. All spatial derivatives are approximated using second-order accurate central differences. The time derivative is computed using Newmark's β method.²² In this approach, the displacement, δw and velocity, $\delta \dot{w}$ are computed according to the following relations

$$\delta \dot{w}^{n+1} = \delta \dot{w}^n + \frac{\Delta t}{2}(\delta \ddot{w}^n + \delta \ddot{w}^{n+1}) \quad (17)$$

$$\delta w^{n+1} = \delta w^n + \Delta t \delta \dot{w}^n + \frac{1}{2}(1 - 2\beta)\Delta t^2 \delta \ddot{w}^n + \beta \Delta t^2 \delta \ddot{w}^{n+1} \quad (18)$$

In the present work, $\beta = \frac{1}{4}$ which corresponds to a constant acceleration over a time interval (average acceleration method). This scheme is second-order accurate in time and unconditionally stable.

Substituting the appropriate finite-difference expressions and Eq. (18) into Eqs. (9)-(11), a set of difference equations is obtained. This system of equations is solved in an iterative fashion using a Gauss-Seidel solution technique. In this approach, Eq. (9) is uncoupled from Eqs. (10) and (11) by lagging the membrane stress terms. Similarly, all terms involving δw are assumed known when solving Eqs. (10)-(11). Successive over-relaxation is used with this iterative process in order to accelerate convergence which is assumed when the change in successive values of δw is less than a specified tolerance. The structural solver has been carefully validated⁷ for both static and dynamic loads.

C. Boundary Conditions and Fluid-Structural Coupling

The aerodynamic boundary conditions were prescribed as follows (see Fig. 1). Supersonic fixed conditions were used along the inflow and front portion of the upper boundary where the shock is imposed by means of the appropriate oblique shock relations. Along the rearmost portion of the upper boundary, as well as on the outflow boundary, extrapolation conditions were invoked. Along the plate surface, for inviscid flows, the normal velocity is obtained from the panel motion and the pressure, density and tangential velocity components are computed by second-order extrapolation. For viscous flows, a no-slip, adiabatic condition is employed.

Boundary conditions for the plate can be specified for either pinned or rigidly clamped edges. For either case, no deflection is allowed along the edges of the plate, i. e. $\delta u, \delta v, \delta w = 0$. For pinned edges, the additional zero-moment condition $\frac{\partial^2 \delta w}{\partial n^2} = 0$ is specified (where n denotes the edge normal). In the case of a clamped panel, $\frac{\partial \delta w}{\partial n} = 0$, corresponding to zero slope at the edge. In all of the results presented here pinned boundary conditions are used.

The two-way fluid-structural coupling is provided through the time-varying loads exerted by the fluid on the plate (i.e. right hand side of Eq.(9)), and through the transfer of the instantaneous panel deflections δw to the deforming aerodynamic mesh. The cavity pressure p_c underneath the panel is prescribed to be constant unless otherwise noted.

In order to accomodate the panel vertical deflections, a new aerodynamic computational mesh is constructed at every time step employing an efficient algebraic procedure. This is achieved by propagating the surface deformations into the mesh according to the following expression

$$\begin{aligned} z_{i,j,k}^{n+1} &= z_{i,j,k}^n + \delta z_{i,j,k} \\ \delta z_{i,j,k} &= \delta z_{i,j,1} G_{i,j,k} \end{aligned} \quad (19)$$

$$G_{i,j,k} = 1 - 3g_{i,j,k}^2 + 2g_{i,j,k}^3$$

$$g_{i,j,k} = s_{i,j,k}/s_{i,j,k_{max}}, 1 \leq k \leq k_{max}$$

where $\delta z_{i,j,1}$ denotes the vertical displacement on the moving surface, s is the arc-length along the ξ, η =constant lines, n is the time level, and k_{max} is the ζ -location in the farfield beyond which the mesh remains undeformed.

The metric terms and grid speeds are evaluated according to the procedures described in Ref. 19 in order to ensure conservation on the deforming mesh. In general, the grid speeds are not known analytically, and must therefore be approximated to the desired degree of accuracy employing the evolving grid coordinates at several time levels. As previously shown for dynamic meshes²³ exhibiting rapid and severe distortion, second-order accuracy was found to be suitable for the evaluation of the grid speed terms. For the case of a flexible panel undergoing transverse deflections, the only relevant grid speed term is in the normal direction and is expressed as

$$z_\tau = (3z^{n+1} - 4z^n + z^{n-1})/2\Delta\tau \quad (20)$$

Since the same spatial discretization is used for both the fluid and the structure, no (spatial) interpolation technique is needed. However, the temporal coupling demands careful treatment. In the present numerical scheme, implicit coupling of these two sets of equations is achieved via the subiteration procedure previously described for the aerodynamic equations. By updating the aerodynamic forces in the structural equations and by providing the new surface displacement to the aerodynamic solver after each subiteration, the temporal lag between the aerodynamic and structural equations is eliminated. The importance of this synchronization between the fluid and the structural modules has been demonstrated previously⁷ for the case of dynamic aeroelastic simulations.

IV. RESULTS

A. Preliminary Considerations

Results are presented for the case of a shock impinging on a flexible panel, as depicted in Fig. 1. For all results included in this paper, a freestream Mach number, $M_1 = 2.0$ is selected. Although the present computational approach has been developed for the general case of 3-D flow past a finite-aspect-ratio panel, only two-dimensional solutions for a semi-infinite ($a/b = 0$) panel are first investigated. This is due to the fact that study of the many non-dimensional parameters involved (i.e., $M_\infty, Re_a, \delta/a, \lambda, \mu_s, a/b, h/a, p_c/p_\infty, \sigma$) becomes computationally prohibitive in the full 3-D situation.

A semi-infinite panel of length a and thickness ratio h/a is considered (Fig. 1). The non-dimensional structural parameters are the mass ratio $\mu_s = \rho_1 a / \rho_s h$ and the dynamic pressure $\lambda = \rho_1 U^2 a^3 / D$, where ρ_s is the panel density and D is the flexural stiffness.²⁴ The structural parameters corresponding to the previous study of Gordnier and Visbal²⁴ are employed ($h/a = 0.002, \mu_s = 0.1$). Unless otherwise noted, the cavity pressure underneath the panel p_c was set equal to the corresponding mean value along the panel length for the theoretical inviscid shock reflection problem. Hence $p_c = \frac{x_i}{a} p_1 + (1 - \frac{x_i}{a}) p_3$ where x_i denotes the theoretical shock impingement location. With this condition, the integrated theoretical load along the undeformed panel vanishes. Most cases considered so far are for $x_i/a = 0.5$ and therefore $p_c = \frac{1}{2}(p_1 + p_3)$. In order to start the flexible panel simulations, the corresponding rigid-plate solution was specified as initial condition. For the case of a shock, no initial perturbations were imposed on the panel to promote a fluid/structure interaction. Instead, the interaction was allowed to evolve from the pressure differences existing above and below the panel coupled with the natural instabilities of the combined system. A small first-mode perturbation in the panel velocity was only prescribed for the case of inviscid panel flutter (i.e., no shock). Even for viscous simulations without a shock, small pressure differences exist across the rigid panel solution and no perturbations are required.

Stretched Cartesian meshes were constructed for the initially undeformed panel. A uniform grid spacing was used in the streamwise direction while the mesh was stretched in the vertical direction to provide clustering near the deforming panel. For the inviscid calculations, three different grids ($201 \times 61, 201 \times 91, 301 \times 91$) were employed in order to explore the effects of spatial resolution. The finest mesh contained 150 points over the flexible panel. This level of resolution is three times finer than that shown by Gordnier and Visbal²⁴ to be sufficient for the case of inviscid panel flutter. The effects of spatial resolution for one of the inviscid fluttering cases are discussed in Section IV.B. The computational mesh was further refined in the normal direction for the viscous interactions and had dimensions 301×133 . In Section IV.D, the effects of spatial discretization are also partially considered.

Inviscid solutions were advanced in time using a non-dimensional time step $\Delta t U_1/a = 0.001$ which is an order of magnitude smaller than the value employed in Ref. 24. This value was further reduced for the viscous simulations

$(\Delta t U_1/a = 0.0005)$. As shown later, the solutions sometimes exhibited very long transients prior to achieving a final oscillatory pattern. Therefore computations were performed over hundreds of characteristic times and time-averaged results were only gathered after these transients had subsided.

B. Inviscid Shock Reflection Over Flexible Panel

The aerodynamic non-dimensional parameters are the incoming Mach number $M_1 = 2.0$ and the incident shock strength given by the shock angle σ . For simplicity, we specify the overall theoretical pressure ratio p_3/p_1 for the inviscid shock reflection on the rigid panel which is used in turn to obtain the value of σ . In this paper, results are presented for pressure ratios $p_3/p_1 = 1.0, 1.2, 1.4$ and 1.8 . The value of $p_3/p_1 = 1.0$ corresponds to the case of standard panel flutter in which no incident shock is present. For all inviscid cases, the flexible panel occupies the region $0.0 < x/a < 1.0$ along the surface.

A summary of inviscid computations for $x/a = 0.5$ is provided in Figs. 2a,b which show the effect of dynamic pressure and shock strength on the panel flutter amplitude $(\delta w/h)_{amp}$ at the $\frac{3}{4}$ -chord panel location and the corresponding non-dimensional frequency $St = fa/U_1$. It should be noted that this non-dimensional frequency is related to that used by Dowell²⁵ according to the expression $K_f = \frac{2}{\pi} \sqrt{\frac{\lambda}{\mu}} St$.

For the case of standard panel flutter in the absence of an impinging shock (i.e., $p_3/p_1 = 1.0$) flutter onset occurs for $\lambda > 600$ (Fig. 2a). The flutter onset displays the features of a supercritical bifurcation and is similar to the behavior observed in previous studies using either the potential or Euler flow equations.^{24,25} The flutter frequency (Fig. 2b) is effectively constant over the range of dynamic pressure considered. The panel deformations are primarily in the first mode with maximum deflections toward the downstream end of the panel ($x/a \approx 0.75$). All of the above characteristics are in qualitative agreement with previous computations²⁴ for a Mach number equal to 1.8.

When a weak shock ($p_3/p_1 = 1.2$) impinges on the flexible plate, the previously observed panel flutter ceases over the range of λ displayed in Fig. 2a. Additional computations (not shown) indicated that flutter onset did not occur up to $\lambda = 2000$. Instead, the panel exhibits a steady second-mode deformation, shown in Fig. 3a, caused by the differences in static pressure above and below the plate. In this case, the cavity pressure is $p_c/p_1 = 1.1$ which as noted earlier corresponds to the mean theoretical pressure along the rigid plate. As expected, the deflections are in the upward direction in the front of the panel, upstream of the shock impingement location. The panel deformation is not symmetric, displaying significantly higher upward deformations in the front of the panel. This asymmetric character is observed to become more pronounced with increasing dynamic pressure. The surface pressure (Fig. 3b) is characterized by a shock at the leading edge of the panel followed by an expansion which slightly undershoots the upstream pressure (p_1). Subsequently, the pressures rises sharply due to the incident shock and actually overshoots the final theoretical inviscid value p_3 by almost 25% for $\lambda = 875$. At the trailing edge of the panel, there is a sharp expansion as the flow returns to a direction parallel to the rigid surface. The present results demonstrate that under the pressure loading imposed by a weak shock the resulting deformation serves to stiffen the panel and delays the onset of flutter. Reduction in panel flutter amplitudes with increasing loading has been discussed by Dowell²⁶ albeit for a constant pressure differential and in the absence of an impinging shock.

For the next higher shock strength considered ($p_3/p_1 = 1.4$), a very interesting panel dynamics emerges. As shown in Fig. 2a, multiple solutions exist beyond $\lambda_{cr} \approx 575$ depending upon the initial conditions prescribed. In order to ascertain the stability of those solutions and to construct the two branches shown in the figure, several initial conditions were employed. These included (i) starting from the steady rigid plate solution for a given λ , (ii) increasing λ from a previous steady deflected-panel solution, and (iii) decreasing λ from a previous fluttering case. The lower branch denoted as "stable" corresponds to solutions with steady panel deflections similar to those discussed earlier for $p_3/p_1 = 1.2$. This branch was obtained by employing as initial condition a steady solution at a lower dynamic pressure. The upper branch (denoted as *LCO*) was obtained by employing the rigid-plate solution as initial condition. These solutions correspond to fluttering cases with frequencies (Fig. 2b) which decrease with dynamic pressure and which are considerably higher than those for standard panel flutter (i.e., $p_3/p_1 = 1.0$). The observed hysteretic behavior appears to emanate from a subcritical bifurcation at λ_{cr} which contrasts with the supercritical bifurcation found in standard panel flutter.

Details on the panel dynamics and flow structure for one of the *LCO* cases ($p_3/p_1 = 1.4, \lambda = 875$) are shown in Figs. 4 and 5. The history of the panel deflection at the $\frac{3}{4}$ -chord point displays a converged limit-cycle solution. The periodic character of the transverse deflections is demonstrated in the phase plot of Fig. 4b where more than 450 cycles of the motion have been plotted. A single dominant peak at $St = 0.29$ is also observed in the corresponding frequency spectrum. The overall behavior of the panel fluctuations is shown in Fig. 4d using the $x-t$ representation introduced in Ref. 10. In addition, the time-averaged panel shape is given in Fig. 4e along with the instantaneous shape at two points

during the cycle. The curves denoted as $\Phi = 0^\circ, 180^\circ$ correspond to the maximum and minimum vertical positions of the panel $\frac{3}{4}$ -chord point. The mean shape itself is not symmetric relative to the shock impingement point, with higher deformation in the front of the panel. It should be noted that the front portion of the panel always displays a positive deflection, unlike the rear of the panel where both positive and negative displacements are present at different points in the cycle. The deflections about the mean (Fig. 4d) exhibit an approximate second-mode characteristic with higher fluctuations in the rear portion of the plate. However, comparison of the instantaneous panel shapes at $\Phi = 0^\circ$ and $\Phi = 180^\circ$ clearly show a more complex plate dynamics.

Surface pressure distributions as well as contours of static pressure above the panel are shown in Fig. 5 for $p_3/p_1 = 1.4, \lambda = 875$. The instantaneous pressure along the panel displays a leading-edge shock associated with the upward deflection in the front portion of the panel. At $\Phi = 0^\circ$, the most prominent feature downstream of the shock impingement location is the reflected shock, followed by weaker expansion and compression waves. However, for $\Phi = 180^\circ$, in addition to the reflected oblique shock, a strong recompression/expansion is present near the panel trailing edge. It is of interest to examine the flow unsteadiness caused by the fluttering panel in terms of the *rms* pressure fluctuations shown in Fig. 5d. For the inviscid shock reflection on a rigid plate no unsteadiness would be present. Clearly, the fluttering panel radiates significant pressure fluctuations which propagate mainly along the reflected shock and the recompression/expansion waves system. This feature would have structural implications for internal flow applications whereby the unsteadiness generated by the flexible panel could induce significant unsteady loading on opposing solid surfaces.

The effect of spatial resolution was investigated for the previous *LCO* case ($p_3/p_1 = 1.4, \lambda = 875$). Figure 6 displays the time-averaged panel deflection and surface pressure for three levels of resolution. There are only minor differences in both distributions. The variations in non-dimensional frequency and *rms* displacement at the panel $\frac{3}{4}$ -chord point were 1.1% and 5.1% respectively. Therefore it is apparent that sufficient grid resolution is already provided to capture the overall dynamics of the fluttering panel.

A higher pressure ratio, $p_3/p_1 = 1.8$ was also considered. As seen in Fig. 2a, for this higher value of p_3/p_1 , the subcritical bifurcation noted earlier disappears and instead the panel exhibits a supercritical instability onset starting at a much lower value of dynamic pressure ($\lambda_{cr} \approx 200$). Both the oscillation amplitudes and frequency are observed to increase with the increased shock strength. The flow features (not shown) are found to be qualitatively similar to those previously described for $p_3/p_1 = 1.4$. Results for the two highest shock strengths considered clearly show that the *LCO* represents a new instability arising from the combined shock system and panel deflections. Standard panel flutter subjected to a transverse load would actually move the onset of instabilities to a higher (not lower) value of dynamic pressure, as is the case described earlier for a weak shock ($p_3/p_1 = 1.2$).

A limited investigation of the effect of shock impingement location was performed for $p_3/p_1 = 1.8$ and $\lambda = 875$. To this end, several values of x_i/a were considered, namely $x_i/a = 0.18, 0.25, 0.38, 0.43, 0.5$. The cavity pressure underneath the panel was changed for each case in order to correspond to the theoretical zero-net loading condition described earlier in Section IV.A. A comparison of the mean panel deflection, surface pressure and frequency spectra is provided in Fig. 7. Displacing the shock impingement point from midchord to $x_i/a = 0.43$ produces no changes in the overall character of the panel fluctuations. There is an increased time-averaged deflection in the aft-end of the panel and minimal effect on the frequency. However, when the shock impinges upstream at $x_i/a = 0.38$, the *LCO* disappears and instead a steady deflected solution is achieved. The same behavior is observed for $x_i/a = 0.25$. For $x_i/a = 0.18$, the *LCO* re-emerges albeit at much higher frequency as seen in the spectra of Fig. 7c. The $x-t$ diagrams of the panel fluctuations shown in Fig. 7d,e clearly show that when the shock impinges near the leading edge of the flexible panel, very high-mode fluctuations ensue. This is in contrast to the mid-chord impingement case characterized by much longer spatial wave length. The sensitivity of the panel dynamics to the shock impingement location may have interesting implications for the case of a moving shock.

C. Laminar Boundary Layer Over a Flexible Panel

To study the influence of viscous effects, the case of a laminar boundary layer flowing over the flexible panel without an incident oblique shock was first considered. The Reynolds number based on panel length was $Re_a = 300,000$ and the corresponding boundary layer thickness at the panel mid-chord was $\delta/a \approx 0.015$. The flexible panel extends over the distance $0.4 < x/a < 1.4$ along the wall. The pressure underneath the panel was prescribed as the spatially-averaged value obtained from the rigid plate solution. Computations were performed for several values of dynamic pressure, but only two representative cases below and above the critical flutter onset are presented in this paper.

For $\lambda = 1500$, a typical panel flutter was encountered with non-dimensional frequency $St = 0.065$ and amplitude $(\delta w/h)_{amp} = 1.54$ at the $\frac{3}{4}$ -chord point. This flutter frequency is found to be close to the values reported for viscous simulations in Ref. 7 at $M = 1.2$.

A much more interesting behavior arises for lower values of dynamic pressure prior to the onset of standard panel flutter. The instantaneous flow structure for $\lambda = 500$ is provided in Fig. 8. The pressure displays significant disturbances in the inviscid region above the fluttering panel. Disturbances are also observed to convect in the boundary layer downstream of the panel. The growth of these coherent boundary-layer disturbances downstream of the leading edge of the flexible panel can be more clearly seen in the contours of density and density gradient magnitude (Figs. 8b,c) where an enlarged vertical scale is employed for clarity. The surface pressure distribution (Fig. 8d) shows that the magnitude of the disturbances increase over the fluttering panel but begin to decay downstream of the panel trailing edge. The *rms* velocity fluctuations within the boundary layer are also displayed in Fig. 9. The convective growth of the disturbances within the boundary layer is again apparent. The wavelength of the disturbances is approximately $\lambda_d = 0.15$ which is of the order of 10δ and propagate with a speed $c_r \approx 0.61$.

The mean and instantaneous panel deflections are shown in Fig. 10a. The panel dynamics is characterized by small-amplitude, high-mode fluctuations about a slightly deflected time-averaged shape. The spectra of the fluctuations at $x/a = 3/4$ (Fig. 10b) indicates periodic oscillations with a very high frequency $St = 3.96$. The $x - t$ -diagram of Fig. 10c demonstrates that these are essentially spatially-stationary very high-mode flexural deflections.

Although a boundary layer stability analysis has not been performed so far, the observed panel dynamics appears to originate from the coupling of boundary layer instabilities with higher-mode flexural deflections of the panel. It should be noted that these oscillations ceased at a lower Reynolds number ($Re_a = 120,000$). These self-sustained oscillations resemble those from a previous computational study¹⁰ in the subsonic regime ($M_\infty = 0.8$) wherein the frequency and wavelength of the deformations were found to be compatible with Tollmien-Schlichting waves.

D. Shock Laminar Boundary Layer Interaction Over a Flexible Panel

Results for a shock laminar boundary interaction over a flexible panel are considered next. The Reynolds number based on panel length is 1.2×10^5 and the nominal boundary layer thickness at the panel midchord in the absence of the shock is $\delta/a = 0.024$. Results are presented for a single shock strength $p_3/p_1 = 1.8$ and shock impingement location $x_i/a = 0.5$. The cavity pressure underneath the panel was set equal to the mean theoretical inviscid value ($p_c/p_1 = 1.4$). For all shock boundary layer interaction cases, the flexible panel extends over the region $0.6 < x/a < 1.6$ along the wall.

A limited study of the effect of spatial resolution was performed by comparing results obtained with the second-order and sixth-order spatial discretizations. The steady flow structure for the SBLI over the rigid panel computed with both schemes is shown in Fig. 11. The pressure field above the wall is found to be similar for both schemes with the higher-order solver exhibiting sharper features. The surface pressure and skin-friction distributions have minor differences in the separation and reattachment locations but display the same overall features, such as the well-defined pressure plateau associated with the large region of separation. Figure 12 shows the effect of spatial discretization for the case of a shock impinging on a flexible panel. The time-averaged surface pressure and skin-friction distributions are in good agreement with each other and there are insignificant differences in the extent of the separated region. A comparison of the spectra of the panel fluctuations at the panel $\frac{3}{4}$ -chord point is shown in Fig. 12c. Despite the complexity of the vibrations, the same discrete frequencies are effectively achieved with the second-order and sixth-order schemes with only minor changes in oscillation amplitude. Although further grid-resolution studies are desirable, the limited differences observed between the low-order and high-order approaches for the shock laminar boundary layer interactions provides some degree of confidence for the results that follow. This situation is however not be expected in transitional/turbulent three-dimensional simulations containing a broad range of fine-scale features.

The shock boundary layer impingement on the flexible panel is considered in detail for the case of $\lambda = 875$. When the panel is allowed to deflect, self-sustaining panel oscillations emerge which result in a much more complex unsteady viscous/inviscid interaction. The response of the panel is provided in Figs. 13 and 14. The history of the panel deflection at the $\frac{3}{4}$ -chord point (Fig. 13a) indicates that the panel response is characterized by a very long transient before it achieves its final state. Initially, the panel undergoes low-frequency high-amplitude oscillations which are slowly damped prior to the onset of high-frequency fluctuations. The final panel response is no longer periodic as in the previous inviscid cases and displays a seemingly chaotic pattern as shown in the phase plot of Fig. 13c. The spectrum (Fig. 13d) displays multiple discrete frequencies with a dominant peak at $St = 1.28$. The overall dynamics of the panel is illustrated in the $x - t$ diagram of Fig. 13e which shows the deflections after subtracting the time-averaged deformation. Although multiple flexural modes are observed, a discernable travelling disturbance is apparent. The mean and a sample instantaneous panel shape are shown in Fig. 14a. The time-averaged deflection exhibits an approximate second-mode pattern and is an order of magnitude smaller than the corresponding level for the inviscid shock reflection (see Fig. 7a). The instantaneous shape displays large-amplitude higher-modes also seen clearly in the panel normal velocity (Fig. 14b).

The instantaneous flow structure above the flexible panel is displayed in Fig. 15. The pressure field is considerably more complex relative to the rigid plate (Fig. 11a). The fluttering panel induces strong unsteady compression and expansion waves systems. At the instant shown, for instance, there is a shock at the panel leading edge due to the upward deflection. The instantaneous density and vorticity fields also indicate the propagation of boundary-layer disturbances downstream of the panel trailing edge. Significant fluctuations can be observed in the instantaneous surface pressure distribution shown in Fig. 16a. At locations near the front of the panel, the instantaneous pressure undershoots the incoming freestream value p_1 . Large overshoots in pressure beyond the theoretical maximum value $p_3/p_1 = 1.8$ are also seen near the end of the panel. A measure of the degree of unsteadiness is provided in Fig. 15d in terms of the *rms* pressure. Significant pressure fluctuations extend over a large portion of the panel. The largest fluctuations are seen in the aft-end of the panel and propagate away from the plate along the reflected compression/expansion system. As noted earlier, this feature would have structural implications for internal flow applications wherein the flexible panel could induce unsteady loading on opposing solid surfaces. Moderate unsteadiness is also seen in the root of the incident oblique shock. This appears to be associated with its interaction with the waves generated by the front of the fluttering panel.

A comparison of the time-averaged flow for the flexible panel with the rigid plate steady solution is provided in Figs. 16 and 17 in terms of the surface pressure, the skin-friction coefficient and the streamwise velocity field. There is a significant reduction in the size of the separated region for the flexible panel. The streamwise extent and maximum height of the separation zone are reduced by 31% and 36% respectively. This effect is attributed to the forcing of the flow as a result of the self-excited panel fluctuations. Therefore, the flexible panel may be viewed as a passive means of flow control which exploits the aeroelastic instabilities of the combined fluid-structural system.

1. Parametric Effects

A limited study of parametric effects was performed for the shock laminar boundary layer interaction problem. The effect of dynamic pressure on the time-averaged panel deformation and surface pressure distribution is shown in Fig. 18. For $\lambda = 500$, there is a reduction in the extent of the pressure plateau due to the oscillations of the panel. This beneficial effect increases for $\lambda = 875$ but appears to saturate at $\lambda = 1000$. For the range $500 \leq \lambda \leq 1000$, a similar mean panel deflection is observed (Fig. 18a). When the dynamic pressure is further increased to $\lambda = 1250$, the self-excited panel fluctuations cease, and instead a steady solution with larger static deformation emerges. This seems to indicate that the instability of the coupled fluid-structural system can be eliminated by increased static deflection and loading. Values of dynamic pressure below $\lambda = 500$ have not been considered so far and therefore the onset of the instability as a function of λ has not been determined. It is worth noting that for $\lambda = 1250$, there is no reduction in the extent of the separation region as can be inferred from the surface pressure distribution which closely matches the rigid plate solution. This reinforces the notion that the separation control seen at lower λ is due to the forcing of the shear layer caused by the oscillating panel.

The effect of Reynolds number was also investigated for a fixed dynamic pressure ($\lambda = 875$). Computations for $Re_a = 60,000$ (not shown) displayed mild panel oscillations which did not alter the time-averaged shock laminar boundary layer separation region. Results for $Re_a = 240,000$ are shown in Fig. 19. A large steady separated region is obtained for the rigid plate. The flexible panel induces pronounced oscillations in the instantaneous surface pressure, even higher than those observed for $Re_a = 120,000$ (Fig. 16a). There is also a dramatic effect on the viscous/inviscid interaction. Most notably, the streamwise extent of the separation region is reduced by almost a factor of two.

2. Forced Panel Deflections

The previously observed reduction in separation induced by the panel self-excited oscillations suggests that a similar flow control might be achievable through imposed forcing of the panel. To explore this possibility, the panel was made to oscillate by prescribing a harmonically-varying cavity pressure p_c underneath the panel

$$p_c(t) = p_{co} + p_{amp} \sin(2kt) \quad (21)$$

where p_{co} is the mean cavity pressure, p_{amp} is the forcing amplitude and $k = \pi f c / U_1$ the reduced frequency.

The case considered is one found previously not to exhibit self-excited fluctuations, namely $p_c = 1.4$, $Re_a = 120,000$ and $\lambda = 1250$. The cavity pressure was forced with amplitude $p_{amp} = 0.6$ and at different frequencies $k = 0.5, 1.0, 2.0, 4.0$ ($St = 0.16, 0.32, 0.64, 1.27$). These forcing frequencies are in the range of self-excited frequencies found in Fig. 13d for $\lambda = 875$. In fact, $k = 4$ corresponds approximately to the dominant peak in the spectrum.

Shown in Fig. 20a-c are the time-averaged panel deformation, surface pressure and skin-friction coefficient as a function of forcing frequency. The results for the unforced flexible panel at the same dynamic pressure are also

included for comparison. For the highest reduced frequency ($k = 4.0$), there is minimal effect on the panel mean deformation relative to the unforced case, although small-amplitude oscillations are present. The surface pressure and skin friction are effectively unaltered. This behavior seems to be restricted by the dynamics of the panel itself which cannot respond effectively beyond certain frequency cut-off. As the frequency is reduced, there is a significant drop in mean deflection and a reduction in the extent of separation. The control effectiveness seems to improve with decreasing forcing frequency, and additional lower values of k need to be considered.

The instantaneous surface pressure for $k = 2$ (Fig. 20d) displays intriguing short-wavelength undulations which prompted examination of the corresponding unsteady flow structure, displayed in Fig. 21. This figure reveals that high-mode flexural deflections (not shown) couple to the shear-layer instabilities, as clearly seen in the contours of density gradient magnitude. The acoustic radiation above these shear-layer sub-structures is also apparent. Despite the time averaging process, coherent short-wave structures remain in the *rms* pressure fluctuations which are most visible within the separated region. This effect is most likely due to the stationary nature of the high-mode flexural deflections, similar to those shown in Fig. 10.

3. Preliminary Three-Dimensional Effects

A preliminary three-dimensional simulation was performed for a shock boundary layer interaction over the rigid panel at flow conditions $M = 2.0$, $p_3/p_1 = 1.8$ and $Re_a = 300,000$. The instantaneous flow structure is shown in Fig. 22 in terms of an iso-surface of vorticity magnitude. Even in the absence of perturbations imposed by an oscillating panel the flow begins to transition downstream of the shock impingement location. This instability is characterized by what appear to be longitudinal Goertler-type vortices of a regular spanwise wavelength induced by the concave curvature of the attaching shear layer. Following reattachment, a full breakdown into fine-scale turbulent structures is apparent. Coupling of this transitional behavior with panel deflections, to be addressed in future work, poses significant challenges given the long transients noted earlier, as well as the disparities in time-scales between fine-scale turbulence and some of the panel fluctuations.

V. SUMMARY AND CONCLUSIONS

The complex self-sustained oscillations arising from the interaction of an oblique shock with a flexible panel have been investigated numerically. The flowfields were obtained by solving the full compressible Navier-Stokes equations employing an extensively validated implicit solver. The flexible panel mechanics was described by means of the non-linear von Karman plate equations which were solved using a previously developed finite-difference procedure. The fluid and structural solvers were coupled accurately in time via a sub-iterative approach. Computations were performed for a freestream Mach number $M_\infty = 2.0$ and for Reynolds numbers in the range $60,000 - 300,000$ based on panel length.

For a two-dimensional inviscid shock reflection, both static deformation and limit-cycle oscillation regimes have been found depending on the shock strength and dynamic pressure. For a weak shock, the stiffening effects induced by the deformation eliminate the standard panel flutter which is present in the absence of a shock. For higher shock strengths, limit-cycle oscillations emerge from either subcritical or supercritical bifurcation points. In addition to the incident and reflected main shocks, the unsteady flow is characterized by a leading-edge shock and by a strong recompression/expansion near the plate trailing edge. For fixed dynamic pressure, the *LCO* amplitude and frequency are observed to increase with shock strength. The critical dynamic pressure also diminishes with increasing shock strength and can be much lower than that corresponding to standard panel flutter in the absence of a shock. This observation suggests that a new aeroelastic instability (distinct from regular panel flutter) is at play and arises from the complex interaction of the incident and reflected wave system with the panel flexural modes even in the absence of viscous separated flow effects. The panel exhibits a complex dynamics as the shock impingement point is displaced from the mid-point towards the plate leading edge. As the shock location moves upstream, the oscillations cease. They subsequently re-emerge, albeit at much higher modes, for an impingement point close to the panel leading edge.

For a laminar boundary layer flowing above the flexible panel, high-frequency panel deflections can emerge at values of dynamic pressure below the critical flutter value. These deformations appear to originate from the coupling of boundary layer instabilities with high-mode flexural deflections. Boundary-layer disturbances are seen to grow along the panel and generate significant acoustic radiation above the surface. A detailed stability analysis of the mean flow profiles is needed in order to confirm this hypothesis.

For a separated shock laminar boundary layer interaction, complex non-periodic self-excited oscillations arise which result in a significant reduction in the extent of the time-averaged separation region. This finding suggests the

potential use of an aeroelastically-tailored flexible panel as a means of passive flow control. Forced panel oscillations, induced by a specified variable cavity pressure underneath the panel, were also found to be effective in reducing separation.

The present study demonstrates for the first time the rich dynamics emerging from the inviscid and viscous interactions generated by the impingement of a shock on a flexible panel. The significant unsteadiness generated by the fluttering panel propagates along the complex reflected expansion/recompression wave system with potential structural implications not only for the panel but for opposing surfaces in internal flow applications.

Acknowledgments

This work was supported in part by AFOSR under a task monitored by Dr. D. Smith, and by a grant of HPC time from the DoD HPC Shared Resource Center at AFRL. The author wishes to acknowledge several useful conversations with Dr. R. Gordnier of the Air Force Research Laboratory.

References

- ¹E. H. Dowell. Panel Flutter: A Review of the Aeroelastic Stability of Plates and Shells. *AIAA Journal*, 8(3):385–399, 1970.
- ²C. Mei, K. Abel-Motagaly, and R. Chen. Review of Nonlinear Panel Flutter at Supersonic and Hypersonic Speeds. *Applied Mechanics Review*, 52(10):321–332, 1999.
- ³E. H. Dowell. *Aeroelasticity of Plates and Shells*. Noordhoff International, Leiden, 1975.
- ⁴G.A. Davis and O.O. Bendiksen. Transonic Panel Flutter. AIAA 93-1476, April 1993.
- ⁵O.O. Bendiksen and G.A. Davis. Nonlinear Traveling Wave Flutter of Panels in Transonic Flow. AIAA 95-1486, April 1995.
- ⁶I. Nydick, P. Friedmann, and X. Zhong. Hypersonic Panel Flutter Studies on Curved Panels. *AIAA Paper 95-1485-CP*, 1995.
- ⁷R. E. Gordnier and M. R. Visbal. Development of a Three-Dimensional Viscous Aeroelastic Solver for Nonlinear Panel Flutter. *AIAA Paper 2000-2337*, 2000.
- ⁸R. E. Gordnier and M. R. Visbal. Computation of Three-Dimensional Nonlinear Panel Flutter. *AIAA Paper 2001-0571*, 2001.
- ⁹R. E. Gordnier and R. Fithen. Coupling of a Nonlinear Finite Element Structural Method with a Navier-Stokes Solver. *Computers and Structures*, 81:75–89, 2003.
- ¹⁰M. R. Visbal and R. E. Gordnier. Numerical simulation of the interaction of a transitional boundary layer with a 2-D flexible panel in the subsonic regime. *Journal of Fluids and Structures*, 19:881–903, 2004.
- ¹¹D.A. Anderson, J.C. Tannehill, and R.H. Pletcher. *Computational Fluid Mechanics and Heat Transfer*. McGraw-Hill Book Company, 1984.
- ¹²Y. C. Fung. *Foundations of Solid Mechanics*. Prentice-Hall, Inc., 1965.
- ¹³C.Y. Chia. *Nonlinear Analysis of Plates*. McGraw-Hill International Book Company, 1980.
- ¹⁴R. Beam and R. Warming. An Implicit Factored Scheme for the Compressible Navier-Stokes Equations. *AIAA Journal*, 16(4):393–402, 1978.
- ¹⁵A. Jameson, W. Schmidt, and E. Turkel. Numerical Solutions of the Euler Equations by a Finite Volume Method Using Runge-Kutta Time Stepping Schemes. *AIAA Paper 81-1259*, 1981.
- ¹⁶T. Pulliam. Artificial Dissipation models for the Euler Equations. *AIAA*, 24(12):1931–1940, 1986.
- ¹⁷T.H. Pulliam and D.S. Chaussee. A Diagonal Form of an Implicit Approximate-Factorization Algorithm. *Journal of Computational Physics*, 39(2):347–363, 1981.
- ¹⁸M.R. Visbal and D.V. Gaitonde. High-Order Accurate Methods for Complex Unsteady Subsonic Flows. *AIAA Journal*, 37(10):1231–1239, 1999.
- ¹⁹M.R. Visbal and D.V. Gaitonde. On the Use of High-Order Finite-Difference Schemes on Curvilinear and Deforming Meshes. *Journal of Computational Physics*, 181:155–185, 2002.
- ²⁰D.V. Gaitonde and M.R. Visbal. Pade-Type High-Order Boundary Filters for the Navier-Stokes Equations. *AIAA Journal*, 38(11):2103–2112, 2000.
- ²¹M.R. Visbal and D.V. Gaitonde. Shock-Capturing Using Compact-Differencing-Based Methods. *AIAA Paper 2005-1265*, January 2005.
- ²²J. L. Humar. *Dynamics of Structures*. Prentice-Hall, Inc., 1990.
- ²³M.R. Visbal and R.E. Gordnier. A High-Order Flow Solver for Deforming and Moving Meshes. *AIAA Paper 2000-2619*, June 2000.
- ²⁴R. E. Gordnier and M. R. Visbal. Development of a three-dimensional viscous aeroelastic solver for nonlinear panel flutter. *Journal of Fluids and Structures*, 16:497–527, 2002.
- ²⁵E. H. Dowell. Nonlinear Oscillations of a Fluttering Plate. II. *AIAA Journal*, 5(10):1856–1862, 1967.
- ²⁶E. H. Dowell. Nonlinear Oscillations of a Fluttering Plate. *AIAA Journal*, 4(7):1267–1275, 1966.

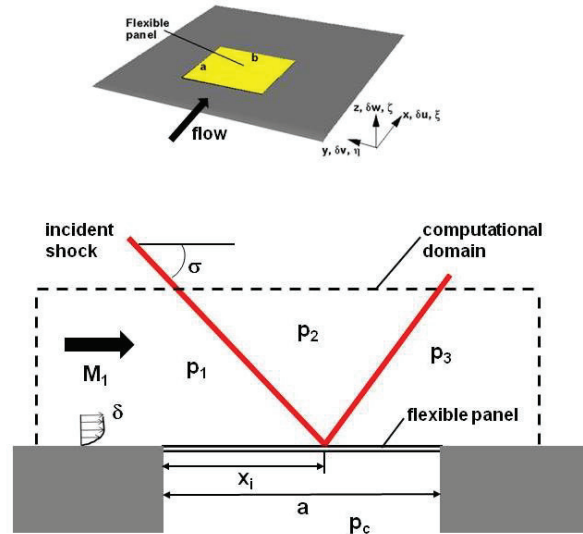


Figure 1. Schematic of flow configuration for oblique shock impinging on a flexible panel

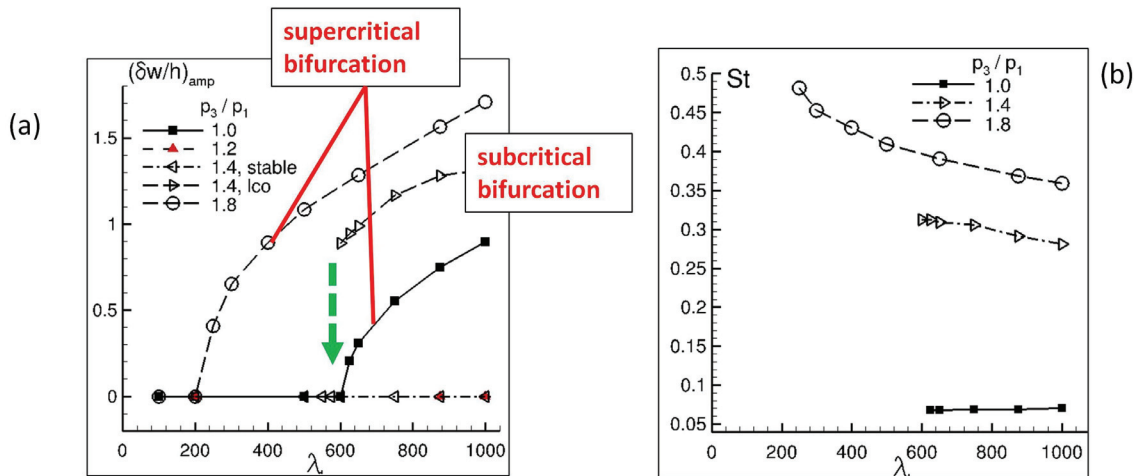


Figure 2. Effect of dynamic pressure and shock pressure ratio on panel dynamics for inviscid interaction: (a) amplitude and (b) frequency of transverse plate oscillations at $x/a = \frac{3}{4}$

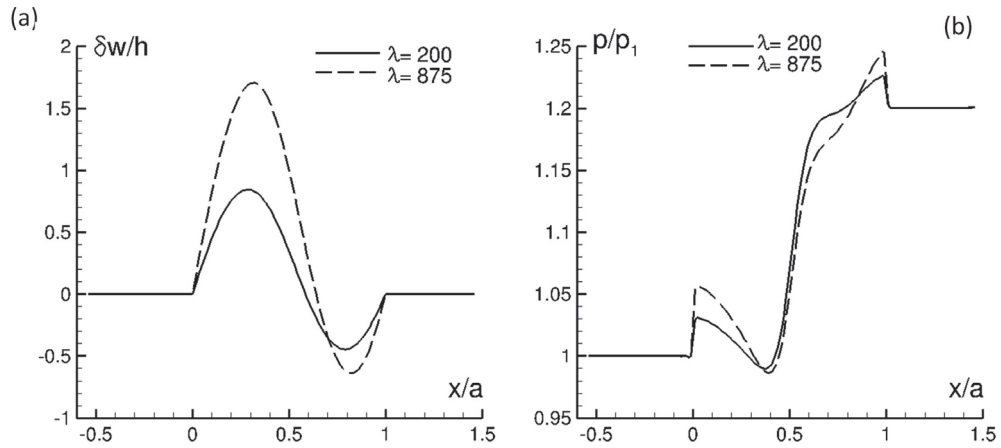


Figure 3. (a) static panel deformation and (b) surface pressure distribution for inviscid interaction with $p_3/p_1 = 1.2$

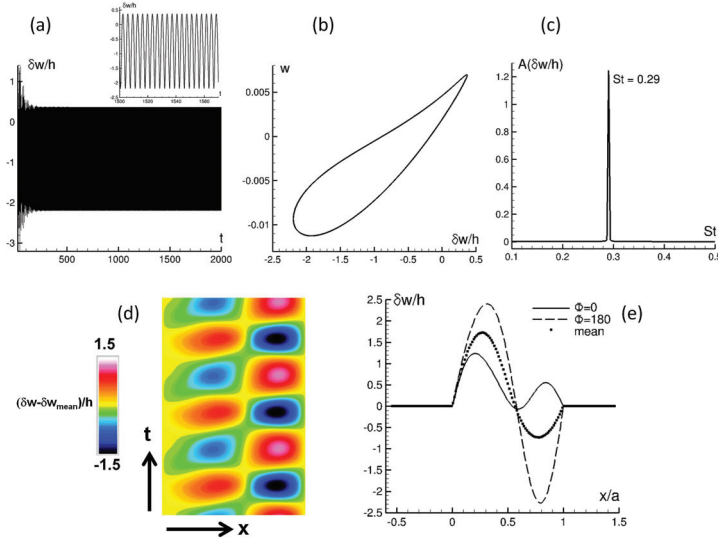


Figure 4. Panel transverse oscillations for inviscid interaction with $p_3/p_1 = 1.4$ and $\lambda = 875$: (a) history of panel deflection at $x/a = \frac{3}{4}$, (b) phase-plane trajectory at same location, (c) frequency spectrum, (d) $x - t$ diagram of panel deflections and (e) mean and selected instantaneous panel shape

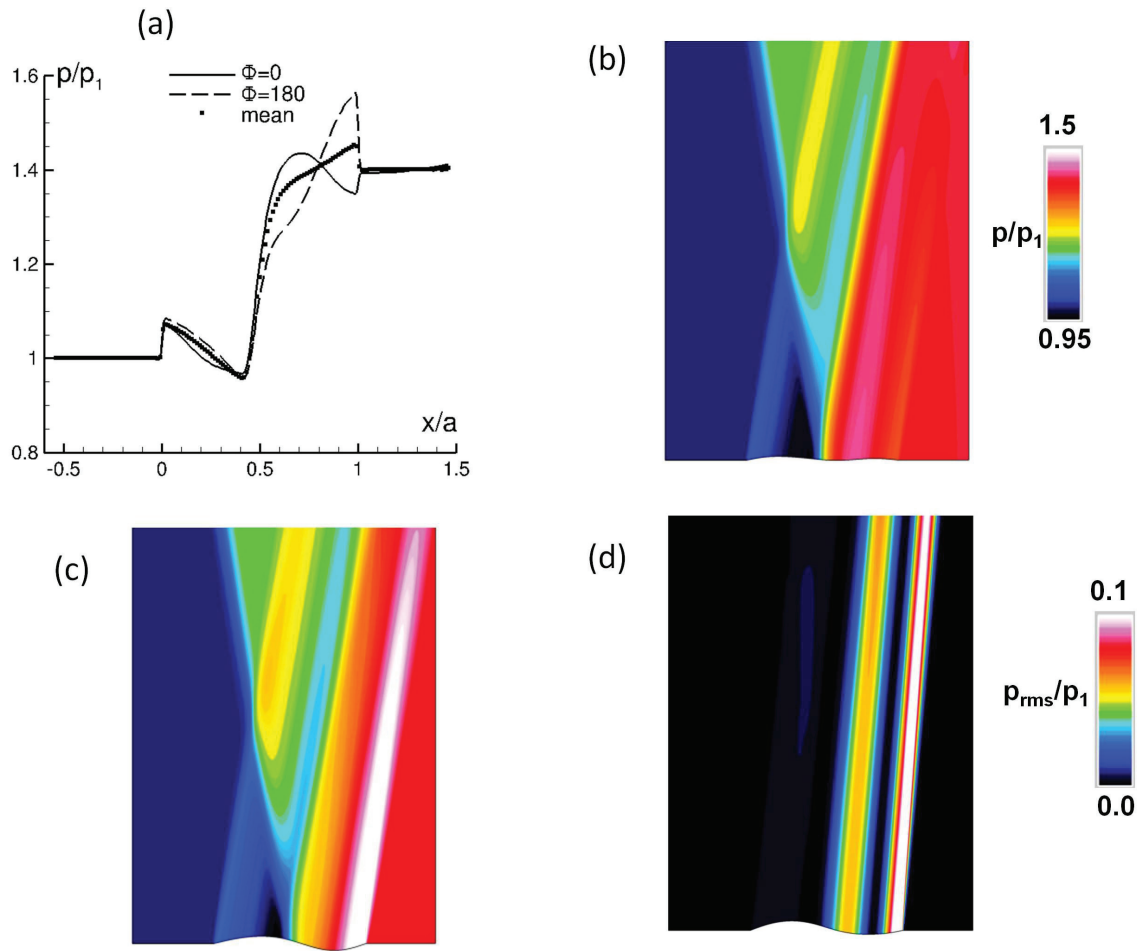


Figure 5. (a) Mean and selected instantaneous surface pressure distributions, pressure contours at phases of (b) maximum and (c) minimum deflection of $\frac{3}{4}$ -chord point, and (d) r_{ms} pressure fluctuations for inviscid interaction with $p_3/p_1 = 1.4$ and $\lambda = 875$. Vertical scale in (b)-(d) has been enlarged by a factor of ten for the purpose of clarity

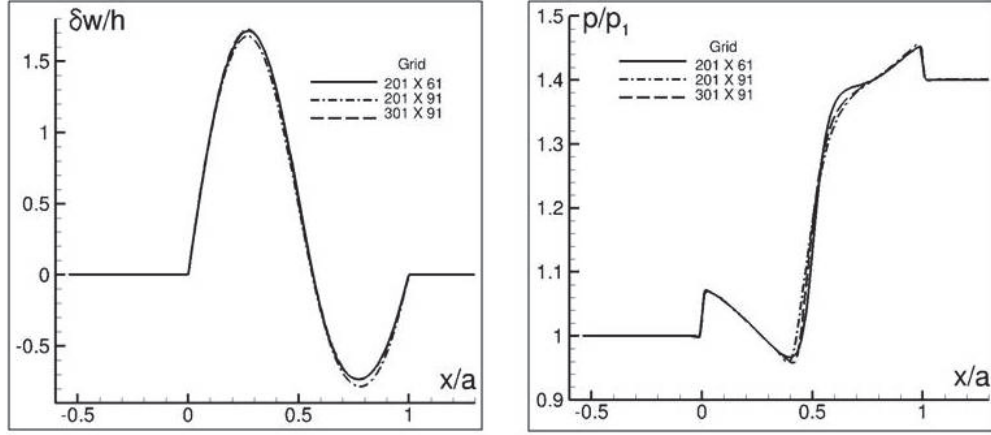


Figure 6. Effect of grid resolution for inviscid interaction with $p_3/p_1 = 1.4$ and $\lambda = 875$. Time-averaged (a) panel deflection and (b) surface pressure distributions

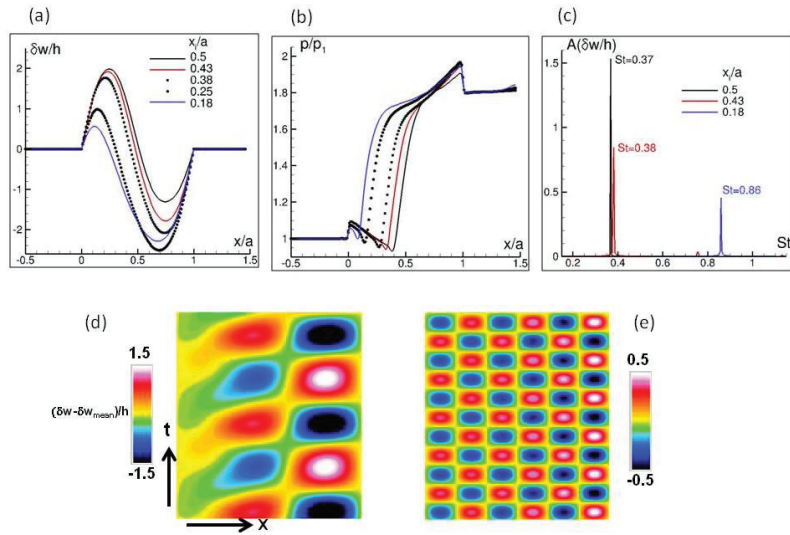


Figure 7. Effect of shock impingement location for inviscid interaction with $p_3/p_1 = 1.8$ and $\lambda = 875$. Time-averaged (a) panel deflection and (b) surface pressure, (c) frequency spectra of oscillations at panel $\frac{3}{4}$ -chord point, and $x - t$ diagram of panel fluctuations for (d) $x_i/a = 0.5$ and (e) $x_i/a = 0.18$. In (a) and (b) the symbols denote steady deflected solutions

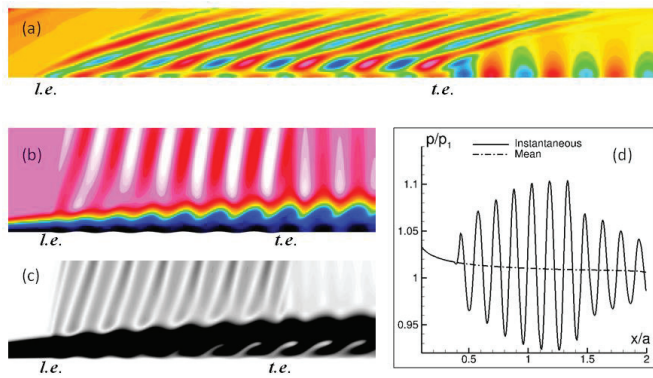


Figure 8. Instantaneous flow structure for laminar boundary layer over a flexible panel, $\lambda = 500$ and $Re_a = 300,000$. (a) pressure, (b) density, (c) density gradient magnitude and (d) wall pressure distribution. Vertical scale in (b) and (c) has been enlarged by a factor of ten for the purpose of clarity

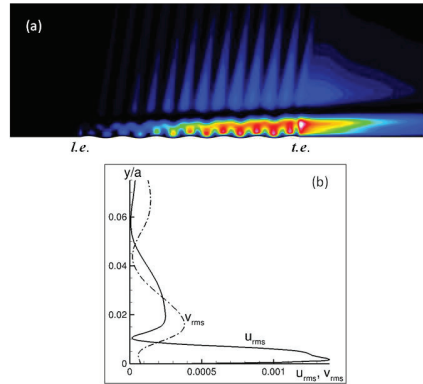


Figure 9. Time-averaged velocity fluctuations in laminar boundary layer over a flexible panel, $\lambda = 500$ and $Re_a = 300,000$. (a) contours of u_{rms} and (b) fluctuation profiles at the panel $\frac{3}{4}$ -chord station. Vertical scale in (a) has been enlarged by a factor of ten for the purpose of clarity

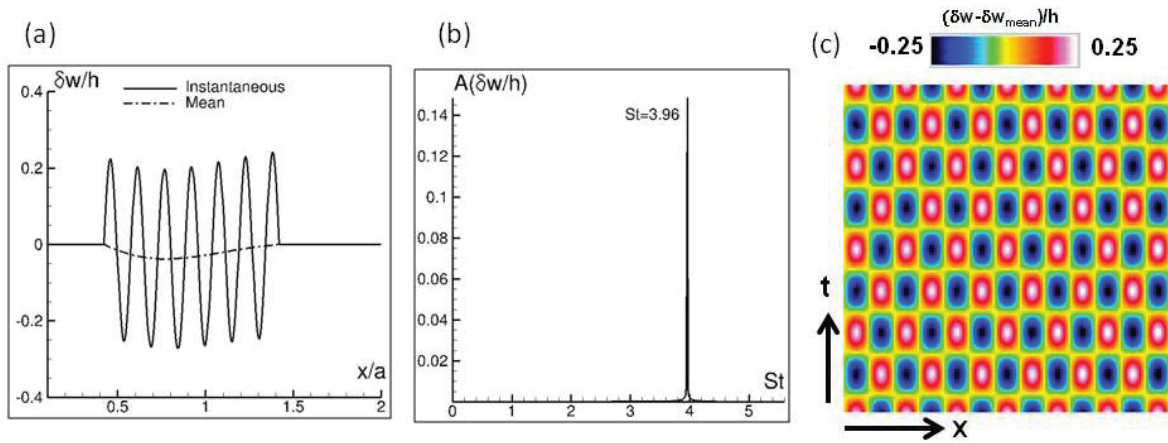


Figure 10. Panel response for laminar boundary layer, $\lambda = 500$ and $Re_a = 300,000$. (a) deflection, (b) spectrum of oscillations at $\frac{3}{4}$ -chord point, and (c) $x - t$ diagram of panel deflections

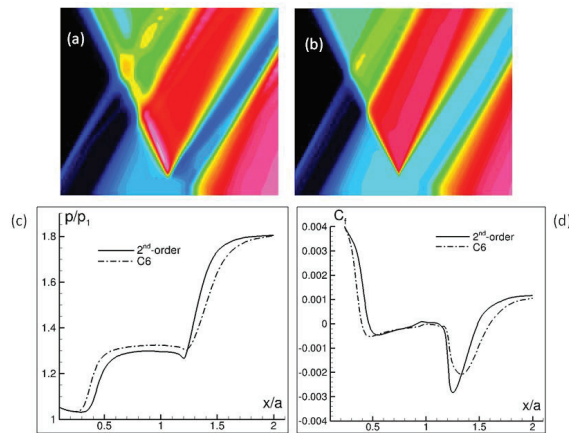


Figure 11. Effect of spatial discretization on shock laminar boundary layer interaction over rigid plate, $p_3/p_1 = 1.8$ and $Re_a = 120,000$. Pressure contours for (a) second-order and (b) 6th-order schemes, (c) surface pressure and (d) skin-friction coefficient. Vertical scale in (a) and (b) has been enlarged for the purpose of clarity

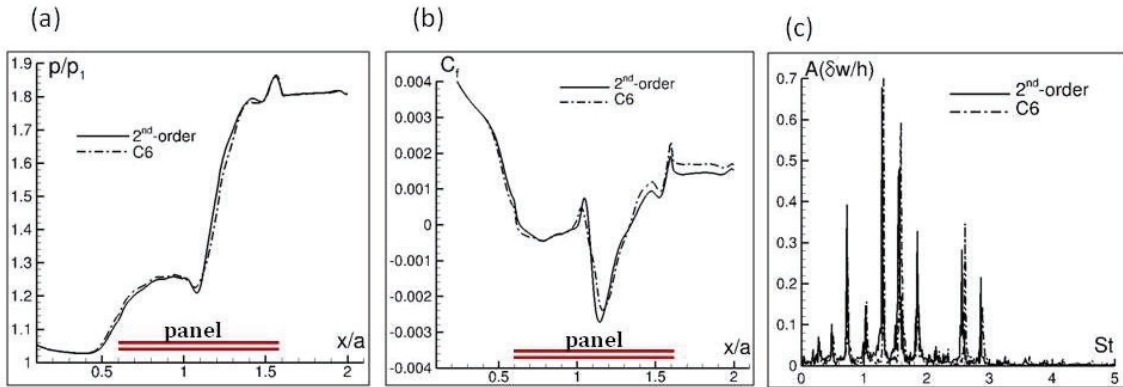


Figure 12. Effect of spatial discretization on shock laminar boundary layer interaction over flexible panel, $p_3/p_1 = 1.8$, $Re_a = 120,000$ and $\lambda = 875$. Time-averaged (a) surface pressure, (b) skin-friction coefficient and (c) spectra of panel fluctuations at $\frac{3}{4}$ -chord point

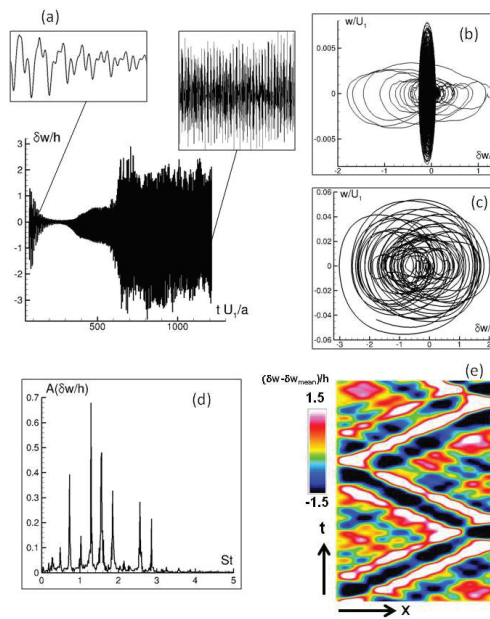


Figure 13. Panel response for shock laminar boundary layer interaction over flexible panel, $p_3/p_1 = 1.8$, $Re_a = 120,000$ and $\lambda = 875$. (a) Time history of deflection at $\frac{3}{4}$ -chord point, (b) phase-trajectory during initial transients, (c) phase-trajectory at late time, (d) frequency spectrum and (e) $x - t$ diagram of deflection

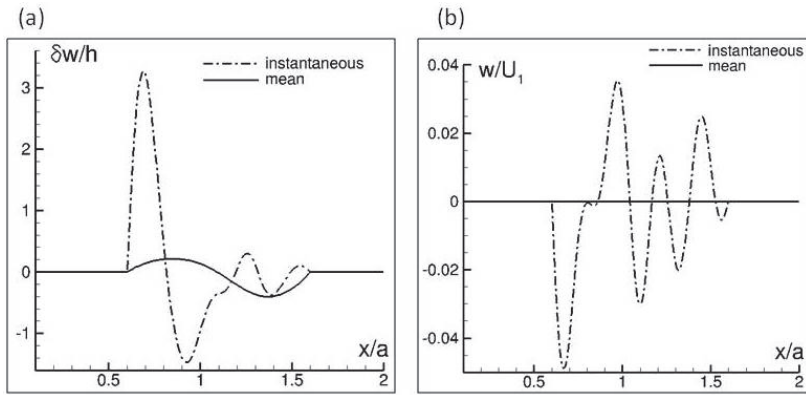


Figure 14. Panel response for shock laminar boundary layer interaction over flexible panel, $p_3/p_1 = 1.8$, $Re_a = 120,000$ and $\lambda = 875$. (a) mean and instantaneous panel shape, and (b) normal velocity

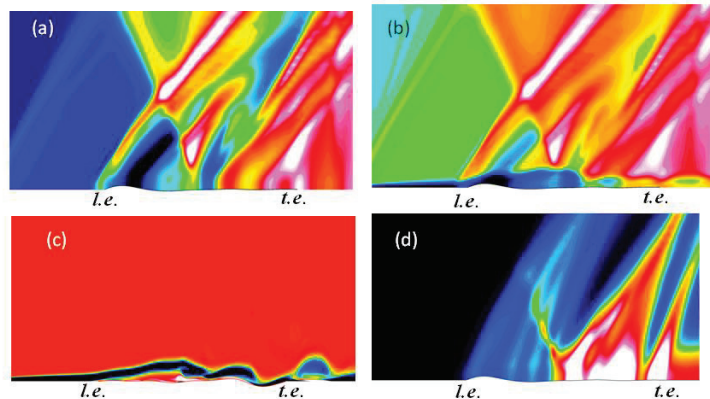


Figure 15. Flow structure for shock laminar boundary layer interaction over flexible panel, $p_3/p_1 = 1.8$, $Re_a = 120,000$ and $\lambda = 875$. (a) pressure, (b) density, (c) spanwise vorticity and (d) rms pressure fluctuations. Vertical scale has been enlarged for the purpose of clarity

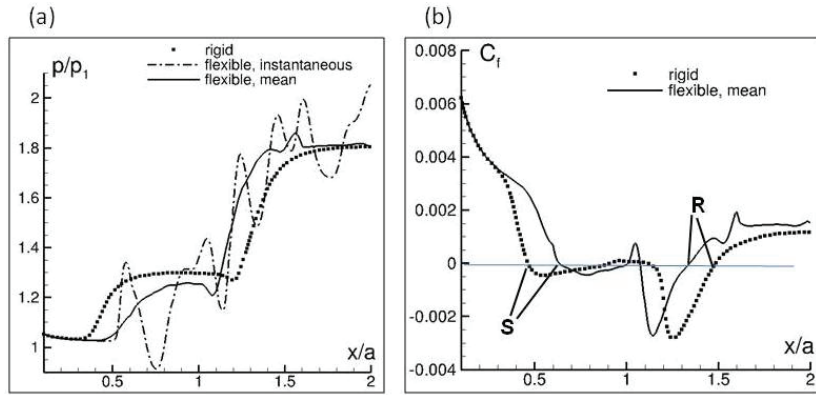


Figure 16. (a) surface pressure and (b) skin-friction distributions for shock laminar boundary layer interaction over flexible panel, $p_3/p_1 = 1.8$, $Re_a = 120,000$ and $\lambda = 875$

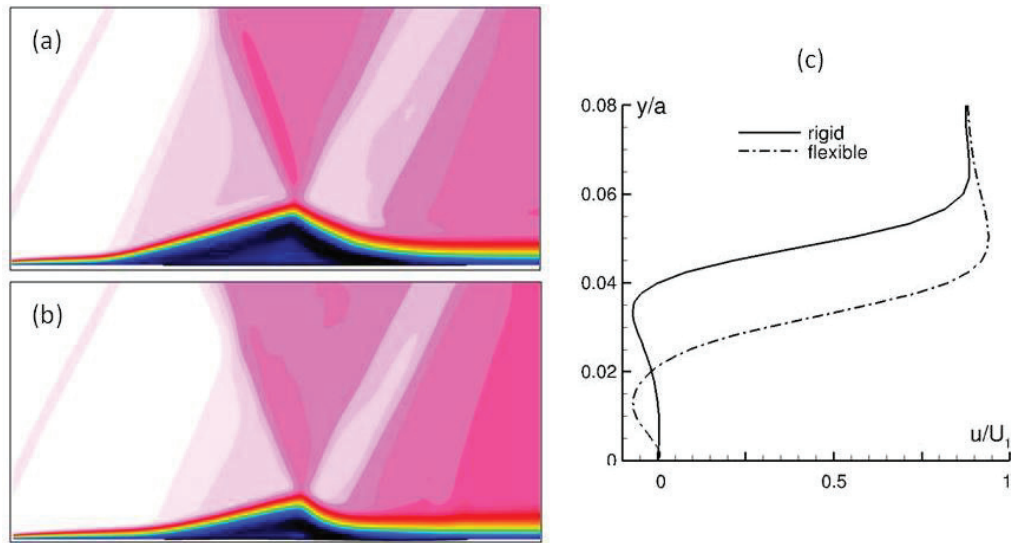


Figure 17. Effect of flexibility on time-averaged separated region generated by shock laminar boundary layer interaction, $p_3/p_1 = 1.8$, $Re_a = 120,000$. Mean streamwise velocity contours for (a) rigid and (b) flexible panel ($\lambda = 875$), (c) velocity profiles at maximum height of separation bubble

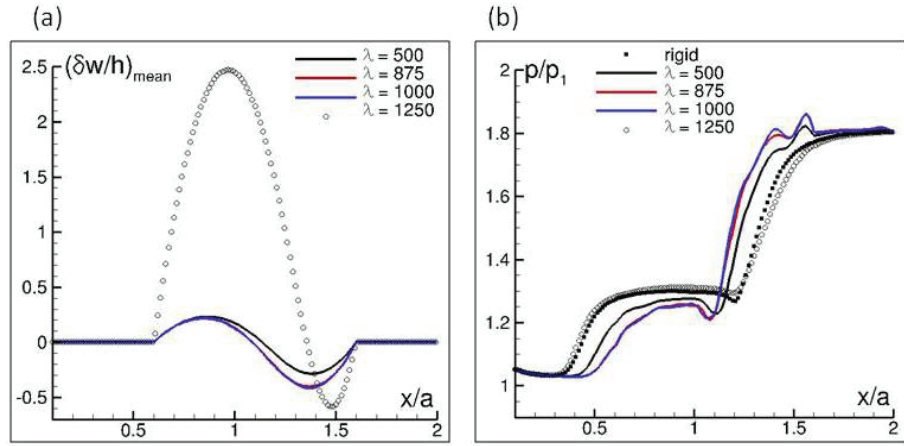


Figure 18. Effect of dynamic pressure on shock laminar boundary layer interaction over flexible panel, $p_3/p_1 = 1.8$ and $Re_a = 120,000$. Time-averaged (a) panel deflection and (b) surface pressure. The symbols denote steady solutions

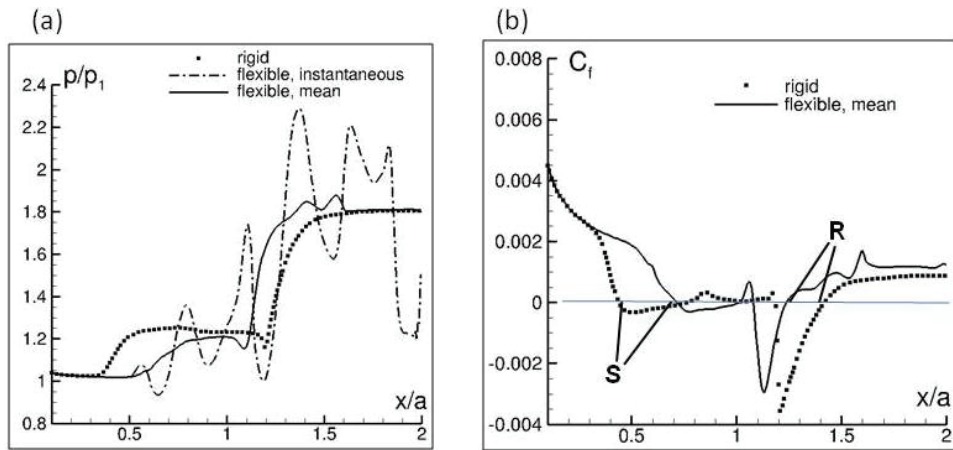


Figure 19. (a) surface pressure and (b) skin-friction distributions for shock laminar boundary layer interaction over flexible panel, $p_3/p_1 = 1.8$, $Re_a = 240,000$ and $\lambda = 875$

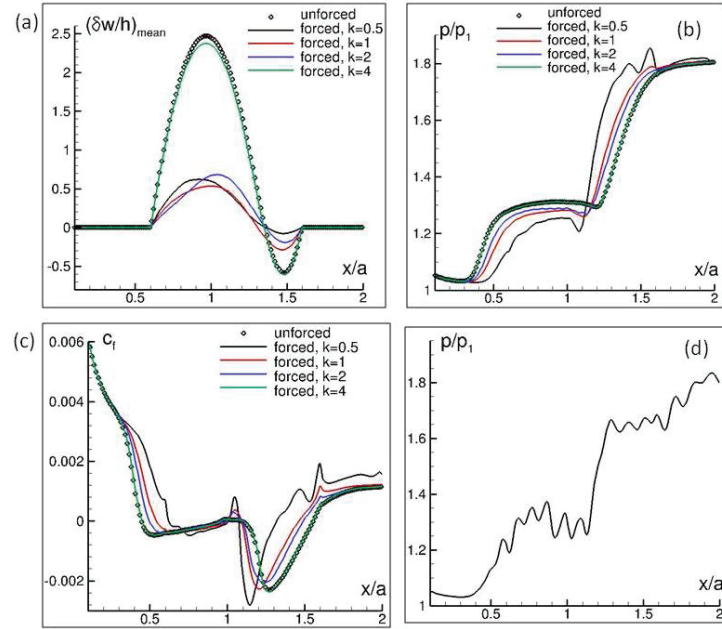


Figure 20. Effect of forcing frequency on shock laminar boundary layer interaction over flexible panel, $p_3/p_1 = 1.8$, $Re_a = 120,000$ and $\lambda = 1250$. Time-averaged (a) panel deflection, (b) surface pressure, and (c) skin-friction distribution; (d) instantaneous surface pressure for $k = 2.0$

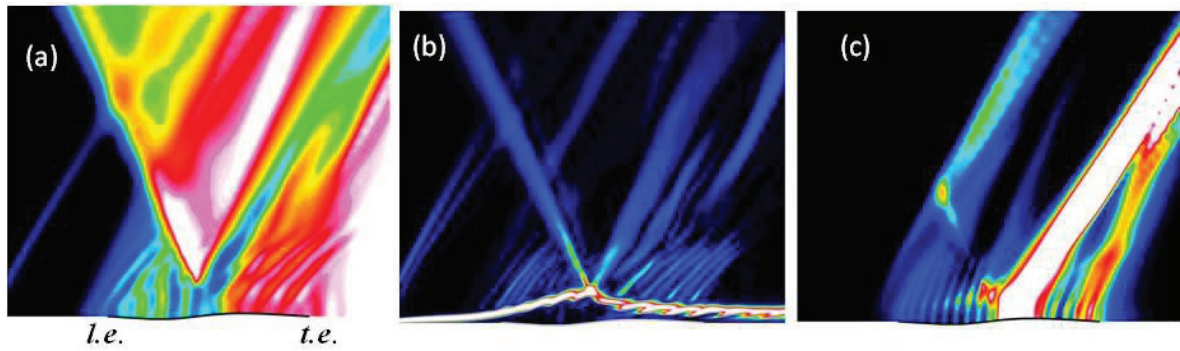


Figure 21. Unsteady flow structure for forced flexible panel, $p_3/p_1 = 1.8$, $Re_a = 120,000$, $\lambda = 1250$ and $k = 2.0$. (a) pressure density gradient magnitude, and (b) pressure, and (c) rms pressure.

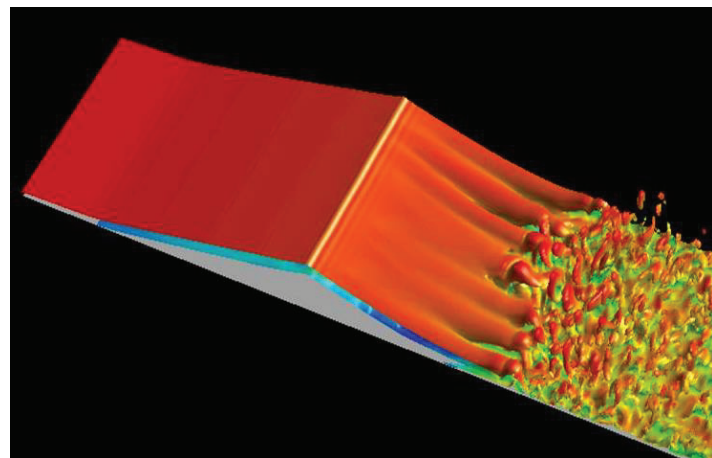


Figure 22. Transitional shock boundary layer interaction over rigid panel depicted using an iso-surface of vorticity magnitude, $p_3/p_1 = 1.8$ and $Re_a = 300,000$

APPENDIX G

Computational investigation of the influence of unsteady shock motion on aberrating structures in supersonic boundary layers

Michael D. White* and Miguel R. Visbal†

Air Force Research Laboratory, Wright-Patterson Air Force Base, Ohio 45433-7512, USA

A computational investigation of aero-optical effects for a shock-boundary layer interaction (SBLI) has been performed in the case of Mach 2 flow into a 20 degree compression ramp. Although over a grid of over 282 million points was used for the initial flow, it was determined that grids which might be acceptable for many SBLI problems was not good enough for the problem of aero-optics. It was found that a combination of grid stretching and misalignment of the shock and grid lead to non-physical density aberrations between the shock and the ramp. The grid system was improved with a new grid that was closer to shock aligned in the far-field and had much more resolution between the shock and the ramp. Preliminary optical results are presented and discussed.

I. Introduction

Supersonic flight poses numerous challenges to the study of aero-optics. Alongside the formidable issues of beam quality due to the presence of turbulent density fluctuations in the boundary layer, an additional difficulty arises with the onset of shock waves. On complex geometries, the potential for a shock boundary layer interaction (SBLI) leads to a more complicated flow-field which must be accurately modeled to resolve the aberrations. Among the more complex SBLI interactions is the shock generated at the foot of a two dimensional compression ramp. This topic has been an area of intense study for over three decades since the pioneering work of Settles, Fitzpatrick and Bogdonoff.¹ The majority of experiments and computations for SBLI compression ramps are in and around Mach 3, which is higher than typical supersonic flight. In terms of high-fidelity computation, some of the more recent work is given by: Adams,² Rizzetta et al.,³ Wu and Martin,⁴ Muppidi and Mahesh⁵ and Bisek et al.⁶ Only Bisek, et al. has a Mach number as low as 2.25, which is still outside typical supersonic flight conditions. Experimentally, lower Mach numbers are also relatively uncommon. Thomas et al.⁷ studied unsteady shock oscillations in a Mach 1.5 corner flow. Hou et al.⁸ and Ganapathisubramani et al.⁹ have in the last decade looked at unsteadiness for a Mach 2 compression ramp using PIV and PLS. SBLIs themselves have a vast literature and the reader is referred to the papers cited and reviews by: Delery,¹⁰ Andreopoulos,¹¹ Dolling,¹² and the book by Smits & Dussauge.¹³

In contrast to atmospheric propagation, the aero-optic environment tends to be much more active with smaller scale density fluctuations that cause significant aberration, degrading the quality of the beam. Reviews of this interaction between flow turbulence and optics can be found in references by Sutton,¹⁴ Jumper¹⁵ and Wang.¹⁶ In the specific area of aero-optics at speeds greater than Mach 1, Stine & Winovich¹⁷ looked at Mach numbers up to 2.5 back in the 1950s and later re-analyzed by Sutton¹⁸ in the 1980s. More recently, Gordeyev, Jumper and Hayden¹⁹ considered aero-optics in a supersonic boundary layer at Ma=2 with a

*Senior Researcher, Ohio Aerospace Institute, Associate Fellow AIAA.

†Technical Area Leader, Aerodynamic Technology Branch, AFRL/RQVA, Fellow AIAA.

Malley probe. Gao et al.²⁰ experimentally considered the statistical characteristics of the beam tilts in a Mach 3 boundary layer. Two recent hypersonic flow studies have conducted: Yanta et al.²¹ at Ma=7 and Wyckham & Smits at Ma=7.8.²² In terms of interaction of aero-optics with shock waves, the study by Gordeyev, Jumper and Hayden¹⁹ placed a wedge in the windtunnel and measured through a weak mach wave. A recent work by Gordeyev et al.²³ looked at a case with a shock wave on a cylindrical turret in transonic flow.

Computationally, Tromeur, et al.²⁴⁻²⁷ performed supersonic Large Eddy Simulations (LES) at Mach 2.3 with both adiabatic and isothermal walls at $Re_\theta = 2900$, where the aero-optics was integrated by the *OPD*. White²⁸ looked at the propagation of a beam through a M=3 boundary layer comparing the parabolic beam equation with integration by optical path differences (*OPD*). White & Visbal^{29,30} looked at multiple configurations of a M=1.3 boundary layer. The current work considers a shock-wave boundary layer interaction at Mach 2 on a compression ramp and its effect on aero-optical aberrations.

II. Governing Equations

A. Fluid Dynamics

The governing equations are the unsteady three-dimensional compressible Navier-Stokes equations. After transforming the equations from Cartesian coordinates to general time-dependent body-fitted curvilinear coordinates, the equations can be cast into strong conservation-law form as

$$\frac{\partial Q}{\partial t} + \frac{\partial}{\partial \xi} (F - \frac{1}{Re_\infty} F_v) + \frac{\partial}{\partial \eta} (G - \frac{1}{Re_\infty} G_v) + \frac{\partial}{\partial \zeta} (H - \frac{1}{Re_\infty} H_v) = 0. \quad (1)$$

Here t is the time, ξ, η, ζ are the computational coordinates, Q the vector of dependent variables, F, G, H the inviscid flux vectors, and F_v, G_v, H_v the viscous flux vectors. The vector of dependent variables is

$$Q = \frac{1}{J} \begin{bmatrix} \rho & \rho u & \rho v & \rho w & \rho E \end{bmatrix}^T \quad (2)$$

and the vector fluxes are

$$F = \frac{1}{J} \begin{bmatrix} \rho U \\ \rho u U + \xi_x p \\ \rho v U + \xi_y p \\ \rho w U + \xi_z p \\ \rho E U + \xi_{x_i} u_i p \end{bmatrix} \quad (3)$$

$$G = \frac{1}{J} \begin{bmatrix} \rho V \\ \rho u V + \eta_x p \\ \rho v V + \eta_y p \\ \rho w V + \eta_z p \\ \rho E V + \eta_{x_i} u_i p \end{bmatrix} \quad (4)$$

$$H = \frac{1}{J} \begin{bmatrix} \rho W \\ \rho u W + \zeta_x p \\ \rho v W + \zeta_y p \\ \rho w W + \zeta_z p \\ \rho E W + \zeta_{x_i} u_i p \end{bmatrix} \quad (5)$$

$$F_v = \frac{1}{J} \begin{bmatrix} 0 \\ \xi_{x_i} \tau_{i1} \\ \xi_{x_i} \tau_{i2} \\ \xi_{x_i} \tau_{i3} \\ \xi_{x_i} (u_j \tau_{ij} - q_i) \end{bmatrix} \quad (6)$$

$$G_v = \frac{1}{J} \begin{bmatrix} 0 \\ \eta_{x_i} \tau_{i1} \\ \eta_{x_i} \tau_{i2} \\ \eta_{x_i} \tau_{i3} \\ \eta_{x_i} (u_j \tau_{ij} - q_i) \end{bmatrix} \quad (7)$$

$$H_v = \frac{1}{J} \begin{bmatrix} 0 \\ \zeta_{x_i} \tau_{i1} \\ \zeta_{x_i} \tau_{i2} \\ \zeta_{x_i} \tau_{i3} \\ \zeta_{x_i} (u_j \tau_{ij} - q_i) \end{bmatrix} \quad (8)$$

where

$$U = \xi_t + \xi_{x_i} u_i, \quad V = \eta_t + \eta_{x_i} u_i, \quad W = \zeta_t + \zeta_{x_i} u_i \quad (9)$$

$$E = \frac{T}{\gamma(\gamma-1)M_\infty^2} + \frac{1}{2}(u^2 + v^2 + w^2). \quad (10)$$

In the preceding expressions, u, v, w are the Cartesian velocity components, ρ the density, p the pressure, T the temperature, E the total specific energy, and J the Jacobian of the coordinate transformation. All length scales have been nondimensionalized by an arbitrary length scale \mathcal{L} , and dependent variables have been normalized by their reference values except for p which has been nondimensionalized by $\rho_\infty u_\infty^2$. Components of the heat flux vector and stress tensor may be expressed as

$$q_i = - \left[\frac{1}{(\gamma-1)M_\infty^2} \right] \left(\frac{\mu}{Pr} \right) \frac{\partial \xi_j}{\partial x_i} \frac{\partial T}{\partial \xi_j} \quad (11)$$

$$\tau_{ij} = \mu \left(\frac{\partial \xi_k}{\partial x_j} \frac{\partial u_i}{\partial \xi_k} + \frac{\partial \xi_k}{\partial x_i} \frac{\partial u_j}{\partial \xi_k} - \frac{2}{3} \delta_{ij} \frac{\partial \xi_l}{\partial x_k} \frac{\partial u_k}{\partial \xi_l} \right). \quad (12)$$

where for compactness of notation, (ξ_1, ξ_2, ξ_3) is used in place of (ξ, η, ζ) . The Sutherland law for the molecular viscosity coefficient μ and the perfect gas relationship:

$$p = \frac{\rho T}{\gamma M_\infty^2} \quad (13)$$

were also employed.

B. Laser Propagation

The main methods for propagating the beam are based on the *OPD*, integral techniques (such as Rayleigh-Sommerfeld, Fresnel or Fraunhofer) or the parabolic beam equations (cf. [28]). The first two of these methods are often combined for propagation to the far-field. The latter technique can be more easily extended to the addition of more physics and can handle results filling a volume more easily than the integral techniques. However, any of these techniques can be used in conjunction with the others for optimal results.

The optical path difference (*OPD*) based on the reference index of refraction n_r is:

$$OPD = \int_0^L (n - n_r) ds \quad (14)$$

The relationship of n to the density, ρ , is given empirically by the Gladstone-Dale constant:

$$n \approx 1 + K_{gd} \rho \quad (15)$$

where K_{gd} is approximately (in SI units):^{31,32}

$$K_{gd} \approx 2.24 \times 10^{-4} \left(1 + \frac{7.52 \times 10^{-3}}{\lambda^2} \right) \left[\frac{m^3}{kg} \right] \quad (16)$$

and the laser wavelength, λ , is measured in microns. If the deflection of the beam or ray is negligible, then the ds may be replaced with dz .

In the present work, the OPD has been referenced to the freestream density and “non-dimensionalized” by $K_{gd}\rho_\infty$ in order to generalize the work for different altitude conditions. A benefit of this choice of reference density is that the OPD becomes independent of L once the freestream is reached. Thus, equation (14) can be re-written as:

$$OPD^* = \frac{OPD}{K_{gd}\rho_\infty} = \int_0^L (\rho^* - 1) dz \quad (17)$$

where $\rho^* = \rho/\rho_\infty$. For simplicity, the * 's will be dropped. Other common optical path differences are the piston removed and tip/tilt corrected OPD . In the former, the instantaneous average over the aperture is subtracted, while in the latter a least-square plane is fit to the instantaneous OPD and subtracted. Thus, the OPD looks qualitative identical to the instantaneous piston corrected OPD , differing only by a constant. The subscripts p and tt of OPD correspond to piston removed and tip/tilt correction, respectively.

In simulations, the OPD is typically defined to some reference calculation in a medium with constant index of refraction (based here on the reference density). However, the experiments typically remove the piston and tip/tilt. For notational purposes OPD_{nr} will refer to the OPD as calculated by the present codes, and OPD_p and OPD_{tt} will correspond to the piston removed and piston, tip/tilt removed path differences, respectively. The rms OPD is calculated first over the aperture:

$$OPD_{rms}(t, z) = \sqrt{\{OPD_{nr}^2(x, y; t, z)\} - \{OPD_{nr}(x, y; t, z)\}^2} = \sqrt{\{OPD_p^2(x, y; t, z)\}} \quad (18)$$

where the $\{\}$'s denote averages over some aperture plane. For the OPD equations x and y refer to a local coordinate system attached to the aperture surface. The direction z is the location of the aperture plane along the beam path. Likewise, the tip/tilt corrected OPD_{rms} is simply:

$$OPD_{tt,rms}(t, z) = \sqrt{\{OPD_{tt}^2(x, y; t, z)\}} \quad (19)$$

For the RMS over all of the unsteady samples, the equation is simply:

$$OPD_{rms}(z) = \sqrt{<OPD_{rms}^2(t, z)> - <OPD_{rms}(t, z)>^2} \quad (20)$$

where the $<>$'s denote averages over time. The tip/tilt corrected rms is calculated in the same manner. Additional details regarding the numerical implementation are covered in detail in Refs. 28,33

C. Computational methodology

The simulations were performed utilizing the extensively validated high-order Navier-Stokes solver *FDL3DI*.^{34,35} The solver is capable of using both high-order compact differences and a Roe solver of up to third order accurate.³⁴ The simulations utilize 6th-order compact differences for the spatial differencing along a coordinate line (ξ, η, ζ) given by:

$$\frac{1}{3}\phi'_{j-1} + \phi'_j + \frac{1}{3}\phi'_{j+1} = \frac{1}{9}\frac{\phi_{j+1} - \phi_{j-1}}{2} + \frac{14}{9}\frac{\phi_{j+2} - \phi_{j-2}}{4} \quad (21)$$

At the boundary, higher order one-sided formulas are utilized which retain the tridiagonal form of the scheme.^{34,35} In the current simulation, the wall Neumann boundary conditions are solved 4th-order one-sided expression. The viscous fluxes are implemented by successive application of the first order scheme.

To eliminate spurious components, the scheme utilizes a high-order, low-pass spatial filter.^{35,36} These filters eliminate the spurious wavelengths of 2Δ while leaving the low frequency components unattenuated. For near boundary points, the schemes are also constructed one-sided in a fashion similar to the derivatives.^{35,36} One benefit to this filtered approach is that by stretching the grid, the filter can be utilized as an effective means of preventing artificial reflections in the far-field boundary conditions.³⁷ For transitional and turbulent flows, the above combination of high-fidelity components is collectively known as high fidelity implicit large-eddy simulation (HFILES) and provides an effective alternative to traditional SGS models.³⁸ Temporal integration is accomplished with an iterative, implicitly approximately-factored procedure.^{38,39}

To prevent unnatural oscillation from an under-resolved shock, the code uses a shock detector based on pressure to switch from high-order compact with filtering to third-order Roe.

$$\phi = \frac{|p_{i+1} - 2p_i + p_{i-1}|}{(1 - \omega)(|p_{i+1} - p_i| + |p_i - p_{i-1}|) + \omega(|p_{i+1} + 2p_i + p_{i-1}|)} \quad (22)$$

If $\phi > 0.05$ then the scheme is replaced by Roe in the shock region. Time advancement is Beam-Warming⁴⁰ in the diagonalized form of Pulliam and Chaussee.⁴¹

III. Results

A. Configuration

The current Mach number is 2.0 with a 20-degree compression ramp. The initial grid was determined using the analytical streamlines and potentials of an inviscid, incompressible 160-degree corner flow. The wall normal stretching was taken from the previous study of a Mach 1.3 flat plate boundary layer. The initial grid dimensions were $2158 \times 317 \times 413$ points in the stream-wise, normal and span-wise directions respectively. The plasma trip for the turbulence was unchanged from previous studies at $M=1.3$. In looking at the results for this grid, it was determined that more refinement was needed between the wall and the shock to resolve the density aberrations for aero-optical integration. There was also a noticeable oscillation in the shock due to grid stretching and lack of shock alignment as seen in figure 1. Based on the mean pressure distribution for an approximate shock location, a new grid was created to bound the shock and provide more resolution as is seen in figure 2. A decision was made to retain the majority of the old grid in a large overlap region to prevent stair-casing from introducing unnecessary interpolation errors. The old grid was cut near the wall to insure that the boundary layer behind the shock was dominated by the improved grid and not the original one. The new grid system comprised of three grids with dimensions $1266 \times 317 \times 413$, $891 \times 93 \times 413$ and the new shock grid of $891 \times 388 \times 413$. The new system comprising of over 342 million grid points. In this configuration, all matching is point-to-point except in the overlap area shown in green in figure 2. For the new shock grid, all interpolation takes place in the supersonic region upstream of the shock. The regions where Roe is solved due to the pressure switch is shown in figure 3. The new grid is benefited not only by the added resolution, but by the closer alignment to the shock. This is clearly demonstrated in figure 4, where the shock is not only sharper, but the unphysical herring-bone pattern coming from the misalignment is no longer present. The differences between the shocks can also be seen in the isosurface of density gradient in figure 5.

A snapshot of the flow variables on the new grid can be seen in figure 6. The mean and fluctuating quantities of the incoming supersonic boundary layer were taken approximately 2.4δ upstream of the separation (as determined by the mean $\partial u / \partial y|_{wall} = 0$) and 6.5δ upstream of the corner. At this location, $Re_\theta = 1300$ and $\Delta y_{wall}^+ = 0.27$. Comparison to the previous $M=1.3$ computation is given in Table 1. The effect of the shock foot on the pressure can be seen in the mean velocity profiles in figure 8(a). The curves in this figure are labeled by wall pressure [recalling that non-dimensionally $p_\infty = 1/(\gamma M_\infty^2)$]. As one moves 1.4δ downstream from the reference boundary layer location, there is a 3.5% increase in the wall pressure. Figure 8(b) compares a boundary layer profile near the end of the resolved region on the ramp with the upstream boundary layer. As can clearly be seen the boundary layer behind the ramp is (as expected) in non-equilibrium, which a significant amount of fluctuation in the inviscid region between the near wall layer and the shock. The non-equilibrium boundary layer behind the shock adds a tremendous amount of aberrating structures. Figure 9 shows the tip/tilt corrected OPD_{tt} for a square aperture in the region of the reference boundary layer and the region behind the shock. The figures show that there aberration is more than three times behind the shock as the boundary layer upstream.

Mach	Grid points	Δy_{wall}^+	Δx^+	Δz^+	Δt^+	Re_θ	c_f
1.3	209 million	0.31	12.2	5.3	0.015	1426	0.00354
2.0	342 million	0.27	10.6	4.6	0.012	1300	0.00320

Table 1. Parameters of $M=2$ upstream boundary layer compared to $M=1.3$ boundary layer.

Motion of the shock in the stream-wise direction can be seen in figure 10 separated by 1.4 non-dimensional

time units. Compression waves from the SBLI interact with the shock downstream and produce localized bending as seen in figure 11. On the old grid, there appears to be less movement of the shock (although the spreading of the shock makes this difficult to determine for certain). Figure 12 shows the mean and rms density on the new and old shock systems. From figure 12 (b) & (d) it can be seen that numerical artifacts lead to noise being radiated from the shock towards the ramp wall. Since the rms is an indicator of shock movement, it can be seen that away from the corner region, the value drops off sharply. In comparison, figure 12(c) shows the rms of the new system does not decrease as one proceeds downstream along the shock. To the contrary, it actually increases. Peak density rms on the new system is approximately 2.7 times that of the old system.

For computing the OPD on the ramp, the solution was interpolated onto an optical grid as shown in figure 13. While high-order is important to resolve and propagate the the turbulence, it has been demonstrated²⁸ that integration of the OPD is often less stringent. In the current case, the density has been interpolated to an optical grid using second-order trilinear interpolation.

The effect of the non-equilibrium boundary layer behind the shock for the two solutions (original configuration and new grid) on the OPD can be seen in figure 14-16. There are three levels. The first encompasses the wall portion of the boundary layer where viscous and vorticity effects are present. The second region is in the inviscid part of the boundary layer, where one can still see a significant number of structures are present. The third region contains the remainder of the inviscid region and the shock. This first thing one notices is that the original SBLI grid completely loses the fine scale structure between the boundary layer and the shock due to a lack of resolution. Similarly the shock is smeared out over a larger distance in real, if not computational, space. As expected, one can see that the dominate feature of the flow is tip/tilt. This is especially clear in figure 16, where the aberrating structures appear only as perturbations. To see the effect of the grids on the different regions, the local tip/tilt-corrected OPD_{tt} between each of two regions is shown in figures 17-19. Also seen in figure 15 and 18 are remnants of the artificial noise that is being radiated from the boundary layer. These figures show that there is a significant amount of small scale structure between the shocks that needs to be resolved. Although there is a large difference in the small aberrating structures, the general tip/tilt is very similar as seen in figure 20. However, it should be mentioned that this this close agreement is in large part due to the original grid sharing the near-wall boundary layer of the new grid. In general, one would not expect the two turbulent solutions to be so closely correlated. The RMS of the tip/tilt corrected $OPD_{tt,rms}$ is given in Table 2.

Levels	New shock grid	Original shock grid
1-0	0.01795	0.01844
2-1	0.0067	0.0021
3-2	0.0078	0.0026

Table 2. $OPD_{tt,rms}$ for the different levels in figures 17-19.

IV. Summary and conclusions

A high-fidelity computation of a Mach 2 shock-boundary layer interaction has been computed in order to investigate the effects of SBLIs on aero-optics. Initial results demonstrate that grids conventionally used for SBLI are insufficient to resolve the structure necessary for an accurate characterization of the aberrating structures. A combination of grid stretching and grid/shock misalignment can lead to non-physical noise radiating from the shock towards the ramp. The lack of an equilibrium boundary layer leads to a much more optically active flow than a simple boundary layer. The resulting tip/tilt corrected OPD_{tt} is more than three times larger in the region behind the shock compared with the upstream equilibrium boundary layer. While large scale motion is prevalent for the shock, the optical integration picks up fine scale structure that is not insignificant. This is a preliminary look at an ongoing effort in this area.

V. Acknowledgements

This project was sponsored by Douglas Smith of the Air Force Office of Scientific Research (AFOSR). The authors would like to thank Dr. Jon Poggie of the Air Force Research Laboratory (AFRL) his helpful discussions regarding this study. Computational resources were supported in part by grants of supercomputer time from the U. S. Department of Defense Major Shared Resource Centers at Wright-Patterson AFB, OH.

References

- ¹Settles, G., Fitzpatrick, T., and Bogdonoff, S., "Detailed study of attached and separated compression corner flowfields in high Reynolds number supersonic flow," *AIAA J.*, Vol. 17, 1979, pp. 579–585.
- ²Adams, N., "Direct Simulation of the turbulent boundary layer along a compression ramp at $M=3$ and $Re_\theta=1685$," *JFM*, Vol. 420, No. 1, 2000, pp. 47–83.
- ³Rizzetta, D. and Visbal, M., "Large-Eddy Simulation of Supersonic Compression-Ramp Flows," AIAA Paper 2001-2858, 2001.
- ⁴Wu, M. and Martin, M., "Direct Numerical Simulation of Supersonic Turbulent Boundary Layer Over a Compression Ramp," *AIAA J.*, Vol. 45, No. 4, 2007, pp. 879–889.
- ⁵Muppudi, S. and Mahesh, K., "DNS of Unsteady Shock Boundary Layer Interaction," AIAA Paper 2011-724, 2011.
- ⁶Bisek, Rizzetta, and Poggie, "Plasma control of a turbulent shock boundary-layer interaction," *AIAA J.*, 2013, pp. 1–16, DOI: 10.2514/1.J052248.
- ⁷Thomas, F., Putnam, C., and Chu, H., "On the mechanism of Unsteady Shock Oscillation in Shock Wave/Turbulent Boundary Layer Experiments," *Exp. in Fluids*, Vol. 18, 1994, pp. 69–81.
- ⁸Hou, Y., Clemens, N., and Dolling, D., "Wide field PIV study of shock-induced turbulent boundary layer separation," AIAA Paper 2003-0441, 2003.
- ⁹Ganapathisubramani, B., Clemens, N., and Dolling, D., "Effects of upstream boundary layer on unsteadiness of shock-induced separation," *J. Fluid Mech.*, Vol. 585, 2007, pp. 369–394.
- ¹⁰Delery, J. and G., M. J., "Shock-wave boundary layer interactions," Tech. Rep. AGARDograph 280, 1986.
- ¹¹Andreopoulos, Y., Agui, J. H., and Briassuis, G., "Shock Wave-Turbulence Interactions," *Ann. Rev. Fluid Mech.*, Vol. 32, 2000, pp. 309–345.
- ¹²Dolling, D. S., "50 years of shock-wave boundary interaction research: What next?" *AIAA J.*, Vol. 39, No. 8, 2001, pp. 1517–1531.
- ¹³Smits, A. J. and Dussauge, J.-P., *Turbulent Shear Layers in Supersonic Flow*, Springer, 2nd ed., 2006.
- ¹⁴Sutton, G. W., "Aero-optical Foundations and Applications," *AIAA J.*, Vol. 23, 1985, pp. 1525–1537.
- ¹⁵Jumper, E. J. and Fitzgerald, E. J., "Recent Advances in aero-optics," *Progress in Aerospace Sciences*, Vol. 37, 2001, pp. 299–339.
- ¹⁶Wang, M., Mani, A., and S., G., "Physics and Computation of Aero-optics," *Ann. Rev. Fluid Mech.*, Vol. 44, 2012, pp. 299–321.
- ¹⁷Stine, H. A. and Winovich, W., "Light Diffusion through High-Speed Turbulent Boundary Layers," Tech. Rep. RM-A56B21, NACA, 1956.
- ¹⁸Sutton, G. W., "Optical Imaging Through Aircraft Turbulent Boundary Layers," *Aero-Optical Phenomena*, edited by K. G. Gilbert and L. J. Otten, Vol. 80 of *Progress in Astronautics and Aeronautics*, 1982, pp. 139–188.
- ¹⁹Gordyev, S., Jumper, E., and Hayden, T., "Aero-optical Effects of Supersonic Boundary Layers," *AIAA J.*, Vol. 50, No. 3, 2012, pp. 682–690.
- ²⁰Gao, Q., Jiang, Z., Yi, S., and Wang, X., "Statistical characteristics of the tilts of the aero-optical aberration caused by the supersonic turbulent boundary layer," *Optics Letters*, Vol. 38, No. 5, 2013, pp. 751–753.
- ²¹Yanta, e. a., AIAA Paper 2000-2357, 2000.
- ²²Wyckham, C. and Smits, A., "Aero-optic Distortion in Transonic and Hypersonic Turbulent Boundary Layers," *AIAA J.*, Vol. 47, No. 9, Sept 2009, pp. 2158–2168.
- ²³Gordyev, S., Burns, R., Jumper, E., Gogineni, S., Paul, M., and Wittich, D., "Aero-Optical Mitigation of Shocks Around Turrets at Transonic Speeds Using Passive Flow Control," AIAA Paper 2013-0717, 2013.
- ²⁴Tromeur, E., Garnier, E., Sagaut, P., and Basdevant, C., "LES of aero-optical effects in a turbulent boundary layer," *J. of Turbulence*, Vol. 4, No. 5, 2003.
- ²⁵Deron, R. D., Tromeur, E., Dussauge, J. P., Garnier, E., and Sagaut, P., "Study of turbulent boundary layer optical effects using Shack-Hartmann wavefront analysis and LES simulations," *Advances in Turbulence X*, 2004, Paper no:801.
- ²⁶Tromeur, E., Garnier, E., and Sagaut, P., "Large-eddy simulation of aero-optical effects in a spatially developing turbulent boundary layer," *J. of Turbulence*, Vol. 7, No. 1, 2006.
- ²⁷Tromeur, E., Garnier, E., and Sagaut, P., "Analysis of Sutton Model for Aero-Optical Properties of Compressible Boundary Layers," *J. of Fluids Engr.*, Vol. 128, March 2006, pp. 239–246.
- ²⁸White, M. D., "High-order parabolic beam approximation for aero-optics," *J. of Comput. Phys.*, Vol. 229, 2010, pp. 5465–5485.
- ²⁹White, M. and Visbal, M., "Simulation of Aero-Optical Interactions in Transonic Boundary Layers," AIAA Paper 2011-3279, June 2011.
- ³⁰White, M. and Visbal, M., "Aero-optics of Compressible Boundary Layers in the Transonic Regime," AIAA Paper 2012-2984, 2012.

³¹Strohbehn, J. W., editor, *Laser Beam Propagation in the Atmosphere*, Vol. 25 of *Topics in Applied Physics*, Springer-Verlag, 1978.

³²Andrews, L. C. and Phillips, R. L., *Laser Beam Propagation Through Random Media*, SPIE Press, 2nd ed., 2005.

³³White, M., Morgan, P., and Visbal, M., "High Fidelity Aero-Optical Analysis," AIAA Paper 2010-433, Jan 2010.

³⁴Gaitonde, D. and Visbal, M., "High-Order Schemes for Navier-Stokes Equations:Algorithm and Implementation into FDL3DI," Tech. Rep. AFRL-VA-WP-TR-1998-3060, Air Force Research Labs, 1998.

³⁵Visbal, M. and Gaitonde, D., "High-Order Accurate Methods for Complex Unsteady Subsonic Flows," *AIAA Journal*, Vol. 37, No. 10, 1999, pp. 1231-1239.

³⁶Lele, S. K., "Compact Finite Difference Schemes with Spectral-like Resolution," *J. Comp. Phys.*, Vol. 103, 1992, pp. 16-42.

³⁷Visbal, M. and Gaitonde, D., "Very High-Order Spatially Implicit Schemes for Computational Acoustics on Curvilinear Meshes," *Journal of Computational Acoustics*, Vol. 9, No. 4, 2001, pp. 1259-1286.

³⁸Visbal, M. and Rizzetta, D., "Large-Eddy Simulation on Curvilinear Grids Using Compact Differencing and Filtering Schemes," *Journal of Fluids Engineering*, Vol. 124, No. 4, December 2002, pp. 836-847.

³⁹Visbal, M., Morgan, P., and Rizzetta, D., "An Implicit LES Approach Based on High-Order Compact Differencing and Filtering Schemes," *AIAA Paper 2003-4098*, June 2003.

⁴⁰Beam, R. and Warming, R., "An Implicit Factored Scheme for the Compressible Navier-Stokes Equations," *AIAA Journal*, Vol. 16, No. 4, 1978, pp. 393-402.

⁴¹Pulliam, T. and Chaussee, D., "A Diagonal Form of an Implicit Approximate-Factorization Algorithm," *Journal of Computational Physics*, Vol. 39, No. 2, 1981, pp. 347-363.

⁴²DeGraaff, D. B. and Eaton, J. K., "Reynolds-number scaling of the flat-plate turbulent boundary layer," *J. Fluid Mechanics*, Vol. 422, 2000, pp. 319-346.

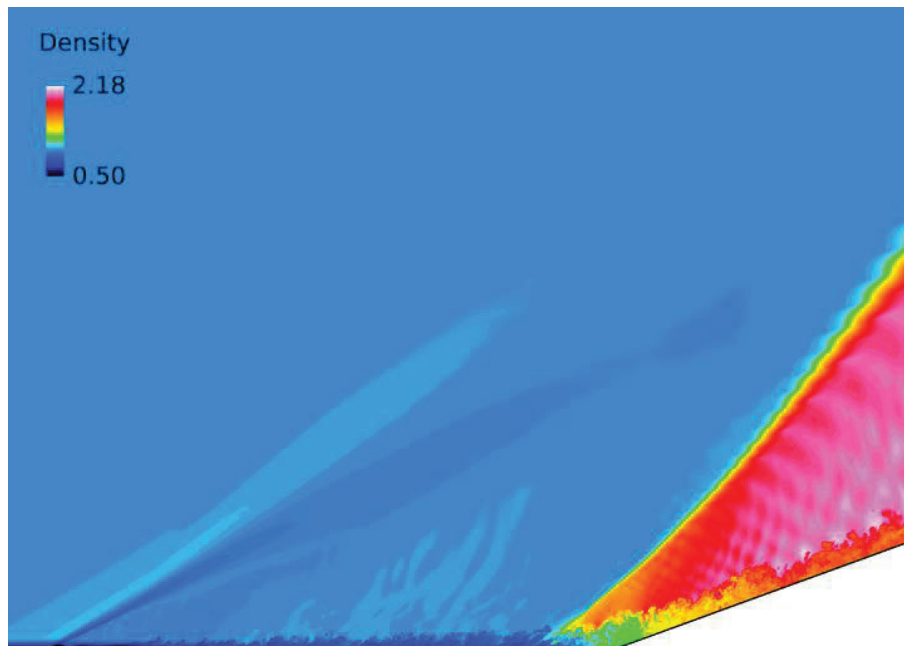


Figure 1. Original grid configuration

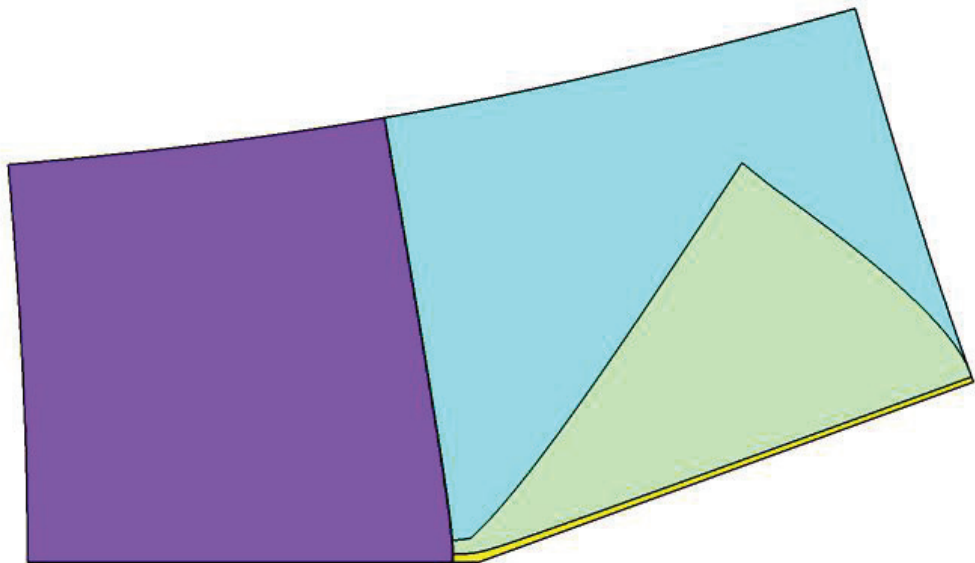


Figure 2. Picture of new grid (yellow/green) inset with the original grid. Green region is the overlap between the new grid and the cutout (blue) of the old grid.

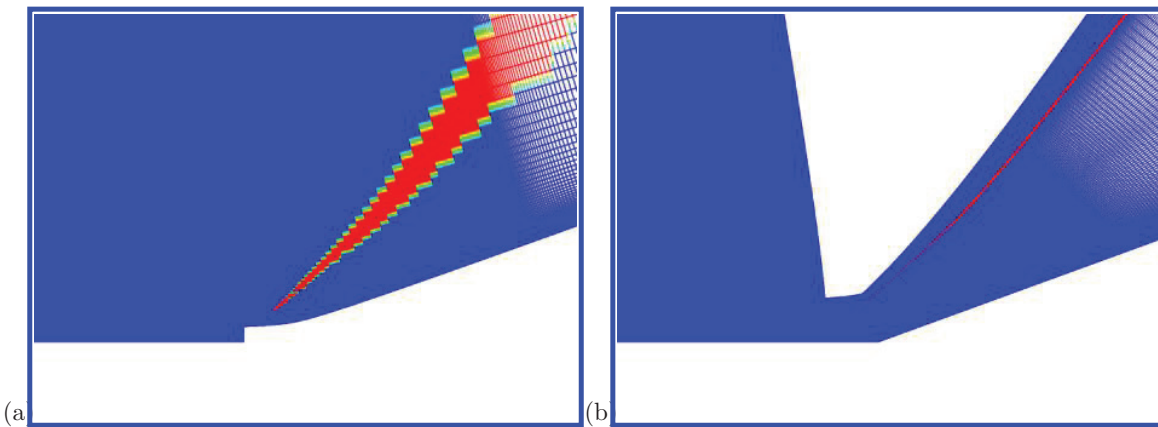


Figure 3. Cutout regions where Roe is solved on for the shock. (a) Original configuration. (b) New configuration

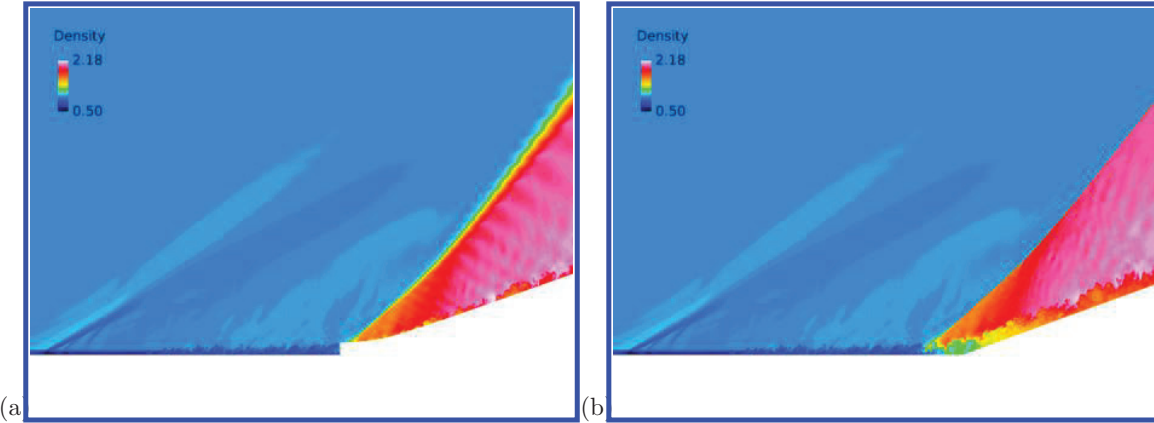


Figure 4. (a) Original grid system modified with boundary layer cutout. (b) Full grid system showing the shock on the new grid.

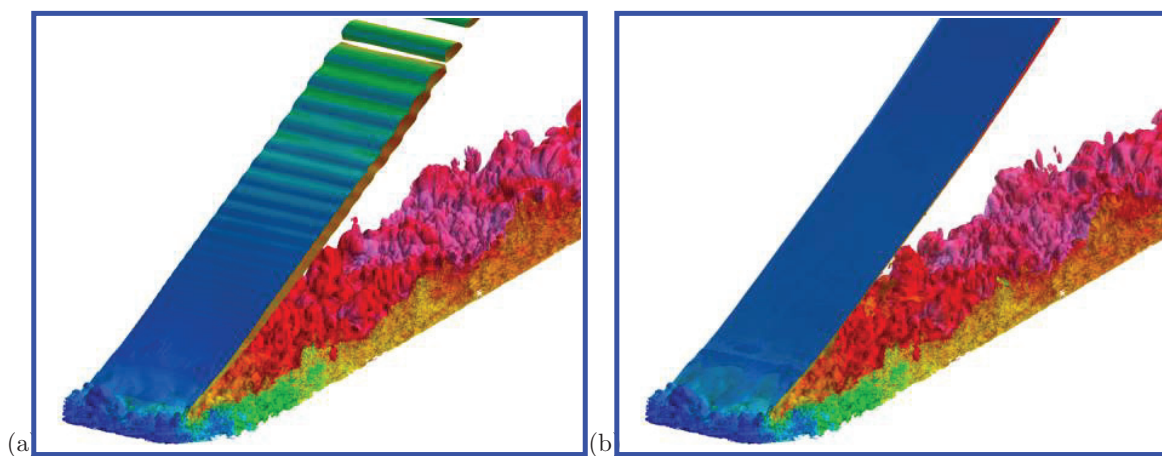


Figure 5. Isosurface of density gradient colored by density (a) Original grid system. (b) New shock grid.

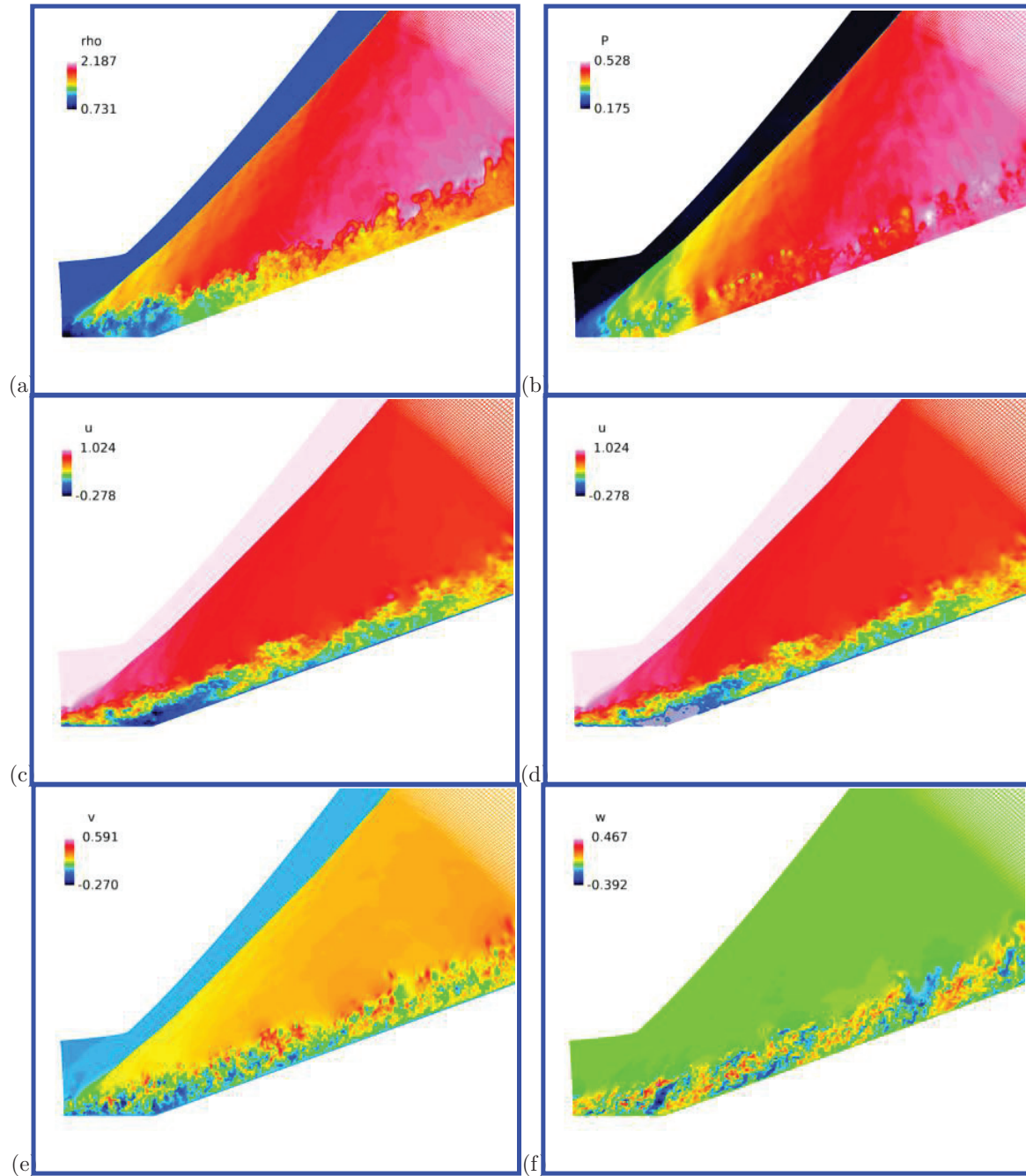


Figure 6. (a) density (b) pressure (c) u-velocity (d) u-velocity with negative velocities washed out (e) v-velocity (f) w-velocity.

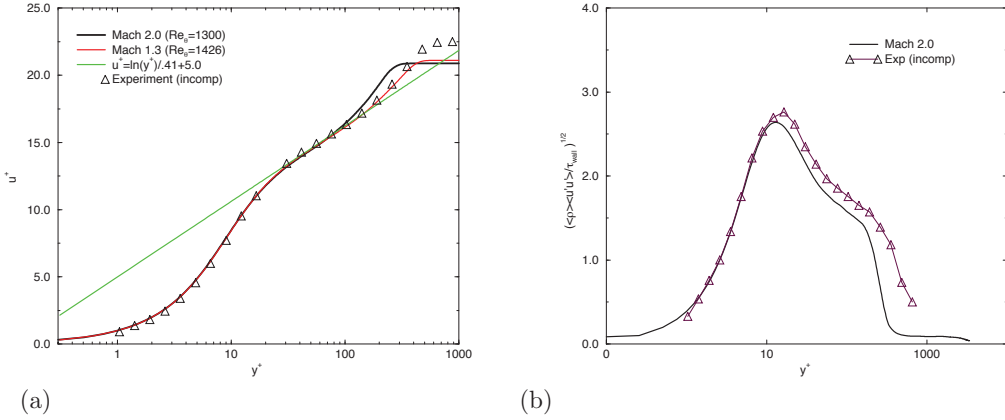


Figure 7. (a) Mean u values ahead of the shock foot. (b) rms values. [Experiment from 42]

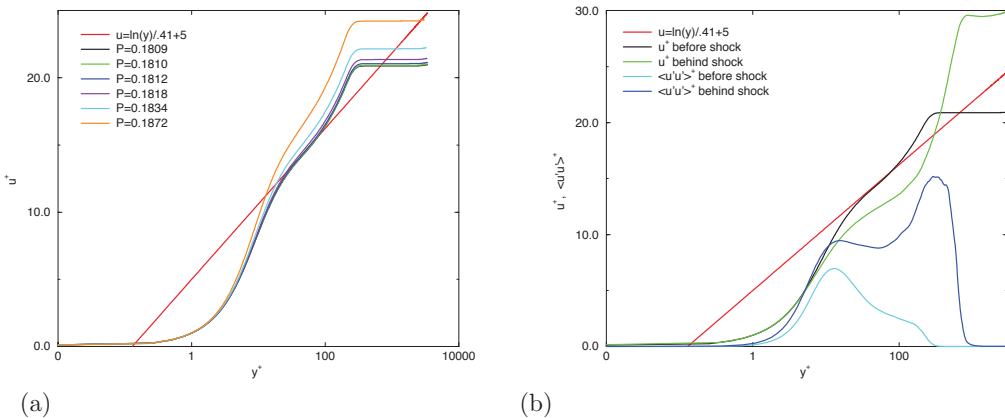


Figure 8. Effect of shock on velocity profiles. (a) Mean u as one approaches the shock foot. (b) mean and mean-square of the u velocity before and after the shock.

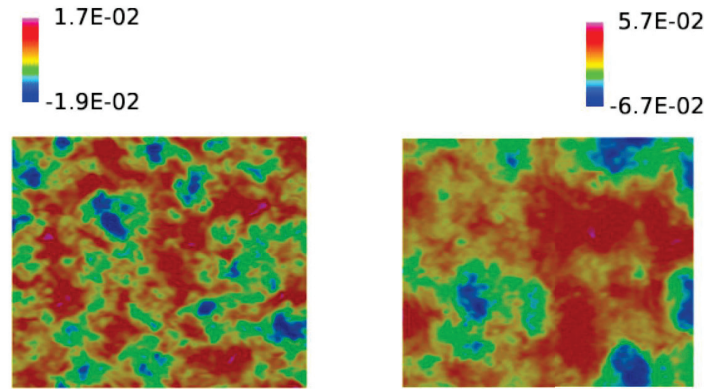


Figure 9. Tip-tilt corrected OPD_{tt} between boundary layer (left) and ramp with shock (right)

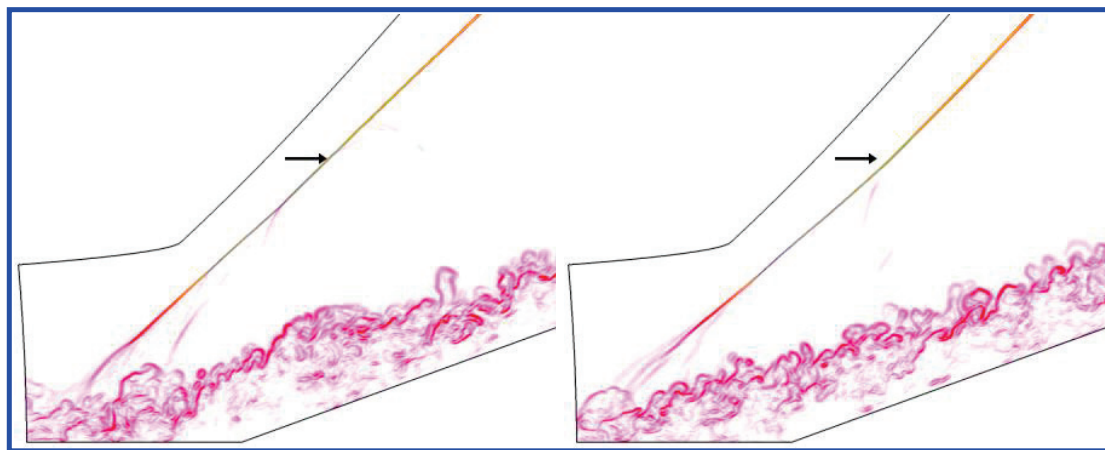


Figure 10. Shock location as shown by the gradient of density at 1.4 non-dimensional time units apart.

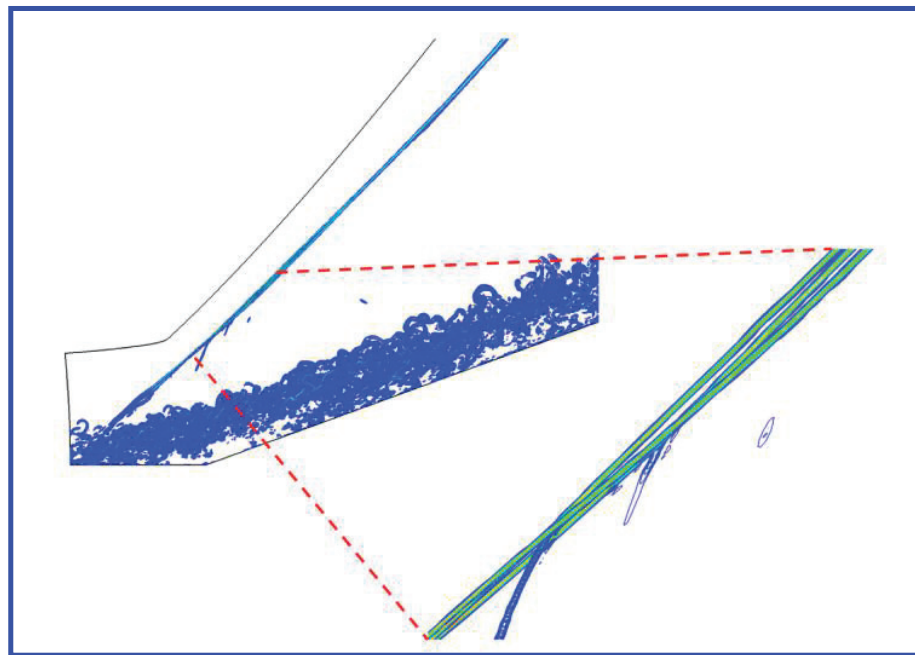


Figure 11. Zoom of shock location at three different times.

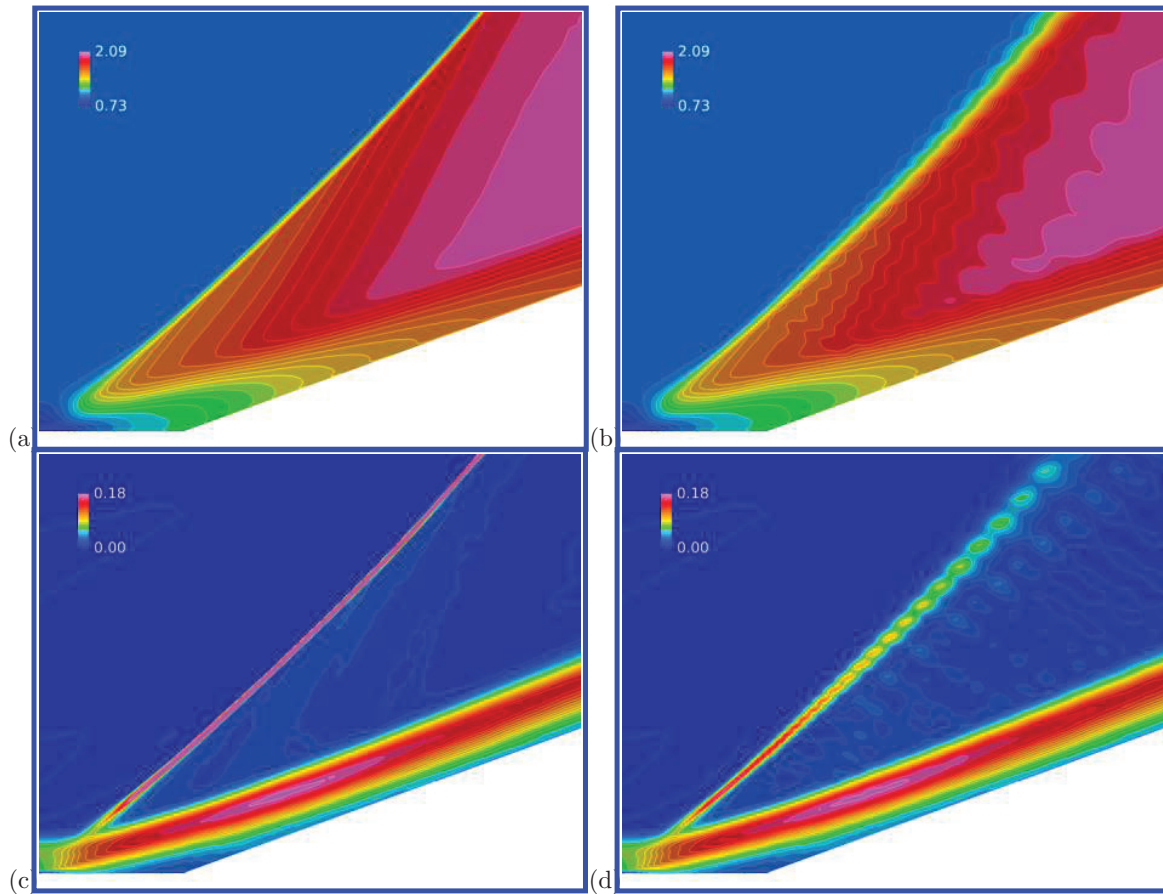


Figure 12. Mean and rms values of density. (a) mean density, new grid (b) mean density, old grid (c) rms density, new grid (d) rms density, old grid.

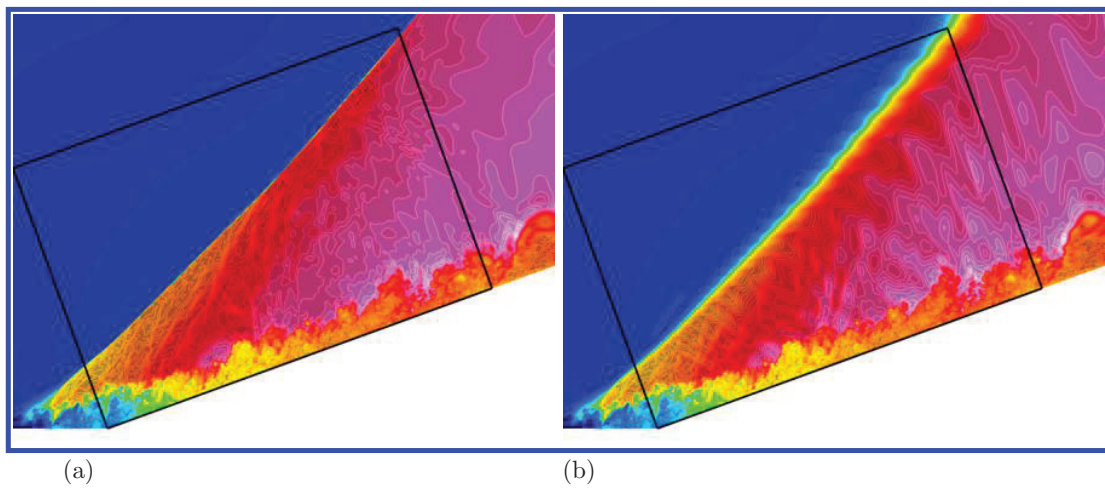


Figure 13. Density showing optical grid. (a) New grid. (b) Old grid

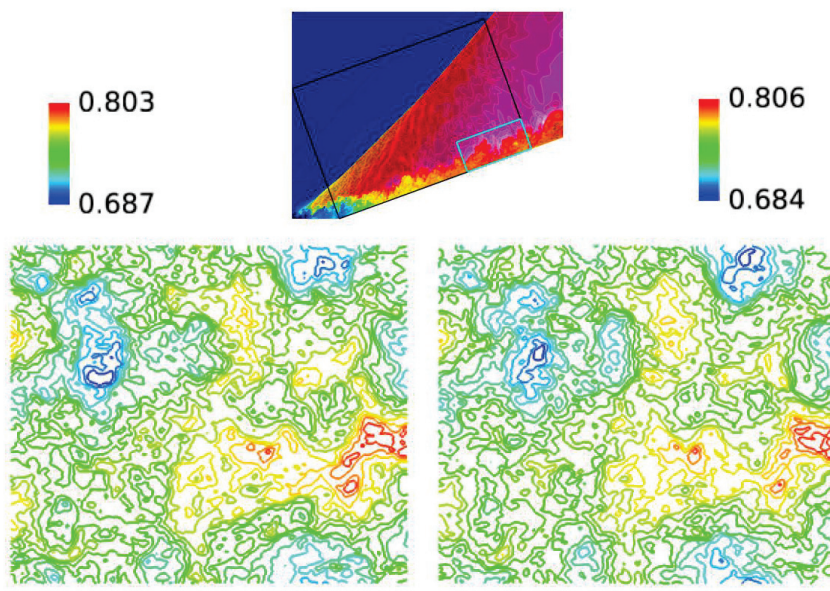


Figure 14. OPD near the top of the boundary layer. Left: new shock grid. Right: original grid

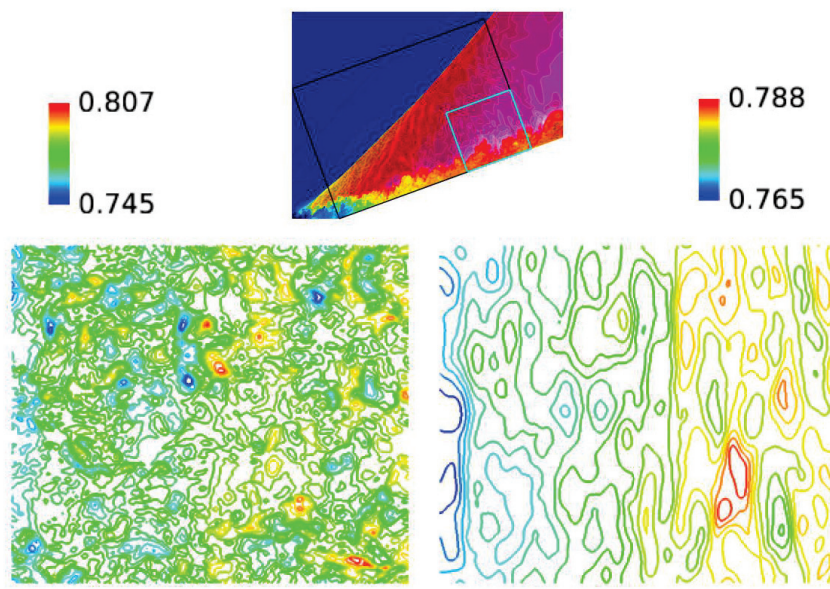


Figure 15. OPD just below the shock. Left: new shock grid. Right: original grid

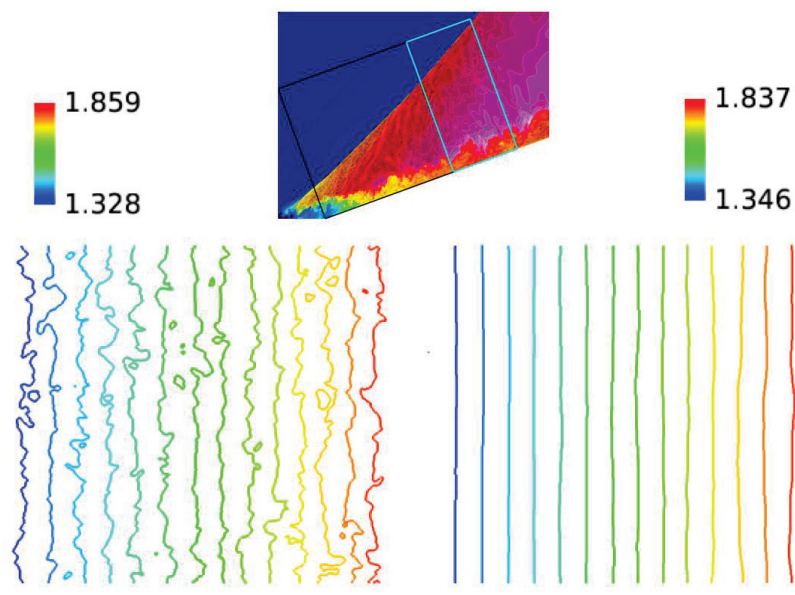


Figure 16. *OPD* beyond the shock. Left: new shock grid. Right: original grid

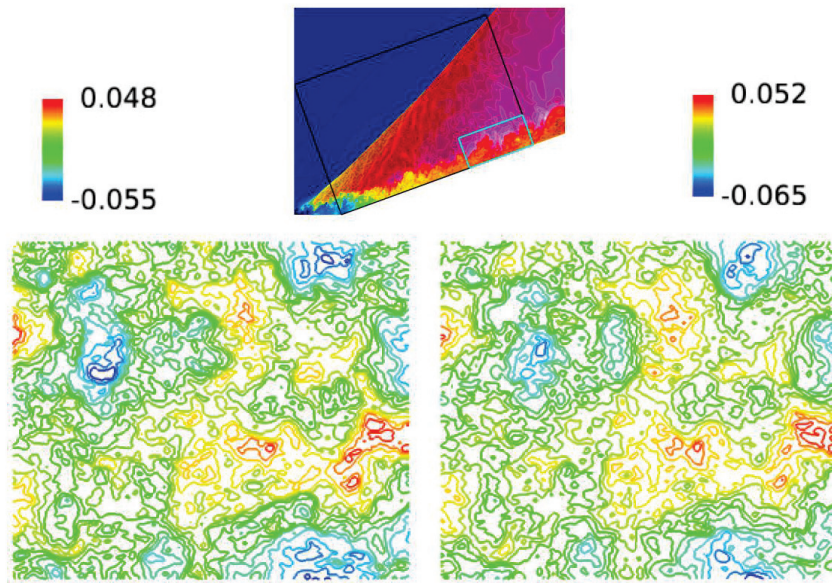


Figure 17. Tip-tilt corrected OPD_{tt} between the top of the boundary layer and the ramp wall. Left: new shock grid. Right: original grid.

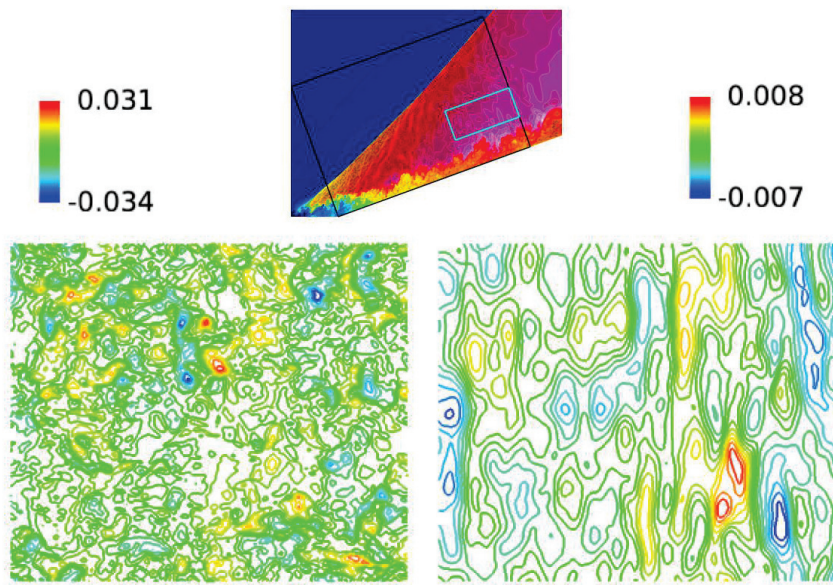


Figure 18. Tip-tilt corrected OPD_{tt} between the top of the boundary layer and the shock. Left: new shock grid. Right: original grid.

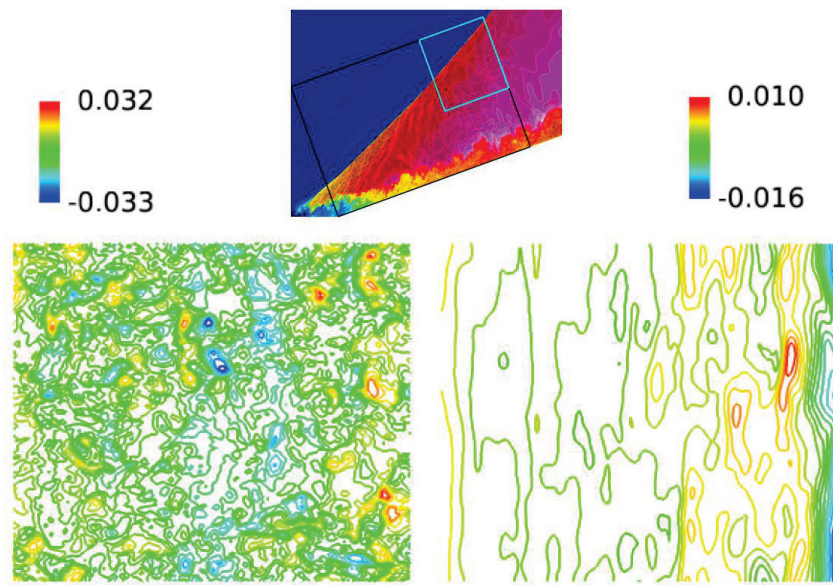


Figure 19. Tip-tilt corrected OPD_{tt} between the bottom and top of the shock. Left: new shock grid. Right: original grid.

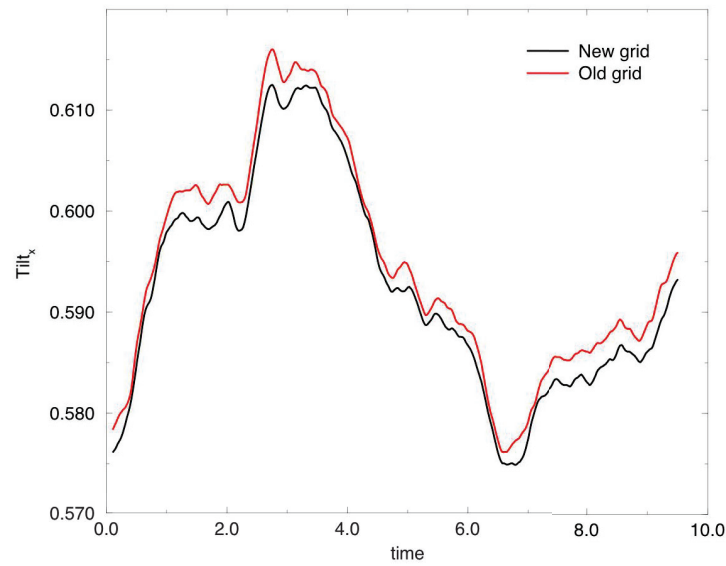


Figure 20. Time history of tip/tilt in the x-direction.